UNIVERSITÉ DE STRASBOURG

ÉCOLE DOCTORALE MATHEMATIQUES, SCIENCES DE L'INFORMATION ET DE L'INGENIEUR

Laboratoire des sciences de l'ingénieur, de l'informatique et de l'imagerie (ICube) – UMR 7357

THÈSE présentée par :

Nicolas Reiminger

Soutenue publiquement le : **21 septembre 2020**

pour obtenir le grade de : **Docteur de l'université de Strasbourg**

Discipline/Spécialité : Sciences de l'Ingénieur – Mécanique des fluides

---

3D Modelling of Air Pollution at Urban Scale

DIRECTION DE LA THESE :

    Pr. VAZQUEZ José   Professeur, ENGEES, Université de Strasbourg, France

RAPPORTEURS :

    Dr. MARTIN Fernando   Directeur de recherche, CIEMAT, Madrid, Espagne
    Dr. JANSSEN Stijn   Directeur de recherche, VITO, Mol, Belgique

---

EXAMINATEURS EXTERNES :

    Pr. HOARAU Yannick   Professeur, ICUBE, Université de Strasbourg, France
    Dr. BLOND Nadège   Chargée de recherche, LIVE/CNRS, Strasbourg, France
    Dr. DUFRESNE Matthieu   Directeur scientifique 3DEAU, Strasbourg, France

3D Modelling of air pollution at urban scale

Nicolas Reiminger

REMERCIEMENTS

A mes grands-parents,
Jean-Marie, Marie-Hélène, Bernard et Estelle

mes parents,
Alain et Véronique

mon épouse.
Eva

" Never give up. Keep pushing."

Pierre Gasly #10

RÉSUMÉ

Le but de ce travail de thèse est le développement et la validation de codes de calcul de type mécanique des fluides numérique, ou CFD (Computational Fluid Dynamics), ainsi que de nouvelles méthodologies pour évaluer la qualité de l'air en zone urbaine. Pour cela, la méthodologie RANS en écoulement transitoire (Unsteady Reynolds-Averaged Navier-Stokes) est retenue et deux nouveaux codes de calcul sont développés. Ceci inclut un modèle à convection forcée (FCS) pour modéliser les atmosphères neutres, ainsi qu'un modèle à convection mixte (MCS) pour modéliser les atmosphères stables et instables, mais aussi d'autres phénomènes tels que les effets de la végétation. Les résultats de ces deux codes de calcul sont comparés à sept cas tests expérimentaux réalisés en soufflerie, mais aussi sur le terrain. Les résultats montrent des erreurs de moins de 10% sur les concentrations modélisées, et que les échanges intérieurs/extérieurs peuvent être modélisés de façon performante. La question du domaine de calcul incluant les dimensions du domaine, le maillage, les conditions aux limites, les émissions et la concentration de fond est traité dans un contexte d'ingénierie visant à l'amélioration de la modélisation de la qualité de l'air en environnement urbain. Plusieurs nouvelles méthodologies sont développées et validées incluant des méthodologies pour évaluer les concentrations en dioxyde d'azote sur la base des concentrations en oxydes d'azote, pour évaluer la distribution continue du vent sur la base de données discrètes issues des roses des vents, ou encore pour évaluer les concentrations moyennes annuelles sur la base de résultats numériques ponctuels. L'intérêt et le potentiel de ce type de modèle numérique et de méthodologies sont enfin mis en avant et des exemples d'application à des fins de conception, de compréhension et de diagnostic sont présentés.

Mots-clefs : CFD, RANS, qualité de l'air, pollution atmosphérique, zones urbaines, environnement.

ABSTRACT

The aim of this thesis is the development and the validation of Computational Fluid Dynamics (CFD) solvers and new methodologies to assess air quality in urban areas. To do so, the Unsteady Reynolds-Averaged Navier-Stokes methodology (URANS) is chosen and two new solvers are built. It includes a Forced Convection Solver (FCS) for neutral atmospheres modelling and a Mixed Convection Solver (MCS) for stable and unstable atmospheres modelling where other important phenomena such as the effects of vegetation are also considered. The results of these solvers are compared to seven test cases including wind tunnel and *in-situ* experiments which show that an error of less than 10% can be expected on modelled concentrations, but also that indoor/outdoor exchange can be efficiently modelled. The issue of computational domain including domain extension, meshing, boundary conditions emissions and background concentrations for air quality modelling in urban areas are dealt in an improvement approach, especially in the engineering context. Numerous new methodologies are developed and validated, and their limits assessed including methodologies to assess nitrogen dioxide concentrations based on nitrogen oxides concentrations, to assess continuous wind distributions based on discrete data such as given by wind roses or to assess mean annual concentration based on punctual numerical results. The interest and potential of such numerical models and methodologies is lastly highlighted and examples of application for the purpose of design, understanding and diagnosis are presented.

Keywords: CFD, RANS, air quality, atmospheric pollution, urban areas, environment.

CONTENTS

FIRST PART:

TOOLS DEVELOPMENT FOR AIR POLLUTION ASSESSMENT AT URBAN SCALE

Chapter 1:

Introduction

The issue of air quality …

Air quality has become a major issue over the past years. According to the Global Health Observatory data (GHO) from the World Health Organization (WHO), it was around 8 million people who prematurely died in 2016 as a result of exposure to air pollution (WHO, 2016a, 2016b). Still according to this source, this number corresponds to around 7.6% of all deaths during this year and includes both ambient (outdoor) and household (indoor) air pollution-related deaths with a respective number of 4.2 million and 3.8 million deaths. Over the European continent, it was around 500 000 of premature deaths with around 83% related to $PM_{2.5}$ (particulate matter under 2.5 µm) exposure, 14% to NO_2 (nitrogen dioxide) exposure and 3% to O_3 (ozone) exposure (European Environment Agency, 2019). Finally, in France, it was 48 000 people who prematurely died from $PM_{2.5}$ exposure linked to human activities (Santé Publique France, 2016).

Indeed, air pollution has a direct impact on health, increasing the number of diseases (Anderson et al., 2012; Chauhan et al., 1998; Kagawa, 1985; Kim et al., 2015), but also on the environment (Fu et al., 2017; Likens et al., 1979; Wang et al., 2020). The risks over human health are increased for people living in the vicinity of high-traffic roads (H. Chen et al., 2017; Finkelstein et al., 2004; Petters et al., 2004) often in urban areas. The United Nations stated that, in 2018, more than 50% of people were living in urban areas (82% in America and 74% in Europe) and that this percentage will continue to grow to reach 68% in 2050 (United

Nations, 2019). Additionally, it is more than 9 over 10 people from the world's population who live in places where air quality exceeds acceptable levels (WHO, 2018).

… the response of international organizations …

By linking all the previous facts, it becomes clear that measures and actions must be taken to change the situation. In this perspective, the World Health Organization gave guidelines in terms of pollutant concentrations not to exceed with different temporalities (annual, monthly, daily and hourly concentrations) (WHO, 2017). In the same way, the European Union (EU) gave limit values and air quality targets (EU, 2008). Many compounds are covered by these regulatory values and, among them, nitrogen dioxide (NO_2) and particulate matter (PM) have been selected as air pollutants with the highest priority (WHO, 2005). The guidelines and the limit values given by both the WHO and the EU for these pollutants are summarized in Table 1.1.

Table 1.1 – Summary of the WHO and EU limit values and guidelines for nitrogen dioxide and particulate matter

	NO_2	PM_{10}	$PM_{2.5}$
European Union limit values			
Annual value	40 µg/m^3	40 µg/m^3	25 µg/m^3
Daily value	-	50 µg/m^3 (not to be exceeded more than 35 times per year)	-
Hourly value	200 µg/m^3 (not to be exceeded more than 18 times a year)	-	-
European Union targets			
Annual value	40 µg/m^3	30 µg/m^3	10 µg/m^3
World Health Organization guidelines			
Annual value	40 µg/m^3	20 µg/m^3	10 µg/m^3
Daily value	-	50 µg/m^3	25 µg/m^3
Hourly value	200 µg/m^3	-	-

… and their consideration in France

In France, in order to comply with the regulatory values and to move towards the target values and the guidelines, local actions have already been taken and are of different types. On the one hand, we can mention the atmospheric protection plans, "PPA" in French, which applies to agglomerations with more than 250,000 inhabitants and to areas in which air quality limit values are not reached. These plans include diagnosis, actions and information plan, as well as alert and evaluation procedures to ensure, for a given deadline, that air quality standards are reached. As an example, the agglomeration of Strasbourg with around 550,000 inhabitants, including 10 to 20% of whom are living in areas subject to limit values exceedances, has its own atmospheric protection plan (DREAL, 2014). On the other hand, more local actions can be mentioned such as the limitation of vehicles allowed to travel in some city centers, during high pollution periods or the progressive banning of diesel vehicles, as planned in the city of Strasbourg by 2025 and its agglomeration by 2030.

With the various actions taken, the air quality is expected to improve in the future (European Commission, 2013). However, it will take time to see a significant improvement. In the meantime, air quality and the impact of the measures taken will have to be monitored. In France, this role is held for several years by organizations called "AASQA" for "Associations Agréées de Surveillance de la Qualité de l'Air", i.e., air quality monitoring organizations approved by the Ministry of Ecology. These organizations are located in all regions of France for a total number of 18 regional agencies. They are responsible for carrying out annual monitoring reports on air quality but also for alerting citizens and collectivities in the event of pollution peaks.

Although measuring pollutant concentrations using sensors gives a concrete result on air quality, this method suffers from some drawbacks. Indeed, the use of sensors alone makes it possible to study air quality in the present but does not allow it to be studied in the future by including possible traffic and building evolution. In addition, a sensor gives a result at a given point (latitude, longitude) and at a fixed altitude, which does not allow a complete spatial representation of the air pollution in all the three dimensions. Indeed, air pollution show a high spatial variability and especially in urban areas. Numerical modelling can then become complementary to on-site measurement.

Modelling air quality at urban scale

Numerical modelling applied to air quality has several advantages (Michelot et al., 2015) which can be summarized in three categories:

- *Diagnosis*, by assessing the exposure of populations to air pollution.
- *Design*, by assessing the impact of the layout and shapes of the building on the air flow and therefore on the transport of pollutants.
- *Understanding*, by allowing to better understand the pollution dispersion phenomena in complex situations.
- *Forecasting*, by assessing air pollution for the next days, inform and prevent high population exposure.

Many different types of numerical models exist for air pollution modelling (Korsakissok, 2009; Michelot et al., 2015). These models and their usual scale of use are summarized in Figure 1.1 based on the previous references.
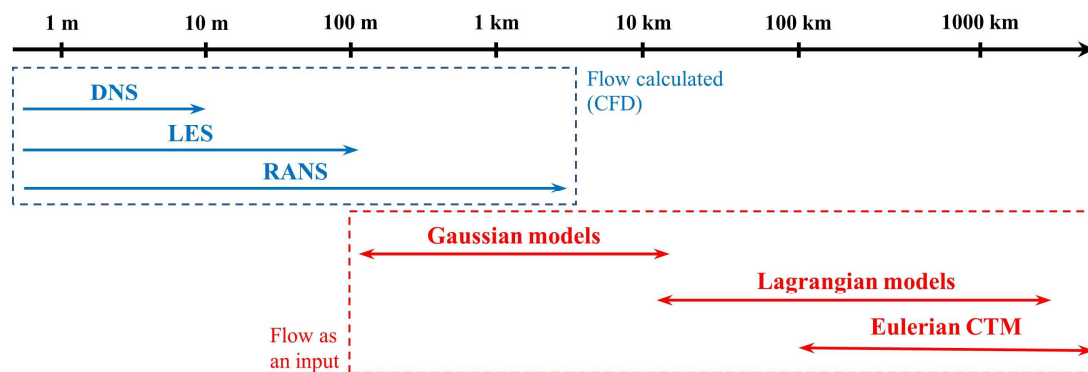
Figure 1.1 – Summary of the different types of numerical models available with their usual domain scales (CTM: Chemistry Transport Model).

According to Figure 1.1, two categories of models exist, distinguishing between models where the flow is calculated and models where the flow must be calculated first and then used as input:

- The first category corresponds to the Computational Fluid Dynamics (CFD) models where the flow around obstacles is computed by solving the flow equations and which includes three types of methodologies: the Direct Numerical Simulation (DNS) where the equations are directly solved, the Reynolds-Averaged Navier-Stokes (RANS)

methodology where the equations of the mean flow field are expressed, and the Large-Eddy Simulation (LES) which is an intermediary between the two previous models (Marchesse, 2009).

- The second category corresponds to models where the flow is not calculated (Gaussian models), or given as an input to a Lagrangian or Eulerian Chemistry-Transport Model (offline-coupled CTM), or also computed with a parametrization of the obstacles and not a direct computation (online-coupled CTM). For these models, obstacles such as buildings are not considered or indirectly considered.

All of these models have different calculations costs and, therefore, different applications. Indeed, while Gaussian and Lagrangian models are mainly used for industrial-risk assessments, CFD models are mainly used for research purposes (Sportisse, 2008), especially LES and DNS models mostly used for research on turbulence (Korsakissok, 2009).

In order to choose the best type of model to use at the urban scale, it is necessary to define what is referred to as "urban scale". For the purpose of this research work, we define urban scale as a scale larger than a single building and smaller than a whole city. Thus, we considered that urban scale applies to areas with lengths ranging from around 100 m to around 1 km (neighbourhood scale). With this definition, two types of models seem to be appropriate: the CFD-RANS models and the Gaussians models.

According to Mazzoldi et al. (2008), both CFD-RANS and Gaussian models are able to predict pollutant dispersion in open-field while the Gaussian models are easier for setting up model runs and gave shorter computation time. Studies done more recently are nonetheless telling us that CFD-RANS models give better results under non-flat terrain cases compared to Gaussian models (Kumar et al., 2015). Finally, for low-level sources such as traffic-related emissions and, furthermore, for high densely built-up areas, Gaussian models are poor in predicting pollutant concentrations compared to CFD simulations (Bady, 2017).

Development challenges of the CFD-RANS model

As mentioned by Blocken (2014), the use of computational fluid dynamics for wind engineering, such as for air pollution modelling, is defined as Computational Wind Engineering (CWE). Several challenges are related to CWE for urban physics, "the science and engineering of physical processes in urban areas" (Blocken, 2015). Indeed, the state of the art in CFD air pollution modelling shows that many physical or chemical processes are governing the evolution of air pollutants in the Urban Canopy Layer (UCL). These phenomena are illustrated in Figure 1.2 and described further below.
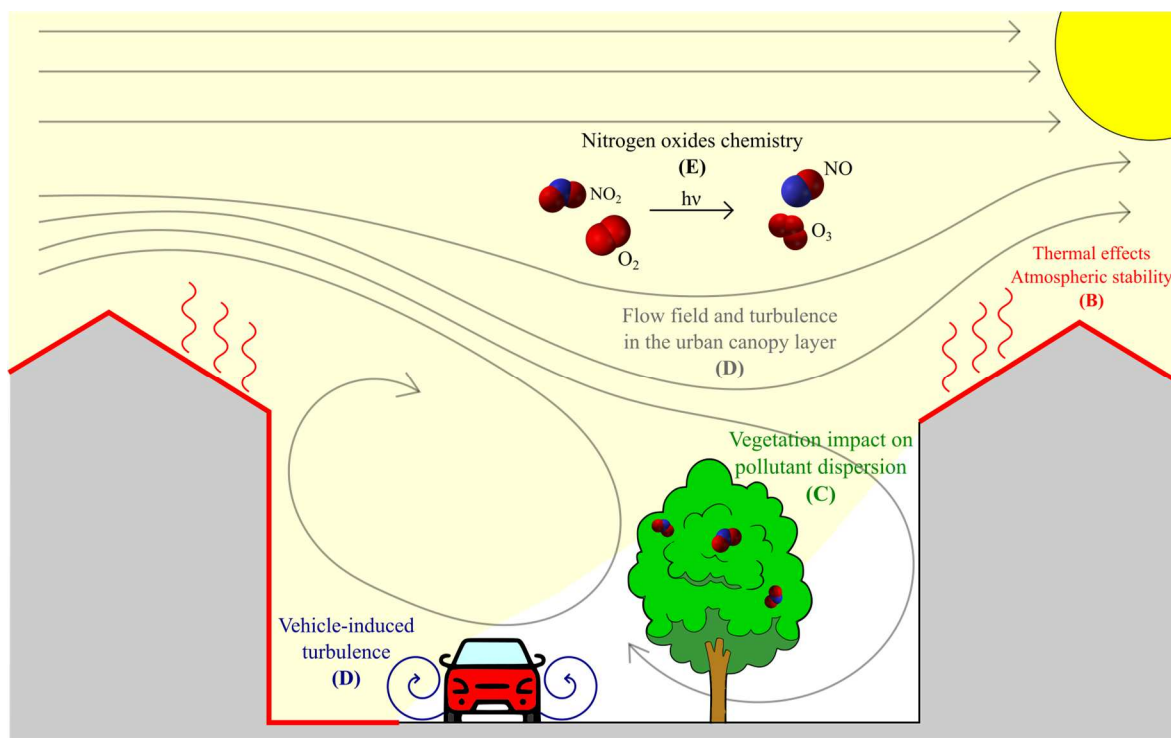
Figure 1.2 – Illustration of the physical or chemical processes are governing the evolution of air pollutants in the urban canopy layer.

In addition, other questions can be raised such as which software choosing or which tools are still needed and can be developed to ease the use of CFD in applied contexts. These different points must be introduced in order to set the limits of this research work but also to formulate the questions on which this thesis tried to provide answers.

Several CFD software does already exist for air pollution modelling and include ANSYS Fluent (de Lieto Vollaro et al., 2014), OpenFOAM (Fiates and Vianna, 2016), Code Saturne (Qu et

al., 2012), MISKAM (Belalcazar et al., 2010), STAR-CMM (Borge et al., 2018), PHOENICS (Liu et al., 2015), ENVI-met (Perini and Magliocco, 2014), etc. Among all these propositions, OpenFOAM offer several advantages: it is a free non-commercial and opensource software allowing visibility, modifications, and customization in the source code. For these reasons, OpenFOAM was therefore chosen for the purpose of this research work. However, as with other models, validations of the results are needed and the conditions of use for engineering applications are poorly described, while air pollution is strongly influenced by complex atmospheric processes. The scientific questions therefore remain open.

Turbulence in the urban canopy layer (A)

Turbulence in urban areas have an impact on pollutant dispersion and, particularly, on the turbulent diffusivity of pollutants (Tominaga and Stathopoulos, 2017). In addition, the use of CFD-RANS models requires the choice of a turbulence model that may over or underestimate the turbulence (Koutsourakis et al., 2012), which can therefore lead to poor estimations of pollutant concentrations. According to these elements, several questions can thus be raised.

> Is a CFD-RANS model sufficient to good reproduce wind speed in urban areas for computational wind engineering applications? What is the best turbulence model for CFD-RANS air pollution modelling? How to consider the effects of turbulence on the pollutants transport?

Atmospheric stability effects (B)

The atmospheric stability depends on both mechanical and thermal effects (Sportisse, 2008). As a function of this stability, pollutant concentrations can change significantly resulting in higher but also lower concentrations and that for various configurations (Cheng et al., 2009; Finn et al., 2010). Thermal effects should therefore be included in the numerical software to consider these effects.

> How to include thermal effects in the CFD code to model different atmospheric stability? Is a CFD-RANS model able to accurately reproduce effects of atmospheric stability on wind velocities and pollutant dispersion? What are the effects of atmospheric stability on pollutant concentrations?

Vegetation impact on pollutant dispersion (C)

Urban forestry and tree planting are used in urban environment to adapt and mitigate air pollution to improve urban sustainability and human health (Salmond et al., 2016). It has been shown that trees are not only impacting pedestrian comfort by mitigating temperatures, but can also impact the pollutant concentrations by modifying the airflow and the dispersion of pollution (Santiago et al., 2019). This impact can be beneficial, but may also contribute to increase pollutant concentrations (Vos et al., 2013). Thus, in order to properly reproduce pollutants dispersion in urban areas, the effects of vegetation must be included in the numerical model.

(?) How to reproduce the effects of vegetation on both flow field and pollutant concentrations in a CFD model? Is such a model able to reproduce accurately flow field and pollutant concentration field in real *in-situ* contexts?

Effects of vehicles on the flow field (D)

Vehicles have also an impact on the flow field. Indeed, as mentioned by Vachon et al. (2002), an increase in the traffic flux increase the turbulence and thus, the pollutant dispersion. Still according to these authors, with too high traffic the pollutant dispersion decreases due to traffic stagnation. Traffic-induced turbulence can therefore impact the pollutant concentrations in urban areas and need also to be considered in the CFD model.

(?) How to include traffic-induced turbulence in the CFD model?

Nitrogen oxides chemistry (E)

Nitrogen oxides are involved in many chemical reactions in the atmosphere with other compounds such as ozone, Volatile Organic Compounds (VOCs), free radicals, etc. (Seinfeld and Pandis, 2016). Nitrogen dioxides (NO_2) being a part of nitrogen oxides (NO_x), it is therefore difficult to model its dispersion without taking this chemistry into account.

(?) How to include the nitrogen oxides chemistry in the CFD model while keeping a calculation time compatible with engineering purposes? Is it possible to know the NO_2 concentration on the basis of NO_x concentration only?

The needs for engineering applications

The interest of the model to be developed is not only limited to research but also, and especially in the context of this thesis, to its application for applied purposes. Many other questions can therefore be raised about how to use and adapt it to the complexity of reality:

⑦ Are the usual inlet conditions adequate enough for computational wind engineering in complex situations (highly built-up areas) and, if not, is it possible to improve them?

⑦ How to take into account all wind conditions, such as direction and intensity, when assessing annual concentrations with a CFD model?

⑦ Is it possible to facilitate engineering studies by using existing or new methods to assess air pollutant concentrations?

⑦ How can a CFD-RANS model be used for engineering purposes?

The present Ph.D. thesis report intends to answer all of these questions.

Purpose of the thesis

This thesis was carried out as part of a Cifre (industrial agreements for training through research) project between the ANRT (national research technology association) and a Strasbourg-based company called AIR&D, which wanted to develop a 3D air quality model for use in engineering.

This project is part of a multidisciplinary framework that includes knowledge in air quality, atmospheric chemistry and physics as well as fluid mechanics and numerical modelling.

It has two different but complementary main objectives:

⇨ To develop a 3D CFD model for urban air pollution modelling including the many processes that govern the transport of pollutants in the urban canopy layer, and to understand the current limitations of this type of model in an improvement approach.

⇨ To improve the use of CFD models for urban air pollution modelling for engineering purposes in technical contexts and illustrate their use for design, understanding and diagnosis purposes.

To achieve these two goals, the word consisted in the development of a CFD-RANS. All phenomena governing air pollution dispersion such as the effects of vegetation, atmospheric stability, etc. were included. A validation of the model's performance against experimental results found in the scientific literature is proposed. Finally, methodologies are detailed to improve the operationality of the model in technical contexts but also to show that such a model is viable for engineering purposes, and for different types of issues such as design, understanding and diagnosis.

Thesis content

The content of this thesis is developed in two parts. The first part is entitled "Tools development for air pollution assessment at urban scale" and mostly describes the development of the CFD model but also the methodologies designed in this thesis for technical purposes. The second part, entitled "Applications for urban planning: design, understanding, diagnosis and optimization", is the application part where is developed the aspect of the CFD model applied to design, understanding and diagnosis purposes. More specifically, these parts include the following chapters:

Part I: Tools development for air pollution assessment at urban scale

Chapter 2 is about processing with the development and the use of the equations needed for 3D air quality modelling at urban scale. The state of the art of the concepts introduced previously such as the effects of atmospheric stability, turbulence, vegetation, etc. are developed and the way they are taken into account is explained. This part also includes numerous comparisons, between numerical and experimental results, performed to assess the model performances.

Chapter 3 is about pre-processing with the application of the equations developed in the previous chapter. The concepts of domain boundaries, mesh size and boundary conditions including wind profiles and emissions calculation are developed and addressed in an optimization approach for urban context purposes, in order to improve the quality of the results obtained for *in situ* modelling while limiting the calculation time required.

Chapter 4 is about post-processing with the exploitation of the results. It describes numerous methodologies to assess mean annual air pollution concentration combining numerical results and wind roses. In particular, this chapter includes two methods to assess wind speed distribution based on wind roses data and three methodologies to compute mean annual concentrations based on numerical results and wind distributions.

Chapter 5 is an extension of the exploitation of the results and describes methodologies that have been developed through this thesis work to improve air quality engineering studies. This chapter includes methods to facilitate the assessment of NO_2 concentrations based on NO_x data for both CFD results and sensors measurements. It also includes a methodology to assess monthly annual NO_2 concentrations based on monthly data.

Subsequently, the reader may refer to Figure 1.3, which will be repeated on a recurring basis to clarify the points covered in the various sections of this thesis.
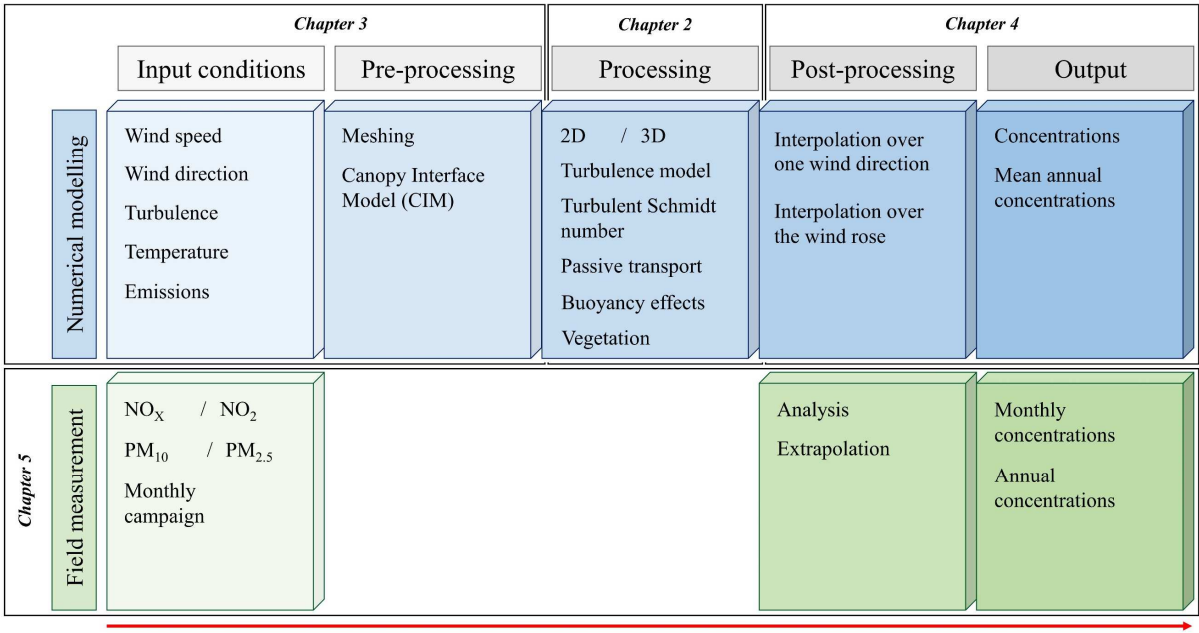
Figure 1.3 – Overview of the thesis content and the work presented

Part II: Applications for urban planning: design, understanding, diagnosis and optimization

Chapter 6 illustrates the use of CFD models for design purposes. This chapter focuses on the study of the evolution of pollutant concentrations in step-down street canyons as a function of the building's heights and the distance between them to provide new information to engineers and architects to achieve sustainable city objectives.

Chapter 7 illustrates the use of the CFD model for understanding purposes. This chapter focuses on the study of the impact of wind conditions and heat exchange on noise barriers-induced pollutants reduction, with the objective of improving actual knowledge on noise barriers for atmospheric pollution reduction purposes.

Chapter 8 illustrates the use of the CFD model for diagnosis purposes. A complete air quality diagnostic study is described, with both numerical modelling and in-field sensor measurements, to illustrate the use of the CFD model and all the methodologies previously presented for a real case study.

Finally, Chapter 9 presents the conclusions and perspectives of this research work.

Thesis results valuation

A part of the results of this thesis have been valued through the following original research papers:

Reiminger, N., Vazquez, J., Blond, N., Dufresne, M., Wertel, J., **2020**. CFD evaluation of mean pollutant concentration variations in step-down street canyons. *Journal of Wind Engineering and Industrial Aerodynamics* 196, 104032. DOI: 10.1016/j.jweia.2019.104032

Jurado, X.[1], Reiminger, N.[1], Vazquez, J., Wemmert, C., Dufresne, M., Blond, N., Wertel, J., **2020**. Assessment of mean annual NO2 concentration based on a partial dataset. *Atmospheric Environment* 221, 117087. DOI: 10.1016/j.atmosenv.2019.117087

---

[1] These authors contributed equally to the paper.

Reiminger, N., Jurado, X., Vazquez, J., Wemmert, C., Blond, N., Dufresne, M., Wertel, J., **2020**. Effects of wind speed and atmospheric stability on the air pollution reduction rate induced by noise barriers. *Journal of Wind Engineering and Industrial Aerodynamics* 200, 104160. DOI: 10.1016/j.jweia.2020.104160

Reiminger, N.[1], Jurado, X.[1], Vazquez, J., Wemmert, C., Dufresne, M., Blond, N., Wertel, J., **2020**. Methodologies to assess mean annual air pollution concentration combining numerical results and wind roses. *Sustainable Cities and Society*, 59, 102221. DOI: 1016/j.scs.2020.102221

Some of the results have also been presented to the scientific community through international conferences during the *"European International Conference on Transforming Urban Systems – EICTUS 2019"*, and are the following:

Reiminger, N., Vazquez, J., Blond, N., Dufresne, M., Wertel, J., **2019**. How pollutant concentrations evolve in step-down street canyons as a function of buildings geometric properties. Presented at the *European International Conference on Transforming Urban Systems (EICTUS)*, 26–28 June 2019, Strasbourg, France.

Reiminger, N., Vazquez, J., Blond, N., Dufresne, M., Wertel, J., **2019**. How can noise barriers reduce pollutant exposure: an example of built area near a highway. Presented at the *European International Conference on Transforming Urban Systems (EICTUS)*, 26–28 June 2019, Strasbourg, France.

Chapter 2:
3D CFD solvers development for urban air pollution modelling

2.1. Introduction

This chapter presents the development of the 3D computational fluid dynamics solvers built for the purpose of air pollution modelling in urban areas and describes the choices of the model used. The state of the art regarding each physical and chemical phenomena to consider in the CFD model is developed and the ways to include them in the solvers are explained. The phenomena considered and described in this chapter are respectively the following:

- The forced convection, and how to model a neutral atmosphere.
- The mixed convection, to take into account thermal effects to model different atmospheric stability.
- The impact of vegetation, on both flow and concentration fields.
- The nitrogen oxides chemistry, for nitrogen dioxide concentration modelling.
- The traffic-induced turbulence.

This chapter also includes several comparisons between numerical and experimental results to assess the model performances. The main points covered in this chapter are highlighted in Figure 2.1.
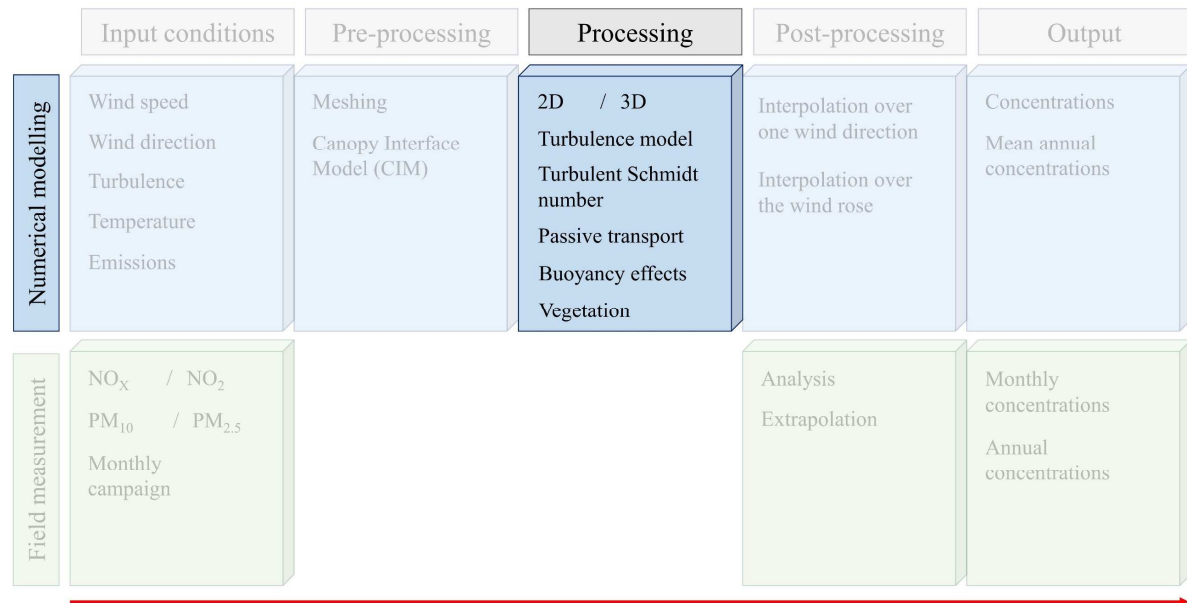
Figure 2.1 – Main points covered in Chapter 2.

The previous questions for which this chapter provides answers are as follows:

Is a CFD-RANS model sufficient to good reproduce wind speed in urban areas for computational wind engineering applications? What is the best turbulence model for CFD-RANS air pollution modelling? How to consider the effects of turbulence on the pollutants transport?

How to include thermal effects in the CFD code to model different atmospheric stability? Is a CFD-RANS model able to accurately reproduce effects of atmospheric stability on wind velocities and pollutant dispersion?

How to reproduce the effects of vegetation on both flow field and pollutant concentrations in a CFD model? Is such a model able to reproduce accurately flow field and pollutant concentration field in real *in-situ* contexts?

How to include traffic-induced turbulence in the CFD model?

How to include the nitrogen oxides chemistry in the CFD model while keeping a calculation time compatible with engineering purposes?

2.2. Forced convection solver: neutral atmosphere modelling

This section deals with the development of the forced convection solver, i.e., a solver for neutral atmosphere modelling where only the wind effects have an impact on the airflow.

2.2.1. Incompressible Navier-Stokes equations

The incompressible Navier-Stokes equations are balance equations that come from the Newton's second law applied to an incompressible fluid. They include two equations, the continuity (Eq. 2.1) and the momentum (Eq. 2.2) equation. The first equation describes the mass conservation in the system while the second equation, derived from the Cauchy momentum equation (see Appendix A for further details), describes the momentum conservation. These equations are used to describe the fluid motion and are given below:

$$\nabla . u = 0 \qquad \qquad \text{(Eq. 2.1)}$$

$$\frac{\partial u}{\partial t} + u . (\nabla u) = -\frac{1}{\rho} \nabla p + \nu \Delta u \qquad \qquad \text{(Eq. 2.2)}$$

where u is the velocity, t the time, ρ the density, p the pressure and ν is the kinematic viscosity.

Navier-Stokes equations are used in many activity fields including hydraulic (water flows in pipes or open channels), aerodynamic (aircraft and vehicle design) but also in aeraulic for computational wind engineering and, in particular, for air pollutant dispersion modelling (Blocken, 2014).

The incompressible version of Navier-Stokes equations should be used with caution. Indeed, while for liquids such as water the incompressibility is obvious, this is not the case for air. Air incompressibility can be verified using the Mach number (Eq. 2.3): for low subsonic Mach number ($Ma < 0.3$), this assumption is true (Amiroudine and Battaglia, 2014; Anderson, 2009). In other words, if the wind velocity is under ~100 m/s, the incompressible Navier-Stokes equations are valid for wind flow modelling.

$$Ma = \frac{u}{c} \qquad \qquad \text{(Eq. 2.3)}$$

where Ma is the Mach number, u is the velocity of the fluid and c is the speed of the sound ($c \sim 343 \, m/s$).

☞ Since the wind speeds modelled will always be under 100 m/s, incompressible Navier-Stokes equations were used for the forced convection solver.

2.2.2. RANS methodology and turbulence closure schemes

Several CFD methodologies exist to solve Navier-Stokes equations and it has been shown previously that the RANS methodology is the most appropriate for the purpose of air pollution modelling at urban scale.

The Reynolds-Averaged Navier-Stokes equations are time-averaged equations of motion for fluid. The idea behind this method is that the instantaneous quantities, such as the velocity or the pressure, are decomposed in a time-averaged and a fluctuating quantity (Reynolds, 1895). The corresponding incompressible equations, (Eq. 2.4) and (Eq. 2.5), are therefore different from the previous incompressible Navier-Stokes equations and are given below:

$$\nabla . U = 0 \qquad \text{(Eq. 2.4)}$$

$$\frac{\partial U}{\partial t} + U.(\nabla U) = -\frac{1}{\rho}\nabla P + \nu \Delta U - \nabla . \overline{u'u'} \qquad \text{(Eq. 2.5)}$$

where U is the time-averaged velocity, t the time, ρ the density, P is the time-averaged pressure, ν is the kinematic viscosity, u' the fluctuating component of the velocity and $\overline{u'u'}$ the Reynolds-stress tensor.

After time-averaging Navier-Stokes equations, a new term called the Reynolds-stress tensor appears (see Appendix B for further details). This new unknown term must be modelled in order to solve the RANS equations, which corresponds to the major issue of CFD-RANS modelling (Alfonsi, 2009).

Several turbulence closure schemes do exist to model the turbulence for CFD-RANS purposes. It includes zero, one and two-equation models but also stress-equation models with both linear and nonlinear formulations (Alfonsi, 2009; Versteeg and Malalasekera, 2007). For CWE and

air pollution modelling, the most commonly used turbulence models are the different variants of the two-equation k-ε model, in particular the standard and the RNG models (Franke et al., 2004). These models, being linear and isotropic, are known to have some limitations for highly turbulent cases. Nonlinear or anisotropic models such as the Reynolds Stress Model (RSM) could be used instead but are more time consuming and more difficult to converge.

Authors have shown that the nonlinear RNG k-ε model yield not to great improvements over the linear model and, moreover, that the linear RNG k-ε model is not always making improvements over the standard k-ε (Papageorgakis and Assanis, 1999). However, other results obtained for six different cases show that the RNG model gives improvements over both the standard k-ε model and the RSM (Koutsourakis et al., 2012). There is therefore no definitive answer on which model to use for air pollution modelling.

☞   Since there is no definitive answer on the turbulence model to choose for air quality modelling, only the k-ε turbulence models will be considered (including the standard and the RNG variants).

One question arises:

⍰   Is a two-equation k-ε turbulence model sufficient to accurately reproduce velocity and concentration fields for air pollution modelling? Is the RNG variant giving more accurate results? The answers will be discussed later at the validation steps.

2.2.3. Computation algorithm for unsteady flows

In order to solve Navier-Stokes equations, a numerical algorithm is required to couple pressure and momentum quantities. This is generally done using SIMPLE, PISO or PIMPLE algorithms:

- SIMPLE: "Semi Implicit Method Of Pressure Linked Equation", used for steady state analyses.
- PISO: "Pressure Implicit Split Operator", used for transient calculations and limited in time step depending on the Courant number.
- PIMPLE: A combination of both PISO and SIMPLE algorithms, allowing for transient calculations with bigger Courant numbers than with the PISO algorithm.

According to Tominaga and Stathopoulos (2017), unsteady calculations can improve the results for the concentration field over a steady state calculation. Thus, the SIMPLE algorithm was excluded.

PISO and PIMPLE algorithms use the Courant number to limit the calculation time steps. While the PISO algorithm is used for $Co \leq 1$, the PIMPLE algorithm can be used for larger Courant numbers ($Co > 1$) (Holzmann, 2016). With the definition of the three-dimensional Courant number given in (Eq. 2.6), it is clear that bigger Courant numbers lead to bigger time steps and therefore lower calculation costs.

$$Co = \Delta t \left(\sum_{i=1}^{3} \frac{u_{x_i}}{\Delta x_i} \right) \qquad \text{(Eq. 2.6)}$$

where Co is the Courant number, Δt is the time step, u_{x_i} is the magnitude of the fluid velocity in the ith direction and Δx_i is the length interval in the ith direction.

☞ Since the PIMPLE algorithm allows Navier-Stokes equations to be solved transiently with bigger time steps than other algorithms, this algorithm was used for the rest of the work. The OpenFOAM 6.0 *pimpleFoam* solver was therefore used as a basis for future modifications.

2.2.4. Passive scalar transport and turbulent diffusivity

An URANS (Unsteady RANS) methodology, using incompressible RANS equations with the PIMPLE algorithm, was adopted to solve the fluid motion. However, the solver used (*pimpleFoam*) does not allow pollutants to be transported in its current state and some modifications are needed.

To allow pollutants to be transported, an advection-diffusion equation is needed. Since no chemical reactions are considered, the transported pollutant can be considered as a passive scalar (i.e., non-reactive scalar) and the corresponding transport equation is given below:

$$\frac{\partial C}{\partial t} + \nabla.(CU) - \nabla.(D\nabla C) = E \qquad \text{(Eq. 2.7)}$$

where C is the pollutant concentration, U is the velocity, D is the diffusion coefficient and E is the source term of emissions.

The diffusion coefficient D corresponds to the total amount of diffusion and is the sum of the molecular diffusivity (D_m) and turbulent diffusivity (D_t). However, although molecular diffusivity is specific to the compound under consideration, the turbulent diffusivity depends on the turbulent kinetic energy and, therefore, directly on the flow and the case studied. Since the turbulent diffusivity coefficient is unknown, to consider the turbulent diffusivity in the advection-diffusion equation it is common to include a new dimensionless term, the turbulent Schmidt number. This number is defined as the ratio between the turbulent viscosity and the turbulent diffusivity (Tominaga and Stathopoulos, 2007) and the equation is given below:

$$Sc_t = \frac{v_t}{D_t} \tag{Eq. 2.8}$$

where Sc_t is the turbulent Schmidt number, v_t the turbulent viscosity and D_t the turbulent diffusion coefficient.

With (Eq. 2.8), the advection-diffusion equation (Eq. 2.7) becomes:

$$\frac{\partial C}{\partial t} + \nabla.(CU) - \nabla.\left[\left(D_m + \frac{v_t}{Sc_t}\right)\nabla C\right] = E \tag{Eq. 2.9}$$

This last equation, commonly used for CFD air pollution modelling (Di Sabatino et al., 2007; Takano and Moonen, 2013; Wen and Malki-Epshtein, 2018), has been implemented in the *pimpleFoam* solver of OpenFOAM 6.0.

☞ A new solver, called *Forced Convection Solver* (FCS), has been developed based on the *pimpleFoam* solver from OpenFOAM 6.0 where the turbulent advection-diffusion equation has been added to transiently solve the pollutant transport. This new solver needs to be compared to experimental data to ensure its validity.

According to (Eq. 2.8), two new parameters are needed to compute the turbulent diffusivity. The turbulent viscosity v_t is already computed in the RANS equations and, especially, when solving the Reynolds stress tensor. The turbulent Schmidt number Sc_t needs nonetheless to be

41

specified, which is a big issue in CWE. Indeed, while commonly values are ranging from 0.7 to 0.9, Tominaga and Stathopoulos (2007) showed that this number is most likely ranging from 0.3 to 1.2 and that this number could highly change pollutant concentrations modelled. Thus, particular attention has been paid to this parameter during this research work and the following question tried to be answered:

How much can the turbulent Schmidt number Sc_t change the concentrations modelled? Which is the best turbulent Schmidt number to choose?

2.2.5. Model validation in case of forced convection

Three experimental test cases were used to assess the performances of the forced convection model and to answer some questions raised previously. The experimental and numerical set-ups as well as the results comparison are successively presented hereafter and a summary of the test cases with the associated objectives is given in Table 2.1.

Table 2.1 – Summary of the three test cases used for the forced convection solver validation.

Authors	2D	3D	Buil.	S.C.	W.T.	In-situ	Objective
Soulhac et al. (2001)	✔			✔	✔		Comparison between CFD and experimental data for a simple case of flow field in a regular street-canyon.
Gamel (2015)	✔		✔		✔		Comparison between CFD and experimental data for a simple case of flow field around a building.
CODASC database		✔		✔	✔		Comparison between CFD and experimental data for a more complex street-canyon case with a 3D flow field.

(Buil.: Building, S.C.: Street-canyon, W.T.: Wind tunnel)

2.2.5.1. Impact of the turbulence closure scheme on the turbulent Schmidt number

The forced convection solver was first tested against experimental data from Soulhac et al. (2001). This test case has been chosen to have a first comparison against experimental data for a simple case (2D) of a street canyon that is on great interest for air pollution modelling (Vardoulakis et al., 2003). Two turbulence models were used, and the results were compared to assess their impact on velocities and pollutant concentrations.

Soulhac et al. (2001) studied in a wind tunnel the dispersion of a passive tracer emitted in the middle of a regular street canyon (i.e., a street where buildings are present on either side and where their height is equal to their distance from each other, $H = W$). Their experimental set-up was symmetrical in the direction transverse to the flow (y-direction) and they used a perpendicular wind direction (along the x-direction). Results are provided for both wind velocity and tracer concentration for different vertical profiles shown in Figure 2.2. The results are all given at $y = 0$ and are therefore two-dimensional.
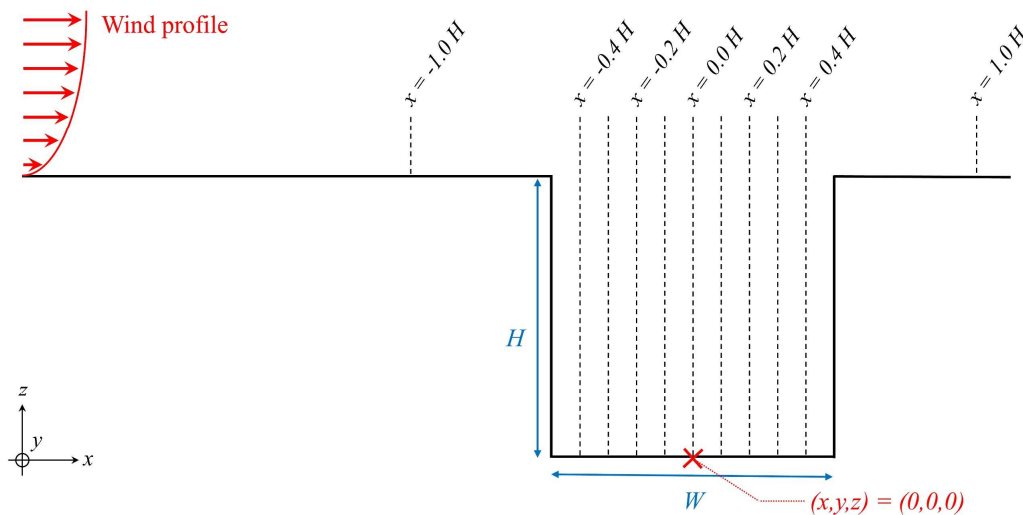
Figure 2.2 – Location of the vertical measurement profiles in the street canyon and dimensions of the canyon with $H = W = 0.1$ m.

Simulations were performed using the inlet velocity and turbulent kinetic energy profiles measured and given by Soulhac et al. (2001). A freestream outlet condition has been specified at the outlet, symmetry conditions were applied at the top and the lateral boundaries of the domain (2D simulation), and no-slip conditions with standard wall function were applied to all other boundaries including the building roofs and walls. Finally, the passive tracer emission was modelled by a line source along the middle of the street ($x = 0$) with a mass flow rate of 10^{-4} µg/s. The recommendations given by Franke et al. (2007) has been followed concerning the minimal distances to have in the computational domain. A summary of the boundary conditions and the distances in the domain is given in Figure 2.3.
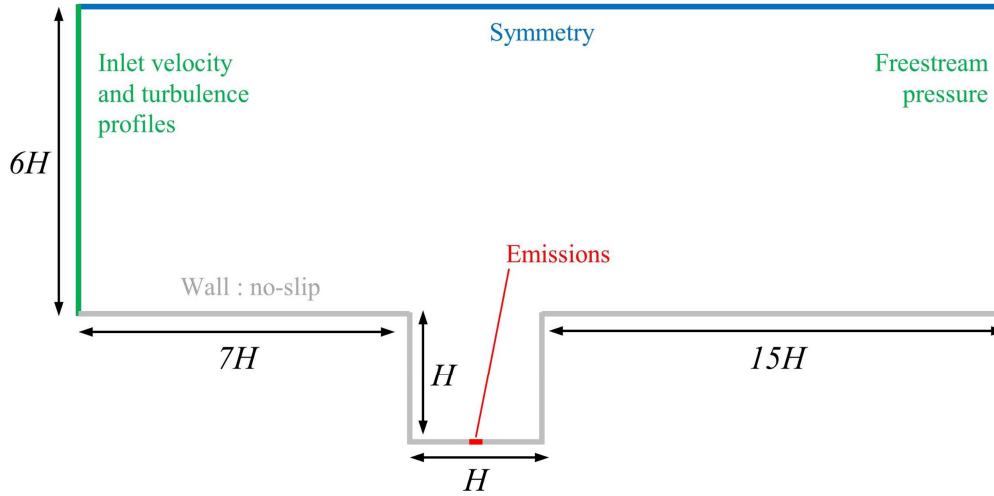
Figure 2.3 – Boundary conditions and domain size.

The numerical geometry has then been meshed in order to allow the calculation to be performed. The meshing was done using the unstructured grid generator *snappyHexMesh* available with OpenFOAM. Three meshes were considered to carry out mesh sensitivity tests and include coarse meshes (5 mm), medium meshes (2.5 mm) and fine meshes (1.25 mm). Sensitivity of results to mesh size was studied using the Grid Convergence Index (*GCI*), which is an estimation of the numerical uncertainty with a 95% confidence level (Roache, 1994). The corresponding equation (Eq. 2.10) is given hereafter:

$$GCI_{fine\ grid} = 3\frac{|f_2 - f_1|}{f_1}(r^p - 1)^{-1} \qquad \text{(Eq. 2.10)}$$

where f_1 are the fine grid results, f_2 the coarse grid results, r is the grid expansion ratio between the fine and the coarse grid and p is the order of the numerical scheme.

The resulting $GCI_{fine\ grid}$ obtained between the 1.25 mm and 5 mm mesh sizes on the results of pollutant concentration is on average 2% and a maximum of 4%, corresponding therefore to a sufficient grid resolution. The meshes of 1.25 mm were therefore chosen, leading to $y^+ = 25$ (see Section 3.2.2.1. for further details on the y^+ criterion), because they did not increase to much the calculation costs, leading to a total number of around 100,000 meshes. The typical dimension of the chosen cells is thus $0.0125 \times H$ in the street canyon and an illustration of the meshes is presented in Figure 2.4.
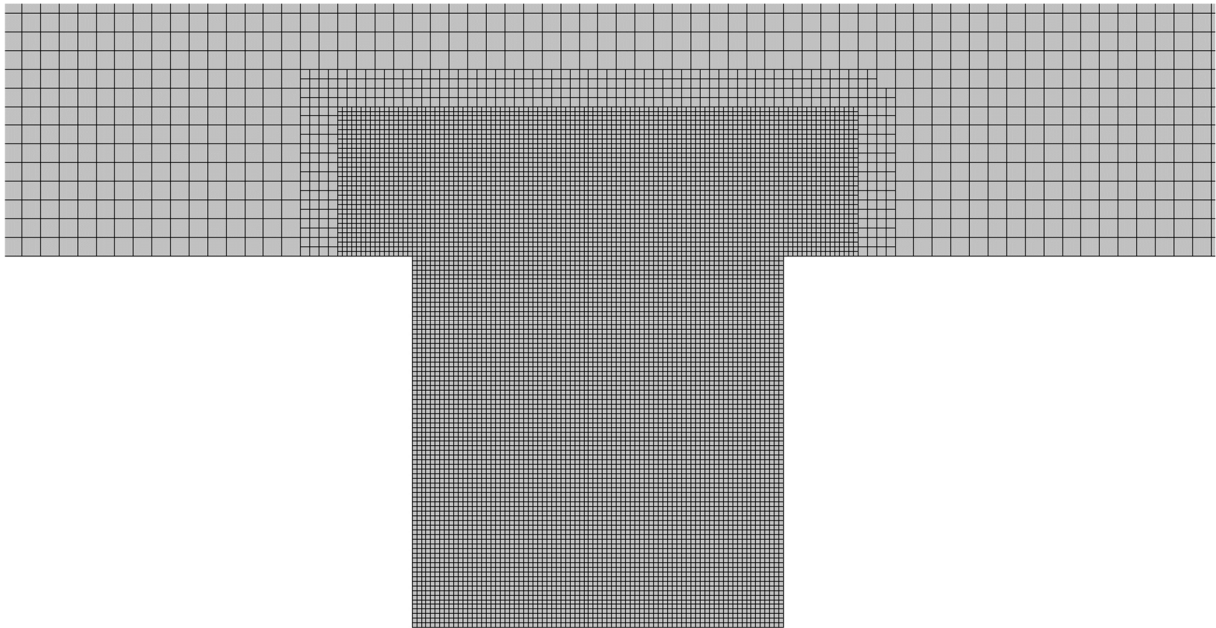
Figure 2.4 – Mesh illustration (1.25 mm inside the street canyon and 5 mm outside).

Simulations were performed using two turbulence models: the standard k-ε model (noted STD) and the RNG k-ε model (noted RNG). The resulting dimensionless velocity magnitude U/U_{ref} as a function of the dimensionless height z/H is presented for four vertical profiles in Figure 2.5 (U_{ref} = 5.3 m/s). Additional results can be found in Appendix C.

Results show that the velocity profile outside the street canyon is well reproduced. The velocities inside the street canyon are also accurately reproduced with both turbulence models but are slightly different between the two models. The RNG turbulence model leads to overall better results although the differences are marginal. It can also be mentioned that results are more accurate on the windward side of the street (x/H ranging from 0.0 to 0.5) than on the leeward side (x/H ranging from -0.5 to 0.0). The numerical model is therefore able to accurately reproduce wind velocities in a 2D street canyon with the RNG k-ε turbulence model but also with the standard one.
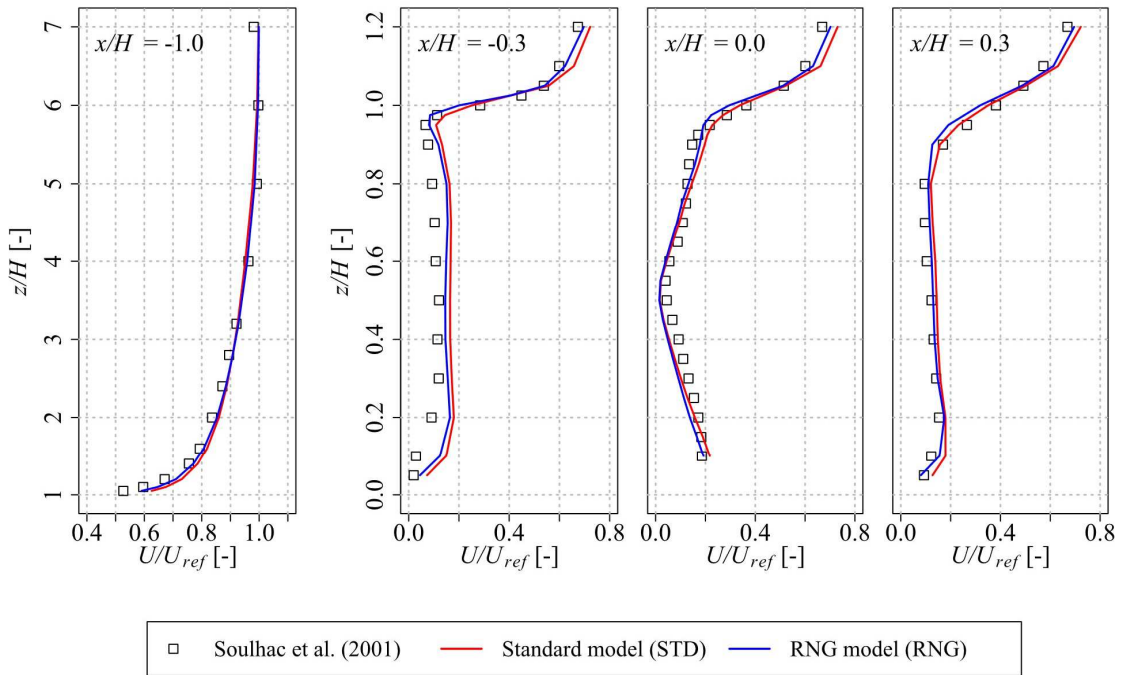
Figure 2.5 – Comparison of dimensionless velocities between the numerical model and the experimental data of Soulhac et al. (2001) for STD and RNG turbulence models.

Figure 2.6 – Comparison of dimensionless concentrations between the numerical model and the experimental data of Soulhac et al. (2001) for STD and RNG turbulence models and three turbulent Schmidt numbers.

Many turbulent Schmidt numbers have been considered to assess if the forced convection solver is able to accurately reproduced concentrations in the street canyon. Figure 2.6 shows the corresponding results for different Sc_t and the two turbulence models. Results are given in the following dimensionless form: z/H for the dimensionless height and C^* for the dimensionless concentration according to (Eq. 2.11) with $U_H = 2.75$ m/s, $H = 0.1$ m, $L = 1.25 \times 10^{-3}$ m and $q_m = 10^{-4}$ μg/s, and are given for two locations, $x/H = 0.0$ and 0.4. Further results can be found in Appendix C.

$$C^* = \frac{C.U_H.H}{q_m/L}$$

(Eq. 2.11)

where C^* is the dimensionless concentration, C is the dimensioned concentration, U_H is the wind speed at $z = H$, L is the pollutant injection length and q_m is the pollutant emission rate.

Several observations can be noticed in Figure 2.6. Firstly, the turbulent Schmidt number has a high impact on the concentrations modelled. Indeed, concentrations can be twice as high for a Sc_t variation of 0.2 for the RNG k-ε model. Secondly, the sensitivity is depending on the turbulence model used. For the case modelled, the variations over concentrations are more than twice smaller for the standard k-ε model compared to the RNG k-ε model for the same Sc_t variation with respectively a maximal variation over concentrations of 100% and 25% between the two turbulence models. Finally, both turbulence models allow reproducing the concentration profiles when choosing the good Sc_t. However, finding the best Sc_t is not simple, as this number also depends on the vertical profile considered (i.e., the location in the street canyon).

To make this choice easier, and to better evaluate air quality model performances, many criteria based on statistical numbers have been suggested by Chang and Hanna (2004) and also Thunis et al. (2012). It includes the fractional bias (FB), the geometric mean bias (MG), the geometric variance (VG), the normalized mean square error ($NMSE$), the fraction of predictions within a factor of two observations ($FAC2$), the normalized absolute error (NAE), and the $Target$. The corresponding equations are given in Appendix D. These criteria have been calculated for the previous results on concentrations and also for supplementary Sc_t not presented previously. The results are summarized in Table 2.2.

Table 2.2 – Evaluation of the forced convection solver performances over the data of Soulhac et al. (2001).

	FB	MG	VG	NMSE	FAC2	NAE	Target
Standard k-ε model							
$Sc_t = 0.4$	0.076	1.079	1.269	0.006	1.350	12%	0.33
$Sc_t = 0.5$	-0.014	0.986	1.213	0.000	1.344	12%	0.32
$Sc_t = 0.6$	-0.085	0.919	1.184	0.007	1.345	17%	0.37
$Sc_t = 0.7$	-0.142	0.868	1.184	0.020	1.360	22%	0.48
RNG k-ε model							
$Sc_t = 0.1$	0.364	1.445	1.584	0.137	1.368	38%	0.67
$Sc_t = 0.2$	0.044	1.045	1.266	0.002	1.371	10%	0.29
$Sc_t = 0.3$	-0.100	0.905	1.171	0.010	1.340	15%	0.29
$Sc_t = 0.5$	-0.319	0.725	1.221	0.104	1.445	35%	0.69
$Sc_t = 0.7$	-0.433	0.644	1.453	0.196	1.540	45%	1.01
Objective							
Target value	0	1	0	0	1	0%	0
Target range	-0.3 < x < 0.3	0.7 < x < 1.3	< 4	< 1.5	0.5 < x < 1.5	-	< 0.5

All the criteria presented in Table 2.2 do not allow to correctly discriminate the best Sc_t for the experimental case considered. For this case, the best criteria are the FB, the $NMSE$, the $Target$ and the NAE. The best corresponding Sc_t are : $Sc_t = 0.5$ for the standard k-ε turbulence model with a global error of 12% (NAE), and $Sc_t = 0.2$ for the RNG k-ε turbulence model with a global error of 10% where the results are illustrated in Figure 2.7.
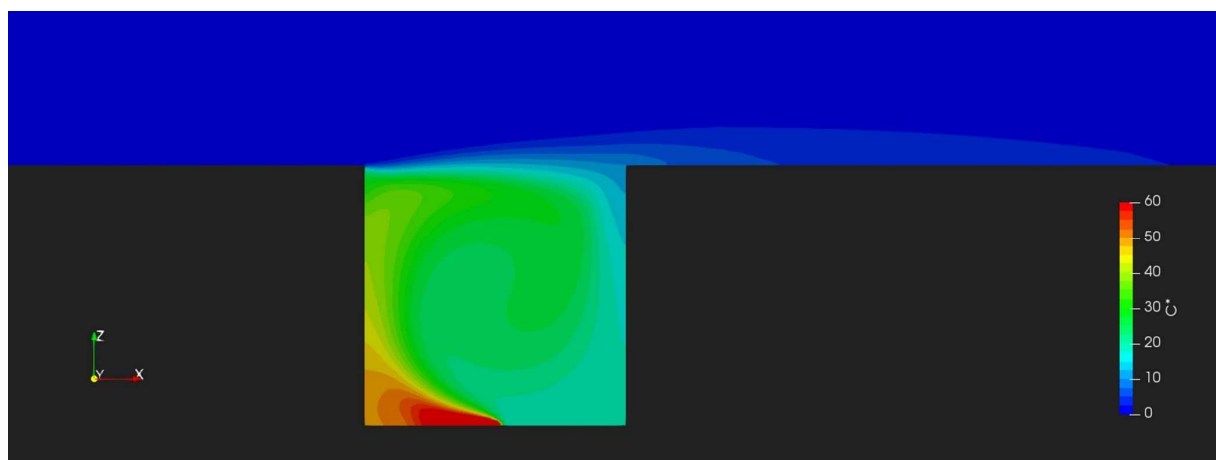
Figure 2.7 – Evolution of dimensionless concentrations inside and outside the street canyon with the RNG k-ε turbulence model and $Sc_t = 0.2$

The previous results have shed light on the following issues:

(?) Is a CFD-RANS model sufficient to good reproduce wind speed in urban areas for computational wind engineering applications? What is the best turbulence model for CFD-RANS air pollution modelling?

(?) Is a two-equation k-ε turbulence model sufficient to accurately reproduce velocity and concentration fields for air pollution modelling?

(?) How much can the turbulent Schmidt number Sc_t change the concentrations modelled? Which is the best turbulent Schmidt number to choose?

The conclusions are as follows:

- ✔ The forced convection solver is able to reproduce well velocities and concentrations in a 2D street canyon with a global error of around 10% on concentrations when choosing the best turbulent Schmidt number.

- ✔ Accurate results can be obtained on velocities and pollutant concentrations with both standard and RNG k-ε models.

- ✔ The turbulent Schmidt number has a high impact on the concentrations modelled and does depend on the turbulence model chosen. The best turbulent Schmidt number in this case being 0.5 for the standard k-ε model and 0.2 for the RNG one.

- ✔ The turbulent Schmidt number seems to be more sensitive when using the RNG k-ε model compared with using the standard k-ε model.

2.2.5.2. Impact of the geometry on the turbulent Schmidt number

The forced convection solver was secondly tested against experimental data from Gamel (2015). This test case has been chosen for its simplicity (2D) but also because the configuration is different from the test case previously considered. The objective was to assess if the solver is able to accurately reproduce velocities and concentrations in a different configuration and, if the same best turbulent Schmidt number as previously ($Sc_t = 0.5$) is obtained when using the standard k-ε turbulence model.

Gamel (2015) studied in a wind tunnel the dispersion of a passive tracer emitted after a cubic obstacle which could be considered as a single building. Their experimental set-up was symmetrical in the direction transverse to the flow and they used a perpendicular wind direction. Results are provided for both wind velocity and tracer concentration for different vertical profiles shown in Figure 2.8. The results are all given at $y = 0$, and are therefore two-dimensional.

Simulations were performed using the same boundary conditions as described in Section 2.2.5.1. and the passive tracer emission was modelled by a line source located at $x/H = 1.5$ with a mass flow rate of 3.206 g/s. Recommendations given by Franke et al. (2007) have been followed and a summary of the boundary conditions and the distances in the domain is given in Figure 2.9.
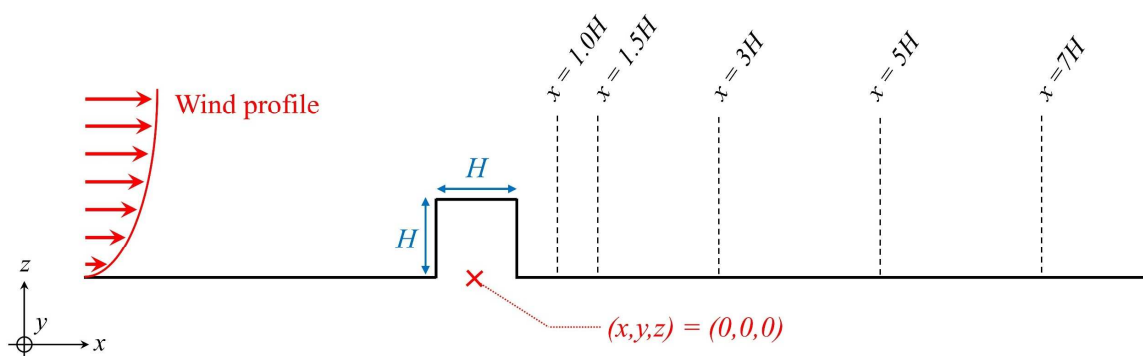
Figure 2.8 – Location of the vertical measurement profiles after the cubic obstacle with $H = W = 0.1$ m.
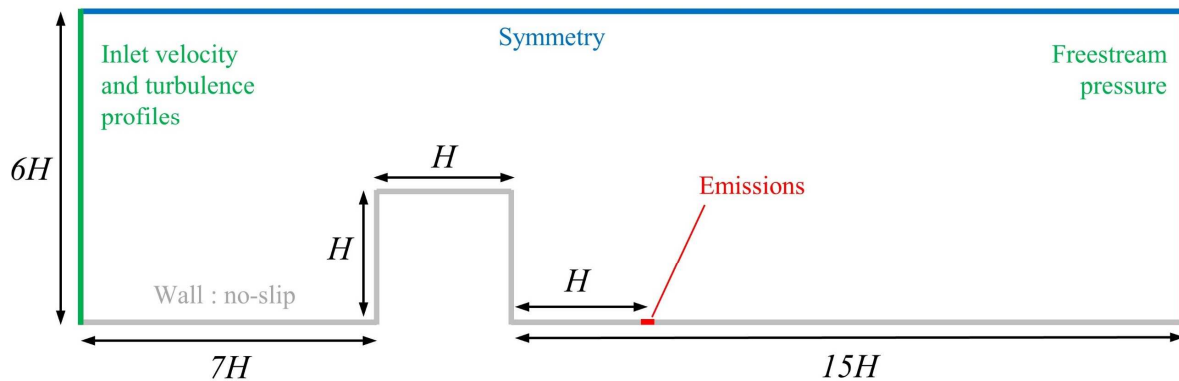
Figure 2.9 – Boundary conditions and domain size.

The study on the mesh sensitivity with the *GCI* showed as previously that 5 mm meshes is a sufficient resolution. This resolution was adopted for the meshes in the overall domain except near the walls were 1.25 mm meshes were used to catch higher gradients giving a total number of around 150,000 meshes. It leads to y^+ ranging from 30 to 100. An illustration of the resulting grid is proposed in Figure 2.10.

Simulations were performed using the standard k-ε model. The resulting dimensionless streamwise velocity U/U_{ref} as a function of the dimensionless height z/H is presented for four vertical profiles in Figure 2.11 (U_{ref} = 6.33 m/s).
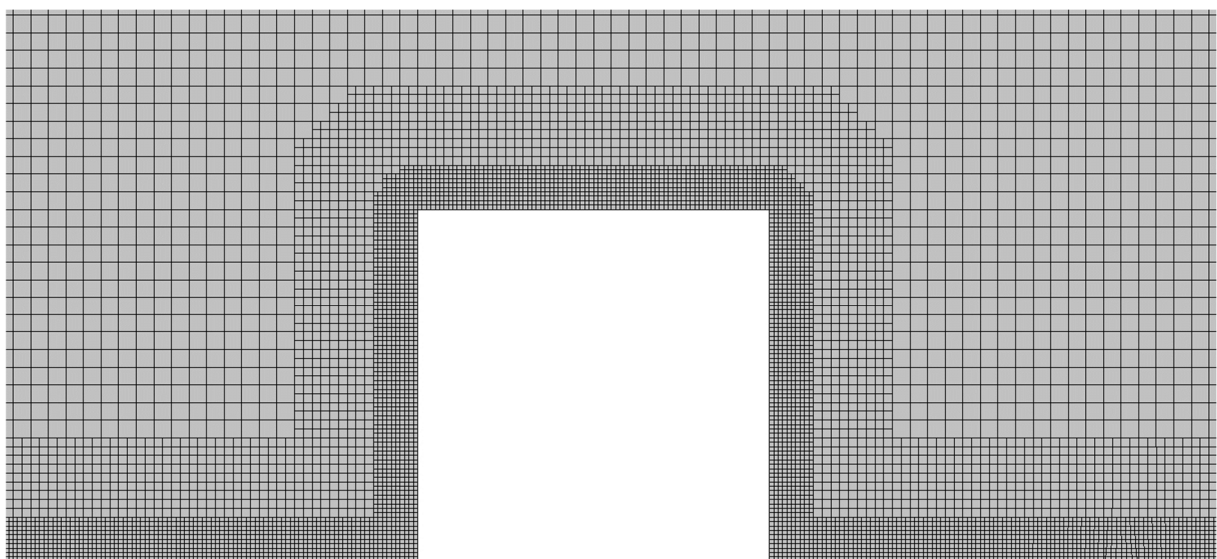
Figure 2.10 – Mesh illustration (1.25 mm near the 2D obstacle and the ground and 5 mm in the overall domain).
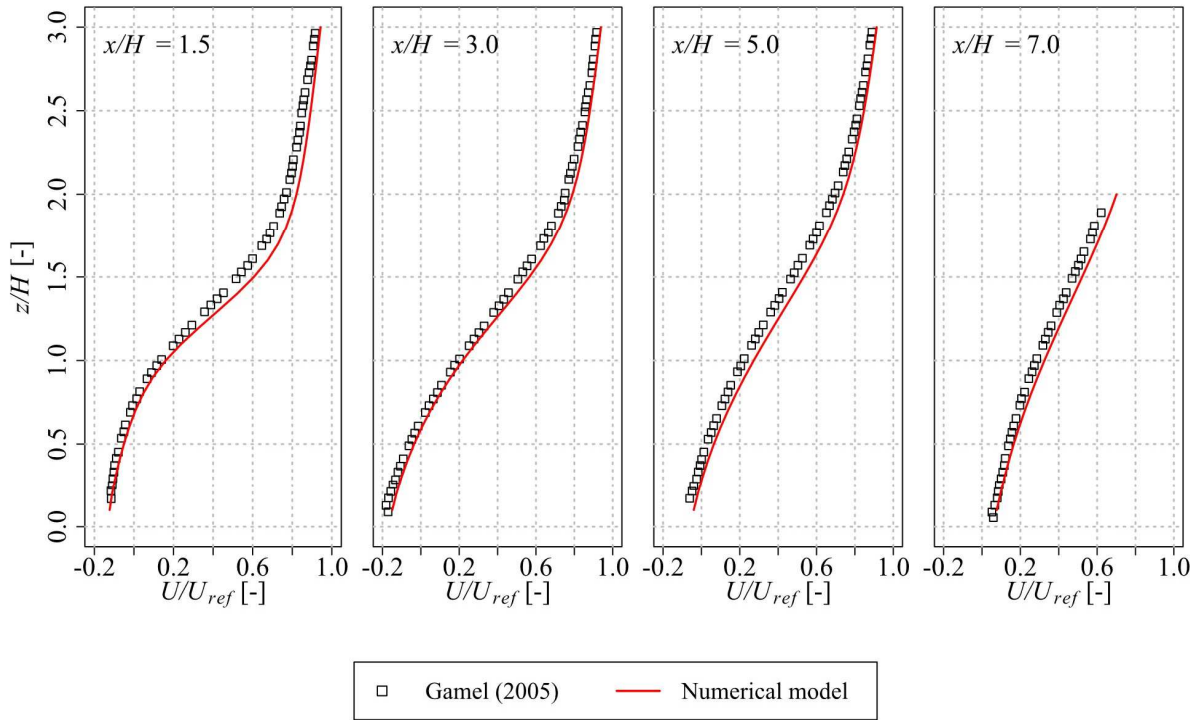
Figure 2.11 – Comparison of dimensionless velocities between the numerical model and the experimental data of Gamel (2005) with the standard k-ε turbulence model.

According to Figure 2.11, the streamwise velocities are well reproduced by the solver, although slightly overestimated, for each vertical profile considered using the standard turbulence model k-ε. The numerical model is therefore able to accurately reproduce wind velocities after a 2D obstacle with the standard k-ε turbulence model.

Five turbulent Schmidt numbers were considered to compare the concentration results against the experimental data. Figure 2.12 illustrates the evolution of the dimensionless concentration C^* as a function of the dimensionless height z/H obtained with $Sc_t = 0.8$, 0.9 and 1.0. The dimensionless concentration was calculated using (Eq. 2.11) with $U_{ref} = 6.33$ m/s the wind speed at H_{ref}, $H_{ref} = 0.55$ m the wind tunnel height, $L = 5 \times 10^{-3}$ m and $q_m = 3.206$ g/s.
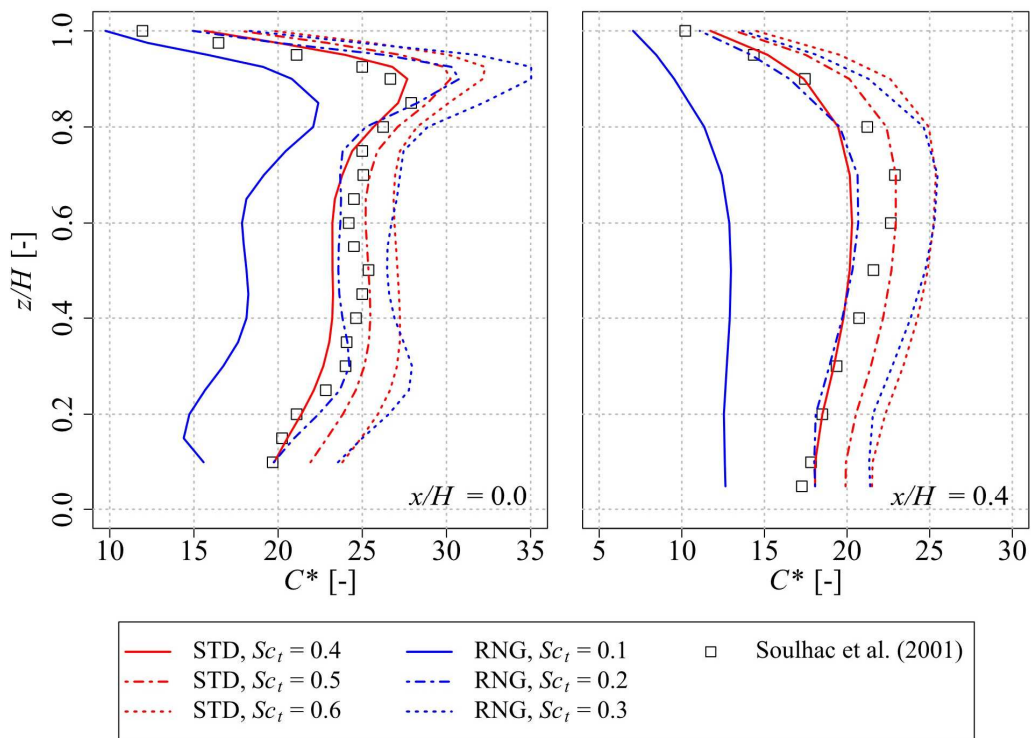
Figure 2.12 – Comparison of dimensionless concentrations between the numerical model and the experimental data of Gamel (2005) with the standard k-ε turbulence model for three turbulent Schmidt numbers.

Concentrations after the 2D obstacle are depending on the turbulent Schmidt number, with a maximal variation over concentrations of around 20% for the Sc_t variation considered ($\Delta Sc_t = 0.2$). However, for this test case, increasing Sc_t is not only increasing the concentrations but can also decrease it. Indeed, as it can be seen in Figure 2.12, for $z/H < 1.5$ the concentrations increase with Sc_t while for $z/H > 1.5$, they decrease slightly. This figure also shows that the best Sc_t do depend on the spatial location considered: while the best Sc_t seems to be 0.8 for $x/H = 3$, a turbulent Schmidt number of 1.0 seems to be a better choice for $x/H = 7$. According to the previous observations, the turbulent Schmidt number has therefore a different impact on concentrations depending on the spatial location considered both in the streamwise direction x and in the vertical direction z. This number being the same in the whole computational domain, the best Sc_t is therefore a compromise and could be found using statistical indicators to evaluate its impact. These indicators or performance criteria, including

53

FB, *MG*, *VG*, *NMSE*, *FAC2*, *NAE* and *Target* have been calculated and the results are summarized in Table 2.3.

Table 2.3 – Evaluation of the forced convection solver performances over the data of Gamel (2005)

	FB	*MG*	*VG*	*NMSE*	*FAC2*	*NAE*	*Target*
Standard k-ε model							
$Sc_t = 0.5$	0.353	1.429	1.411	0.129	0.827	33%	0.36
$Sc_t = 0.7$	0.178	1.196	1.429	0.032	0.789	17%	0.21
$Sc_t = 0.8$	0.117	1.124	1.617	0.014	0.806	11%	0.16
$Sc_t = 0.9$	0.067	1.070	1.967	0.005	0.830	8%	0.13
$Sc_t = 1.0$	0.026	1.026	2.568	0.001	0.857	10%	0.12
Objective							
Target value	0	1	0	0	1	0%	0
Target range	-0.3 < x < 0.3	0.7 < x < 1.3	< 4	< 1.5	0.5 < x < 1.5	-	< 0.5

As it can be seen in Table 2.3, all the criteria do not have the same tendencies. Indeed, while for the geometric variance *VG*, the best results are obtained with $Sc_t = 0.5$, for the geometric mean bias *MG* the best results are obtained with $Sc_t = 1.0$. These criteria should therefore not be used standalone but the global result of all the criteria should be considered instead. Considering all the criteria simultaneously, the best results are obtained with $Sc_t = 1.0$. If it is the minimal error over the experimental data that is required, then $Sc_t = 0.9$ is the best choice with an overall error of 8%, where the results are illustrated in Figure 2.13.
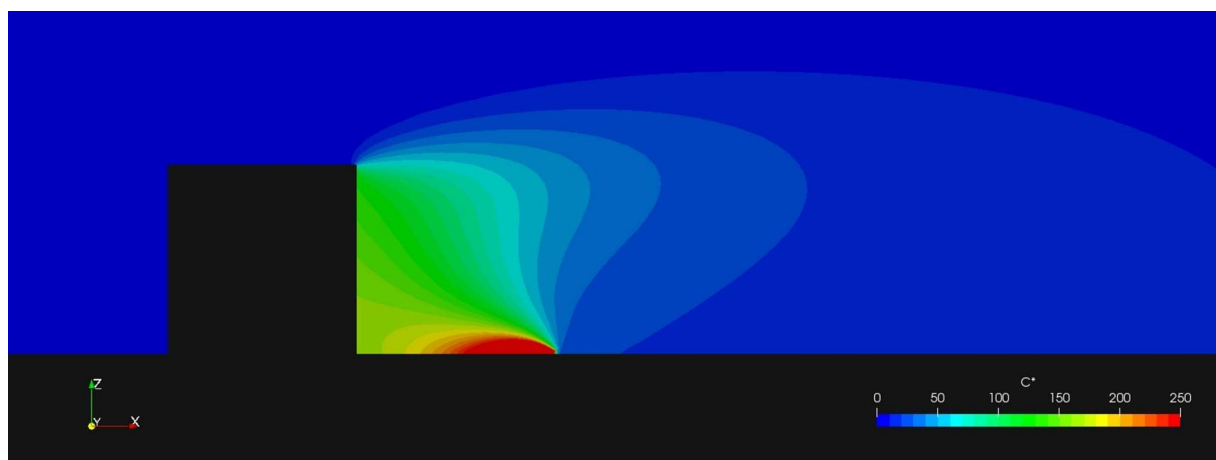
Figure 2.13 – Evolution of dimensionless concentrations after the 2D obstacle with the standard k-ε turbulence model and $Sc_t = 0.9$

The previous results have shed light on the following issues:

ⓘ Is a CFD-RANS model sufficient to good reproduce wind speed in urban areas for computational wind engineering applications?

ⓘ Is a two-equation k-ε turbulence model sufficient to accurately reproduce velocity and concentration fields for air pollution modelling?

ⓘ How much can the turbulent Schmidt number Sc_t change the concentrations modelled? Which is the best turbulent Schmidt number to choose?

The conclusions are as follows:

- ✔ The forced convection solver is able to reproduce well velocities and concentrations in a different configuration (after a 2D isolated building) with a global error of around 10% on concentrations when choosing the best turbulent Schmidt number.

- ✔ The turbulent Schmidt number has an impact on the concentrations modelled and the best turbulent Schmidt number to choose depends on the spatial location considered, both on the streamwise and vertical directions.

- ✔ The best turbulent Schmidt number for a given turbulence closure scheme could be different depending on the case considered (the best Sc_t was previously 0.5 for the 2D street canyon while it is 0.9 for the 2D isolated building).

- ✔ With the same variation over the turbulent Schmidt number as for the 2D street canyon ($\Delta Sc_t = 0.2$), the same maximal variation over concentration (~20%) is obtained using the same turbulence model (standard k-ε).

2.2.5.3. Identification of weaknesses in isotropic models

The forced convection solver was finally tested against experimental data from the CODASC database (COncentration DAta of Street Canyons). This test case has been chosen to have a final validation for a street-canyon case but with cross-flows (3D case). The objective was to assess if the solver is able to accurately reproduce concentrations in the same configuration as in Section 2.2.5.1. but in 3D and, if the standard k-ε turbulence model is sufficient for 3D modelling.

The experiments have been performed in the Laboratory of Building and Environmental Aerodynamics at the Karlsruhe Institute of Technology (KIT). Several street-canyon test cases can be found in the CODASC database with different aspect ratios (i.e., different building heights and lengths between the buildings) and some cases with vegetation are also available. The case discussed below is the case where $W = H$ (the distance between the two buildings is equal to their height) without vegetation in the street.
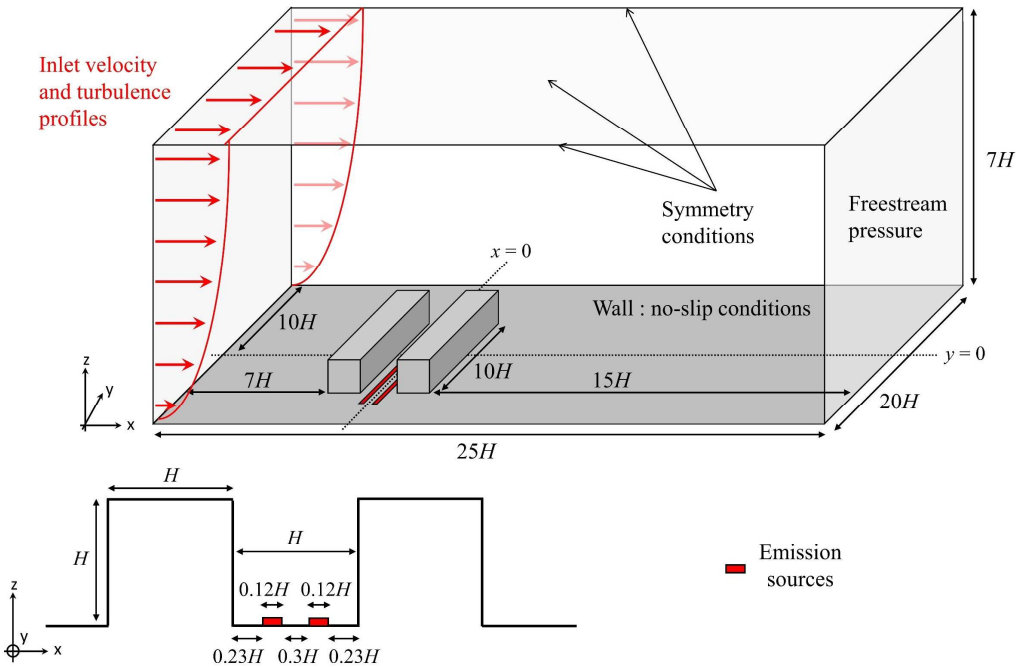
Figure 2.14 – Boundary conditions and domain size.

Simulations were performed using the same boundary conditions as described previously and the passive tracer emission was modelled by two volumetric sources located between the two

buildings with a mass flow rate of 100 µg/s. Recommendations given by Franke et al. (2007) have been followed and a summary of the boundary conditions and the distances in the domain is given in Figure 2.14.

Three mesh sizes were considered to study the mesh sensitivity with the *GCI* including 5 mm, 2.5 mm, and 1.25 mm. The results show that 2.5 mm meshes is not a sufficient grid resolution giving an average *GCI* of 13%. The 1.25 mm meshes, giving an average *GCI* of 5%, is nonetheless sufficient and has been adopted for the simulations leading to $y^+ = 35$ and around 6.5 million meshes. This mesh size corresponds to the meshes near the building walls and in the whole street. An illustration of the resulting grid is proposed in Figure 2.15.
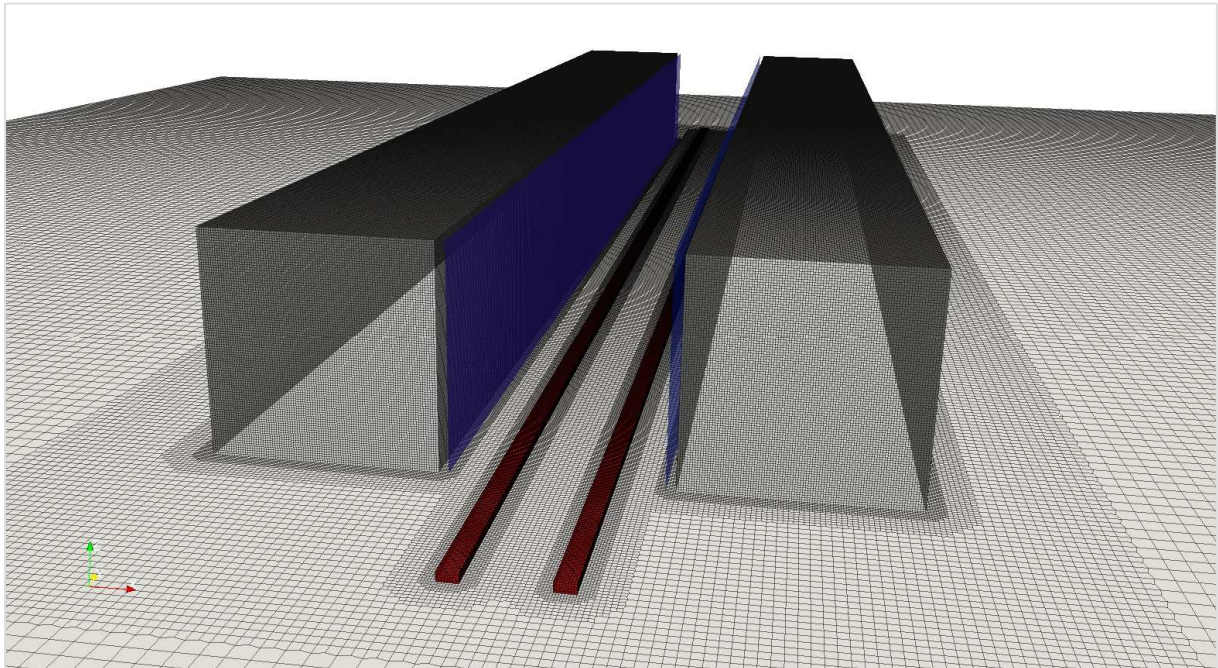
Figure 2.15 – Mesh illustration (1.25 mm between the buildings and near the emission source and 5 mm in the overall domain) with "Wall A" the left blue wall and "Wall B" the right one.

Six turbulent Schmidt numbers were considered to compare the concentration results against the experimental data. Figure 2.16 illustrates the evolution of the dimensionless concentration C^* as a function of the dimensionless lateral distance in the canyon y/H for three altitudes z/H and at two x/H locations (Wall A: -0.457 / Wall B: 0.457) obtained with $Sc_t = 0.2$, 0.3 and 0.4. The location of the experimental measurements is specified in blue in the figure for a better understanding. The dimensionless concentration was calculated using (Eq. 2.11) with

U_{ref} = 4.63 m/s the wind speed at H_{ref}, H_{ref} = 0.12 m the buildings height, L = 1.42 m and q_m = 100 µg/s. Additional results can be found in Appendix E.
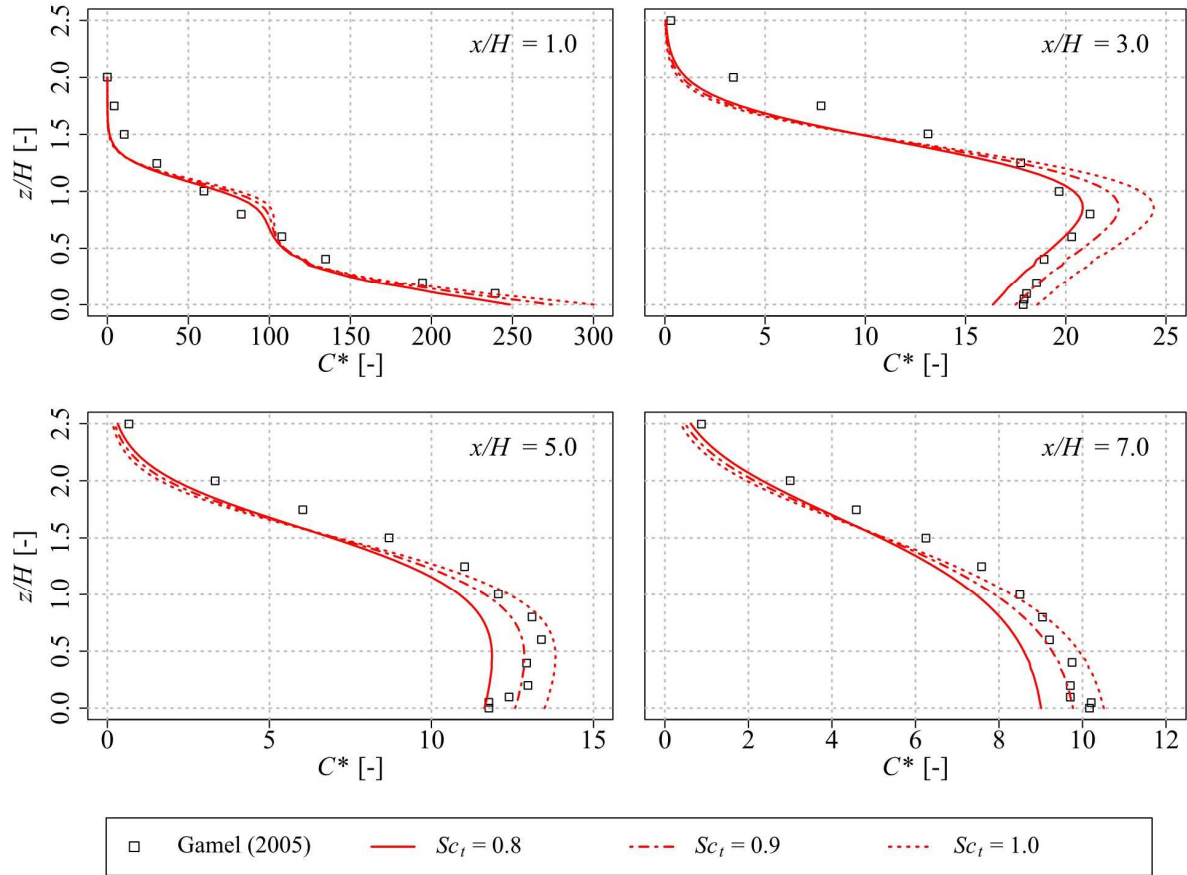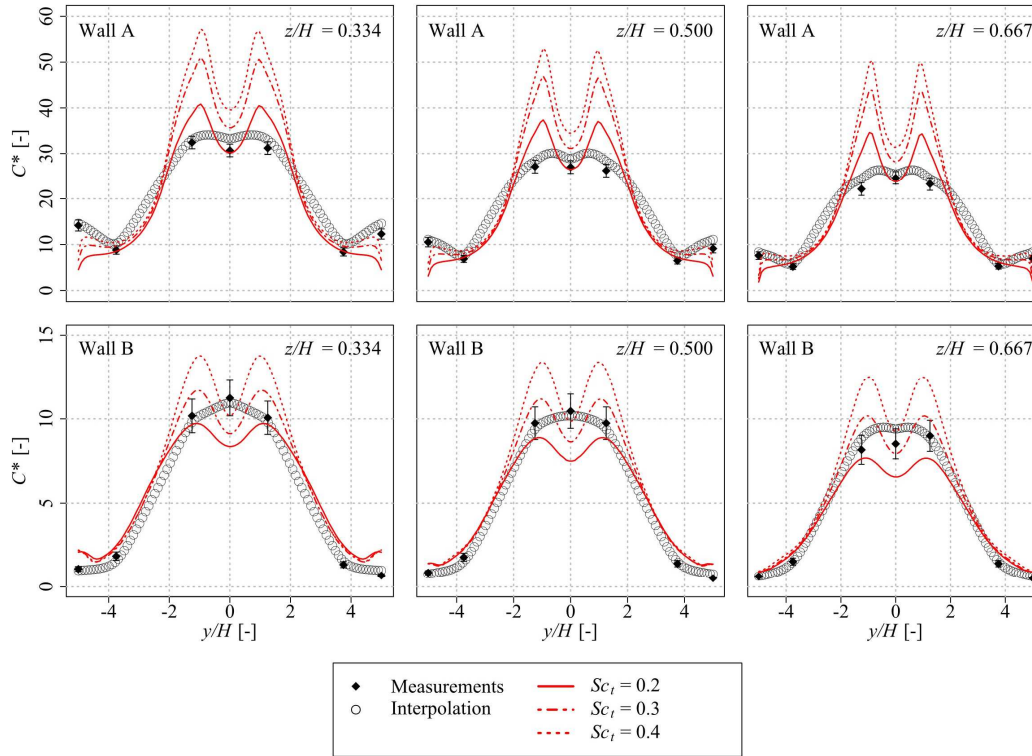

Figure 2.16 – Comparison of dimensionless concentrations between the numerical model and the experimental data from the CODASC database ($W = H$) with the standard k-ε turbulence model.

The agreement between the experimental data and the numerical results is again depending on the turbulent Schmidt number considered. According to the performance criteria summarized in Table 2.4, the best results are obtained for a turbulent Schmidt number ranging between 0.2 and 0.3 with an error of around 25%.

However, it can be seen in the Figure 2.16 that the best Sc_t to choose is not the same for the wall A as it is for the wall B. The performance criteria have therefore been calculated with a distinction between these two locations, and the results are given in Table 2.5. The results show that the error is not significatively different between Sc_t = 0.2 and Sc_t = 0.3 at the wall A with 23% and 26% respectively. The error is significatively more different between these two turbulent Schmidt numbers at the wall B with 22% and 16% respectively. The best turbulent Schmidt number is therefore depending on the spatial location.

Table 2.4 – Evaluation of the forced convection solver performances over the CODASC dataset.

	FB	MG	VG	NMSE	FAC2	NAE	Target
Standard k-ε model							
$Sc_t = 0.2$	0.089	1.093	1.206	0.008	0.976	22%	0.37
$Sc_t = 0.3$	-0.075	0.927	1.127	0.006	1.084	24%	0.51
$Sc_t = 0.4$	-0.170	0.843	1.126	0.029	1.186	27%	0.64
$Sc_t = 0.5$	-0.288	0.748	1.167	0.085	1.296	36%	0.93
$Sc_t = 0.6$	-0.365	0.691	1.216	0.138	1.382	43%	1.14
$Sc_t = 0.7$	-0.130	0.646	1.271	0.193	1.465	49%	1.34
Objective							
Target value	0	1	0	0	1	0%	0
Target range	-0.3 < x < 0.3	0.7 < x < 1.3	< 4	< 1.5	0.5 < x < 1.5	-	< 0.5

Table 2.5 – Evaluation of the forced convection solver performances over the CODASC dataset for $Sc_t = 0.2$ and $Sc_t = 0.3$ with distinction between the two data locations (Wall A and Wall B).

	FB	MG	VG	NMSE	FAC2	NAE	Target
Wall A							
$Sc_t = 0.2$	0.106	1.112	1.290	0.011	0.818	23%	0.51
$Sc_t = 0.3$	-0.080	0.923	1.165	0.006	0.986	26%	0.72
Wall B							
$Sc_t = 0.2$	0.031	1.031	1.128	0.001	1.135	22%	0.42
$Sc_t = 0.3$	-0.056	0.945	1.090	0.003	1.181	16%	0.30
Objective							
Target value	0	1	0	0	1	0%	0
Target range	-0.3 < x < 0.3	0.7 < x < 1.3	< 4	< 1.5	0.5 < x < 1.5	-	< 0.5

According to the previous results, the forced convection solver is able to accurately reproduce pollutant dispersion in a 3D street canyon. However, it should be noticed in Figure 2.16 that two maximal values of concentrations are systematically reached according to the numerical results (at y/H = -1.5 and 1.5), but this is not the case in the experimental data. To understand the origin of this difference, streamlines have been drawn and the results are presented in Figure 2.17. According to the results, the pollutants emitted at the edges of the street canyon seems to be dragged into recirculating flows directed towards the middle of the street. The pollutants emitted in the middle of the street (y/H = 0) are only dragged into vertical vortices before being released at the top of the downwind building which could explain lower concentrations at the

middle of the street compared to y/H = -1.5 and y/H = 1.5. However, this phenomenon is not existing in the reality according to the experimental results.
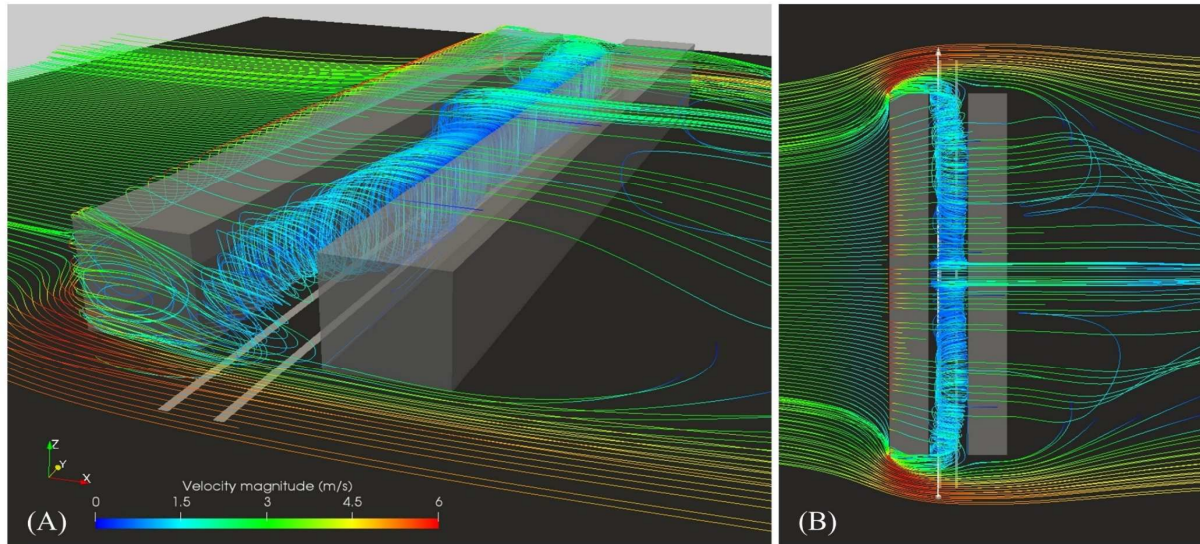
Figure 2.17 – Illustration of streamlines and vortices in the street canyon for 3D view (A) and a 2D top view (B)

The use of an isotropic turbulence model such as the standard k-ε model could explain these results, the turbulence being anisotropic in real life. To verify this hypothesis, new simulations were conducted using an anisotropic turbulence model, the Reynolds Stress Model (RSM), and the results are given in Figure 2.18 for Sc_t = 0.3. The previous results obtained with Sc_t = 0.2 and Sc_t = 0.3 are also given for a better comparison.

It can be seen in Figure 2.18 that the shape of the concentration profiles are closer to the experimental data with the RSM turbulence model than with the standard k-ε model, confirming the previous hypothesis. However, the absolute results are too far from the experimental data with Sc_t = 0.3. Using a lower turbulent Schmidt number in the common range of values (0.3 to 1.2) will not sufficiently improve the results especially at the wall B location. The overestimation of the concentration at this location could be explained by an underestimation of the turbulent viscosity v_t. The RSM was demonstrated to be improved before to be used for real applications but, the investigation is out of the scope of this thesis work nonetheless.
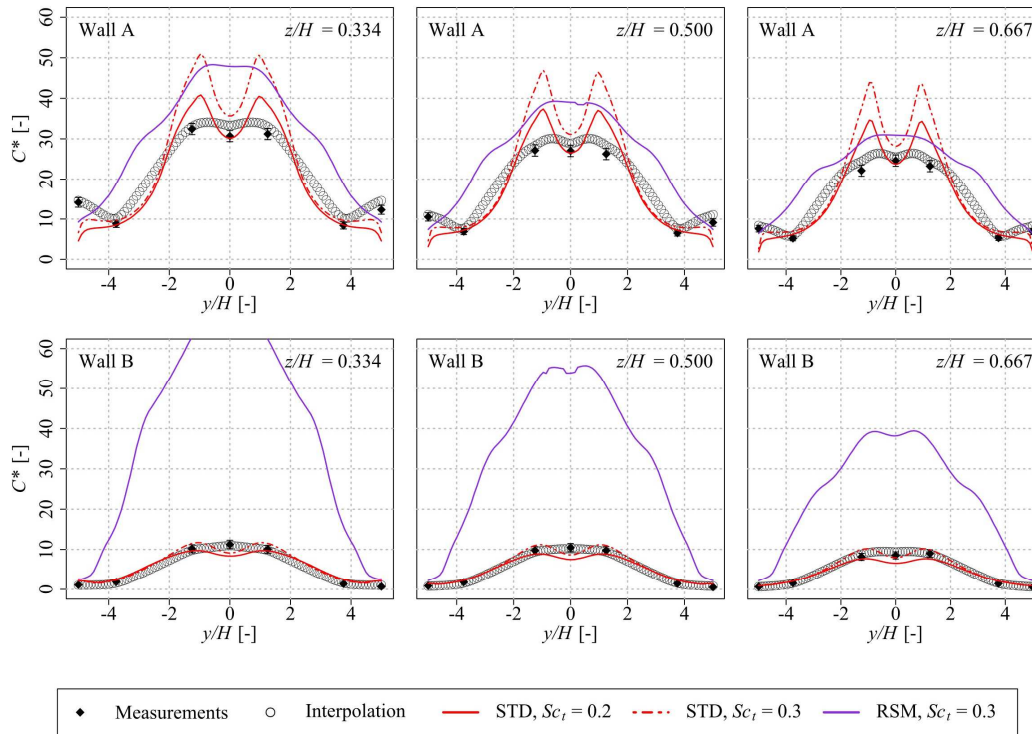
Figure 2.18 – Comparison of dimensionless concentrations between the numerical model and the experimental data with the standard k-ε turbulence model (STD, red curves) and the Reynolds stress model (RSM, purple curve).

The previous results have shed light on the following issues:

Is a CFD-RANS model sufficient to good reproduce wind speed in urban areas for computational wind engineering applications? What is the best turbulence model for CFD-RANS air pollution modelling?

Is a two-equation k-ε turbulence model sufficient to accurately reproduce velocity and concentration fields for air pollution modelling? Is the RNG variant giving more accurate results?

How much can the turbulent Schmidt number Sc_t change the concentrations modelled? Which is the best turbulent Schmidt number to choose?

The conclusions are as follows:

- ✔ The forced convection solver is able to reproduce well concentrations in a three-dimensional configuration with a global error of around 25% on concentrations when choosing the best turbulent Schmidt number.

- ✔ The turbulent Schmidt number has an impact on the concentrations modelled and the best turbulent Schmidt number to choose depends on the spatial location considered.

- ✔ Isotropic models such as the standard k-ε turbulence model can give overall good results in 3D but can lead to punctual differences compared to the reality.

- ✔ The results also show that anisotropy does not significantly impact the flow.

2.3. Mixed convection solver: stable and unstable atmosphere modelling

The forced convection solver described and validated in Section 2.2. is able to accurately reproduce wind profiles and pollutant dispersion in neutral atmosphere. However, this solver cannot reproduce the thermal effects which appear when the atmosphere is stable or unstable. It is therefore necessary to build a second solver, able to model non-neutral atmospheres.

This section deals with the development of the mixed convection solver, i.e., a solver for non-neutral atmosphere modelling where both wind effects and thermal variations have an impact on the airflow.

2.3.1. Atmospheric stability and Richardson number

The atmospheric stability can be described studying the sign of the potential temperature gradient $\partial\theta/\partial z$, where z is a vertical and ascendant axis (Sportisse, 2008):

- When $\partial\theta/\partial z > 0$, the atmosphere is called *stable*.
- When $\partial\theta/\partial z < 0$, the atmosphere is called *unstable*, and an additional turbulence is generated from the thermal effects.
- When $\partial\theta/\partial z = 0$, the atmosphere is called *neutral*.

Another way to qualify the stability of the atmosphere is the Richardson number. This dimensionless number, being the ratio between the buoyancy forces and the flow shear forces, also allow evaluating the intensity of the turbulence destruction due to thermal effects. The equation of the Richardson number is given in (Eq. 2.12) and corresponds to the most common form found for CFD purposes (Li et al., 2010; Uehara et al., 2000).

$$Ri = \frac{Gr}{Re^2} = \frac{g\Delta H}{U_H{}^2}\frac{\left(T_H - T_g\right)}{T_{air}} \qquad \text{(Eq. 2.12)}$$

where Gr is the Grashof number, Re is the Reynolds number, g is the gravitational acceleration, ΔH is the distance between a reference height H and the ground, U_H is the reference velocity (which is the velocity at $z = H$), T_{air} is the ambient temperature, T_H is the temperature at $z = H$, and T_g is the surface temperature of the ground.

In the equation of the Richardson number, the temperature T can be replaced by the potential temperature θ, using (Eq. 2.13), to consider the normal decrease of the temperature with the altitude (Woodward, 1998). However, for urban scale modelling, since ΔH is generally small, the normal decrease of the temperature can be neglected, and it can be considered that $\theta \approx T$.

$$\theta = T - \lambda.\Delta H \qquad \text{(Eq. 2.13)}$$

where λ is the adiabatic lapse rate being around 0.01 K/km.

In practice, for unstable cases, an additional turbulence is generated due to the thermal effects and $Ri < 0$. For stable cases $Ri > 0$, and, the mechanical turbulence is destroyed due to the

thermal effects when $Ri > 1$. For Ri ranging between 0 and 1, there is a competition between thermal and mechanical effects. Thus atmospheric stability have a high impact on the turbulence of the atmosphere, on the velocity field (Bottillo et al., 2014) and, therefore, on pollutant concentrations. It is especially the case in street canyons were mixed convection, i.e. the combination of forced and natural convection, can significatively change pollutant concentrations compared to forced convection alone (Allegrini et al., 2013; Wang et al., 2011). Thermal effects, often neglected in CFD, must therefore be considered, and was implemented in the CFD solver to model stable and unstable atmosphere. For this purpose, the compressible Navier-Stokes equations must be considered in order to take into account the dependency of the air density with the temperature. Two question arise:

⍰ How much can thermal effects change the pollutant dispersion in urban areas ? Is the stable or unstable atmosphere leading to higher pollutant concentrations ?

2.3.2. Compressible Navier-Stokes equations

The compressible Navier-Stokes equations are balance equations that come from the Newton's second law applied to a compressible fluid. Compared to their incompressible equivalents, they include three equations: the continuity (Eq. 2.14), the momentum (Eq. 2.15) and the energy (Eq. 2.16) equation. The temperature can be calculated from the thermal energy obtained in this last equation.

$$\frac{\partial \rho}{\partial t} + \nabla.(\rho u) = 0 \qquad \text{(Eq. 2.14)}$$

$$\rho \left(\frac{\partial u}{\partial t} + u.\nabla u \right) = -\nabla p + \nabla.\left(2\mu_{eff}D(u) \right) - \nabla \left(\frac{2}{3}\mu_{eff}(\nabla.u) \right) + \rho g \qquad \text{(Eq. 2.15)}$$

$$\frac{\partial \rho e}{\partial t} + \nabla.(\rho u e) + \frac{\partial \rho K}{\partial t} + \nabla.(\rho u K) + \nabla.(up) = \nabla.\left(\alpha_{eff}\nabla e \right) + \rho g.u \qquad \text{(Eq. 2.16)}$$

where u is the velocity, p the pressure, ρ the density, e the thermal energy, $D(u)$ the rate of strain tensor given in (Eq. 2.17), K the kinetic energy given in (Eq. 2.18), g the gravitational acceleration, μ_{eff} the effective viscosity defined as the sum of molecular and turbulent viscosity

and α_{eff} the effective thermal diffusivity defined as the sum of laminar and turbulent thermal diffusivities.

$$D(u) = \frac{1}{2}[\nabla u + (\nabla u)^T] \qquad \text{(Eq. 2.17)}$$

$$K \equiv |u|^2/2 \qquad \text{(Eq. 2.18)}$$

☞ The previous equations, from (Eq. 2.14) to (Eq. 2.18) are included in the *buoyantPimpleFoam* solver from OpenFOAM 6.0. Using this solver as a basis, all the points discussed from Section 2.2.2. to Section 2.2.4. (the use of a RANS methodology, the use of a PIMPLE algorithm and the implementation of the advection-diffusion equation respectively) were applied and a new solver, which will be called *Mixed Convection Solver* (MCS), was obtained. With this new solver, thermal effects on the velocity field and turbulence are considered, and different atmospheric stability can be modelled.

2.3.3. Model validation in case of mixed convection

Two experimental test cases were used to assess the performances of the mixed convection solver in modelling different atmospheric stability, and to answer some questions raised previously. The experimental and numerical set-ups as well as the results comparison are successively presented hereafter and a summary of the test cases with the associated objectives is given in Table 2.6.

Table 2.6 – Summary of the two test cases used for the mixed convection solver validation.

Authors	2D	3D	Buil.	S.C.	W.T.	In-situ	Objective
Uehara et al. (2000)	✔			✔	✔		Comparison between CFD and experimental data for a simple regular street-canyon case with a slightly unstable atmospheric stability.
Cui et al. (2016)		✔	✔		✔		Comparison between CFD and experimental data for an asymmetric case of buildings with a 3D flow field, indoor/outdoor exchanges, and an unstable atmospheric stability

(Buil.: Buildings, S.C.: Street-canyon, W.T.: Wind tunnel)

2.3.3.1. Modelling an unstable atmosphere

The mixed convection solver was first tested against experimental data from Uehara et al. (2000). This test case has been chosen to have a first comparison against experimental data for a simple case (2D) of street canyons with thermal effects. Only one turbulence model was used, the RNG k-ε model, since it led not to significant differences with the use of the standard one. The results were compared to assess the ability of the mixed convection solver to model an unstable atmosphere.

Uehara et al. (2000) studied in a wind tunnel the evolution of the streamwise wind velocity and the temperature in the middle of a succession of regular street canyons (10 buildings with equal widths and heights: $W = H = 0.1$ m) for different Richardson numbers. Among the seven test cases available, an unstable case ($Ri = -0.19$) has been chosen, with therefore a thermal generation of turbulence, but a flow mostly under control of the mechanical effects. Their experimental set-up was symmetrical in the direction transverse to the flow (y-direction) and they used a perpendicular wind direction (along the x-direction). Results are provided for both streamwise velocity and temperature in the middle of the 5th street (between the 5th and the 6th building) as shown in Figure 2.19. The results are all given at $x = 0$ and $y = 0$.
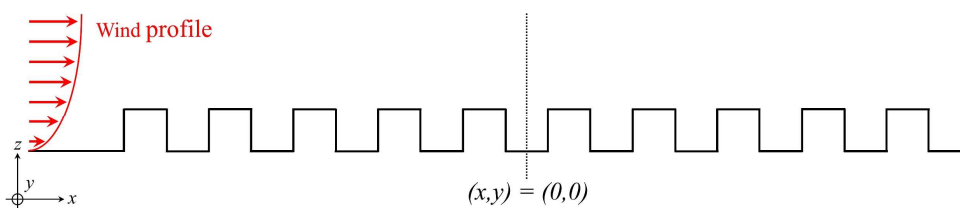
Figure 2.19 – Location of the vertical measurement profile.

Simulations were performed using the inlet velocity profile measured and given by Uehara et al. (2000) and a temperature of T_{air} = 292 K. A freestream outlet condition has been specified at the outlet and symmetry conditions were applied at the top and the lateral boundaries of the domain. No-slip conditions were applied to all other boundaries including the building roofs, walls and the ground. The wall temperature was fixed to T_{ground} = 332 K. The recommendation from COST Action 732 guidelines has been followed (Franke et al., 2007) and a summary of the distances in the computational domain and the boundary conditions is given in Figure 2.20.
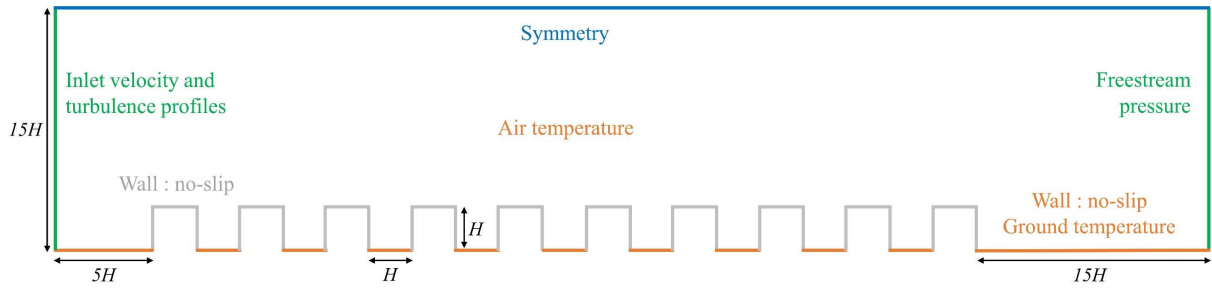
Figure 2.20 – Boundary conditions and domain size

A study on the mesh sensitivity based on the grid convergence index was conducted. The *GCI* between 1.25 mm and 2.5 mm meshes gave a global error of less than 5%. However, it was shown previsouly that sometimes 2.5 mm meshes are not sufficient and to ensure the reliability of the results, 1.25 mm meshes has been selected and 5 mm meshes were used for z ranging from $2H$ to $15H$ to avoid too high calculation costs ($10 < y^+ < 30$). This grid resolution lead to a total number of 1.2 million meshes. An illustration of the grid is presented in Figure 2.21.
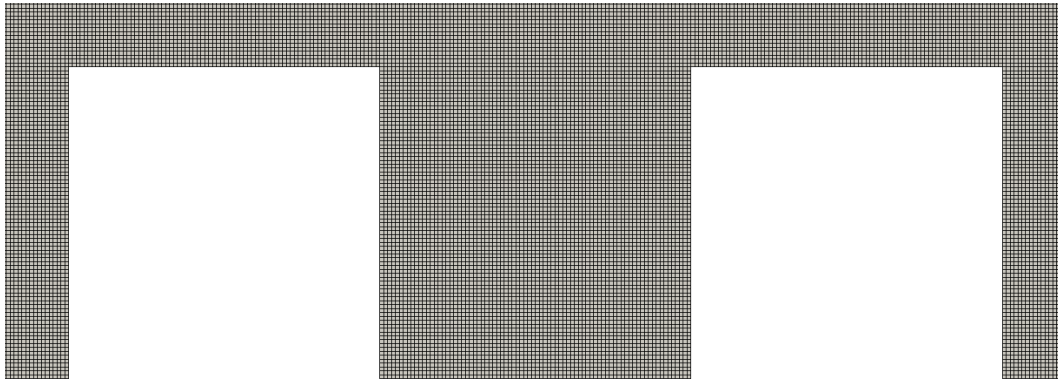
Figure 2.21 – Mesh illustration (1.25 mm for $z < 2H$ and 5 mm in the rest of the domain).

Simulations were performed using the RNG k-ε turbulence model. The dimensionless streamwise velocity U/U_{ref} and the dimensionless temperature T^* as a function of the dimensionless height z/H are presented in Figure 2.22 (U_{ref} = 1.61 m/s). The dimensionless temperature was calculated according to (Eq. 2.19).

$$T^* = \frac{T - T_a}{T_g - T_a}$$
(Eq. 2.19)

where T^* is the dimensionless temperature, T is the temperature, T_a is the air temperature and T_g is the ground temperature.

Figure 2.22 – Comparison of the dimensionless streamwise velocity and the dimensionless temperature between the numerical model and the experimental data of Uehara et al. (2000).

According to Figure 2.22, the streamwise velocity is globally accurately reproduced inside ($z/H < 1$) and outside ($z/H > 1$) the canyon, except near the ground. The differences between the numerical model and the experimental data at this location can be explained by the boundary conditions used. Indeed, a no-slip condition was used for the ground. In other words, a velocity of $U = 0$ m/s was applied at this boundary and is probably the cause of the differences with the experimental data for low altitudes.

Regarding the temperature, the CFD model is able to accurately reproduce the dimensionless temperature profile with a slight overestimation for $z/H < 0.1$ and a very good agreement with experimental data for higher altitudes. A slight temperature spike is nonetheless observed around $z/H = 0.9$, but is also observed from other authors (Li et al., 2010).

The previous results have shed light on the following issues:

(?) Is a CFD-RANS model sufficient to good reproduce wind speed in urban areas for computational wind engineering applications?

(?) Is a CFD-RANS model able to accurately reproduce effects of atmospheric stability on wind velocities?

The conclusions are as follows:

- The forced convection solver is able to reproduce with good concordance a streamwise velocity profile in a 2D street canyon configuration with thermally induced turbulence (unstable atmosphere).

- The solver is able to reproduce with a very good accuracy a temperature profile in an unstable atmosphere.

2.3.3.2. Modelling a stable atmosphere with indoor/outdoor exchanges

The mixed convection solver was then tested against experimental data from Cui et al. (2016). This experimental test case has been chosen for multiple reasons. Firstly, the test case corresponds to a complex situation including asymmetrical buildings, edge effects and 3D flow motions. Secondly, the results are given for both wind velocity and pollutant concentration considering local unstable atmosphere. Finally, this test case also allows assessing model accuracy for indoor/outdoor exchanges modelling. Only one turbulence model was used, the RNG k-ε model, and the results were compared to assess the ability of the mixed convection solver to model a more complex unstable atmosphere and indoor/outdoor exchanges.

Cui et al. (2016) studied in a wind tunnel the evolution of the wind velocity and the pollutant concentration for a vertical profile between two buildings ($x = L/2$), and, for a horizontal profile inside a room in the downstream building ($z = 5L/8$). The ground between the two

buildings was heated to variable temperatures T_g and the air in the wind tunnel was injected with a fixed temperature T_a = 288 K, leading to 8 distinct Richardson numbers. Among the available test cases, a more unstable case than previously was used (Ri = -1.22) leading to a higher thermal generation of turbulence than previously. Their experimental set-up was fully 3D with a higher downwind building and a room located inside of this building with two windows, one opened to the upwind building and the second opened to the outlet boundary. An emission source was also located on the roof of the upwind building at $x = y = 0$ where an emission rate of 0.087 g/s was applied.

Simulations were performed using the same inlet velocity and turbulence profiles as used in Cui et al. (2016) with a ground temperature of T_g = 423 K. A freestream outlet was specified for the outlet boundary and symmetry conditions were applied to lateral and top boundaries. No-slip conditions were specified to all other boundaries including buildings roofs, building walls and the ground. Finally, recommendation of Franke et al. (2007) were followed for the minimal distances in the computational domain. The experimental set-up with distances, boundary conditions, location of the emission source and the heated ground, and location of the experimental measurements profiles is presented in Figure 2.23. Further information can be found in the original paper.

Mesh sensitivity tests were carried out using the grid convergence index. It was assessed for both outdoor (between the two buildings) and indoor (inside the downwind building room) environment. A *GCI* of less than 5% was obtained for meshes of 2.5 mm in the outdoor environment and 0.625 mm in the indoor environment compared to 5 mm and 1.25 mm meshes results respectively. This low numerical uncertainty and the high number of cells (7.3 millions) which results in high computational time lead to the selected mesh. The resulting y^+ is 50 in the outdoor environment and 15 in the indoor one. An illustration of the meshes for the outdoor and the indoor environment is presented in Figure 2.24 (A) and Figure 2.24 (B) respectively.
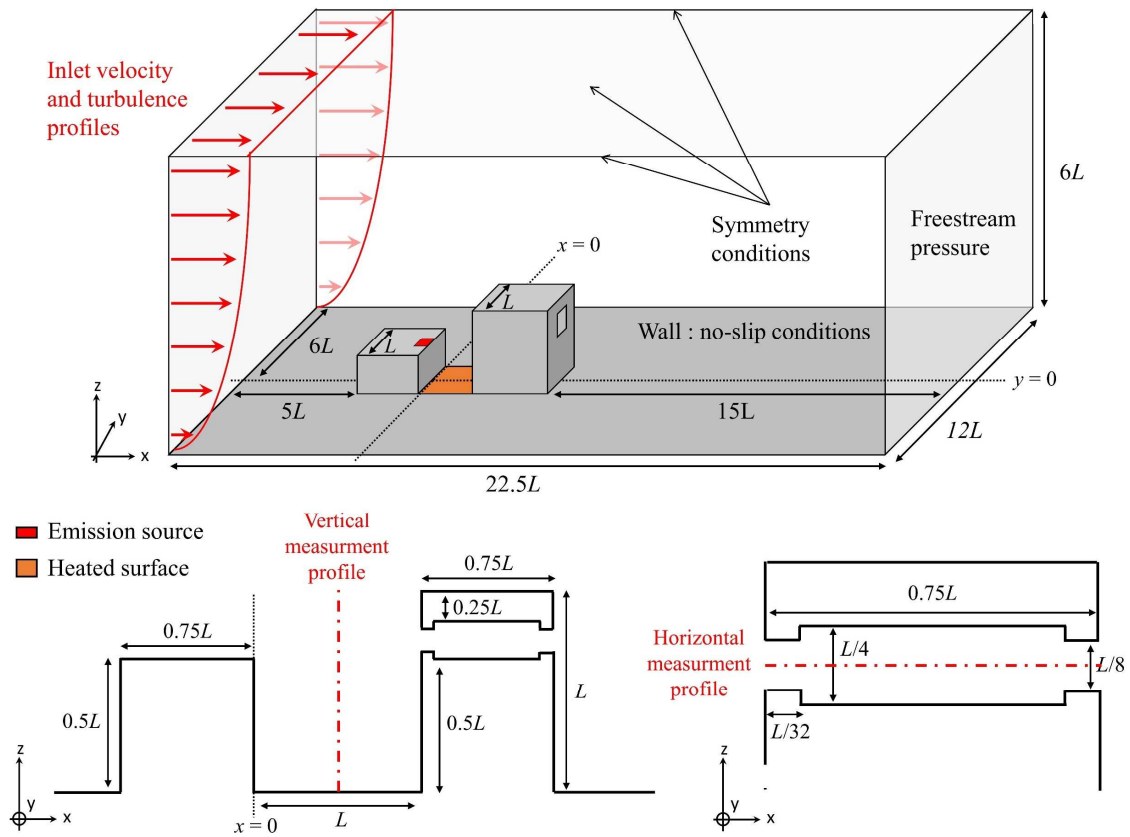
Figure 2.23 – Boundary conditions and domain size.
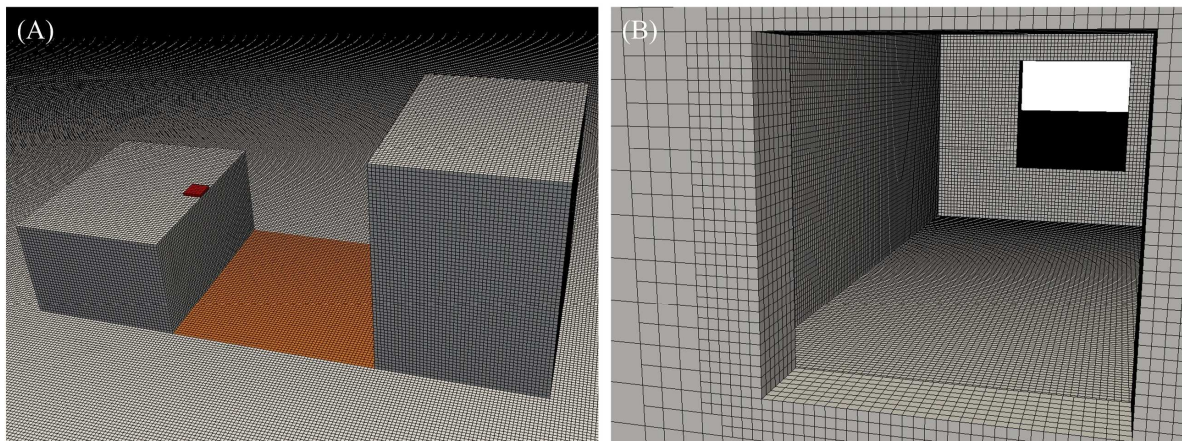
Figure 2.24 – Mesh illustration of (A) the two buildings with the heated surface in orange and the emission source in red (mesh size of 2.5 mm) and (B) the indoor environment of the downwind building (mesh size of 0.625 mm).

The dimensionless streamwise velocity U/U_{ref} and the dimensionless concentration between the buildings ($x = L/2$) as a function of the dimensionless height z/L are proposed in Figure 2.25. The dimensionless concentration was calculated according to (Eq. 2.11) with $U_{ref} = 0.7$ m/s, $H_{ref} = 0.08$ m, $L = 0.16$ m and $q_m = 0.087$ g/s according to Cui et al. (2016).

The dimensionless streamwise velocity U/U_{ref} and the dimensionless concentration in the downwind building room as a function of the dimensionless distance in the streamwise direction x/L are presented in Figure 2.26.

According to Figure 2.25, the wind profile is accurately reproduced by the numerical model. Indeed, numerical results are very close from experimental results, especially for $z/L > 0.55$. Velocities are nonetheless slightly underestimated for lower altitudes. Concerning the results on concentrations, it can be seen that the experimental results are well reproduced by the numerical model using the turbulent Schmidt numbers considered (ranging from 0.2 to 0.3) and the best results are obtained for $Sc_t = 0.2$.
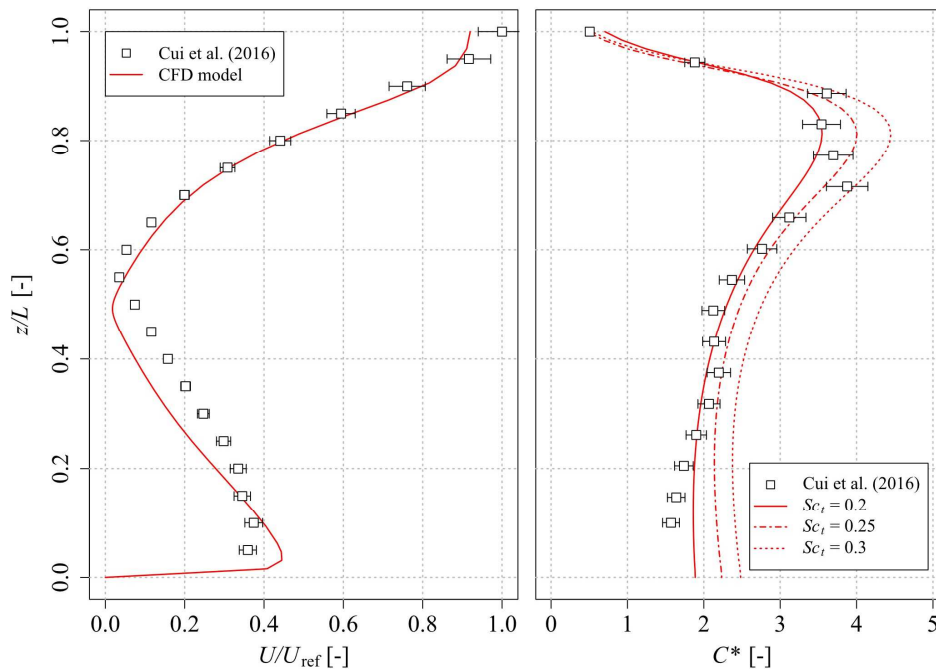
Figure 2.25 – Comparison of the dimensionless streamwise velocity and the dimensionless concentration between the numerical model and the experimental data of Cui et al. (2016), the red curves, in the outdoor environment.

According to Figure 2.26, there is a high overestimation of the wind velocity just after the first window ($x/L = 1.0$). The velocities are, however, very well reproduced starting from $x/L = 1.1$ and up to the second window. In terms of concentrations, the experimental results are also well reproduced by the numerical model, especially with $Sc_t = 0.25$. It should finally be noted that, whichever the turbulent Schmidt number considered, the numerical model is globally giving a constant concentration along the room while the experimental concentration has some variations. These variations are nonetheless very small and globally included in the experimental uncertainties.
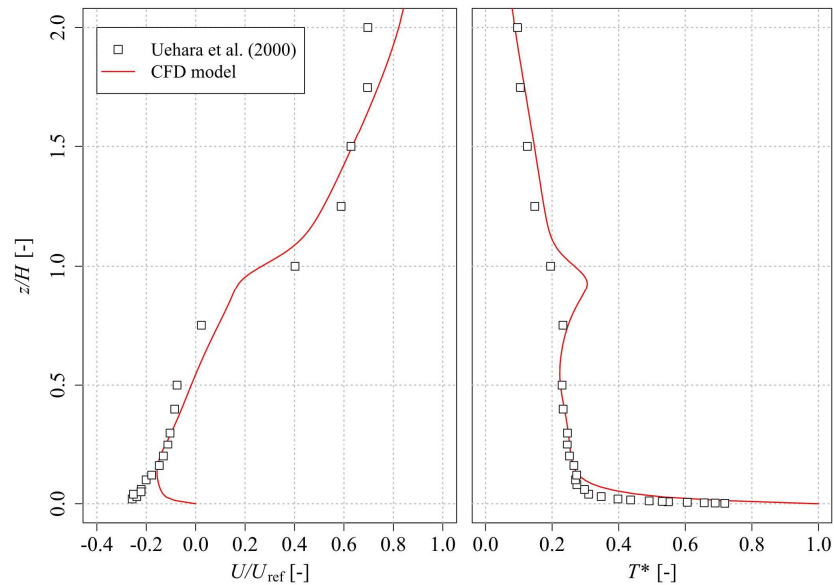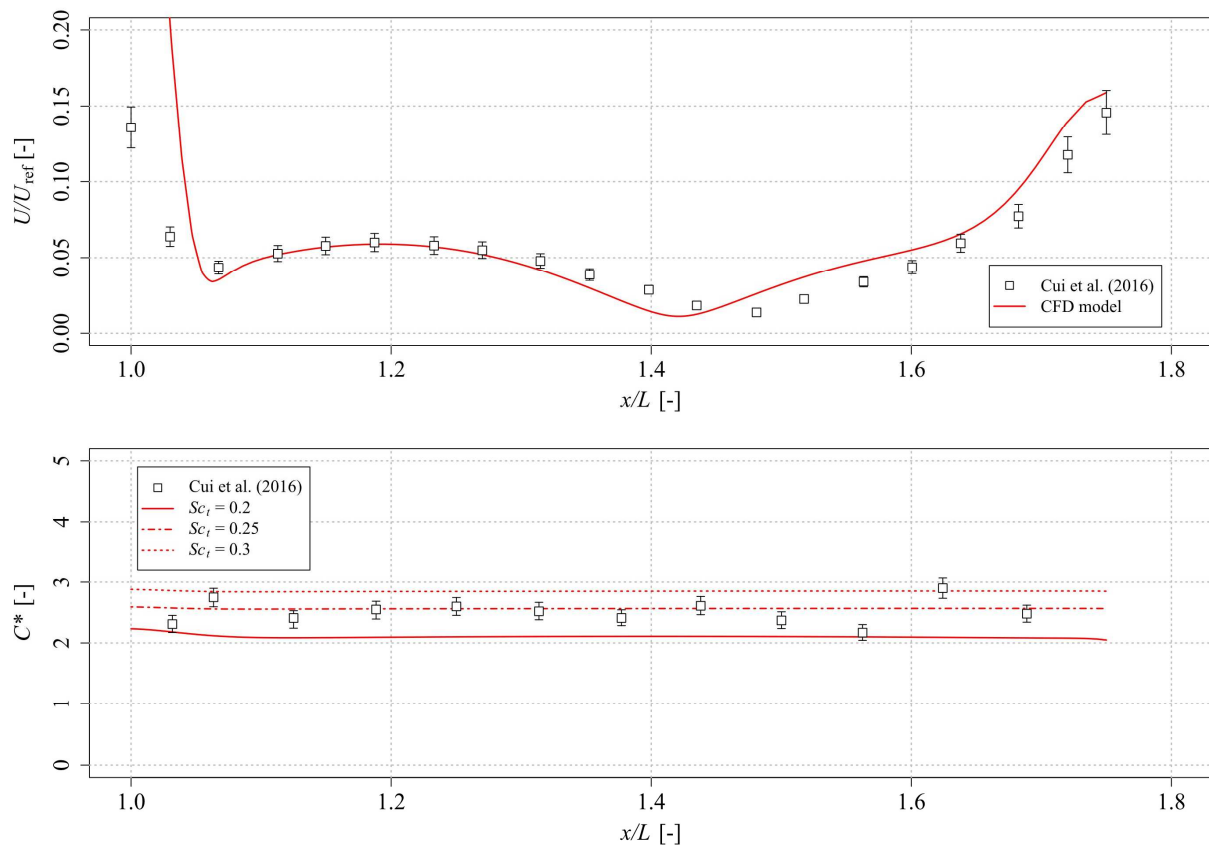

Figure 2.26 – Comparison of the dimensionless streamwise velocity and the dimensionless concentration between the numerical model and the experimental data of Cui et al. (2016) in the outdoor environment.

Finally, the performance criteria have been calculated to compare numerical and experimental concentrations distinguishing indoor and outdoor locations and the results are summarized in Table 2.7. According to these results, the best outdoor results are achieved with $Sc_t = 0.2$ leading to an overall error or 8%. The results using $Sc_t = 0.25$ are also very good with an overall error of 10%. The best indoor results are obtained for $Sc_t = 0.25$ leading to a global error of

6%. The best turbulent Schmidt number considering both indoor and outdoor environments is therefore $Sc_t = 0.25$, leading to an overall error of less than 10%.

According to the previous results, the mixed convection solver is able to very well reproduced wind profiles and concentration profiles in both outdoor and indoor environment for a highly unstable 3D case.

Table 2.7 – Evaluation of the mixed convection solver performances over the data of Cui et al. (2016) in the indoor and the outdoor environment

	FB	MG	VG	NMSE	FAC2	NAE	Target
RNG k-ε, outdoor							
$Sc_t = 0.2$	0.016	1.016	1.014	0.000	1.024	8%	0.27
$Sc_t = 0.25$	-0.070	0.932	1.018	0.005	1.090	10%	0.32
$Sc_t = 0.3$	-0.175	0.839	1.047	0.031	1.210	17%	0.57
RNG k-ε, indoor							
$Sc_t = 0.2$	0.173	1.189	1.036	0.030	0.846	17%	2.27
$Sc_t = 0.25$	-0.023	0.977	1.006	0.001	1.029	6%	1.01
$Sc_t = 0.3$	-0.128	0.879	1.023	0.017	1.143	13%	2.01
Objective							
Target value	0	1	0	0	1	0%	0
Target range	-0.3 < x < 0.3	0.7 < x < 1.3	< 4	< 1.5	0.5 < x < 1.5	-	< 0.5

The previous results have shed light on the following issues:

(?) Is a CFD-RANS model sufficient to good reproduce wind speed in urban areas for computational wind engineering applications?

(?) Is a two-equation k-ε turbulence model sufficient to accurately reproduce velocity and concentration fields for air pollution modelling?

(?) How much can the turbulent Schmidt number Sc_t change the concentrations modelled? Which is the best turbulent Schmidt number to choose?

(?) Is a CFD-RANS model able to accurately reproduce effects of atmospheric stability on wind velocities and pollutant concentrations?

The conclusions are as follows:

- ✔ The mixed convection solver is able to reproduce very well velocity and concentration profiles for a highly unstable 3D case.

- ✔ The CFD solver is also able to model accurately indoor and outdoor exchanges.

- ✔ The best results on concentrations are obtained using a turbulent Schmidt number of 0.25, leading to an overall error of 10%.

- ✔ Isotropic models such as the standard RNG k-ε turbulence model are sufficient to give good results in 3D with thermal effects.

2.4. Effects of vegetation on aerodynamics and pollutants transport

Two distinct CFD solvers have been developed and include (1) the forced convection solver (FCS), an incompressible solver for neutral atmosphere modelling and, (2) the mixed convection solver (MCS), a compressible solver for non-neutral atmosphere modelling.

This section deals with the inclusion of new terms in Navier-Stokes, turbulence, and pollutant transport equations to account for the effects of vegetation.

2.4.1. Impact of vegetation on flow: wind speed and turbulence

A first step to take vegetation into account in the forced and mixed convection solvers is to include its effects on the airflow that will inevitably lead to a modification of the pollutant dispersion. Indeed, it seems obvious that vegetation will have an impact on the airflow, firstly

because of the trunks and branches that will stop the flow, but also because of the leaves that will slow it down with more or less impact depending on leaves density.

The effects of vegetation on airflow and how to include them for CFD RANS modelling were well investigated by several authors including Katul et al. (2004), Dalpé and Masson (2009) and more recently by Santiago et al. (2017b) and Buccolieri et al. (2018). According to these authors, for CFD modelling, three new terms noted S_u [Pa/s], S_k [kg/m/s^3] and S_ε [kg/m/s^4] need to be added in the Navier-Stokes momentum equation, in the turbulent kinetic energy equation and in the turbulence dissipation equation respectively. The corresponding equations are given hereafter:

$$S_u = -\rho C_D \alpha |u| u_i \quad\quad\quad \text{(Eq. 2.20)}$$

$$S_k = \rho C_D \alpha \left[\beta_p |u|^3 - \beta_d k |u| \right] \quad\quad\quad \text{(Eq. 2.21)}$$

$$S_\varepsilon = \rho C_D \alpha \frac{\varepsilon}{k} \left[C_{4\varepsilon} \beta_p |u|^3 - C_{5\varepsilon} \beta_d k |u| \right] \quad\quad\quad \text{(Eq. 2.22)}$$

where ρ is the density, C_D is the drag coefficient, α is the leaf area density (also noted LAD), u is the velocity, k is the turbulent kinetic energy, ε is the turbulence dissipation rate, β_p is the fraction of mean kinetic energy converted into turbulent kinetic energy by means of drag (Buccolieri et al., 2018), β_d is the dimensionless coefficient for the short-circuiting of the turbulence cascade (Buccolieri et al., 2018) and $C_{4\varepsilon}$ and $C_{5\varepsilon}$ are new turbulence model constants.

It should be mentioned that the previous equations are given considering the density ρ. In the forced convection solver, as for any incompressible solver in OpenFOAM, this parameter cannot be found in the source code since the variable p/ρ is considered. The density is nonetheless considered in the mixed convection solver to consider buoyant effects.

One questions arise:

(?) Are the forced convection solver (FCS) and the mixed convection solver (MCS) able to accurately reproduce the flow field for cases with vegetation ?

Precision about C_D and α

When including (Eq. 2.20) in the Navier-Stokes momentum equation, two new parameters appear and need to be specified: the drag coefficient C_D [-] and the leaf area density α [m^2/m^3] (or LAD).

- The drag coefficient is a dimensionless constant related to the aerodynamic features of the vegetation and usually ranges from 0.1 to 0.3. An average value of 0.2 is usually taken for CFD modelling (Buccolieri et al., 2018).
- The leaf area density corresponds to the ratio between the leaves surface and the total volume of the vegetal. This parameter is a function of the altitude (z). A global parameter over the vegetal, called the leaf area index (LAI), can be calculated from it using (Eq. 2.23). The link between LAI and $LAD(z)$ is given in Figure 2.27.

$$LAI = \int_0^h LAD(z).dz \tag{Eq. 2.23}$$

where LAI is the leaf area index, LAD is the leaf area density and h is the vegetation height.
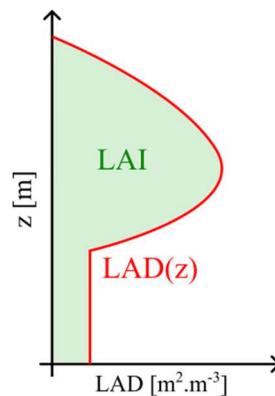
Figure 2.27 – Link between *LAI* and *LAD(z)*.

There is no specific range for the leaf area density, this parameter being different for each vegetal species and also depending on the season. In practice, this parameter can be assessed using light measurements (Stadt and Lieffers, 2000) or photographic methods (Meir et al., 2000). However, in applied context it is not always possible to measure this parameter and some empirical relations has been developed and can be used instead (Lalic and Mihailovic, 2004; Ross et al., 2000). As an example, the relation of Lalic and Mihailovic (2004) is given hereafter in (Eq. 2.24).

$$LAD(z) = L_m \left(\frac{h - z_m}{h - z} \right)^n exp \left[n \left(1 - \frac{h - z_m}{h - z} \right) \right]$$ (Eq. 2.24)

where $LAD(z)$ is the leaf area density, L_m is the maximal leaf area density, z_m the altitude where the maximal leaf area density is reached, h is the vegetal height, z is the altitude and n a parameter equal to 6 for $0 \leq z < z_m$ and to 0.5 for $z_m \leq z \leq h$.

Precision about β_p, β_d, $C_{4\varepsilon}$ and $C_{5\varepsilon}$

When including (Eq. 2.21) and (Eq. 2.22) in the turbulence equations, four additional parameters appear in addition to the drag coefficient and the leaf area density : β_p, β_d, $C_{4\varepsilon}$ and $C_{5\varepsilon}$. These parameters are all dimensionless constants which can be calculated using the following equations (Katul et al., 2004):

$$\beta_d = \sqrt{C_\mu} \left(\frac{2}{a} \right)^{2/3} \beta_p + \frac{3}{\sigma_k}$$ (Eq. 2.25)

$$C_{\varepsilon 4} = C_{\varepsilon 5} = \sigma_k \left(\frac{2}{\sigma_\varepsilon} - \frac{\sqrt{C_\mu}}{6} \left(\frac{2}{a} \right)^{\frac{2}{3}} (C_{\varepsilon 2} - C_{\varepsilon 1}) \right)$$ (Eq. 2.26)

where β_d is taken equal to 1 as in Katul et al. (2004) and Santiago et al. (2017b, 2017a), $a = 0.05$ (Dalpé and Masson, 2009) and C_μ, σ_k, σ_ε, $C_{\varepsilon 1}$ and $C_{\varepsilon 2}$ are turbulence model constants summarized in Table 2.8 for the standard k-ε turbulence model.

Table 2.8 – Values of constants for the k-ε turbulence model in OpenFOAM.

Model	C_μ	σ_k	σ_ε	$C_{\varepsilon 1}$	$C_{\varepsilon 2}$
Standard k-ε	0.09	1.0	1.3	1.44	1.92

☞ The three terms of source and sink to consider the impact of vegetation on the airflow have been added in the FCS and MCS as well as all necessary constants for the numerical calculation.

☞ A python code has been developed to simplify the solver parametrization for simulations with multiple vegetation locations and different vegetation types (i.e., different $LAD(z)$ and C_D).

2.4.2. Pollutant deposition

The vegetation has an impact on the airflow which leads to a modification of the pollutant dispersion and, therefore, of the pollutant concentrations. However, the vegetation also has an impact directly on pollutant concentrations. Indeed, by means of a deposition on leaves, air pollutants can be removed by the presence of vegetation (Buccolieri et al., 2018).

In CFD modelling, deposition can be considered including a sink term of concentration in the advection-diffusion equation (Buccolieri et al., 2018; Santiago et al., 2017b). The deposition sink term, noted S_d [kg/m³/s], is given in (Eq. 2.27).

$$S_d = -\alpha V_d C \qquad \text{(Eq. 2.27)}$$

where α is the leaf area density, V_d is the deposition velocity and C is the pollutant concentration.

Slightly different formulations can also be found, as in Bruse (2007), where S_d is multiplied by another term, f_{cap}, corresponding to a leaf capacity dependent scale factor. This parameter, ranging from 0 for a dirty leaf to 1 for a clean fresh leaf is usually set to a fixed value of 1 due to a lack of information and empirical data to assess it. When taking $f_{cap} = 1$, it is assumed that all the leaves have a full filtering capacity and can therefore lead to an overestimation of the deposition effects.

Precision about V_d

When including (Eq. 2.27) in the advection-diffusion equation, another new term need to be specified: the deposition velocity V_d. The deposition velocity depends on the type of vegetation but also on the pollutant modelled. According to the review of Buccolieri et al. (2018), V_d for vegetated surfaces is usually less than 1 cm/s for gases and more than 1 cm/s for particles with

high variations depending on the authors: for PM_{10}, the deposition velocity ranges from 0.5 to 10 cm/s while for $PM_{2.5}$, the deposition velocity ranges from 0.02 cm/s to 30 cm/s. However, deposition velocities of around 1 cm/s or less are more frequent.

For heavier particles, such as pollen, the deposition velocity becomes the settling velocity which is based on the Stokes' drag law (Salesky et al., 2019). The corresponding equation is given in (Eq. 2.28).

$$v_s = \frac{\rho_p g d_p^2}{18 \mu_{air}}$$
(Eq. 2.28)

where v_s is the settling velocity, ρ_p is the particle density, g is the gravitational acceleration, d_p is the particle diameter and μ_{air} is the air dynamic viscosity.

Finally, it should also be noted that another way, called the resistance model, does exist for computing deposition velocity. The resistance model, as well described by Seinfeld and Pandis (2016), is based on electrical resistance analogy and conduct to two different velocity depositions for gazes and particles.

$$v_{d_{gazes}} = \frac{1}{r_a + r_b + r_c}$$
(Eq. 2.29)

$$v_{d_{particles}} = \frac{1}{r_a + r_b + r_a r_b v_s} + v_s$$
(Eq. 2.30)

where $v_{d_{gazes}}$ is the deposition velocity for gazes, $v_{d_{particles}}$ is the deposition velocity for particles, r_a is the aerodynamic resistance, r_b is the quasilaminar layer resistance, r_c is canopy resistance, and v_s is the settling velocity. The equation of these parameters can be found in Seinfeld and Pandis (2016).

The resistance model has been used for microscale modelling as in the ENVI-met software (Bruse, 2007). However, according to Santiago et al. (2017b), since in urban areas the traffic emissions are located below the urban vegetation canopy, this model cannot give accurate results for microscale modelling as in forest configurations.

Two questions arise:

(?) Are the forced and mixed convection solvers able to accurately reproduce pollutant concentrations with vegetation and deposition effects ? Is the resistance model able to give a correct estimation of the deposition velocity when this velocity is unknown ?

☞ The sink term to consider the pollutant deposition due to vegetation has been added to the advection-diffusion equation in both the FCS and the MCS.

☞ The deposition velocity v_d can be directly specified in both CFD solvers and can also be calculated based on the resistance model added in the solvers.

2.4.3. Pollutant resuspension

Vegetation has an impact on pollutant concentrations due to changes in air flow and pollutant deposition effects. A final phenomenon can also occur and corresponds to the resuspension of pollutants deposited on plant surfaces (L. Chen et al., 2017).

The pollutants resuspension is ranging from 4.5% to 12% for wind velocities ranging from 3 m/s to 9 m/s according to (Nowak et al., 2013). In a recent study, pollutants resuspension has been included in CFD modelling as a volumetric source term (Hong et al., 2018). The resuspension source term, S_r [kg/m³/s], used by these authors is given in (Eq. 2.31).

$$S_r = -\alpha V_r C_{sink} \qquad \text{(Eq. 2.31)}$$

where α is the leaf area density, V_r is the resuspension velocity and C_{sink} is the pollutant concentration deposited on vegetation surfaces

Finally, there is not as much information for resuspension velocity as for deposition velocity and, according to Buccolieri et al. (2018), the pollutant resuspension is usually neglected in CFD simulations.

☞ The pollutant resuspension source term has not been yet included in the forced and mixed convection solvers since there is not much information about resuspension velocities. This term will be added later, in future developments.

2.4.4. Model validation

Two *in* situ experimental test cases were used to assess the performances of the forced and the mixed convection solver in modelling the impact of vegetation on airflow and pollutant concentrations, and to answer some questions raised previously. The experimental and numerical set-ups as well as the results comparison are successively presented hereafter and a summary of the test cases with the associated objectives is given in . Since the results were strictly the same between the forced and the mixed convection solver (no thermal effects modelled in both test cases), only the results obtained with the forced convection solver are presented.

Table 2.9 – Summary of the two test cases used for the mixed convection solver validation.

Authors	2D	3D	W.T.	In-situ	Objective
Irvine et al. (1997)	✔			✔	Comparison between CFD and *in-situ* experimental data on the evolution of the wind profile before, at the beginning and in a forest.
Vermeulen et al. (2009)		✔		✔	Comparison between CFD and *in-situ* experimental data on the evolution of traffic-induced pollutants after a vegetative barrier.

(W.T.: Wind tunnel)

2.4.4.1. Modelling the effects of vegetation on flow

The solver with vegetation was firstly tested against experimental data from Irvine et al. (1997). These experimental data have been chosen mainly because the experimentation was conducted *in situ*, in a real forest. The results were given only for the wind speed but allow a first assessment of the model accuracy with vegetation. For the turbulence modelling, it is the modified k-ε turbulence model (the standard model with source and sink terms due to vegetation) that has been used.

Irvine et al. (1997) studied the evolution of the wind velocity profile when entering a Sitka spruce forest at Hartwood Forest, in Northumberland, England. The forest was characterized by an averaged vegetation height of around 6 m (noted H) and a density of approximately 2,000 stems/ha uniformly planted. To do their measurements, they used four masts where three wind sensors were placed at different altitudes ($z/H = 0.46$, $z/H = 1.00$ and $z/H = 2.00$). One mast was placed before the forest ($x/H = $ -6.1), the second was located at the forest edge ($x/H = 0.0$) and the two other were located inside the forest ($x/H = 3.6$ and $x/H =$14.5). Additional information on the vegetation where available, like the drag coefficient ($C_D = 0.2$), and the leaf area index ($LAI = 2.15$). Since no information about the leaf area density was available, it has been estimated using (Eq. 2.23) considering, as a first approach a uniform distribution and, as a second approach, a non-uniform distribution (noted "chosen LAD") to represent a Sitka spruce shape. The LAD distribution is illustrated in Figure 2.28 and respect the criterion $LAI = 2.15$.
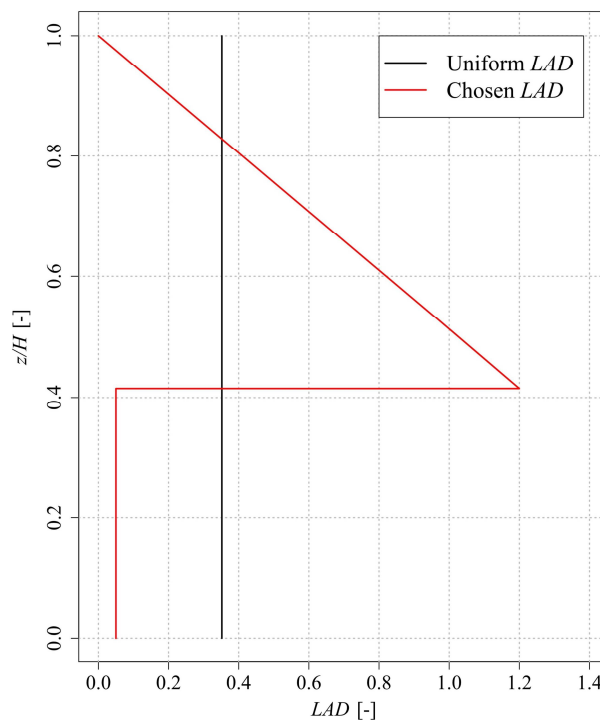
Figure 2.28 – Leaf area density with an uniform density (black line) and a chosen density (red line).

Simulations were performed using the inlet velocity profile measured before the forest at x/H = -6.1. A freestream outlet was used for the outlet boundary and symmetry conditions were applied to the top and the lateral boundaries. The drag coefficient and the leaf area density were set to zero in all the domain except in the forest area where C_D was set to 0.2 and the uniform or the chosen LAD were specified. The recommendations of Franke et al. (2007) concerning the minimal distances in numerical domain are given as a function of a building height. Since in this case there are no buildings, the vegetation height H was used instead with higher distances than recommended. The experimental set-up with distances, boundary conditions and the forest location, is presented in Figure 2.29.
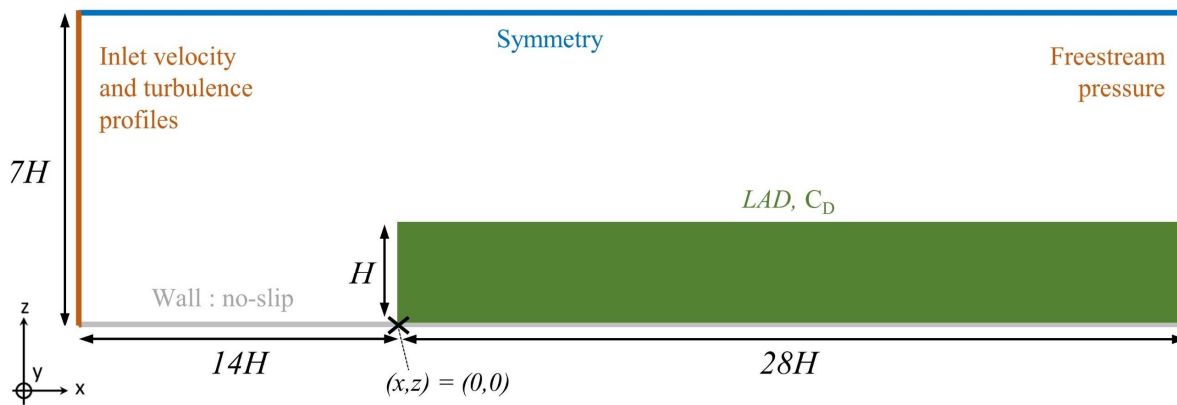
Figure 2.29 – Boundary conditions and domain size.

Mesh sensitivity tests were carried out at the four mast locations on both LAD distributions using the grid convergence index. The mesh insensitivity was difficult to reach in the vegetated area, probably because of the source and sink terms of momentum and turbulence. To reach a *GCI* of less than 5%, a degressive mesh size has been applied in the vertical direction which leads to a minimal mesh height of 0.65 m (at ground level), a maximal mesh height of 3.5 m (at the top boundary) and an intermediate mesh height of 1 m at the forest top. The corresponding y^+ at the ground level is around 9,000. A mesh length of 0.4 m in the streamwise direction was sufficient in both cases and a total number of 43,000 meshes was reached. An illustration of the resulting grid is given in Figure 2.30 with the two LAD conditions illustrated.
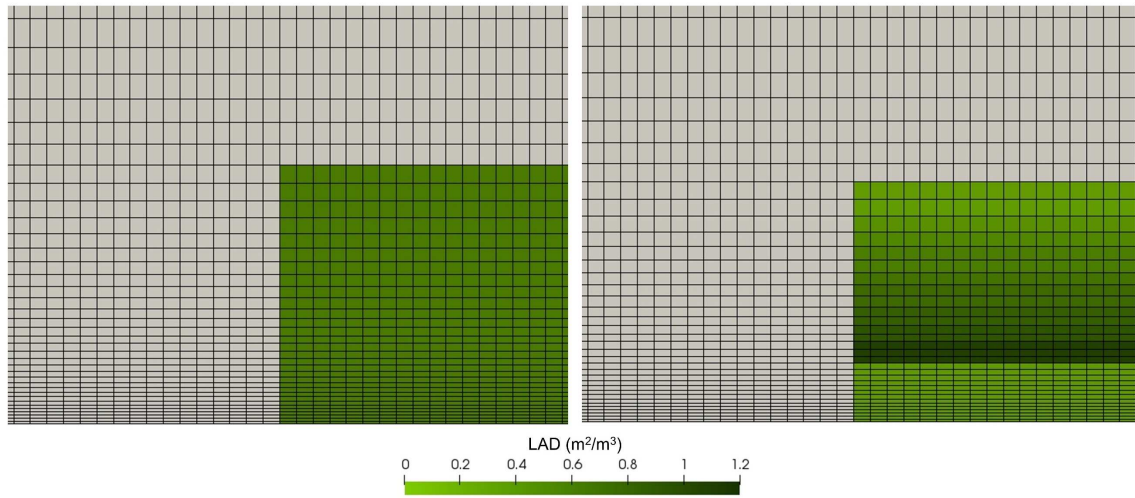
Figure 2.30 – Mesh illustration for the uniform *LAD* (left) and the chosen *LAD* (right).

The experimental and the numerical dimensionless velocity profiles U/u^* as a function of the dimensionless height z/H are presented below in Figure 2.31 ($u^* = 0.5$ m/s).
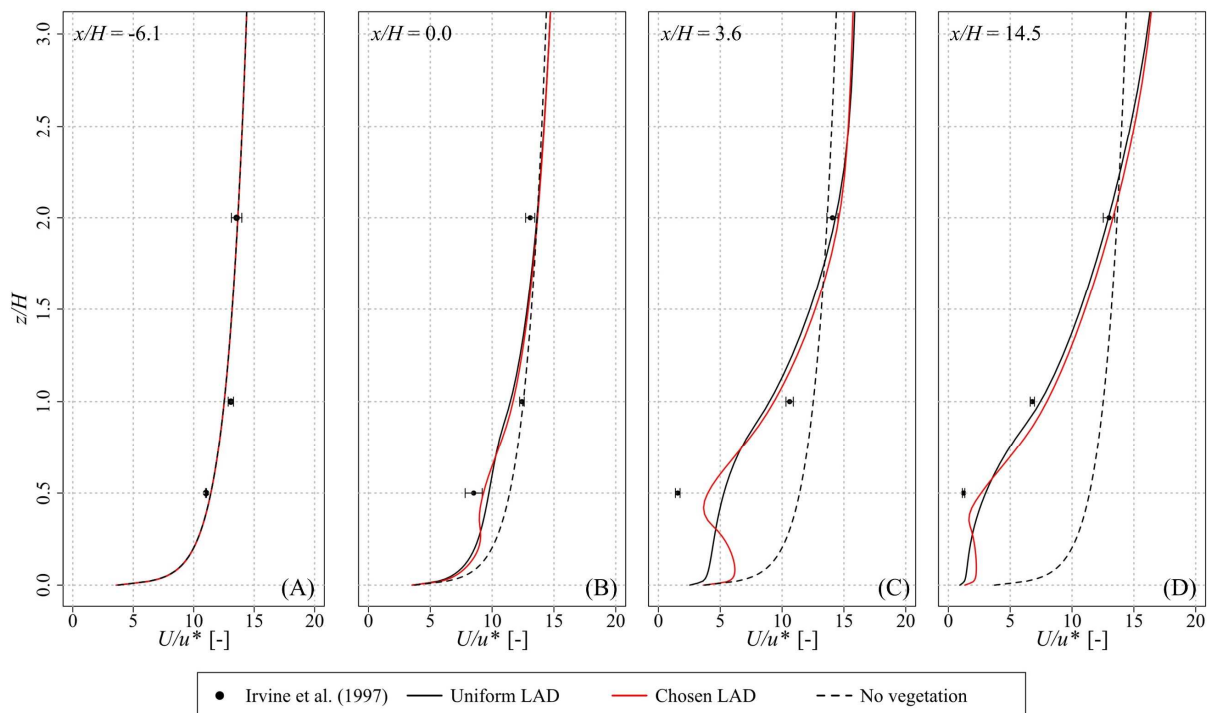
Figure 2.31 – Comparison of the dimensionless streamwise velocity and the dimensionless concentration between the numerical model and the experimental data of Irvine et al. (1997).

According firstly to Figure 2.31 (A), it can be seen that the inlet profile is accurately maintained until the first mast (x/H = -6.1) for the three cases considered (without vegetation, with the uniform LAD and with the chosen LAD). The results are strictly the same at this location understandably because this mast is located outside the forest.

According to Figure 2.31 (B–D), it can be seen that the experimental measurements in the forest deviate from the without-vegetation profile and a maximal deviation is reached at the farthest mast from the forest edge. As a first result, it can be seen that using the uniform LAD distribution gives an overall good prediction of the wind velocity profile modification due to the vegetation, especially at x/H = 0.0 and x/H = 14.5. As a second result, using the chosen LAD distribution gives overall the same results as the uniform distribution for the second and the fourth mast. However, it improves significatively the results at the third mast (x/H = 3.6).

The previous results have shed light on the following issues:

⁇ Are the forced convection solver (FCS) and the mixed convection solver (MCS) able to accurately reproduce the flow field for cases with vegetation ?

⁇ Are these solvers able to reproduce accurately the flow field in real *in-situ* contexts?

The conclusions are as follows:

- ✔ The mixed and forced convection solvers are able to accurately reproduce a real wind velocity profile impacted by a dense vegetation (forest) in neutral conditions.

- ✔ Accurate results were obtained using a uniform leaf area density distribution based on a measured leaf area index and a given drag coefficient.

- ✔ Results were improved using a leaf area density distribution based on the tree theoretical shape.

- ✔ Mesh-size independence is more sensitive with vegetation.

2.4.4.2. Modelling the effects of vegetation on the flow and pollutant deposition

The solver with vegetation was secondly tested against experimental data from Vermeulen et al. (2009). These experimental data have been chosen because it was a true 3D experimentation done *in situ* where results were available on both wind velocity and pollutant concentrations on nitrogen oxides (NO_x) and particulate matters (PM_{10}) emitted from traffic. The modified k-ε turbulence model has been used to model the turbulence and, since no information on the deposition velocity was available, the resistance model has been tested to assess if it is able to give an accurate estimation of deposition velocities for microscale modelling.

Vermeulen et al. (2009) studied the evolution of the wind velocity and the NO_x and PM_{10} dispersion in two areas, the first protected by a vegetative barrier, and the second directly exposed from the A50 highway emissions at Vaassen, Netherland. These areas were located side to side and the only difference was the presence of vegetation in one of them. Different sensors including 3D anemometers, 2D ultrasonic anemometers, NO_x, O_3 and PM_{10} concentration sensors were placed after the vegetative barrier to study the evolution of wind velocity and pollutant concentrations as a function of the distance from the roadside. The same disposition has been used for the area without vegetation. Information on the type of vegetation (blackthorn, oak and ash) and the leaf area density distribution were available, but no information on the drag coefficient was given.

Simulations were performed using an inlet velocity profile based on meteorological data given by Vermeulen et al. (2009) : wind speed of 3.5 m/s and a wind direction of 240° (data from June 26, 2018 between 1 p.m. and 4 p.m.). A freestream outlet has been applied to the outlet boundary and symmetry conditions were applied to the top and the lateral boundaries of the domain. The drag coefficient and the leaf area density were set to zero in the whole domain except in the meshes were vegetation was present. Traffic-related emissions of 365 g/km/h and 5 846 g/km/h for PM_{10} and NO_x respectively were specified at the road location according to the traffic information and emission factors given by Vermeulen et al. (2009). Finally, the resistance model also needs two parameters which was not given in the test case : the air surface temperature (T_s) and the solar radiation (G). The values of $T_s = 20°C$ and $G = 126$ W/m² has been used according to data from SolarGIS in June in Vaassen.

Recommendations of Franke et al. (2007) were followed for the minimal distances in the numerical domain considering H = 14 m, the vegetation height, as the reference height. The experimental setup with distances, boundary conditions, the vegetation and the road locations is given in Figure 2.32. Further details on the geometry can be found in Vermeulen et al. (2009).
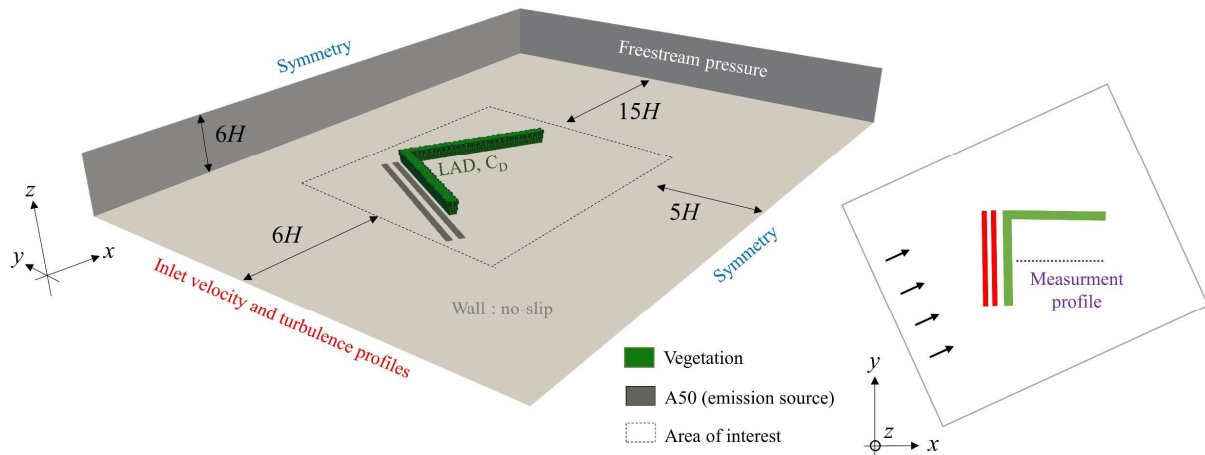
Figure 2.32 – Boundary conditions and domain size.

Mesh sensitivity tests were carried out in the area of interest. To ensure a grid convergence index of less than 5%, meshes of 0.8 m in the x and y directions and 0.2 m in the z direction were used which lead to a total of 12.9 million meshes and y^+ = 1,850. It should be noted that, as for the previous test case, a higher resolution in the vertical direction was needed than for the other directions which was not the case before for the validation steps without vegetation. An illustration of the resulting grid also showing the leaf area density is given in Figure 2.33.
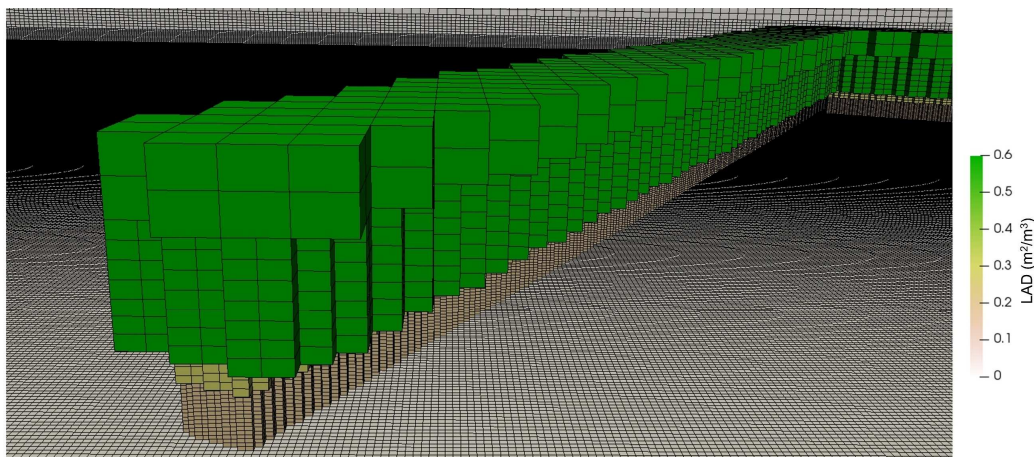
Figure 2.33 – Mesh illustration with the leaf area density used.

A comparison between the experimental and numerical results is given in Figure 2.34. Particularly, this comparison is about (A) wind velocity without vegetation and wind velocity with vegetation for two different drag coefficients and (B) NO_x and (C) PM_{10} concentrations with vegetation as a function of the turbulent Schmidt number. The vegetation is located at a distance ranging from 5 to 8 m from the road.
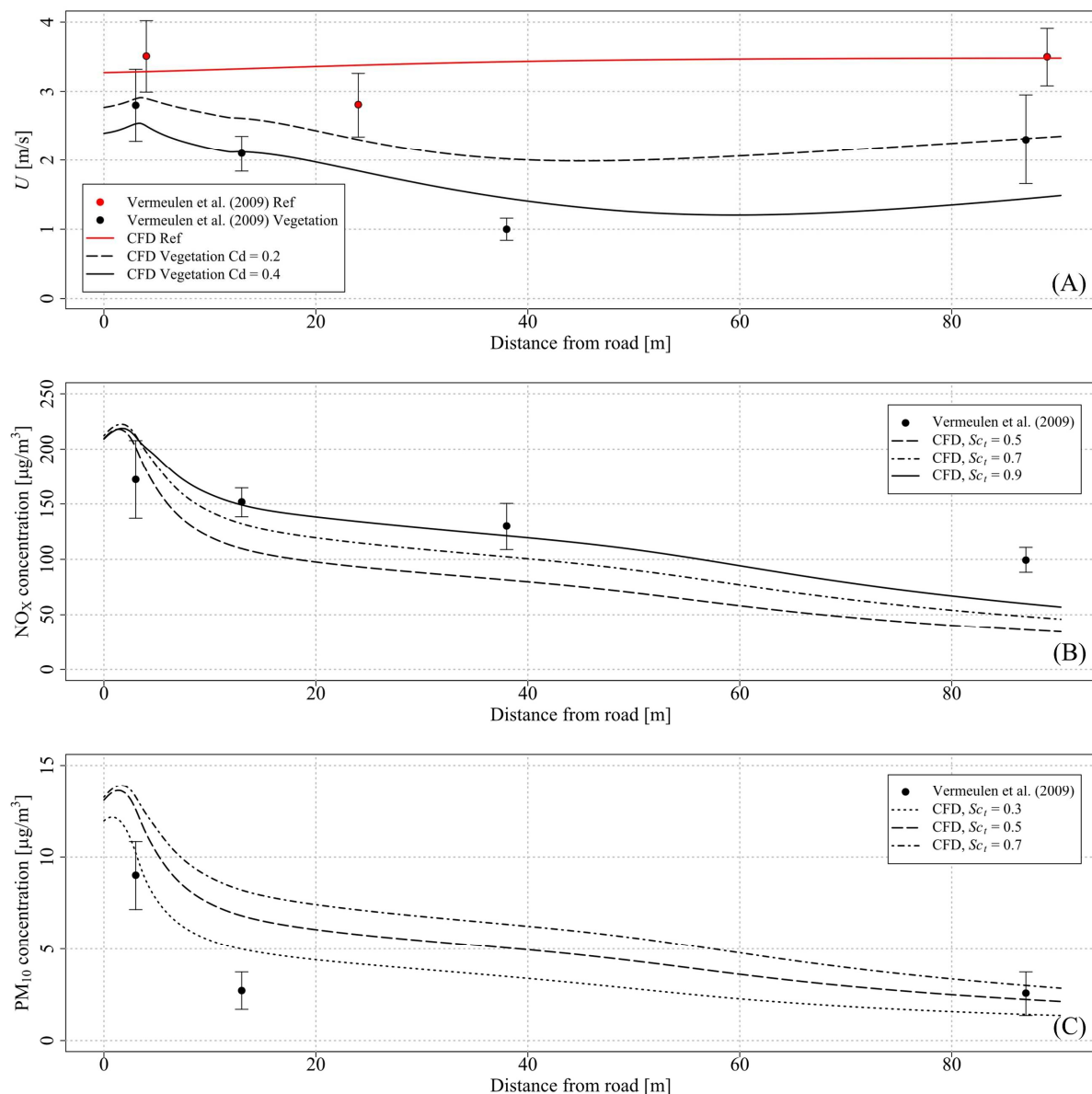
Figure 2.34 – Comparison of the streamwise velocity with and without vegetation and the NO_x and PM_{10} concentrations between the numerical model and the experimental data of Vermeulen et al. (2009).

According to Figure 2.34 (A), it can firstly be seen that the reference velocity (the velocity without vegetation) is globally in the uncertainty ranges of the experimental data. It should, however, be noted that the velocity modelled is almost constant with the distance to the road when for the experimental data the velocity is firstly decreasing and then increasing.

This figure is also showing the evolution of the wind velocity with vegetation for two drag coefficients. Since no drag coefficient where specified in the test case, an average drag coefficient value of 0.2 (Buccolieri et al., 2018) was firstly used. The modelled velocities are in the uncertainty ranges before the vegetation ($x = 3$ m) and far from it ($x = 87$ m). However, just after the vegetation ($x = 13$ m and $x = 38$ m), the velocity is highly overestimated. This result can be explained by the choice of $C_D = 0.2$ which correspond to an average value for multiple vegetation species. However, higher values can be found in the literature such as $C_D = 0.8$ (Cao et al., 2012) or $C_D = 1.2$ (Gromke and Ruck, 2007). The value of $C_D = 0.4$ has then secondly been set. With this value, better results are obtained for $x = 13$ m and $x = 38$ m without changing too much the results for the two other locations. It should finally be noted that the shape of the wind velocity evolution is well reproduced.

The evolution of the NO$_x$ concentration as a function of the distance from the road is illustrated in Figure 2.34 (B). The numerical results are presented for three turbulent Schmidt numbers including $Sc_t = 0.5$, 0.7 and 0.9. According to the comparison with the experimental data, the best overall results are obtained using $Sc_t = 0.9$. With this turbulent Schmidt number, NO$_x$ concentrations are in the uncertainty ranges for the first three measurement locations. The concentration at the fourth location is, however, underestimated as for the two other turbulent Schmidt numbers used. An explanation for this observation can be the use of a constant turbulent Schmidt number in the whole domain. Indeed, $x = 87$ m is far from the vegetation barrier were the turbulent viscosity and, therefore, turbulent dispersion of the nitrogen oxides may be overestimated due to the turbulence model. A higher turbulent Schmidt number may be required at this location to overcome this overestimation of the turbulent viscosity.

Then, the evolution of the PM$_{10}$ concentration is given in Figure 2.34 (C) as a function of the distance from the road. Numerical results are given for three turbulent Schmidt numbers including $Sc_t = 0.3$, 0.5 and 0.7. The best results are obtained with $Sc_t = 0.3$, with a slight overestimation of the concentration at the second location. The best turbulent Schmidt number

assessed for the PM_{10} (0.3) is therefore not the same and is far from the best value for the NO_x (0.9). This difference is difficult to explain since the turbulent diffusion is theoretically depending to the turbulence and not to the transported species. It should, however, be noted that an overestimation of the NO_x emissions or an underestimation of the PM_{10} emissions can also conduct to that kind of difference which is one explanation. Additionally, both NO_x and PM_{10} were modelled as passive scalar without consideration of molecular mass, which can also be an explanation of these differences.

Finally, the previous results cannot give the certitude that the resistance model gave good deposition velocities since the turbulent Schmidt number has also an impact on pollutant dispersion. Nonetheless, the trends of the concentration evolution with the distance from the road were globally accurate whatever the turbulent Schmidt number considered. It can therefore be supposed that, when the deposition velocity is unknown and when this parameter is not assessable, the resistance model can be used instead. The user should nevertheless be aware of the limitations of this model for microscale modelling, as discussed in Santiago et al. (2017b).

The previous results have shed light on the following issues:

   Are the forced convection solver (FCS) and the mixed convection solver (MCS) able to accurately reproduce the flow field for cases with vegetation ?

   Are these solvers able to reproduce accurately flow field and pollutant concentration field in real *in-situ* contexts?

   Are the forced and mixed convection solvers able to accurately reproduce pollutant concentrations with vegetation and deposition effects ? Is the resistance model able to give a correct estimation of the deposition velocity when this velocity is unknown ?

The conclusions are as follows:

- ✔ The mixed and forced convection solvers are able to accurately reproduce a real wind velocity streamwise profile impacted by a vegetative barrier in neutral conditions. The choice of the drag coefficient is nonetheless crucial.

- ✔ Accurate results were obtained on NO_x and PM_{10} dispersion considering the impact of the vegetation on the air flow and on the pollutant dispersion (deposition on the vegetation). The results are, as for the previous test cases, dependent of the turbulent Schmidt number used.

- ✔ The resistance model was used because no specific deposition velocities were specified in the test case. According to the results, when no other options are available, the resistance model can be useful to assess deposition velocity, but it is important to be aware of the model limitations for microscale modelling.

2.5. Nitrogen oxides chemistry

As discussed in the first chapter, nitrogen dioxide (NO_2) has been selected as one of the highest priority air pollutants by the World Health Organization. It is therefore important to monitor it, as well as to model it. Although it is possible to directly measure the nitrogen oxide concentrations, it is more difficult to model it due to several chemical mechanisms in the atmosphere. This section deals with nitrogen oxides chemistry and how to include it for numerical modelling purposes.

2.5.1. Main mechanisms on nitrogen dioxide transformation in the troposphere

Several chemical mechanisms involve nitrogen dioxides in the troposphere and include reactions with ozone, free radicals, volatile organic compounds (VOCs) and formaldehyde (Bliefert and Perraud, 2008). A schematic representation of these mechanisms taken from Aumont (2015) is given in Figure 2.35. According to this figure, it can be seen that only the

ozone acts directly on the nitrogen dioxides. Free radicals, volatile organic compounds and the formaldehyde act indirectly on the nitrogen dioxides through the catalytic cycle.

Figure 2.35 – Schematic representation of the main mechanisms involving nitrogen dioxides in the troposphere (Aumont, 2015).

According to the literature, complex mechanisms such as described in Figure 2.35 can be included in computational fluid dynamics software. Indeed, Kim et al. (2012) incorporated in a CFD solver a full O_3–NO_x–VOC chemical system including 343 reactions and 110 chemical species. Simpler mechanisms were also studied such as the Reduced Chemical Scheme (RCS) with 136 reactions and 51 chemical species (Bright et al., 2013).

According to the previous authors, it is therefore possible to compute nitrogen dioxides concentrations (NO_2) considering other chemical species such as nitrogen oxides ($NO_x = NO + NO_2$) ozone (O_3) or VOCs. However, these complex mechanisms increase significatively the calculation costs which can be twice higher compared to a standard simulation with non-reactive species (Sanchez et al., 2016). For engineering purposes, since it is necessary to minimize calculation costs, it is essential to find other ways to compute accurately NO_2 concentrations. Finally, because emissions are computed for NO_x species rather than NO_2, it is especially important to be able to compute NO_2 concentrations from NO_x concentrations to compare numerical results with regulatory standards (see Section 3.3.3. for further details on emission calculation).

2.5.2. The photostationary steady state equilibrium (PSS)

An alternative of taking into account a full chemical mechanism and a simpler approach is to consider the photostationary steady state equilibrium (PSS). This equilibrium is based on reactions involving NO$_2$, NO and O$_3$ given in (Eq. 2.32) to (Eq. 2.34). According to these equations, the concentrations of the different species are balanced depending on a photolysis rate coefficient J_1 and two chemical rate constants k_2 and k_3 (Bliefert and Perraud, 2008). This series of equations lead to a "null cycle" where there are no changes in the species concentrations and, since the ozone is very reactive and the dioxygen abundant, the ozone can be assumed in steady state leading to the photostationary steady state, and the Leighton relationship can be derived (Leighton, 1961). This equation is given in (Eq. 2.35).

$$NO_2 + h.v \xrightarrow{J_1} NO + O \tag{Eq. 2.32}$$

$$O + O_2 + M \xrightarrow{k_2} O_3 + M \tag{Eq. 2.33}$$

$$NO + O_3 \xrightarrow{k_3} NO_2 + O_2 \tag{Eq. 2.34}$$

where NO_2 is the nitrogen dioxide specie, NO is the nitric oxide specie, O is the oxygen specie, O_2 is the dioxygen specie, O_3 is the ozone specie, M is a given specie acting like a contact partner, $h.v$ are photons, J_1 is the photolysis rate coefficient and k_2 and k_3 are two chemical rate constants.

$$[O_3]_{PSS} = \frac{J_1 \, [NO_2]_{PSS}}{k_3 \, [NO]_{PSS}} \tag{Eq. 2.35}$$

where $[O_3]_{PSS}$, $[NO_2]_{PSS}$ and $[NO]_{PSS}$ are the O$_3$, NO$_2$ and NO concentrations at the photostationary steady state respectively, J_1 is the photolysis rate coefficient and k_3 is the chemical rate constant of the reaction involving NO and O$_3$.

The Leighton relationship basically used to assess tropospheric O$_3$ concentrations on the basis of nitrogen oxides concentrations can be used inversely to assess the proportion of NO and NO$_2$ in the total amount of NO$_x$. In order to use it, it is nonetheless necessary to specify the ozone concentration and to compute J_1 and k_3.

The chemical rate constant

The chemical rate constant k_3 [ppb^{-1}/s] is the rate at which nitric oxide and ozone are transformed into nitrogen dioxide and dioxygen. It is a first-order kinetic constant which can be calculated following (Eq. 2.36) as a function of the temperature T [K] (Hanrahan, 1999).

$$k_3 = \frac{15.33}{T} \cdot e^{\frac{-1450}{T}}$$

(Eq. 2.36)

where k_3 is the chemical rate constant and T the temperature in Kelvin.

The photolysis rate coefficient

The photolysis rate coefficient J_1 [s^{-1}] is the rate at which nitrogen dioxide is photolyzed into nitric oxide and oxygen according to (Eq. 2.32). By definition, the photolysis rate coefficient, also called photolysis frequency, can be calculated by integrating a product involving the solar actinic flux for a given wavelength (Dickerson et al., 1982). However, for engineering purposes, it is difficult to use this definition because it needs numerous parameters usually assessed with measurements. According to Wiegand and Bo (2000), an alternative way based on empirical expressions does exist and the photolysis frequency can be computed as a function of two constants and the zenithal angle following (Eq. 2.37).

$$J_1 = A \cdot e^{(-B.sec\,\theta)}$$

(Eq. 2.37)

where J_1 is the photolysis frequency, θ is the zenithal angle and A and B two constants.

It should be noted that the constants A and B are different depending on the authors, and a summary of the different values found in the literature is proposed in Table 2.10.

Table 2.10 – A and B coefficients for photolysis frequency calculation

Source	A	B
Dickerson et al. (1982)	0.0167	0.575
Parrish et al. (1983)	0.0130	0.360
Lattuati (1997)	0.0155	0.526

Using (Eq. 2.36) and (Eq. 2.37), it is finally possible to use the Leighton relationship to assess the NO_2 concentrations based on NO_x and O_3 concentrations. This methodology, leading to analytical solutions, is about twice less time consuming than considering full chemical mechanisms (Sanchez et al., 2016).

Still according to these authors, in winter and for low ozone concentrations (~5 ppb), the PSS lead to less than 2% of errors compared to full chemical mechanisms for VOC/NO_x ratios of 0.5 and 0.2 and the PSS is therefore more suitable for engineering purposes. However, they also found that in summer, when ozone concentrations are higher than 10 ppb and solar radiation are high, the error increase to reach more than 15% for VOC/NO_x ratios of 0.5, and the PSS is not sufficient anymore. Finally, according to AASQAs data, the mean annual ozone concentrations are higher than 10 ppb over the French country. The PSS is therefore not sufficient to compute NO_2 concentrations from NO_x concentrations in France.

☞   Since a full chemical mechanism greatly increases calculation costs, no such mechanism has been implemented in the forced or the mixed convection solvers.

☞   The photostationary steady state equilibrium equations have been included in the forced and the mixed convection solvers as a first basis of a simple chemical mechanism.

On question arises:

⊘   As the PSS is not sufficient to calculate NO_2 concentrations from NO_x concentrations in France, are there alternatives to avoid increasing calculation costs?

The answer to the question is the topic of Chapter 5.

2.6. Consideration of traffic-induced turbulence

Finally, a last phenomenon which can modify pollutant dispersion and therefore the pollutant concentrations can be described and correspond to the traffic-induced turbulence. This last section of the second chapter introduces this phenomenon and explains how to include it in the numerical models.

2.6.1. The vehicle-induced turbulence (VIT)

When vehicles travel along a road, an overpressure is created at the front of the vehicle and a depression at the rear. These overpressure and depression results in new fluid motions which induced traffic-related turbulence due to vehicle movements. This particular generation of turbulence called VIT (Vehicle-Induced Turbulence) can modify the pollutants dispersion since it modifies the fluid motion and the local turbulence.

The vehicle induced turbulence is depending on multiple parameters such as the number of road lanes, the number of vehicles travelling on each lane, etc. (Kastner-Klein et al., 2001). In addition, the preponderance of its impact depends on the wind velocity (Di Sabatino et al., 2007). Indeed, a measurement campaign done in Nantes, France has shown that for a street canyon and for a wind velocity of 1.1 m/s at the roof level, the vehicle-induced turbulence become preponderant compared to the wind-induced turbulence (Vachon et al., 2002). It is therefore interesting to include the VIT in the CFD solvers to avoid underestimation of turbulence for low wind velocities.

2.6.2. Modelling the phenomenon

Klein et al. (2000) proposed to model the vehicle-induced turbulence as a supplementary source term of turbulent kinetic energy. This source term, noted P_T [kg/m/s^3], can directly be included in the TKE equation as done more recently by Thaker and Gokhale (2016), and it formulation is given in (Eq. 2.38).

$$P_T = \frac{\rho C_d A_T \eta_T v_v^{\,3}}{BH}$$

(Eq. 2.38)

where P_T is the source term of turbulent kinetic energy due to vehicles, ρ is the density, C_d is the drag coefficient of the vehicle, A_T is the frontal vehicle area, η_T is the number of vehicles per unit length of the street, v_v is the vehicle velocity, B is the width of the street and H is a characteristic height.

Some authors have also directly modelled the vehicle motion using mobile mesh in the vehicle direction to quantify the VIT for complex traffic scenarios (Kim et al., 2016). They showed

that the overall VIT of multiple vehicles can be calculated by superimposing the VIT of each vehicle without any consideration of the distances between them. Their results are interesting especially because it gives insight to ease the set of the parameters of the VIT in (Eq. 2.38).

☞ The Vehicles-Induced Turbulence (VIT) has an impact on pollutant dispersion due to modifications of the turbulence and, thus, the airflow. This phenomenon was not yet included in the forced and mixed convection solver. However, it is planned to add it in future developments of the solvers.

2.7. Conclusion of the chapter

One of the main objectives of this thesis work was to develop a CFD-RANS model for the study of the atmospheric pollutants transport in urban environments intended for an operational audience dealing with engineering issues.

The bibliographic analysis and the resulting state of the art presented in this chapter showed that several phenomena can be considered to model pollutant dispersion in urban areas. In particular, the effects of the forced convection, the mixed convection, the vegetation, the nitrogen oxides chemistry and the vehicle-induced turbulence have been discussed. It should be noted that other phenomena can be found in the literature such as wet deposition, heavy particle transportation, etc. but were not addressed in the scope of this thesis.

Based on the state of the art, two OpenFOAM 6.0 CFD-RANS solvers using the PIMPLE algorithm have been developed : (1) an incompressible solver called Forced Convection Solver (FCS) intended for neutral atmosphere modelling (no thermal effects) and (2) a compressible solver called Mixed Convection Solver (MCS) intended for stable or unstable atmosphere modelling (with thermal effects such as buoyancy). The effects of vegetation on the air flow and the pollutant deposition were added to both solvers but the resuspension effects was not yet included. Additionally, a simple chemical mechanism called Photostationary Steady State (PSS) was also included, but alternatives to compute NO_2 concentrations from NO_x concentrations are still required to avoid the uncertainties of the PSS in France (see Chapter 5 for further details). More complex chemical mechanisms were not considered to avoid

increasing calculation costs. Finally, the vehicle-induced turbulence was not yet coded, and it impacts not assess, but is planned for future developments.

A part of the questions raised in Chapter 1 and in the current chapter were also answered. The corresponding questions and their respective answers are the following:

(?) *Is a CFD-RANS model sufficient to good reproduce wind speed in urban areas for computational wind engineering applications?*

A CFD-RANS model can give accurate results on wind speed and pollutant dispersion in urban areas for computational wind engineering applications and pollutant dispersion assessment. According to the results of the solvers presented in this chapter, overall errors ranging from 10 to 25% can be expected.

(?) *What is the best turbulence model for CFD-RANS air pollution modelling? Is a two-equation k-ε turbulence model sufficient to accurately reproduce velocity and concentration fields for air pollution modelling? Is the RNG variant giving more accurate results?*

Anisotropic turbulence models such as the Reynolds Stress Model (RSM) may improve the results on pollutant concentrations. However, isotropic models such as the standard and the RNG k-ε turbulence models are sufficient to reach accurate results for engineering purposes on both flow field and pollutant concentrations.

(?) *How to consider the effects of turbulence on the pollutants transport? How much can the turbulent Schmidt number Sc_t change the concentrations modelled? Which is the best turbulent Schmidt number to choose?*

The effects of turbulence on the pollutant dispersion can be included in CFD-RANS modelling considering a turbulent diffusivity in the advection-diffusion equation. This turbulent diffusivity involves an additional parameter, the turbulent Schmidt number (Sc_t), systematically taken constant in the numerical domain and usually ranging from 0.2 to 1.3. The best turbulent Schmidt number to choose depends on the case considered

but also on the turbulence model used, the standard k-ε turbulence model leading to less sensitive results on concentrations compared to the RNG model. For the cases considered in this chapter, the bests Sc_t ranged from 0.2 to 0.9 with the majority between 0.2 and 0.3.

(?) *How to include thermal effects in the CFD code to model different atmospheric stability? Is a CFD-RANS model able to accurately reproduce effects of atmospheric stability on wind velocities and pollutant dispersion?*

Thermal effects such as buoyancy and, therefore, the atmospheric stability, can be included in CFD-RANS modelling by considering the compressible Navier-Stokes equations with the energy equation. Accurate results can be obtained on flow, temperature and pollutant concentration fields using isotropic turbulence models and mixed convection solvers.

(?) *How to reproduce the effects of vegetation on both flow field and pollutant concentrations in a CFD model? Is such a model able to reproduce accurately flow field and pollutant concentration field in real in-situ contexts? Is the resistance model able to give a correct estimation of the deposition velocity when this velocity is unknown ?*

The effects of vegetation on the wind speed, the turbulence and the pollutant concentration (pollutant deposition and resuspension) can also be included in CFD-RANS modelling. Such model including vegetation phenomena is able to accurately reproduce wind velocities and pollutant concentrations observed in real *in situ* situations. The resistance model for deposition velocity calculation can be used in absence to other ways to assess this parameter, but it is important to keep in mind that this model was not designed for micro-scale modelling.

Regarding other findings: Apart from the initial questioning of this thesis, it has also been shown that CFD-RANS modelling can give accurate results for outdoor/indoor pollutant exchanges modelling in urban areas.

The availability of specific CFD-RANS solvers is the first step to model air pollution dispersion in urban areas. However, a second important step is necessary to use them for engineering purposes and *in situ* applications. Indeed, it is necessary to define, discuss and improve if possible, the computational domain dimensions, the meshing, and the boundary conditions. These points are the subject of the Chapter 3.

Chapter 3:

Modelling air quality in urban areas: computational domain and boundary conditions

---

3.1. Introduction

Air pollution in urban areas can be assessed using computational fluid dynamics (CFD) and various phenomena can be considered and accurately reproduced. CFD solvers are only one part of the issue of modelling air pollution in urban areas. Another part is about the computational domain and the boundary conditions that are necessary for the solver to run and that can significatively change the results. This chapter, dedicated to these two points, gives an overview of the state-of-the-art on the strategies to choose the domain extension, the meshing, but also to provide the boundary conditions in the particular case of full-scale CFD modelling. Development and studies over some of these points are also discussed. In particular, mesh sensitivity tests are carried out at the emission location to ensure grid independence where the pollutant is emitted. The CFD solver is coupled to the 1D Canopy Interface Model (CIM, Mauree 2014) to improve the inlet boundary conditions in urban areas especially in the engineering context. The main points discussed in this chapter are highlighted in Figure 3.1.

Input conditions	Pre-processing	Processing	Post-processing	Output
Numerical modelling — Wind speed, Wind direction, Turbulence, Temperature, Emissions	Meshing, Canopy Interface Model (CIM)	2D / 3D, Turbulence model, Turbulent Schmidt number, Passive transport, Buoyancy effects, Vegetation	Interpolation over one wind direction, Interpolation over the wind rose	Concentrations, Mean annual concentrations
Field measurement — NO_X / NO_2, PM_{10} / $PM_{2.5}$, Monthly campaign			Analysis, Extrapolation	Monthly concentrations, Annual concentrations

Figure 3.1 – Main points covered in Chapter 3.

A question, previously issued in Chapter 1, and for which this chapter provides answers is recalled below. Additional questions will be issued and answered in this chapter.

(?) Are the usual inlet conditions adequate enough for computational wind engineering in complex situations (highly built-up areas) and, if not, is it possible to improve them?

3.2. Computational domain

3.2.1. Domain extension, a compromise between accuracy and calculation costs

3.2.1.1. The COST Action 732 guidelines

For numerical modelling, it is necessary to define a computational domain in which the equations will be solved. Computational fluid dynamics is no exception to the rule, and the domain extension, i.e. the minimum distances in all three dimensions within the computational domain, must be chosen carefully. Indeed, choosing too low distances can conduct to edge effects and, thus, numerical errors while choosing too large distances conduct to higher calculation costs. For engineering applications, there is therefore a need to achieve the best compromise between results accuracy and calculation costs.

According to the literature, it is mainly the recommendations from COST Action 732 guidelines (Franke et al., 2007) that are followed concerning the domain extension. These recommendations are well accepted by the scientific community (Blocken, 2015, 2014) and can be find in numerous papers dealing with air flow and pollutant dispersion modelling in urban areas using CFD (Allegrini et al., 2013; Santiago et al., 2019, 2017b).

The recommendations on the minimal distances to have in the computational domain are based on a characteristic length, H, which is the height of the tallest building in the domain and are summarized in Table 3.1.

Table 3.1 – Summary of the recommendations of Franke et al. (2007)

Minimal distance between the area of interest and the…	Recommendations of Franke et al. (2007)
…inlet boundary	5 to 8 $\times H$
…outlet boundary	15 $\times H$
…lateral boundaries	5 $\times H$
…top boundary	5 $\times H$ (over the highest building)

The recommendations of the COST Action 732 guidelines are a good basis for the minimal distances to apply in the numerical domain. However, it is obvious that in the case of a really high building, the dimensions will highly increase leading to high calculation costs. Some questions can therefore be raised such as should we only consider the height of the highest building? Or should we consider the average height of the buildings? These questions can be a good starting point for further studies to improve applicability of CFD to air pollution in applied contexts. One question has nonetheless been addressed in this thesis and is the following:

(?) Which height should we considered when there is not any building?

3.2.1.2. Assessment of the minimal vertical distance in the domain in absence of buildings

For the purpose of this thesis, a study was conducted to assess the minimal vertical distance that should be applied in the numerical domain in absence of buildings. To this end, an empty numerical domain of 200 m width and 600 m long was built with different domain heights

H_D (16 m, 32 m, 48 m, 80 m, 96 m and 128 m). A surface source of emission was specified 100 m after the inlet boundary to simulate traffic-induced emissions, and the same boundary conditions as used previously in Chapter 2 were used. The inlet velocity and turbulence profiles suggested by Richards and Norris (2011) were specified with a wind speed of 1.5 m/s at 10 m height (see Section 3.3.1. for further details on these profiles). This information is summarized in Figure 3.2.

The grid sensitivity was firstly checked and, according to the results on the grid convergence index, meshes of 0.5 m near the ground and 1 m in the rest of the domain were used. The results on concentrations were secondly compared for four different horizontal profiles at $z = 1$ m, 3 m, 10 m and 20 m starting from the source of emission and finishing 50 m before the outlet boundary, and the relative errors on concentrations compared to the results obtained with a domain height of $H_D = 128$ m are presented in Table 3.2.
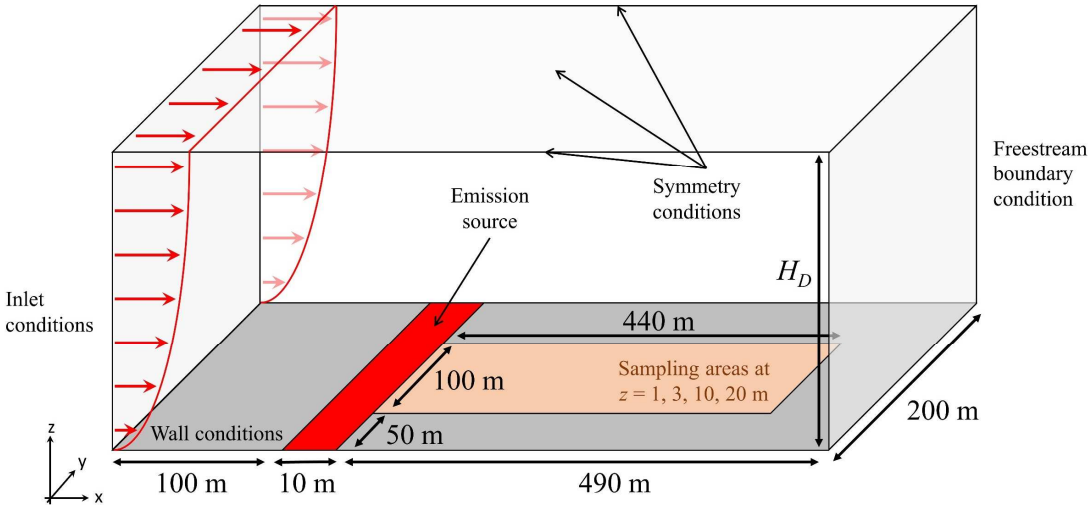
Figure 3.2 – Boundary conditions and domain size.

Table 3.2 – Relative error for the different horizontal profiles as a function of the domain height.

Domain height, H_D [m]	16	32	48	80	96	128
$z = 1$ m	231%	23%	4%	1%	1%	-
$z = 3$ m	243%	26%	6%	1%	1%	-
$z = 10$ m	280%	30%	8%	2%	1%	-
$z = 20$ m	-	41%	10%	2%	1%	-

According to Table 3.2, even without any obstacle, the results are sensitive to the domain height with more than 100% of difference on concentration when comparing the results with $H_D = 16$ m and $H_D = 128$ m. Then, the relative error decrease with the increase of the domain height to reach less than 10% for $H_D = 48$ m and 1% for $H_D = 96$ m.

☞ A minimal domain height of 96 m should be used in absence of obstacles. Thus, for full scale modelling in presence of obstacles, this minimal distance should also be applied and according to these results, it is suggested to use the maximal height between 96 m and $5 \times H$ rather than only $5 \times H$.

3.2.2. Domain meshing

3.2.2.1. Usual meshing and consideration of the turbulent boundary layer

The numerical domain being established, it is then necessary to define the size of the mesh where the different equations will be solved. The question of the mesh is, in a way, similar to the question of the size of the domain. Indeed, the use of small mesh sizes will guarantee a certain quality of the results but will lead to a higher number of meshes and, consequently, to calculation costs, whereas larger meshes will reduce calculation costs but may lead to numerical errors.

The choice of the mesh size is therefore very important and can be done considering the theorical mesh size needed to compute both velocity and turbulent variables in the turbulent boundary layer near the walls, using a dimensionless parameter noted y^+. The definition of this parameter is given in (Eq. 3.1).

$$y^+ = u^* \frac{y}{\nu}$$
(Eq. 3.1)

where y is the distance to the wall, ν is the kinematic viscosity and u^* is the friction velocity.

For RANS simulations, gradients in areas close to the wall are usually modelled using wall functions and the first layer of cells near the wall must include the boundary layer, leading to a y^+ criterion ranging from 30 to 500 (Versteeg and Malalasekera, 2007). Based on these two

extremum, it is possible to compute the theorical wall spacing needed using (Eq. 3.2) (see Appendix G for further details).

$$\Delta s = \frac{\left(\frac{2}{0.026}\right)^{\frac{1}{2}} y^+ \mu^{\frac{13}{14}}}{(\rho U)^{\frac{13}{14}} L^{-\frac{1}{14}}}$$

(Eq. 3.2)

Where Δs is the wall spacing, y^+ the dimensionless criterion, μ the viscosity, ρ the density, U the velocity and L the turbulent reference length.

The theorical wall spacing range based on $y^+ = 30$ and $y^+ = 500$ were calculated for several wind velocities considering $\mu = 18.5 \times 10^{-6}$ kg.m^{-1}.s^{-1}, $\rho = 1.225$ kg.m^{-3} and $L = 10$ m (a given averaged building height). The results are presented in Table 3.3.

Table 3.3 – Theorical wall spacing based on the y^+ criterion

Wind speed [m.s^{-1}]	1	2	3	4	5
Δs for $y^+ = 30$ [m]	0.010	0.006	0.004	0.003	0.002
Δs for $y^+ = 500$ [m]	0.172	0.091	0.062	0.048	0.039

According to the results, a wall spacing of a few millimeters to a few tens of centimeters is needed for wind velocities ranging from 1 m/s to 5 m/s. However, a resolution of few millimeters is never used in practice for full scale modelling since it would lead to very high calculations costs and resolutions leading to $y^+ > 500$ are most likely to be used (Allegrini et al., 2015). The finest grid resolution find in scientific literature is about 0.25 m but is used for specific situations such as consideration of thermal mechanisms (Allegrini et al., 2015) or chemical mechanisms (Kim et al., 2012). Otherwise, a resolution of 0.5 m near the emission sources and 1 m near the walls and buildings is globally used (Di Sabatino et al., 2007; Flores et al., 2013; Sanchez et al., 2017; Vranckx et al., 2015) and sometimes even more (Baik et al., 2003; Kim et al., 2014).

The point of mesh size was also discussed by Franke et al. (2007). They made the recommendation of having (1) at least 10 cells of free space between buildings and (2) at least 10 cells in the three directions defining the volume of the building. These recommendations has been followed by some researchers (Santiago et al., 2017a).

Franke et al. (2007) also specified that the meshes must ideally be equidistant and hexahedral.

Few questions arise from this work:

(?) How to improve calculation efficiency by using small mesh sizes without increasing too much the total number of meshes?

(?) Is 0.5 m a sufficient mesh size at the emission sources, as used by several researchers?

(?) What is the impact of the injection height at the emission sources?

3.2.2.2. Improving calculation efficiency through vertical refinement

The question of the mesh size was very important in the context of this thesis. Indeed, for engineering applications, it is necessary to obtain a good compromise between calculation efficiency and results accuracy.

To reach this compromise we firstly chose to use 1 m meshes and a greater refinement of 0.5 m near the walls and the buildings to better catch strong gradients, this choice being consistent according to the previous section. Secondly, a progressive increase of the mesh size with altitude is used until reaching meshes of 16 m for the highest altitudes. An example of the mesh size evolution with altitude is given in Table 3.4 and an illustration is presented in Figure 3.3.

Table 3.4 – Evolution of the mesh size with altitude

Mesh size [m]	0.5	1	2	4	8	16
Altitude [m]	0 to 2	2 to 14	14 to 24	24 to 40	40 to 64	64 to 96
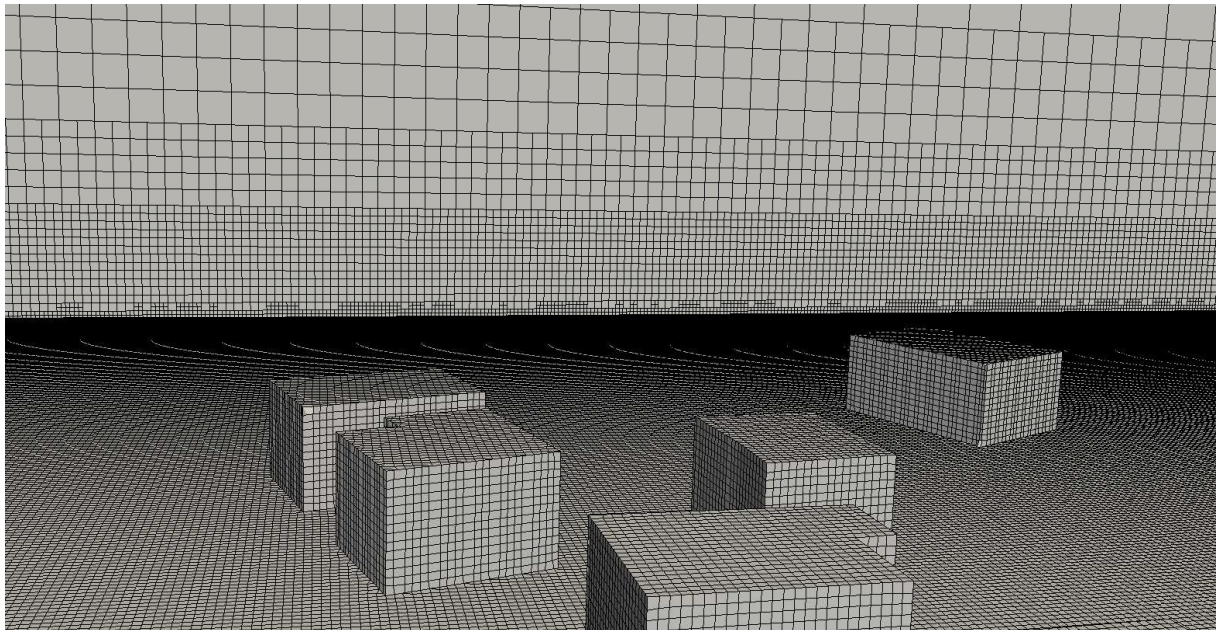
Figure 3.3 – Illustration of the mesh size evolution with altitude.

In this example, a total number of 2.2 million meshes was reached for a numerical domain area of 7.5 ha (300 m × 250 m) and a domain height of 96 m, which needed less than one calculation day to reach convergence with the forced convection solver, confirming its applicability to engineering studies.

It should be highlighted that the example of mesh size evolution given in Table 3.4 is not applicable to every situation. In this example, the maximum height of the buildings was 10 m, which explains why the mesh sizes begin to be greater than 1 m for altitudes greater than 14 m. For higher buildings and more complex situations, the mesh refinement will have to be done at greater heights. Lastly, this choice on the evolution of the mesh size with the altitude does not dispense mesh sensitivity tests which must be routinely carried out.

☞ A way to improve calculation efficiency through vertical mesh refinement has been presented and can be used for future full-scale studies. Mesh sensitivity tests must, however, be systematically conducted to ensure the results reliability.

3.2.2.3. Assessment of the impact of meshing at the emission source

The mesh size at the emission source is often finer than the mesh size in the global domain and is generally taken as 0.5 m for full-scale modelling (see Section 3.2.2.1. for the references). However, there is no explicit justification on why choosing this mesh size and not a finer refinement. Thus, a study has been conducted to ensure that 0.5 m is a sufficient mesh resolution at the emission source.

A fictitious area with three buildings and a "L-shaped" road with a 10 mg/s emission rate was considered. Recommendation of Franke et al. (2007) were followed using a domain height of 96 m and the mesh size evolution presented in Section 3.2.2.2. was applied. Four cases were examined that only differ by the mesh size at the emission source (1 m, 0.5 m, 0.25 m and 0.125 m), the mesh size in the rest of the domain being strictly identical. An illustration of the four cases is given in Figure 3.4. It should be noted that the same injection height was applied in all four cases to avoid multi-parameter comparison explaining why there is one layer of 1 m meshes, two layers of 0.5 m meshes, etc. Finally, a wind profile following a power law was used with $U_{ref} = 6$ m/s and $\alpha = 0.3$ (see Section 3.3.1. for further details on the power law).

The results obtained for the different cases were compared for four given altitudes: 2 m, 4 m, 6 m and 8 m. An illustration of the results obtained at 2 m is given in Figure 3.5. According to these results, a noticeable difference can be seen between the first two cases (1 m and 0.5 m meshes), especially for the highest concentrations which are more present for the case with 1 m meshes. For finer refinements, the differences are less perceptible, and a quantitative comparison is needed. These observations are the same for the three other altitudes considered.
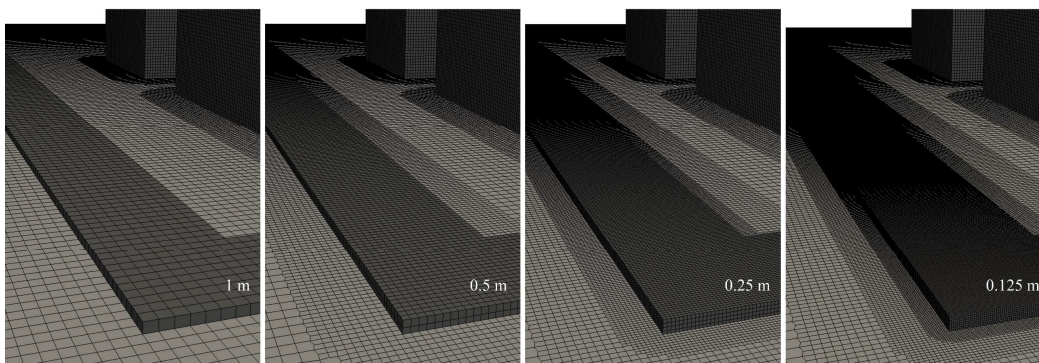
Figure 3.4 – Illustration of the four cases considered with from the left to the right, 1 m, 0.5 m, 0.25 m and 0.125 m meshes at the emission source.
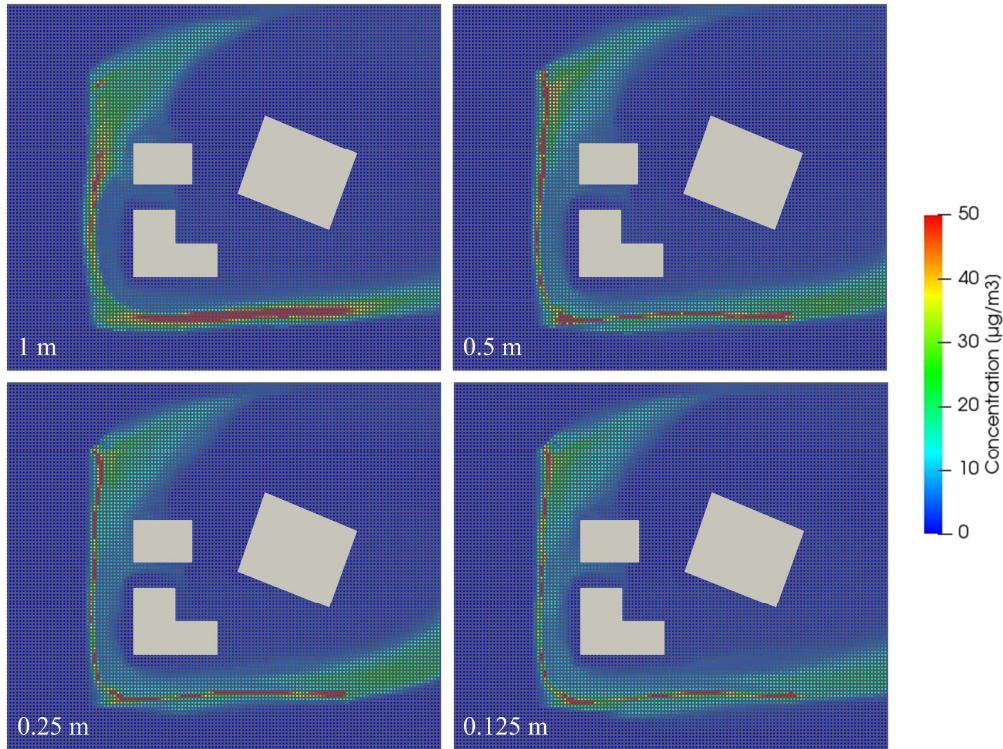
Figure 3.5 – Comparison of the results at z = 2 m for the different mesh size considered at the emission source.

To have a better comparison, the averaged relative difference was calculated using (Eq. 3.3), for the four altitudes (2, 4, 6 and 8 m) and considering the results with 0.125 m meshes as a reference. The resulting averaged relative differences are summarized in Table 3.5.

$$\overline{RD}\ [\%] = \frac{1}{N} \sum_{x,y} \frac{\left|C_{ref}(x,y) - C_{mesh}(x,y)\right|}{C_{ref}(x,y)} \times 100 \qquad \text{(Eq. 3.3)}$$

where $\overline{RD}$ is averaged relative error, N is the number of points considered, $C_{ref}(x,y)$ is the concentration at a the (x,y) location using 0.125 m meshes at the emission source and $C_{mesh}(x,y)$ is the concentration at a the (x,y) location using 1, 0.5 or 0.25 m meshes at the emission source.

Table 3.5 – Averaged relative difference for the 0.25, 0.5 and 1 m grid resolution and different altitudes (reference: 0.125 m grid resolution).

Altitude	Averaged relative difference		
	1 m	0.5 m	0.25 m
2 m	10.1%	1.7%	1.9%
4 m	18.0%	2.1%	2.0%
6 m	12.4%	1.6%	1.8%
8 m	4.9%	1.3%	1.9%
Average	11.3%	1.7%	1.9%

The results presented in Table 3.5 show as previously supposed that 1 m is not a sufficient grid resolution at the emission source leading to averaged relative differences ranging from 5% to 18% depending on the altitude considered. Comparable differences are, however, obtained for the 0.5 m and 0.25 m meshes with averaged differences ranging from 1% to 2%. According to these results, meshes of 0.5 m at the emission source is a sufficient resolution.

☞ A mesh sensitivity study has been done on the mesh size at the emission source. The results show that 0.5 m meshes which are usually used is a sufficient resolution and 1 m meshes must be avoided at the emission sources.

3.2.2.4. Assessment of the impact of injection height at the emission source

Finally, the injection height is also an important point. The traffic-related pollutants are emitted from tailpipes usually close to the ground. However, in CFD models, emissions are usually specified as source terms in meshes specified by the operator. Thus, for a given mass of pollutants, increasing the injection height will increase the total volume were pollutants are emitted and, therefore, decrease the pollutant concentrations.

A study on the injection height sensitivity has been performed. The numerical domain and the boundary conditions were the same as in Section 3.2.2.3. with 0.5 m meshes at the emission source. Three injection heights were considered including 0.5 m, 1 m and 2 m, and are illustrated in Figure 3.6.
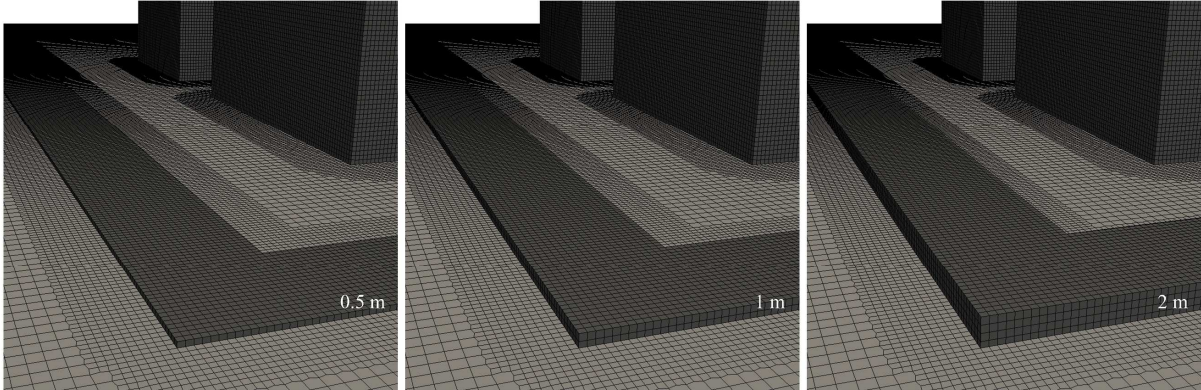
Figure 3.6 – Illustration of the three cases considered with a respective injection height of 0.5 m, 1 m and 2 m.

As done in the previous section, the results obtained for the different cases were compared for four given altitudes including 2, 4, 6 and 8 m and an illustration of the results obtained at 2 m is given in Figure 3.7. According to these results, slight differences can be observed between the cases with an injection height of 1 m and 2 m, but no real differences can be observed for the cases with 0.5 m and 1 m.

The averaged relative difference was calculated using (Eq. 3.3), for the four altitudes and considering the results with an injection height of 0.5 m as a reference. The results are summarized in Table 3.6.
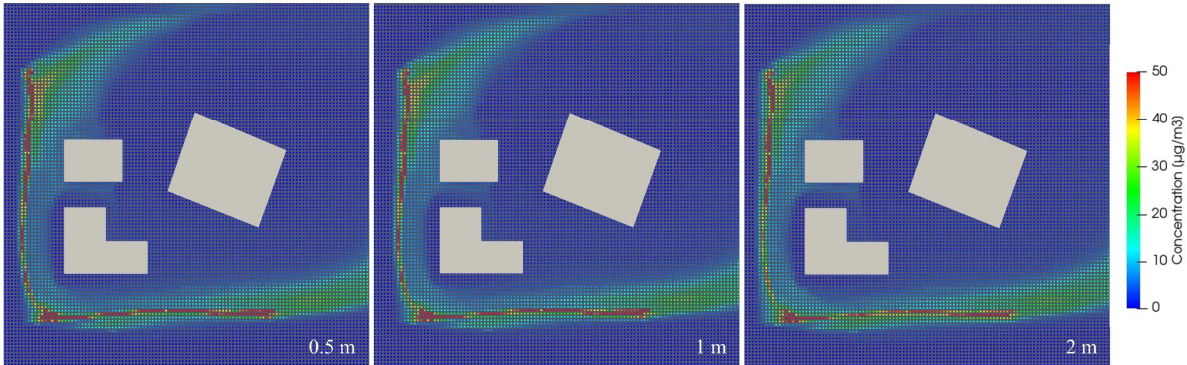
Figure 3.7 – Comparison of the results at z = 2 m for the different injection heights considered.

Table 3.6 – Averaged relative difference at different altitudes for the 1 m and 2 m injection heights (reference: 0.5 m injection height.

Altitude	Averaged relative difference	
	1 m	2 m
2 m	1.6%	39.0%
4 m	1.4%	25.3%
6 m	1.3%	23.8%
8 m	1.1%	21.8%
Average	1.3%	27.5%

The results presented in Table 3.6 show that there are no significative differences between the results obtained with an injection height of 0.5 m and 1 m. However, the differences between the results obtained with an injection height of 0.5 m and 2 m are high, ranging between 20% and 40% depending on the altitude considered. These differences were not observed in the results presented in Figure 3.7 and are mainly obtained for low concentrations. According to these results, injection heights of 0.5 m or 1 m can be used without particular distinction. For future studies, injection heights of 0.5 m will be used.

☞ A sensitivity study over the injection height has been done. The results show that there are no significative differences between choosing 0.5 m or 1 m for the injection height. Higher injection heights lead nonetheless to significative differences. For the purpose of this thesis, injections heights of 0.5 m are used considering that traffic exhausts emissions are emitted at less than 50 cm from the ground, where vehicle's tailpipe are located.

3.3. Boundary conditions

3.3.1. Usual boundary conditions

The question of the boundary conditions is an important point and is closely linked to the numerical domain definition. Indeed, boundary conditions are values or functions that are specified at the boundaries of numerical models to consider the effects of phenomenon occuring outside the domain but having an impact inside it. The boundary conditions must therefore be carefully chosen to avoid altering the model results.

For computational wind engineering, five specific boundaries are usually considered : the inlet boundary, the outlet boundary, the lateral boundaries, the top boundary and the walls boundaries. The usual conditions used for each of these boundaries are described hereafter.

Inlet boundary conditions

The conditions at the inlet boundary are chosen to describe the inflow and, more precisely, the wind and turbulence profiles entering in the numerical domain. To describe these profiles, two sets of equations are available in the literature.

The first set of equations is described by Tominaga et al. (2008). The equations for the wind velocity, the turbulent kinetic energy and the turbulence dissipation rate are respectively given in (Eq. 3.4), (Eq. 3.5) and (Eq. 3.6). The wind velocity equation given in (Eq. 3.4), is better known as the power law profile.

$$U(z) = U_{ref} \left(\frac{z}{z_{ref}} \right)^{\alpha}$$ (Eq. 3.4)

$$k(z) = [U(z)I(z)]^2$$ (Eq. 3.5)

$$\varepsilon(z) = \alpha k(z) C_\mu^{\frac{1}{2}} \frac{U_{ref}}{z_{ref}} \left(\frac{z}{z_{ref}} \right)^{\alpha-1}$$ (Eq. 3.6)

where $U(z)$ is the velocity, z is the altitude, U_{ref} is the reference velocity at the reference altitude z_{ref}, α is the power law exponent, $k(z)$ is the turbulent kinetic energy, $I(z)$ the turbulent intensity, $\varepsilon(z)$ the turbulence dissipation rate and C_μ a model constant (usually 0.09).

The turbulent intensity $I(z)$ is needed to calculate the turbulent kinetic energy, this parameter can be calculated using (Eq. 3.7).

$$I(z) = 0.1 \left(\frac{z}{z_G} \right)^{(-\alpha-0.05)}$$ (Eq. 3.7)

where z_G is the boundary layer height which can be determined by the terrain category according to Tominaga et al. (2008).

The second set of equations is described by Richards and Norris (2011). The equations for the wind velocity, the turbulent kinetic energy and the turbulence dissipation rate are respectively

given in (Eq. 3.8), (Eq. 3.9) and (Eq. 3.10). The wind velocity equation given in (Eq. 3.8), is better known as the log law profile.

$$U(z) = \frac{u_*}{\kappa_{k-\varepsilon}} ln \left(\frac{z}{z_0} \right) \qquad \text{(Eq. 3.8)}$$

$$k(z) = \frac{u_*^2}{\sqrt{C_\mu}} \qquad \text{(Eq. 3.9)}$$

$$\varepsilon(z) = \frac{u_*^3}{\kappa_{k-\varepsilon}z} \qquad \text{(Eq. 3.10)}$$

where $U(z)$ is the velocity, u_* is the friction velocity, $\kappa_{k-\varepsilon}$ is the von Kármán constant implied by the k-ε model, z is the altitude, z_0 the roughness length, $k(z)$ the turbulent kinetic energy, $\varepsilon(z)$ the turbulence dissipation rate and C_μ a model constant (usually 0.09).

The friction velocity can be calculated from a specific velocity U_h at a reference height h using (Eq. 3.11) derived from (Eq. 3.8), and $\kappa_{k-\varepsilon}$ can be calculated using (Eq. 3.12).

$$u_* = \frac{\kappa_{k-\varepsilon}U_h}{\ln\left(h/z_0\right)} \qquad \text{(Eq. 3.11)}$$

$$\kappa_{k-\varepsilon} = \sqrt{(C_{\varepsilon 2} - C_{\varepsilon 1})\sigma_\varepsilon\sqrt{C_\mu}} \qquad \text{(Eq. 3.12)}$$

where $C_{\varepsilon 1}$, $C_{\varepsilon 2}$ and σ_ε are turbulence model constants.

Using the standard k-ε turbulence model ($C_{\varepsilon 1} = 1.44$, $C_{\varepsilon 2} = 1.92$, $\sigma_\varepsilon = 1.3$ and $C_\mu = 0.09$) leads to $\kappa_{k-\varepsilon} = 0.433$ which is slightly higher than the usual von Kármán constant ($\kappa = 0.41$). According to Richards and Norris (2011), $\kappa_{k-\varepsilon}$ should be preferred than κ but using the usual constant will not lead to significant differences despite adjustments will occur on the flow development. Finally, it should be noted that some variations of (Eq. 3.8) and (Eq. 3.10) can be found in the literature, for example in Richards and Hoxey (1993) where $z = z' + z_0$.

☞ Both of these sets of equations are used according to the literature and are available in OpenFOAM. Unless otherwise stated, the set of equations given by Richards and Norris (2011) is used for the purpose of this thesis.

117

Outlet boundary condition

At the outlet boundary, open boundary conditions are usually applied such as constant static pressure or any velocity which has to satisfy a null gradient (Franke et al., 2007). In OpenFOAM, the corresponding outlet boundary condition for external flow is the free stream condition.

Lateral boundary condition

The lateral boundaries are usually set to symmetry conditions which enforce a parallel flow. Using these conditions assumed nonetheless that the flow is parallel to the lateral boundaries and that a sufficient distance is taken between them and the buildings (Franke et al., 2007). The symmetry condition is also already available in OpenFOAM libraries.

Top boundary condition

According to Richards and Hoxey (1993), a constant shear stress following (Eq. 3.13) must be applied over the top boundary layer to maintain the boundary layer profiles in the numerical domain.

$$\frac{\mu_t}{\sigma_\varepsilon}\frac{d\varepsilon}{dz} = -\frac{\rho u_*^4}{\sigma_\varepsilon z} \qquad\qquad \text{(Eq. 3.13)}$$

where μ_t is the turbulent dynamic viscosity, ε is the turbulence dissipation rate, ρ is the density, u_* is the friction velocity, z is the altitude and σ_ε a constant related to the turbulence model.

This recommendation has been discussed by Franke et al. (2007) and later enhanced by Richards and Norris (2011). However, since this condition is not usually available in CFD software, a symmetry condition is generally used instead (Hargreaves and Wright, 2007).

☞ This condition is not yet available in OpenFOAM and further work is necessary to include this specific condition and is planned for future developments. A symmetry condition is used instead as a top boundary condition since this condition is frequently used in the literature, lead to accurate results.

Wall boundary condition

At the wall boundaries (the ground and the building walls), no slip conditions ($U = 0$ m.s^{-1}) are usually applied for the velocity. In addition, wall functions are needed to consider smooth and rough walls that are usually implemented in CFD software for sand-roughened surfaces using a roughness height k_s. The issue of using sand-grain roughness wall functions instead of functions using the roughness height z_0 (also noted y_0) has been well discussed by Blocken et al. (2007). In OpenFOAM, a specific library built for atmospheric flows modelling is available and include roughness height wall functions. For the purpose of this thesis, this type of wall function is used rather than sand-grain roughness wall functions.

3.3.2. Improving inlet boundary conditions with 1D/3D models coupling

3.3.2.1. The issue of modelling continuous urban areas with finite size numerical domains

The usual inlet velocity and turbulence boundary conditions for CWE have been previously introduced with the power law and the log-law profiles. These boundary conditions, although adequate for flat terrains, are nevertheless not suitable in the urban canopy. Indeed, according to the results of Coceal et al. (2007), the streamwise velocity is highly impacted by the presence of multiple obstacles and the log or power-law profiles are only reached for higher altitudes than the obstacles heights. More recently, the same observations were noted by Mauree et al. (2017b) as a result of vertical meteorological measurements performed in a university campus in Switzerland. Thus, one important question arises when modelling airflow and pollutant dispersion in urban areas: how many buildings must be considered in the numerical domain to reach consistent velocity and turbulence profiles from the usual inlet boundary conditions? Unfortunately, the answer is not available in the literature and some studies need therefore to be done in this sense.

This point was not studied for the purpose of this thesis. However, some investigations were conducted to improve the inlet boundary conditions (velocity and turbulence profiles) for engineering purposes, i.e., improving the inlet profiles directly at the boundary rather than finding the minimal number of buildings needed to reach consistent profiles in the numerical domain. To this end, a coupling has been considered and the 1D Canopy Interface Model (CIM) has been retained for this purpose.

3.3.2.2. Assessing CFD inlet conditions with the Canopy Interface Model

The Canopy Interface Model (CIM) is a Fortran coded software developed during the Ph.D. thesis of Mauree (2014). The idea behind this model was to build an interface between urban climate mesoscale models and building energy microscale models. For this purpose, and as an example, CIM has been coupled with the meteorological mesoscale model WRF (Weather Research and Forecasting). The software has, however, not yet been coupled with microscale models such as CFD models which is the issue addressed here.

Briefly, CIM is able to reproduce spatially averaged wind velocity profiles but also turbulent kinetic energy (TKE) and temperature profiles from given inlet conditions (wind velocity/direction and air temperature) which are modified by the presence of buildings (with their given dimensions and surface temperatures) located in a given urban area. By considering both air and surface temperatures, the model is therefore able to reproduce these profiles under different atmospheric stability: stable, neutral and unstable atmospheres. Further details on the model, the hypothesis and the governing equations can be found in Mauree (2014) and Mauree et al. (2017a).

The interest behind a CIM/CFD coupling is illustrated hereafter. Figure 3.8 (A) shows that, when modelling a given area of interest in an urban environment using CFD, several buildings can be located outside of the numerical domain. In this case, using a power or a log-law wind profile at the inlet boundary can lead to false results. To avoid this issue, two possibilities are available:

- The first possibility, illustrated in Figure 3.8 (B), is to increase the numerical domain size to include several buildings upwind of the area of interest. These buildings will impact the power or log-law profile and will therefore lead to better results in the area of interest. This possibility has nonetheless two major problems, it is firstly not currently possible to know how many buildings are needed upwind and, secondly, it will inevitably lead to bigger numerical domains and, thus, higher calculation costs.

- The second possibility, illustrated in Figure 3.8 (C), is to keep the numerical domain used in Figure 3.8 (A) but changing the inlet conditions for CIM's outputs, these

outputs being obtained considering the upwind buildings in the Canopy Interface Model. This second option is better for engineering purposes since it will lead to more accurate results without increasing the calculation costs and could even decrease them.

It should be noted that an intermediary possibility also exists considering both few buildings upwind and the changing the inlet conditions for CIM's outputs but was not considered in this work.
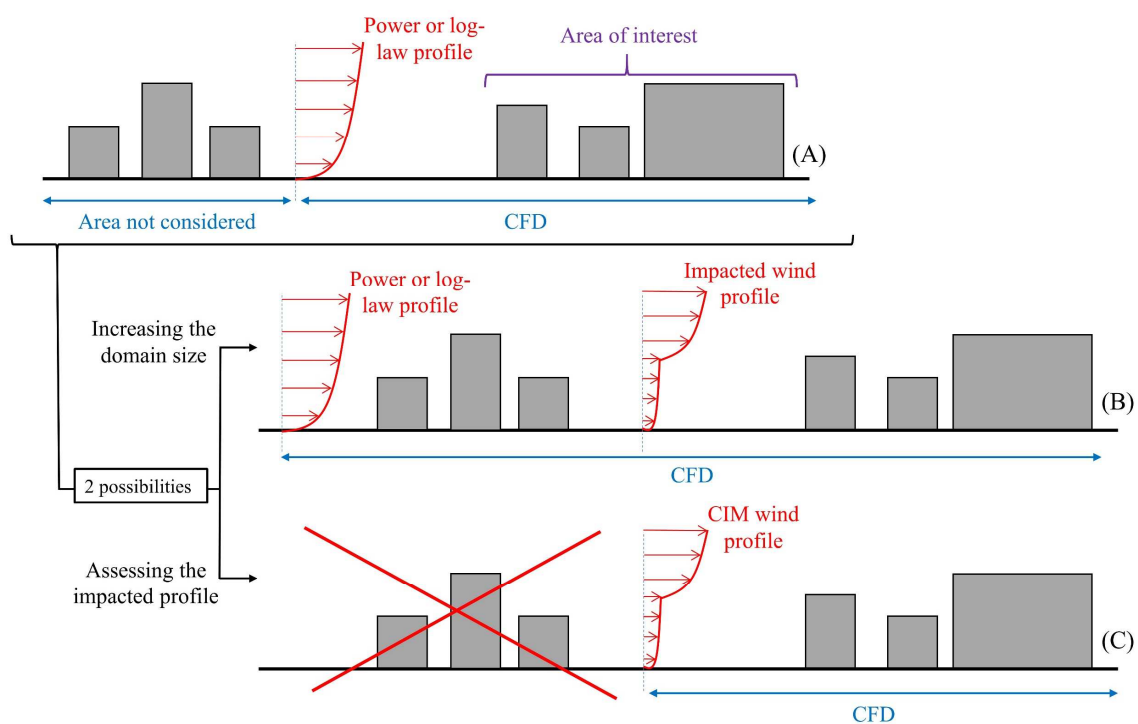
Figure 3.8 – Illustration of the CIM/CFD coupling interest with (A) the issue of not modelling upwind buildings, (B) a solution involving an increase in the domain size and (C) a solution involving the use of CIM.

3.3.2.3. Comparison of a velocity profiles computed with CIM and RANS CFD.

The Canopy Interface Model was validated against CFD results (Mauree et al., 2017a). Indeed, these authors showed good agreements between the model and Large Eddy Simulations (LES) results. They also showed that accurate results can be obtained using CIM compared to *in situ* measurements (Mauree et al., 2017b). However, since the aim of a CIM/CFD coupling here is to reproduce averaged CFD results using CIM, it is necessary to check beforehand whether the results of the CFD software currently in use can be obtained and for which accuracy. A comparison between CIM and CFD results has therefore been firstly done.

To do this comparison, an area located in Schiltigheim, France has been considered. The buildings in this area were numerically reproduced and an illustration is given in Figure 3.9.
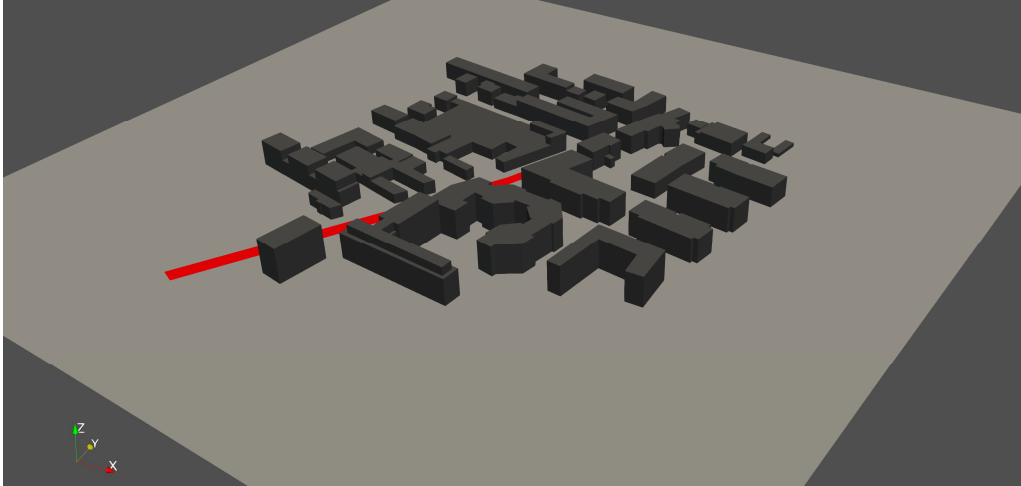
Figure 3.9 – Illustration of the numerical domain used to compare CIM and CFD results.

The simulation has been performed using the forced convection solver without any pollutant source and considering the log-law profile with $U(z) = 3$ m/s for $z = 10$ m. The initial conditions in CIM were chosen to obtain, without any building, the same log-law profile than used as the inlet boundary condition in the CFD model. Then, the buildings characteristics were set in CIM.

The Canopy Interface Model is a 1D model giving results as a function of the altitude z. Thus, there is no discretization according to the other Cartesian coordinates x and y. In a given urban area, it is therefore not possible to specify each building individually, and a "representative" building must be specified instead as illustrated in Figure 3.10. This illustration shows that for a given urban environment, with numerous building dimensions (B_x and B_y) and street dimensions (W_x and W_y) shown in (A), a representative building with its own dimensions as well as a representative street must be defined (B). These representative building and street dimensions can then be set in CIM for several altitudes chosen by the operator.

Figure 3.10 – Illustration on how to set up buildings characteristics in CIM with (A) the actual building configuration and (B) the representative building defined in CIM.

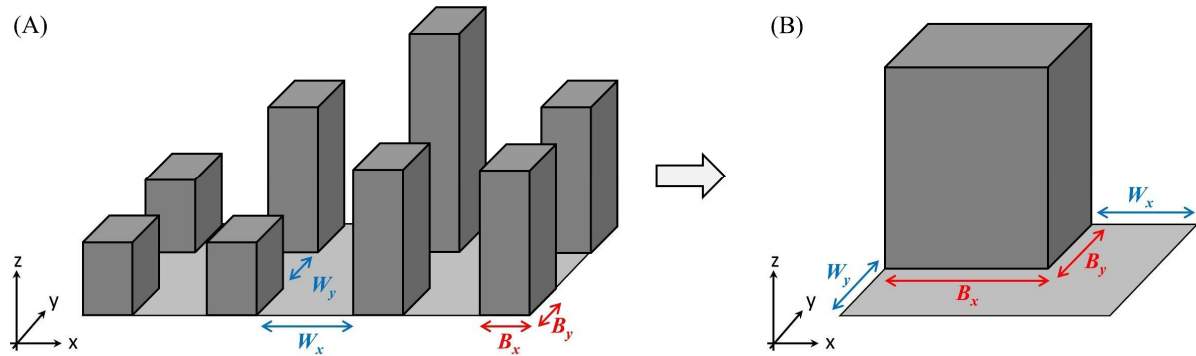For this comparison, two CIM setup cases were compared : a first case with constant building and street dimensions with the altitude and a second case with a variable evolution of these dimensions. The representative building and street dimensions as a function of the altitude are summarized in Table 3.7.

Table 3.7 – Building and street dimensions set in CIM for the two cases considered (left: case 1 / right: case 2).

Height [m]	B_x [%]	B_y [%]	W_x [%]	W_y [%]	Height [m]	B_x [%]	B_y [%]	W_x [%]	W_y [%]
1					1	11	11	89	89
3					3	11	11	89	89
5					5	11	11	89	89
7	11	11	89	89	7	11	11	89	89
9					9	8	8	92	92
11					11	6	6	94	94
13					13	4	4	96	96
15					15	4	4	96	96
17					17	2	2	98	98
19	0	0	100	100	19	1	1	99	99
21					21	0	0	100	100

The wind velocities obtained with the CFD solver were spatially averaged in the x and y directions to allow a comparison with the CIM wind profiles computed. The results are presented in Figure 3.11 (A). The results obtained with both CIM and the CFD solver show the same trends, especially for the first case with constant building and street dimensions as a function of the altitude. However, the velocities computed with CIM are lower than the velocities obtained with the CFD solver. CIM is actually not conservative on the flow rate and

allow loss of movement quantities on a domain at the top of grid domain. Thus, for a given velocity condition set in CIM, two given couples of building and street dimensions lead logically to two different velocity profiles but also to two distinct flow rates. CFD is by nature conservative. The non-conservation of the flow rate by CIM is the origin of the differences observed between the two models.
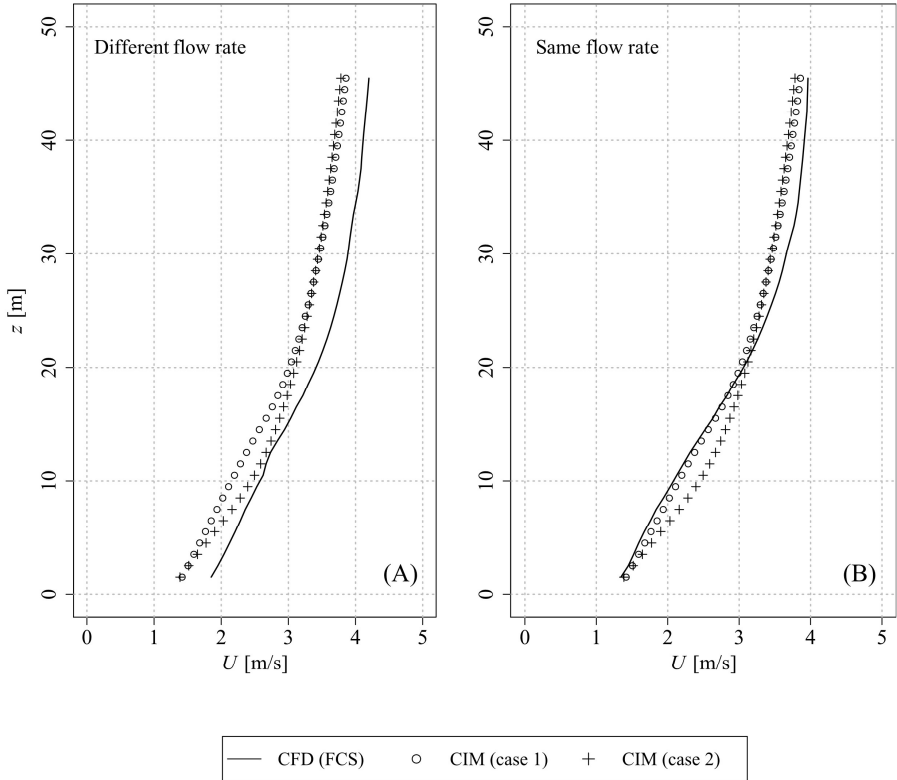
Figure 3.11 – Comparison of the velocity profiles obtained with both CIM and the CFD solver with (right) and without (left) the same flow rate.

In order to illustrate the effect of the flow rate, the CFD model was also run with a lower wind velocity ($U_{z=10\,m}$ = 2.3 m/s), but the same flow rate. The results are presented in Figure 3.11 (B). The results obtained with CIM for the first case are almost equal to the results obtained with the CFD solver, especially for the lower altitudes ($z < 20$ m) with less than 5% of relative difference. The differences increase for higher altitudes but are still under 10%. When considering a variable evolution of the building and street dimensions as a function of the altitude (case 2), the differences are higher but are kept under 10%. Finally, one of the most important point to consider in this comparison is that the velocity profiles were obtained with

CIM in tens of seconds compared to the CFD solver which needed almost one day of computation using 48-core CPUs.

☞ CIM is able to reproduce velocity profiles obtained with the forced convection solver, a RANS CFD solver, in no time. However, special care must be taken to faithfully reproduce CFD profiles with CIM since it is not conservative.

3.3.2.4. CIM/CFD coupling to improve CFD inlet conditions

A coupling between the Canopy Interface Model and the forced convection solver has been considered, since CIM is able to accurately reproduce wind profiles obtained with the CFD solver. In order to assure the viability of such a coupling, it is lastly necessary to compare results obtained with CFD alone and with CFD using CIM to compute the inlet boundary conditions. The same urban area as used before has been considered for this comparison with this time pollutants emitted from a road with an emission rate of 20 mg/s. Three cases illustrated in Figure 3.12 were considered and are the following:

- Case 1 : the full numerical domain was considered, with all the buildings, and a log-law profile ($U_{z=10\,m}$ = 2.3 m/s) has been set at the inlet boundary; this case being the reference.

- Case 2 : the full numerical domain was considered, but the first line of building in the streamwise direction was deleted, and a log-law profile ($U_{z=10\,m}$ = 2.3 m/s) has been set at the inlet boundary; this case being the control case.

- Case 3 : the numerical domain was reduced and starts after the first line of deleted buildings with the CIM's outputs as the inlet boundary conditions following 24 m steps (a CIM profile is computed each 24 m in the direction transverse to the flow); this case being the CIM/CFD coupling case.
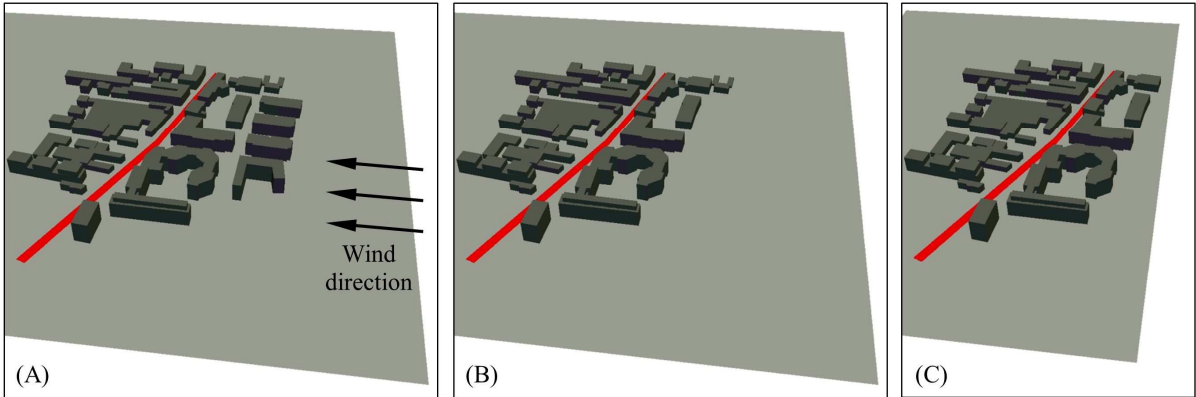
Figure 3.12 – Illustration of the three cases considered with (A) the case 1 with all buildings, (B) the case 2 with reduced buildings and logarithmic inlet BC and (C) the case 3 with reduced buildings and CIM inlet BC (BC: Boundary Condition).

Before comparing the results on pollutant concentrations, a first comparison can be done on the velocity field especially at the location where the buildings were deleted in the case 2 and 3. This comparison is presented in Figure 3.13. According to this figure, it can be seen that the velocity field obtained with CIM and showed in Figure 3.13 (C) is closer than the velocity field using directly a log-law profile (B) compared to the reference (A). In other words, the coupling seems working as expected on predicting the actual CFD velocities where the buildings were deleted.

Figure 3.13 – Comparison of the velocity field in the area where the buildings were deleted for (A) the case 1, (B) the case 2 and (C) the case 3.

The results on pollutant concentrations obtained for these cases are presented in Figure 3.14. According to Figure 3.14 (A) and Figure 3.14 (B), differences can be observed when deleting the first line of buildings in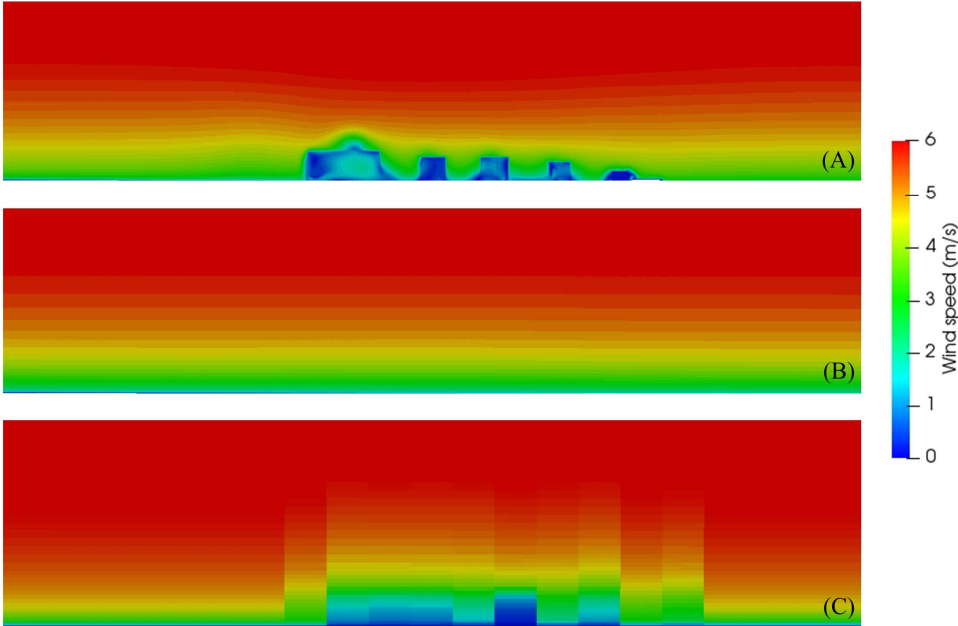 the streamwise direction (the main differences are highlighted by white arrows). The results obtained using the CIM/CFD coupling, shown in Figure 3.14 (C), are for their part closer to the reference (A), showing that the removal of the first line of buildings has been compensated by the use of CIM. Lastly, it should be noted that using the meshing discussed in Section 3.2.2. lead to around 7.25 million meshes for the cases 1 and 2 and around 5.5 million meshes for the case 3. In this case, using the coupling CIM/CFD allowed to decrease the calculation time approximatively by 20%.
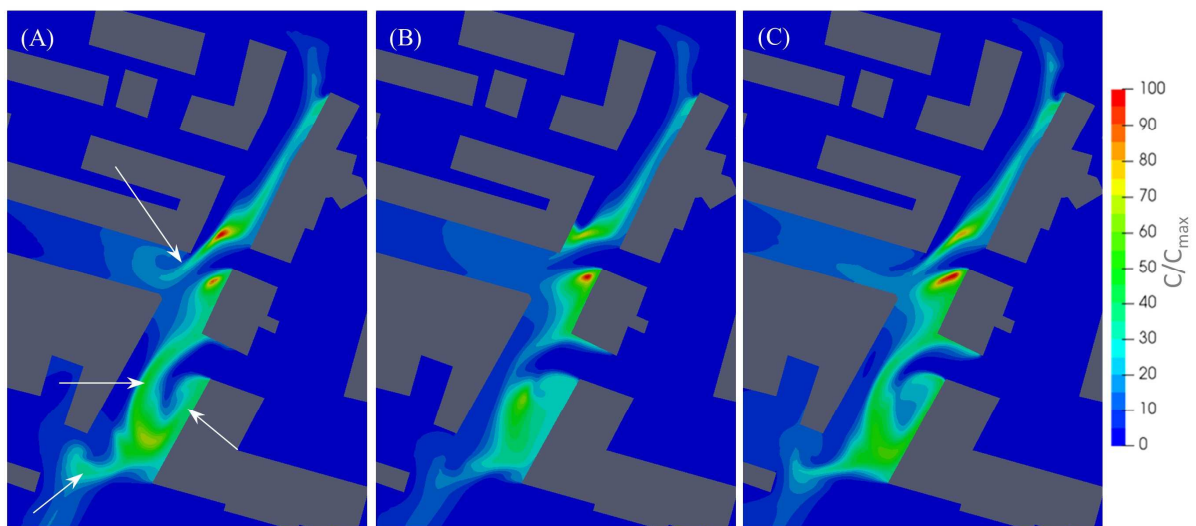
Figure 3.14 – Results on pollutant concentrations for the three cases considered with (A) the case 1, (B) the case 2 and (C) the case 3.

☞ A CIM/CFD coupling allows the possibility of removing buildings in the computational domain, decreasing the computation costs needed without altering significatively the results on pollutant concentrations. Such a coupling allows therefore also to better consider buildings outside of the numerical domain and, therefore, improve the inlet boundary conditions.

☞ The results about CIM/CFD coupling are encouraging but the study must be extended to other wind directions and other urban areas to ensure their accuracy in general cases.

3.3.3. Traffic-related emissions

It is not possible to consider air pollution modelling in urban areas without discussing the consideration and calculation of emissions. As discussed previously, emissions are specified in the numerical model by the means of a source term in the advection-diffusion equation (see Section 2.2.4. for further details). These emissions can be specified simultaneously in any grid cell at any location in the computational domain including low altitudes, for traffic-related emissions, and higher altitudes, as an example for industrial or residential chimney-related emissions. Emission rates from chimneys are usually known, especially for the industrial sector, and need generally not to be computed. However, the traffic-related emissions are more difficult to know and involve numerous parameters. The assessment of traffic-related emissions is therefore an important issue in air pollution modelling in urban areas.

Traffic-related emissions correspond to around 55%, 25% and 35%, respectively for NO_x, PM_{10} and $PM_{2.5}$ pollutants, of the total emissions of these pollutants in the Paris region in France (AIRPARIF, 2016). For other regions such as the Grand-Est region in East France, these percentages are lower but are still significative with for example 50% of NO_x traffic-related emissions (ATMO Grand-Est, 2017). It is therefore necessary to accurately assess traffic-related emissions in order to limit errors in the numerical model results. The question is:

(?) *How to assess traffic-induced emissions?*

The European Environment Agency (EEA) publishes each three- or four-years guidebooks entitled "EMEP/EEA air pollutant emission inventory", the last published in 2019. These guidebooks are precious documents for both researchers and engineers since they give a lot of information about emissions for several activity sectors, including notably energy and particularly road transport.

Traffic-related exhaust emissions

According to these guidebooks, traffic-related exhaust emissions are composed of hot and cold emissions which can be calculated for three different tiers. Equations for hot and cold exhaust emissions calculation using Tier 3, the highest tier for exhaust emissions, are given in (Eq. 3.14) and (Eq. 3.15) respectively (EEA, 2019a).

$$E_{HOT}(i,k,V) = N(k) \times d(k) \times e_{HOT}(i,k,V) \qquad \text{(Eq. 3.14)}$$

$$E_{COLD}(i,k,V) = \beta(i,k) \times N(k) \times d(k) \times e_{HOT}(i,k,V) \times \left(\left. \frac{e^{COLD}}{e^{HOT}} \right|_{i,k} - 1 \right) \qquad \text{(Eq. 3.15)}$$

where $E_{HOT}(i,k)$ are hot emissions (considering all warm running vehicles) for the pollutant i, vehicle technology k and a vehicle speed V, $E_{COLD}(i,k)$ the extra exhaust emissions to cold vehicle's contribution, $N(k)$ is the number of vehicles considered, $d(k)$ is the travelled distance, $\beta(i,k)$ is the fraction of distance driven with a cold engine, $e_{HOT}(i,k,V)$ the hot emission factor and $e^{COLD}/e^{HOT}|_{i,k}$ is the cold/hot emission quotient.

The equation for hot emission factors calculation is a function of the vehicle's speed and is given below in (Eq. 3.16).

$$e_{HOT}(i,k,V) = \frac{\alpha(i,k).V^2 + \beta(i,k).V + \gamma(i,k) + {\delta(i,k)}/{V}}{\varepsilon(i,k).V^2 + \zeta(i,k).V + \eta(i,k)} . (1 - RF(i,k)) \qquad \text{(Eq. 3.16)}$$

where $e_{HOT}(i,k,V)$ is the hot emission factor, V is the vehicle speed, $\alpha(i,k)$ to $\eta(i,k)$ are constant parameters for a given pollutant i and a vehicle technology k and $RF(i,k)$ is a reduction factor. The different constants and the reduction factors can be found in EEA (2019b).

Finally, the total amount of exhaust emission $E_{exhaust}(i,V)$ for a pollutant i and vehicle's speed V can be calculated following (Eq. 3.17).

$$E_{exhaust}(i,V) = \sum_k E_{HOT}(i,k,V) + E_{COLD}(i,k,V) \qquad \text{(Eq. 3.17)}$$

Note : the vehicle technology k consider vehicle type (small passenger car, heavy-duty trucks, etc.), fuel type (petrol, diesel) and Euro Standard (EURO I, EURO II, etc.).

Other traffic-related emissions (road, tyre and break wear)

For particulate matters (PM), it is not only important to consider exhaust emissions but also emissions due to the road, vehicle and break wear. To assess these emissions, the European Environment Agency also gave numerous equation not given here but which can be found in EEA (2019c).

Lastly, several information is needed to compute traffic-related emissions according to the EEA guidebooks. While some information can be easily obtained for a given road such as the travelled distance, the vehicles speed and the total number of vehicles, other information can hardly be known such as the ratio between petrol and diesel fuels, the number of vehicles in each category (car, trucks, etc.), the Euro Standards, etc. Assuming that statistically these parameters are the same at the local as at the country level, data on a country's vehicle fleet can be used. For the purpose of this thesis, the data for the French metropolitan fleet in 2017 given by the CITEPA (Centre Interprofessionnel Technique d'Etudes de la Pollution Atmosphérique, or in Interprofessional Technical Centre for Air Pollution Studies in English) were used for traffic-related emissions calculation (CITEPA, 2019). These data are summarized in Table 3.8 and Table 3.9.

Table 3.8 – Proportion of the different European Standards per type of vehicle (P: petrol / D: diesel).

Type	EURO I	EURO II	EURO III	EURO IV	EURO V	EURO VI
Passenger cars (P)	6.8%	8.1%	14.2%	28.2%	27.4%	15.4%
Passenger cars (D)	2.5%	4.4%	14.0%	39.3%	31.0%	8.8%
Light commercial vehicles (P)	5.3%	7.1%	13.2%	21.0%	36.2%	17.2%
Light commercial vehicles (D)	5.2%	9.5%	21.8%	28.9%	29.1%	5.6%
Buses (D)	1.6%	8.6%	16.3%	17.2%	27.0%	29.3%
Heavy-duty trucks (P)	1.9%	13.0%	21.0%	13.7%	16.8%	33.6%
Heavy-duty trucks (D)	0.1%	3.3%	17.5%	17.5%	27.7%	33.8%
L-category (P)	1.9%	38.1%	45.2%	14.8%	-	-

Table 3.9 – Proportion of petrol and diesel per type of vehicle and proportion of the type of vehicle.

Type	Proportion of petrol	Proportion of diesel	Proportion of the type
Passenger cars	36.7%	63.3%	73.6%
Light commercial vehicles	18.2%	81.8%	16.7%
Buses	0%	100%	0.3%
Heavy-duty trucks	0.2%	99.8%	1.9%
L-category	100%	0%	7.5%
Total	37.5%	62.5%	100%

3.3.4. Background concentration

Finally, the last point to address concerning computational domain and boundary conditions is about the background concentration. The background concentration is usually defined as the pollutant concentration resulting from all other pollution sources in the city, i.e. not considered in the simulation, and from long-range transport such as regional or even further sources (Vranckx et al., 2015). The background concentration has no direct impact on the simulations, since it is usually taken into account as post processing after calculation convergence. However, the background concentration representing from 50% to 70% of the total concentration (Gómez-Losada et al., 2016a), this concentration has a great impact on the final results and a false estimation of the background concentration can lead to misleading final numerical results. The question is therefore the following:

(?) *How to assess background concentrations?*

The background concentration is usually obtained using background monitoring stations generally located either in a place without too much local emission sources or at the top of buildings at a sufficient height to avoid including local traffic-related emissions. Such stations are frequently found in big cities as in Strasbourg, with two background stations downtown and three stations out of the city center according to ATMO Grand-Est data. However, such stations are not always available and other stations as traffic or urban stations can be the only way to assess background concentration.

The pollutant concentrations monitored with traffic or urban stations are, in theory, higher compared to the background concentrations since these stations are usually located in areas with several local emission sources and at low altitudes. A proposition to assess background concentrations from this type of station is to only consider concentration monitored during the night, for example between 2:00 A.M. and 5:00 A.M. In this way, the concentration of pollutants from local sources from the previous day has time to abate and same-day traffic-related pollutants have still only been emitted to a limited extent.

Another proposition suggested by Gómez-Losada et al. (2016a), is to use statistical models such as the Hidden Markov Model (HMM). According to these authors, a probability density

function (PDF) based on one year of daily averaged concentrations can be described by normal distributions. Using the HMM, it is possible to find the different possibilities which best describe the PDF using one to several normal distributions. Finally, the number of normal distributions needed to obtain the best interpolation of the PDF is determined by the Bayesian Information Criterion (BIC) which give the lower value. The number of normal distributions corresponds then to the number of distinct clusters describing the PDF (clusters corresponding to the background concentration, traffic contribution, etc.) and, according to this methodology, the value of the background concentration is given by the lowest mean of the normal distributions assuming that the lowest distribution is the background concentration.

Gómez-Losada et al. gave all the necessary information, such as R source code, to carry out their approach on different data (Gómez-Losada et al., 2016b). Thus, this methodology has been applied for example to NO_2 data from two monitoring stations in Strasbourg named "STG Est" and "STG Clémenceau" from 2007 to 2016 provided by ATMO Grand-Est[1] to ensure its applicability. As an example of result, the interpolation giving the lowest BIC for the STG Est station in 2015 is given in Figure 3.15.
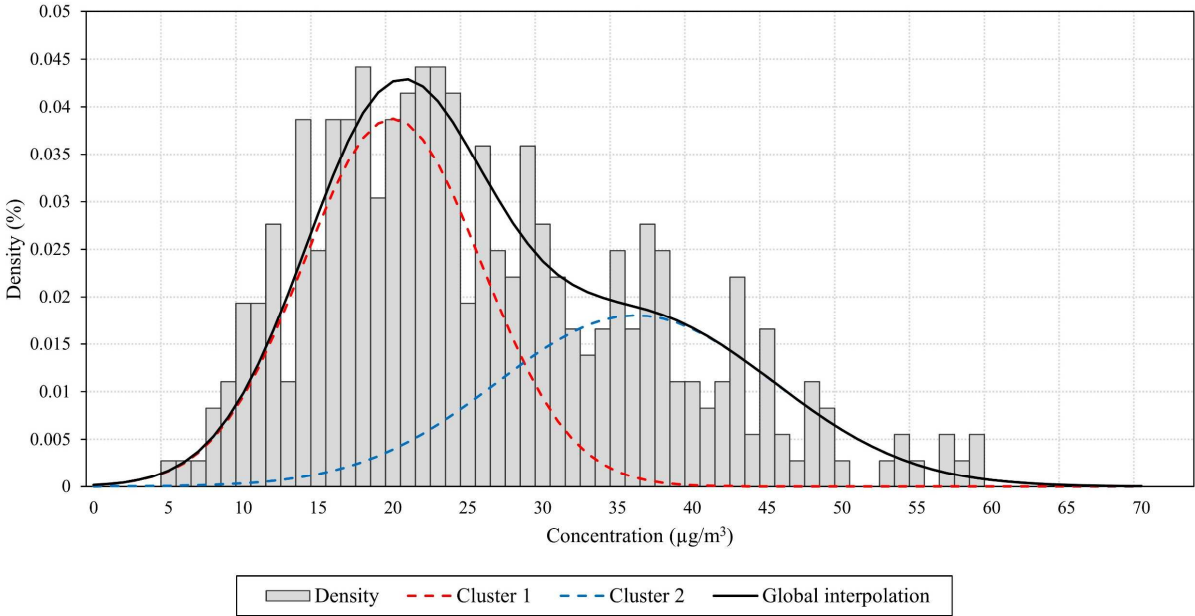

Figure 3.15 – Application of the Hidden Markov Model methodology to assess NO_2 background concentration from 2015 STG Est station data.

---

[1] Data provided under the reference WK-ADM-COE-17-1372

This figure shows that the best description of the data monitored during 2015 at the STG Est station is obtained using two normal distributions with means of 20.0 µg/m^3 and 36.2 µg/m^3, the minimal mean being the background concentration.

A summary of the background concentrations from 2007 to 2016 for the STG Est and STG Clémenceau stations assessed with the HMM methodology is given in Table 3.10. This table also summarize statistical indicators over the datasets such as the three quartiles and the averaged concentration.

Table 3.10 – NO$_2$ background concentrations assessed using HMM methodology over STG Est and STG Clémenceau dataset and statistical indicators.

Station	Year	Background [µg/m^3]	1st quartile [µg/m^3]	2nd quartile [µg/m^3]	3rd quartile [µg/m^3]	Average [µg/m^3]
STG Clémenceau	2007	50.2	47.0	58.0	69.0	59.2
	2008	43.7	45.0	58.8	69.5	58.6
	2009	44.5	43.8	54.0	68.0	56.6
	2010	50.0	45.0	56.0	67.0	56.9
	2011	45.5	46.0	54.0	66.0	56.3
	2012	40.8	43.0	53.0	62.5	54.3
	2013	43.6	42.0	50.5	61.0	52.4
	2014	38.6	40.0	49.0	60.0	50.7
	2015	43.6	40.0	49.0	58.0	49.8
	2016	43.6	38.6	46.4	55.2	48.0
STG Est	2007	26.0	25.0	33.0	43.0	34.7
	2008	20.3	22.0	31.0	40.0	32.1
	2009	23.2	22.0	31.0	42.0	33.4
	2010	19.5	22.0	30.0	39.0	31.4
	2011	19.5	22.0	31.0	41.0	31.8
	2012	22.1	20.0	28.0	38.0	29.7
	2013	17.3	19.0	26.0	34.5	28.0
	2014	17.3	19.0	25.0	33.0	26.6
	2015	20.0	19.0	25.0	34.0	26.8
	2016	16.2	17.5	24.4	32.6	26.1

According to these data for the considering stations and years, the background concentration assessed using the HMM methodology is always under the median (2nd quartile) and the

averaged concentration. Furthermore, the background concentrations are fluctuating around the 1st quartile with more or less 10% of difference.

Lastly, the Hidden Markov Model methodology is easily applicable for operational purposes.

☞ The background concentration usually assessed with background monitoring stations, is an important parameter in air pollution modelling since it can significatively change the final results on concentrations.

☞ If no such stations are available, the background concentration can be estimate using other type of stations (rural, urban, etc.) assuming that this concentration is reached during the night or, with statistical methodologies such as the Hidden Markov Model methodology.

3.4. Conclusion of the chapter

When doing computational fluid dynamics, and more broadly numerical modelling, it is necessary to accordingly set up the model to avoid bad results and misleading interpretations.

The bibliographic analysis presented in this chapter showed that several points must be considered to best set up the model, and includes the meshing, the domain extension, and the boundary conditions.

All of these points were discussed in this chapter and improved when it was both necessary and possible. The main results are summarized below:

(?) *Which height should we considered when there is not any building?*

The COST Action 732 guidelines are a good starting point to ensure sufficient distance in the numerical model in the streamwise, lateral and vertical dimensions to avoid side effects. However, it has been shown that a minimal domain height of 96 m should be used even in absence of obstacles to avoid result variations, this minimal height being therefore also necessary when modelling obstacles such as buildings.

How to improve calculation efficiency by using small mesh sizes without increasing too much the total number of meshes? Is 0.5 m a sufficient mesh size at the emission sources, as used by several researchers?

Meshes in the vicinity of wall surfaces shall normally satisfy a y^+ criterion ranging from 30 to 500. However, this range cannot be reached for full scale modelling without increasing too much the number of cells in the numerical domain and, therefore, the calculation costs. The best compromise is to use 1 m meshes in the area of interest and larger meshes as altitude increases. Finest refinements such as 0.5 m can be used near the wall surfaces such as near the buildings but, in any case, this refinement must at least be used at the emission source, which also corresponds to a good injection height.

Are the usual inlet conditions adequate enough for computational wind engineering in complex situations (highly built-up areas) and, if not, is it possible to improve them?

The boundary conditions are generally always the same with symmetry conditions at the lateral and top boundaries, open boundary conditions at the outlet and no-slip conditions at the wall surfaces. There is, nevertheless, an exception at the inlet boundary were both power and log-law profiles can be considered. However, such conditions may be unsuitable for densely built urban areas modelling where a model coupling can improve the inlet conditions, as with the Canopy Interface Model.

How to assess traffic-induced emissions?

Since it is a major source of air pollution in urban areas, the traffic-related emissions must be calculated as fine as possible to avoid any misleading result. To do so, the European Environment Agency produced guidebooks which can be followed to calculate traffic-related emissions due to vehicle exhausts but also road, tyre and brake wear.

⍰ *How to assess background concentrations?*

The background concentration should be considered when modelling air pollution in urban areas with CFD since it is the only way to consider external and long-range pollutant sources. This concentration is usually assessed using background monitoring stations but can also be assessed using urban of traffic station assuming that the background concentration is reached during the night, or, using a Hidden Markov Model methodology.

With both specific CFD solvers and all the necessary information for their parametrization, it is now possible to assess air pollution in urban areas. However, it is currently not possible to use such a model to compare with regulatory values such as annual standards since methodologies to do so are still required. This point is the subject of the Chapter 4. In the same way, the issue of calculating NO_2 concentrations from NO_x concentrations without using the PSS or any chemical mechanism has not been addressed yet. This point is the subject of the Chapter 5.

Chapter 4:

Methodologies to assess mean annual air pollution concentration combining numerical results and wind roses

This chapter has been published as an original research paper in the *Sustainable Cities and Society* journal:

Annual standards and guidelines given by the European Union and the World Health Organization cannot be directly compared with CFD results, these results being obtained for specific wind directions and velocities. This chapter presents (1) methodologies to assess continuous wind speed distribution based on wind roses data and (2) methodologies to assess mean annual concentrations based on numerical results and wind distributions. These methodologies, illustrated with CFD results, can be used for any other type of numerical model and are of relevance for engineering purposes, allowing the comparison between numerical results and annual regulatory standards.

---

[1] These authors contributed equally to the paper.

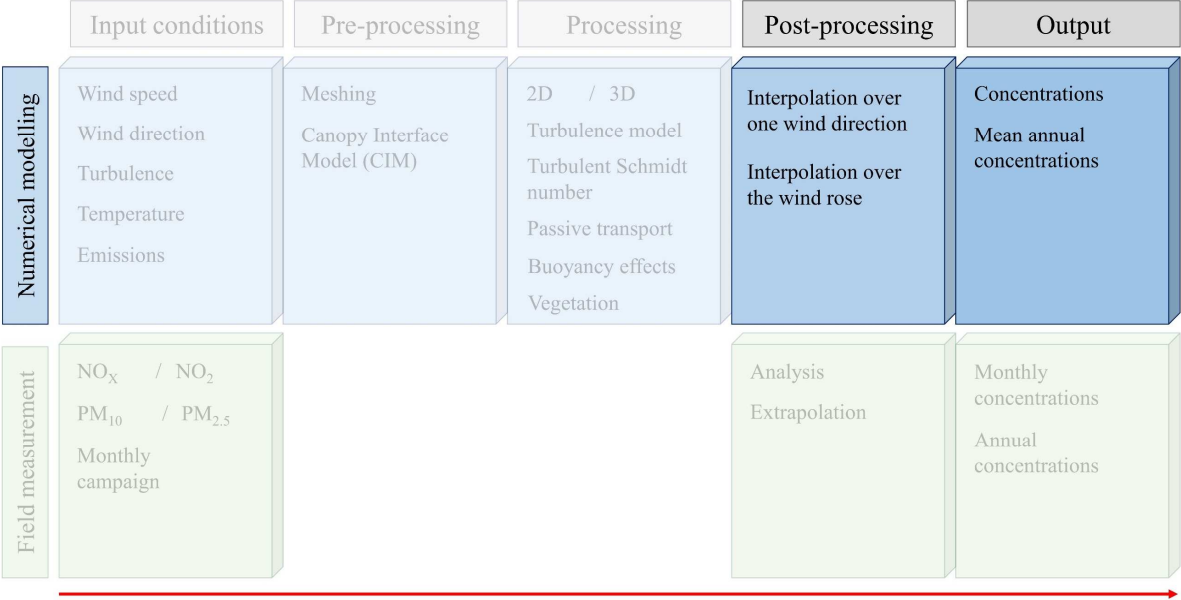The points covered in this chapter are highlighted in Figure 4.1.

Figure 4.1 – Main points covered in Chapter 4.

Particularly, the following question is addressed in this chapter:

How to take into account all wind conditions, such as direction and intensity, when assessing annual concentrations with a CFD model?

4.1. Introduction

Over the past decades, outdoor air pollution has become a major issue, especially in highly densified urban areas where pollutant sources are numerous and air pollutant emissions high. In order to protect people from excessive exposure to air pollution, which can cause several diseases (Anderson et al., 2012; Kim et al., 2015), the World Health Organization (WHO) have recommended standard values that must not be exceeded for different pollutants such as nitrogen dioxide (NO_2) and particulate matter (EU, 2008; WHO, 2017) to protect population health, and the European Union (EU) decided to respect the same or other standards depending on the air pollutants. Among the different types of values given as standards, studies have shown that annual standards are generally more constraining and harder to reach than the other standards (Chaloulakou et al., 2008; Jenkin, 2004; Yuan et al., 2019).

In the meantime, recent studies have shown that the indoor air quality is strongly correlated with the outdoor one: while for nitrogen dioxide a 5% increase in indoor air pollutant concentrations can be expected for only a 1% increase in outdoor concentrations (Shaw et al., 2020), for particulate matters such as $PM_{2.5}$ the outdoor concentration can contribute from 27% to 65% of the indoor concentration (Bai et al., 2020). Being able to assess outdoor pollutant concentrations is therefore a necessity to improve air quality in the outdoor built environment, but also in the indoor one (Ścibor et al., 2019).

Annual concentrations can be assessed using both on-site monitoring and numerical modeling. On site monitoring requires measurements over long periods to be able to assess mean annual concentrations of pollutants, although a recent study has shown that mean annual concentration of NO_2 can be assessed using only one month of data (Jurado et al., 2020), which significantly reduces the measurement time required. Monitoring nonetheless has other limitations: it does not allow assessing the future evolution of the built environment or pollutant emissions, thus, limiting its applicability to achieve the smart sustainable cities of the future as defined by Bibri and Krogstie (2017). Numerical modelling can overcome these limitations and can help define new strategies to improve air quality in cities combining wind data, various air pollution scenarios and urban morphologies (Yang et al., 2020). Among the several models currently available, Computational Fluid Dynamics (CFD) has shown great potential for modeling pollutant dispersion from traffic-induced emissions by including numerous physical phenomena such as the effects of trees (Buccolieri et al., 2018; Santiago et al., 2019; Vranckx et al., 2015) and heat exchanges (Qu et al., 2012; Toparlar et al., 2017; Wang et al., 2011) on the scale of a neighborhood. However, this type of numerical result cannot be directly compared with the annual standards. Methodologies designed to assess mean annual concentrations based on numerical results can be found in the literature (Rivas et al., 2019; Solazzo et al., 2011; Vranckx et al., 2015), but further work is required to improve them and assess their limits.

The aim of this study is to provide tools and methodologies to assess mean annual concentrations based on numerical results and wind rose data to improve air quality in built environment and cities. It is firstly to evaluate whether it is possible to assess continuous wind speed distributions based on wind rose data. To do so, a statistical law called Weibull distribution is compared with a new sigmoid-based function built for the purpose of this study.

Secondly, it is to present and compare a discrete methodology usually used to assess mean annual concentrations based on numerical results with a continuous methodology built for the purpose of this study, and to discuss their respective advantages and limitations.

4.2. Material and methods

4.2.1. Meteorological data

4.2.1.1. Data location

This work uses wind velocity and wind direction data from four cities in France. These cities were chosen to cover most of France to obtain representative results and include the cities of Strasbourg (Grand-Est region), Nîmes (Occitanie region), Brest (Bretagne region) and Lille (Hauts-de-France region). In particular, the data were obtained from the stations named Strasbourg-Entzheim, Nîmes-Courbessac, Brest-Guipavas and Lille-Lesquin, respectively. The location of these stations and their corresponding regions is presented in Figure 4.2.
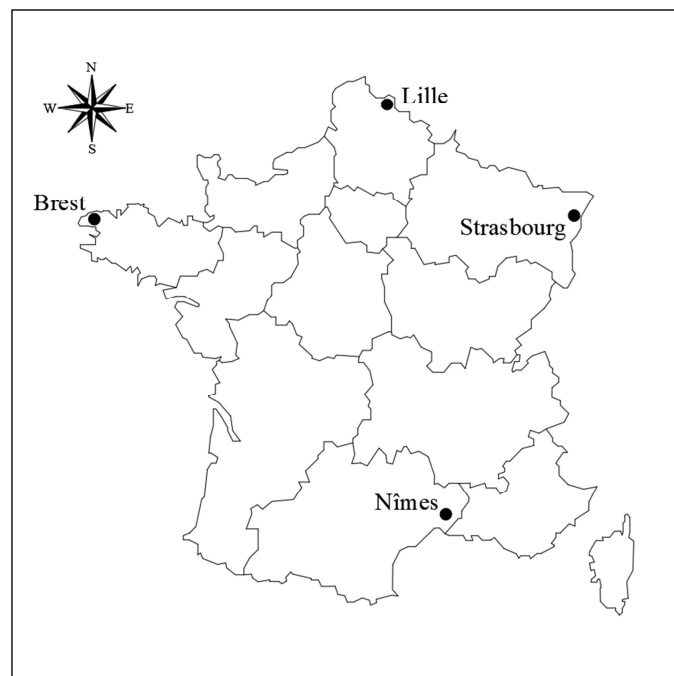

Figure 4.2 – Location of the different meteorological stations used.

4.2.1.2. Data availability

The data used in this work were provided by Météo-France, a public institution and France's official meteorology and climatology service. The data are mainly couples of wind velocity and wind direction over a twenty-year period from 1999 to 2018, except for the Strasbourg-Entzheim station where it is a ten-year period from 1999 to 2008. The data were obtained via a personal request addressed to Météo-France and were not available on open-access. A summary of the information of the stations is presented in Table 4.1, with the time ranges of the data and the number of data available (the coordinates are given in the World Geodetic System 1984).

Table 4.1 – Summary of the available data.

Station				Data availability		
Location	Latitude	Longitude	Altitude	Time range	Number of valid cases	Number of missing cases
Brest - Guipavas	48°27'00"N	4°22'59"O	94 m	1999 - 2018	29,171	45
Lille - Lesquin	50°34'12"N	3°05'51"E	47 m	1999 - 2018	29,185	31
Nîmes - Courbessac	43°51'24"N	4°24'22"E	59 m	1999 - 2018	29,214	2
Strasbourg - Entzheim	48°32'58"N	7°38'25"E	150 m	2009 - 2008	29,199	25

All the data were monitored from wind sensors placed 10 meters from the ground and the wind frequencies are available for each wind direction with 20° steps for two distinct wind discretizations: a "basic" discretization giving wind frequencies for 4 velocity ranges (from 0 to 1.5 m/s, 1.5 to 3.5 m/s, 3.5 to 8 m/s and more than 8 m/s), illustrated in Figure 4.3 (A); and a "detailed" discretization giving wind frequencies by 1 m/s steps except between 0 and 0.5 m/s, illustrated in Figure 4.3 (B). The "basic" discretization is a common format mostly found in wind roses (possibly with different velocity ranges) while the "detailed" data are less common and more expensive.

The wind roses for each meteorological station considered in this work and based on the "basic" 4-velocity-range discretization described in Figure 4.3 (A) are provided in Figure 4.4. This figure shows how the monitoring locations considered in this study give distinct but complementary information, with for example many high velocities at Brest compared to Strasbourg and Nîmes, where almost no velocities were monitored over 8 m/s, and with dominant wind directions at Nîmes and Strasbourg compared to the other stations.
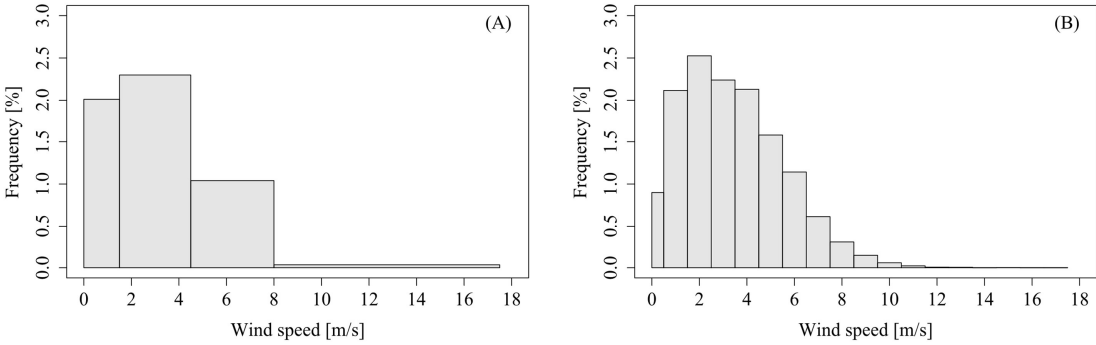
Figure 4.3 – Examples of data for Strasbourg and a 200° wind direction with (A) only 4 ranges of velocities and (B) the detailed data discretized in 18 ranges.
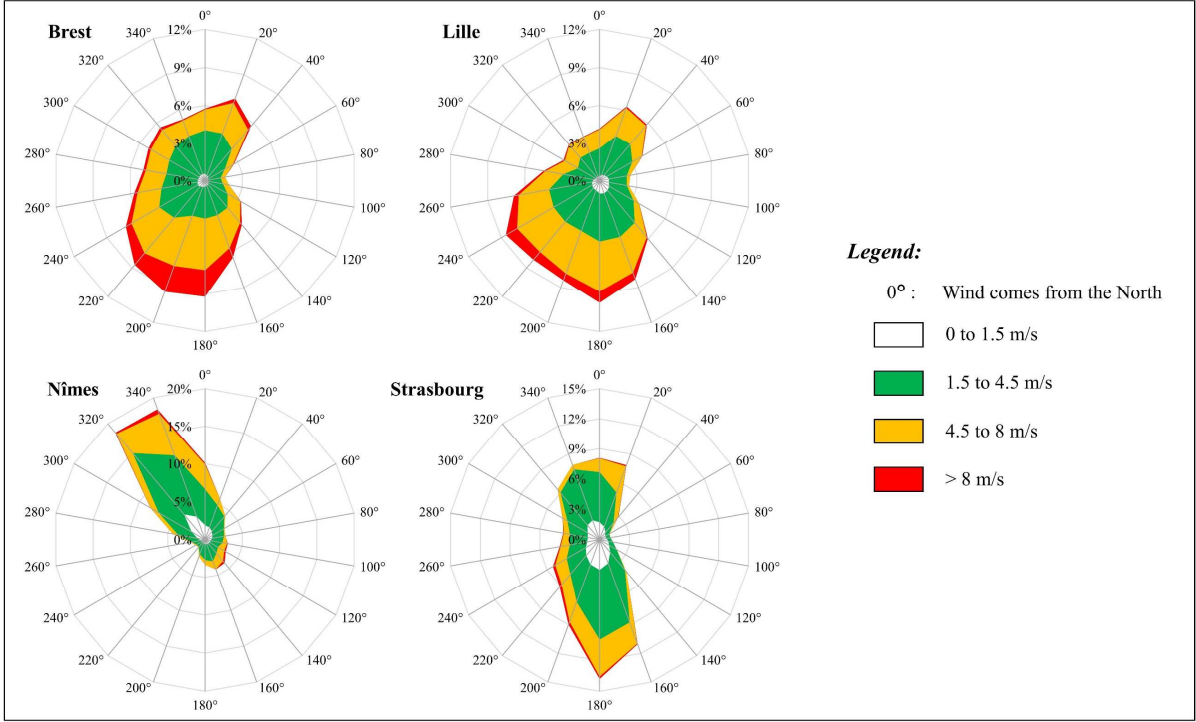

Figure 4.4 – Wind roses for each location considered.

4.2.1.3. Wind data interpolation functions

A two-parametric continuous probability function, the Weibull distribution, mainly used in the wind power industry, can be used to describe wind speed distribution (Kumar et al., 2019; Mahmood et al., 2019). The equation of the corresponding probability density function is given in (Eq. 4.1).

$$f(v) = \frac{k}{\lambda}\left(\frac{v}{\lambda}\right)^{k-1} e^{-(v/\lambda)^k} \tag{Eq. 4.1}$$

where v is the wind velocity, k is the shape parameter and λ is the scale parameter of the distribution, with k and λ being positive.

For the purpose of this study, a 5-parametric continuous function was built to determine the "detailed" wind discretization based on the "basic" 4-velocity-range wind discretization. This function, called Sigmoid function, based on the composition of two sigmoid functions, is given in (Eq. 4.2). The two functions will be compared in the results section.

$$f(v) = \alpha.\left(-1 + \frac{1}{1 + \beta_1.e^{-\gamma_1.v}} + \frac{1}{1 + \beta_2.e^{\gamma_2.v}}\right) \tag{Eq. 4.2}$$

where $\alpha, \beta_1, \beta_2, \gamma_1$ and γ_2 are positive parameters.

4.2.2. Numerical model

Simulations were performed using the unsteady and incompressible solver *pimpleFoam* from OpenFOAM 6.0. A Reynolds-Averaged Navier-Stokes (RANS) methodology was used to solve the Navier-Stokes equations with the RNG k-ε turbulence model, and the transport of particulate matter was performed using a transport equation. This solver was validated previously in Reiminger et al. (2020c).

The area chosen to illustrate the methodologies discussed in this paper is located in Schiltigheim, France (48°36'24", 7°44'00"), a few kilometers north of Strasbourg. This area, as well as the only road considered as an emission source in this study (D120, rue de la Paix), are illustrated in Figure 4.5 (A). PM_{10} traffic-related emissions were estimated at 1.39 mg/s using daily annual mean traffic and were applied along the street considering its length in the numerical domain (200 m), its width (9 m) and an emission height of 0.5 m to take into account initial dispersion.

The recommendations given by Franke et al. (2007) were followed. In particular, with H being the highest building height (16 m), the distances between the buildings and the lateral

143

boundaries are at least $5H$, the distances between the inlet and the buildings as well as for the outlet and the buildings are at least $5H$ and the domain height is around $6H$. An illustration of the resulting 3D sketch is presented in Figure 4.5 (B). A grid sensitivity test was performed and showed that hexahedral meshes of 1 m in the study area and 0.5 m near the building walls are sufficient, leading to a more comparable resolution than other CFD studies (Blocken, 2015) and leading to a total number of around 800,000 cells. The resulting mesh is illustrated in Figure 4.6.

Figure 4.5 – Illustration of (A) the area of Strasbourg modeled with the road considered for the traffic-related emissions (white dashed lines), and (B) the corresponding area built in 3D for the numerical simulations with the emission source (red).

No-slip conditions ($U = 0$ m/s) were applied to the building walls and ground, and symmetry conditions to the lateral and the top boundaries. A freestream condition was applied to the outlet boundary, and neutral velocity, turbulent kinetic energy and turbulent dissipation profiles suggested by Richards and Norris (2011) were applied to the inlet boundary.
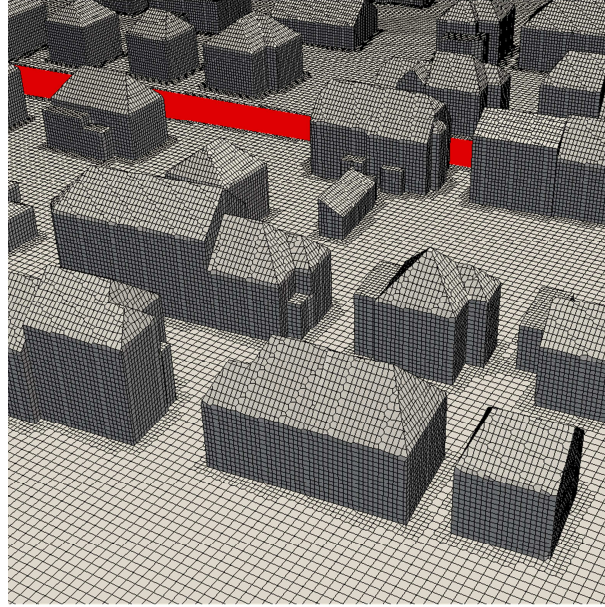
Figure 4.6 – Illustration of the meshes in the computational domain with the emission source (red), with 0.5 m meshes near the buildings and 1 m in the study area.

A total of 18 simulations were performed using the same wind velocity ($U_{10\,m}$ = 1.5 m/s) but with different wind directions from 0° to 340° using a 20° step. Since the simulations were performed in neutral conditions and without traffic-induced turbulence, the dimensionless concentration C^* given in (Eq. 4.3) is a function only of the wind direction (Schatzmann and Leitl, 2011). In other words, this means that considering the previous hypothesis, and for a given emission and building configuration (leading to constant $H.L/q$ ratio), only one simulation is needed for each wind direction simulated. The pollutant concentrations for a non-simulated wind velocity u can therefore be computed using (Eq. 4.4).

$$C^* = \frac{C.U.H.L}{q} \qquad \text{(Eq. 4.3)}$$

where C^* is the dimensionless concentration, C is the concentration, U the wind velocity, H the characteristic building height and q/L the source strength of emission.

$$C_u = U_{ref}.\frac{C_{ref}}{u} \qquad \text{(Eq. 4.4)}$$

where C_u is the pollutant concentration for the wind velocity u not simulated and C_{ref} the pollutant concentration for the simulated wind velocity U_{ref}.

4.3. Results

4.3.1. Wind data interpolation

4.3.1.1. Comparison between the Weibull distribution and the sigmoid function

The best fitting parameters of the two functions were determined for the whole dataset using a non-linear solver and the "basic" 4-velocity-range wind data. The solver was set up to solve equation (Eq. 4.5) for the four-velocity ranges [0, 1.5[, [1.5, 4.5[, [4.5, 8[and [8, +∞[for both the Weibull and the sigmoid functions. This equation reflects that the sum of the frequencies between two wind velocities (i.e. the area under the curve) must be equal to the frequency given in the "basic" 4-velocity-range wind data. Since the sigmoid function has five parameters, a fifth equation to be solved was added only for this function and corresponds to (Eq. 4.6). With this equation, it is assumed that the wind frequency tends toward 0% when the wind speed tends toward 0 m/s, as for the Weibull distribution.

$$\int_a^b f(v).dv = FVR_{[a;b[}$$
(Eq. 4.5)

$$f(0) = 0$$
(Eq. 4.6)

where $f(v)$ is the Weibull or the sigmoid function and $FVR_{[a;b[}$ is the wind frequency given in the 4-velocity-range data for wind velocities ranging from a included to b excluded.

Figure 4.7 (A–D) shows a comparison between the Weibull distribution, the sigmoid function and the "detailed" 18-velocity-range data for one wind direction of each meteorological station. According to these figures, the two functions generally give the same trends, and both appear to give a good estimation of the "detailed" wind data. However, depending on the case, the Weibull function can provide improvements in comparison to the sigmoid function, as in Figure 4.7 (A), or vice versa, the sigmoid function can provide improvements in comparison to the Weibull function, as in Figure 4.7 (D).
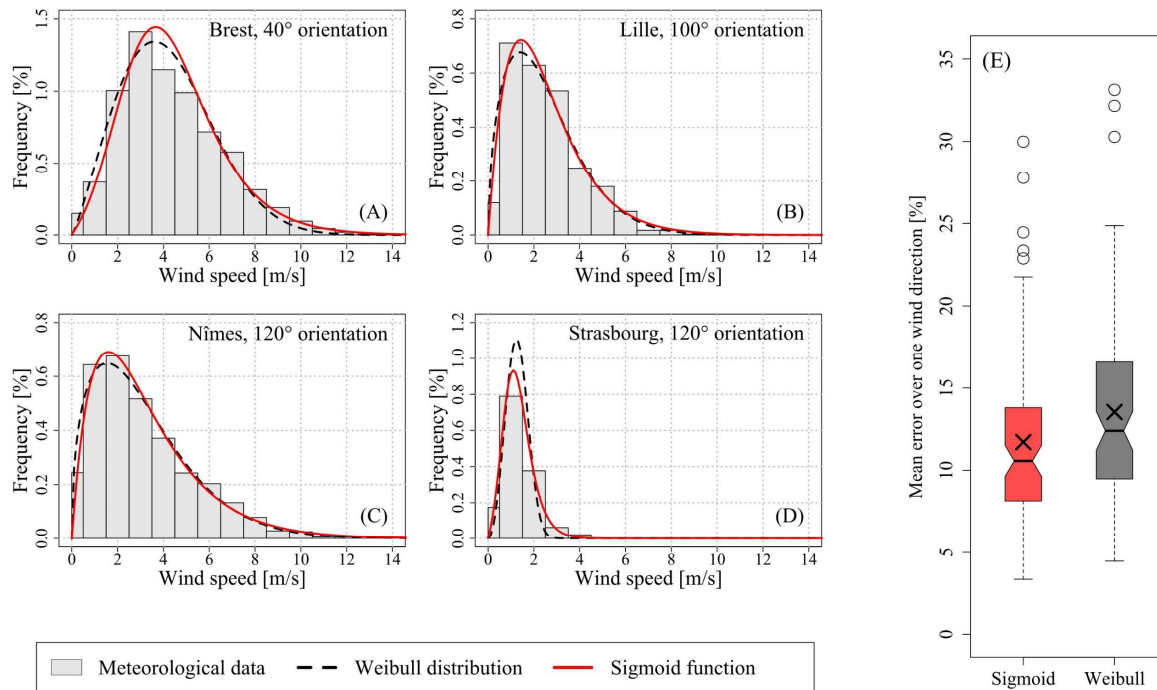
Figure 4.7 – (A–D) Weibull distribution and sigmoid function results compared to the detailed meteorological wind frequency data for one wind direction at each station considered and (E) a notched box plot of the mean error over one wind direction with all station

To better compare the two functions, a notched box plot of the mean error over one wind direction is given in Figure 4.7 (E). According to this figure, the sigmoid function gives generally better results compared to the Weibull distribution, with a lower maximal error (30.0% and 33.1% respectively); a lower first quartile (8.1%% and 9.5%% resp.); a lower third quartile (13.8% and 14.5% resp.); a lower mean (11.7% and 13.5% resp.); and a lower median (10.6% and 12.4% resp.). The differences are, however, small and may not be significant, especially for the median because the notches slightly overlap. These differences between the Weibull distribution and the sigmoid function are also location dependent, with for example better prediction of the wind distribution in Strasbourg using the sigmoid function and an equivalent prediction in Brest. Finally, it should be noted that both functions can lead to underestimations of the lower wind velocity frequencies, as shown in Figure 4.7 (A) and (D).

According to the previous results, the Weibull distribution and the sigmoid function can accurately reproduce the "detailed" wind distribution based on a "basic" 4-velocity-range discretization with an average error of around 12% over the four stations considered in France.

They can nonetheless lead to underestimations of the low wind velocity frequencies, for which the highest pollutant concentrations appear.

4.3.1.2. Optimization of the sigmoid function interpolation for low wind velocities

The parametrization of the sigmoid function, called standard sigmoid function, was modified to improve the estimation of the low wind velocity frequencies in order to avoid underestimating pollutant concentrations.

Based on all the meteorological data considered in this study, it was found that the underestimation of low wind velocity frequencies occurs mostly when the frequency of the first velocity range is lower than the frequency of the second velocity range. In this specific case, the optimized sigmoid function still needs the equation (Eq. 4.5) for the four-velocity ranges given in the "basic" wind data, but equation (Eq. 4.6) is replaced by equation (Eq. 4.7); otherwise, the previous parametrization using equations (Eq. 4.5) and (Eq. 4.6) is kept.

$$f(0) = FVR_{[0;\alpha[} \frac{FVR_{[0,\alpha[}}{FVR_{[\alpha,\beta[}} \tag{Eq. 4.7}$$

where $FVR_{[0,\alpha[}$ is the wind frequency for the first range of velocities given in the 4-velocity-range data and $FVR_{[\alpha,\beta[}$ is the wind frequency for the second range of velocities (e.g., in this study $\alpha = 1.5$ and $\beta = 4.5$).

The methodology for the optimized sigmoid function is illustrated in Figure 4.8 (A–B): when the frequency of the first velocity range is higher than the second, as in Figure 4.8 (A1), the standard parametrization of the sigmoid function can be used because the low wind velocity frequencies are estimated accurately, as in Figure 4.8 (A2), when the frequency of the first velocity range is lower than the second, as in Figure 4.8 (B1), the standard parametrization leads to underestimations of low wind velocity frequencies and the optimized parametrization should be used instead, leading to a better estimation of the frequencies, as shown by the blue curve in Figure 4.8 (B2) compared to the red curve.
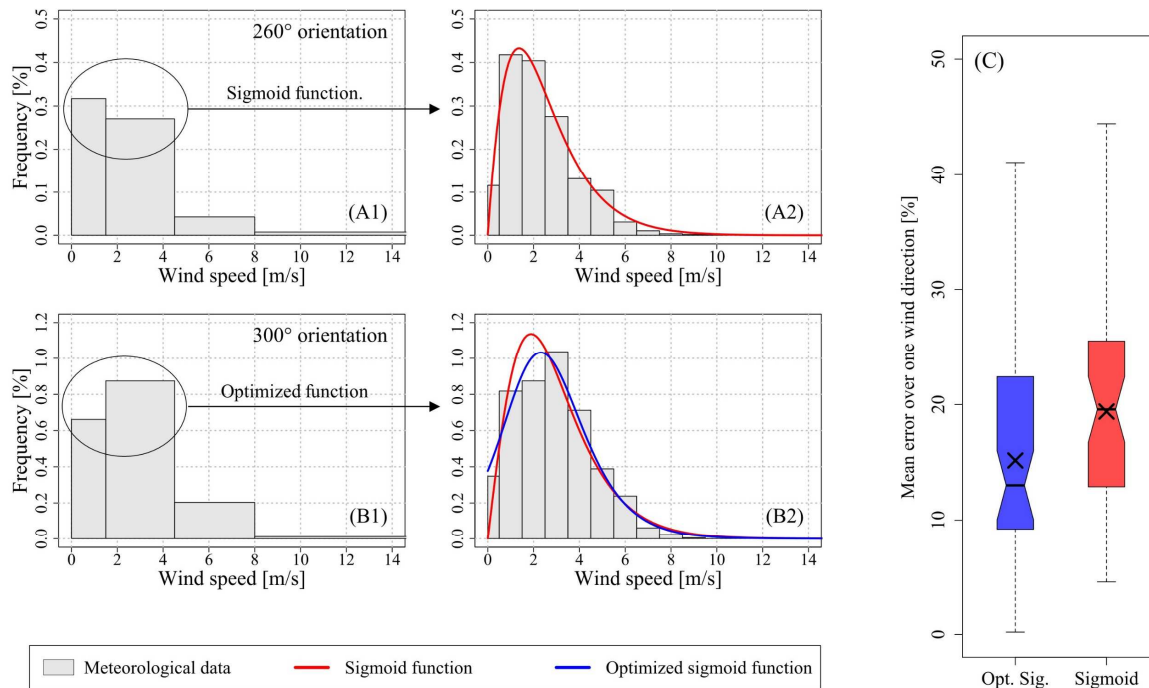
Figure 4.8 – (A–B) Illustration of the optimized sigmoid function methodology and (C) comparison with the standard sigmoid function results.

The improvements with the optimized sigmoid function compared to the standard function were assessed and the results are presented in Figure 4.8 (C). For this comparison, only the wind directions where the optimized function was applied are considered (49 wind directions within the 78 previously used) and the errors compared to the "detailed" 18-velocity-range data were calculated for the low wind velocity frequencies (between 0 and 3.5 m/s). According to this figure, the optimized sigmoid function gives improvements over the standard sigmoid function with a lower maximal error (41.0% and 44.4% respectively); a lower first quartile (9.2% and 12.9% resp.); a lower third quartile (22.4% and 25.5% resp.); a lower mean error (15.2% and 19.4% resp.); and a lower median (13.0% and 19.6% resp.). The improvements using the optimized function are significative, in particular for the median since the box plot notches do not overlap; they are also location dependent. A global improvement of the wind distribution prediction ranging between 20% and 45% is observed in Strasbourg, Lille and Nîmes while no improvement is observed in Brest.

According to the previous results, using the optimized sigmoid function can improve the reproduction of the "detailed" wind distribution based on a "basic" 4-velocity-range compared to the standard sigmoid function, especially for low wind velocities.

4.3.2. Mean annual concentration assessment

4.3.2.1. Discrete methodology with intermediate velocities

Initially, mean annual concentrations based on the CFD results can be calculated using a discrete methodology. This methodology considers that the mean annual concentration at a given location is composed of several small contributions of different wind velocities and wind directions. The mean concentration over one wind direction can be calculated with equation (Eq. 4.8) and the mean annual concentration with equation (Eq. 4.9). A similar methodology can be found in Solazzo et al. (2011) or in Rivas et al. (2019).

$$\bar{C}_d = \frac{\sum_{r=1}^{n} C_{d,r} \cdot f_{d,r}}{\sum_{r=1}^{n} f_{d,r}} + C_{bg} \tag{Eq. 4.8}$$

$$\bar{C} = \frac{\sum_{d=1}^{n} \bar{C}_d \cdot f_d}{\sum_{d=1}^{n} f_d} \tag{Eq. 4.9}$$

where $\bar{C}_d$ is the mean concentration over one wind direction, $C_{d,r}$ is the concentration for a given wind direction d and a given wind velocity range r, $f_{d,r}$ is the frequency for a given wind direction and a given wind velocity range, C_{bg} is the background concentration, $\bar{C}$ is the mean annual concentration and f_d the total frequency of a given wind direction.

With this methodology, it is necessary to choose a wind velocity in each velocity range for which the concentration will be calculated based on the CFD result. A simple choice is to consider an intermediate velocity, noted v_i, corresponding to the average between the minimal and the maximal value of the velocity range (e.g., for the velocity range [1.5, 4.5[, the intermediate value is 3 m/s).

A comparison of results for this methodology is given in Figure 4.9 with distinct cases considering (A) the "basic" 4-velocity-range frequencies, (B) the "detailed" 18-velocity-range

frequencies, (C) the frequencies calculated with the sigmoid function, and (D) the frequencies calculated with the optimized sigmoid function. No background concentration is considered in this study to permit better comparison of the results and the CFD results used as inputs for the methodologies were strictly the same.
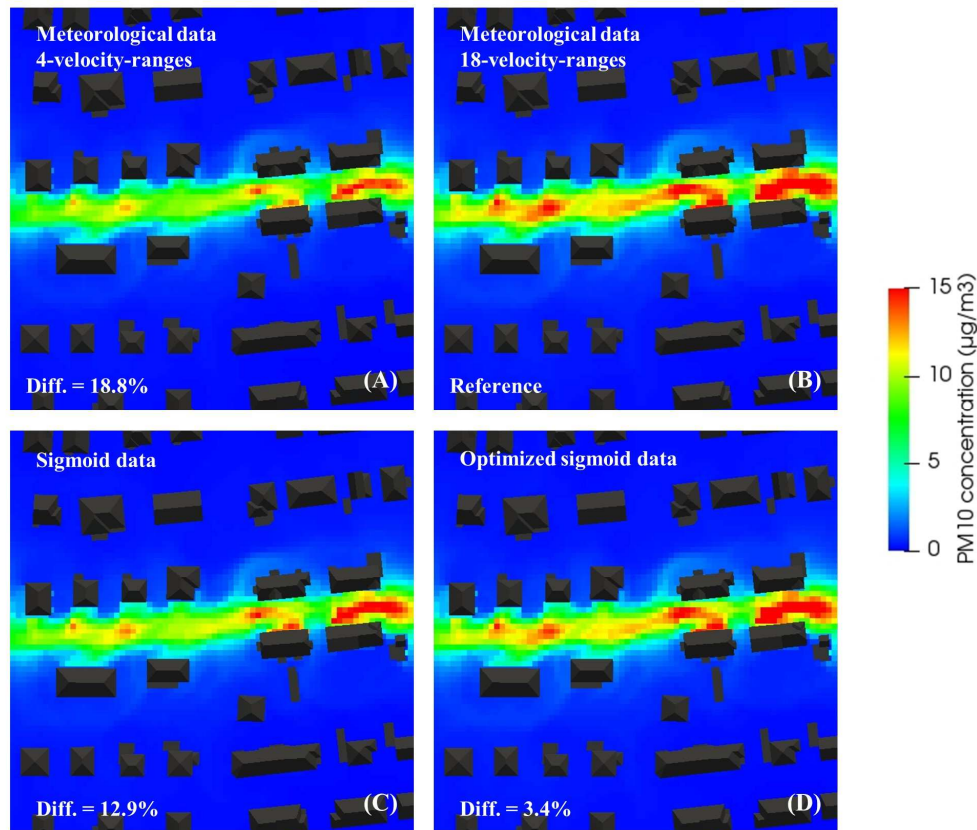

Figure 4.9 – Mean annual concentrations without background concentration based on (A) the "basic" 4-velocity-range monitoring data, (B) the "detailed" 18-velocity-range monitoring data, (C) the sigmoid interpolation data and (D) the optimized sigmoid interpolation.

Initially, it can be seen that using the "basic" 4-velocity-range data leads to an underestimation of the concentrations compared to the case using "detailed" 18-velocity-range data by around 19%. When calculating the "detailed" wind velocity distribution based on the "basic" data with the sigmoid function, the difference is reduced to 12.9%. Finally, the best results are obtained when using the optimized sigmoid function with an underestimation of 3.4%. According to these results, using the "basic" 4-velocity-range frequencies can give an estimation of the mean annual concentrations but is not sufficient to reach good accuracy compared to the mean annual concentration calculated with the "detailed" wind velocity distribution. However, using the

151

sigmoid function and especially the optimized variant significatively improves the results, leading to almost the same results as those obtained with the "detailed" wind velocity distribution.

4.3.2.2. Discrete methodology with representative velocities

The previous methodology used to compute annual concentrations, which was easy to set up, nonetheless has certain weaknesses that mostly concern the choice of the wind velocity for which the concentrations will be calculated, based on the CFD results. Using an intermediate velocity v_i corresponding to the average between the minimal and the maximal value of the velocity range can lead to underestimations of the mean annual concentrations. Indeed, in doing so, it is implicitly assumed that the concentration is constant with the wind velocity in a given wind velocity range. However, the concentration is not constant within a velocity range, especially when this range is large. A function describing the evolution of the concentration depending on the wind speed is therefore needed. As an example, for neutral atmosphere usually assumed in CFD, the concentration evolves hyperbolically with velocity according to equation (Eq. 4.4). The representative velocity over one velocity range, considering the hyperbolic evolution of the concentration, is given in (Eq. 4.11) as a result of (Eq. 4.10) and (Eq. 4.4).

$$\frac{1}{2}\int_{v_{min}}^{v_{max}} c(v).dv = \int_{v_{min}}^{v_r} c(v).dv \qquad \text{(Eq. 4.10)}$$

$$v_r = \sqrt{\frac{2}{\frac{1}{v_{max}^2} + \frac{1}{v_{min}^2}}} \qquad \text{(Eq. 4.11)}$$

where v_{max} and v_{min} are respectively the maximal and the minimal velocities of the velocity range, v_r is the representative velocity of the velocity range and $c(v)$ the equation describing the evolution of the concentration as a function of the wind velocity, i.e. equation (Eq. 4.4).

The representative velocities v_r were calculated with equation (Eq. 4.11) and compared to the intermediate velocities v_i. It is noteworthy that for a velocity range with a minimal velocity of 0 m/s, it is mathematically not possible to compute the representative velocity due to the domain

definition of the function. A choice is therefore required; for the purpose of this study, the same ratio v_r/v_i as for [0.5, 1.5[was considered.

According to the results summarized in Table 4.2 for wind velocities ranging from 0 to 6.5 m/s, the intermediate velocity can be much higher than the representative velocity for low velocities. For example, for wind velocities ranging from 0.5 to 1.5 m/s, the intermediate velocity of 1 m/s is almost twice as high as the representative velocity of 0.67 m/s. For higher velocity ranges, such as [2.5, 3.5[or more, the differences can be neglected. This last statement is true for 1 m/s steps between the minimal and the maximal velocities of the velocity range but can become wrong for higher velocity steps.

Table 4.2 – Comparison between the intermediate velocity v_i and the representative velocity v_r (*: the representative velocity was calculated considering the same ratio v_r/v_i as for [0.5, 1.5[ ).

v_{min} [m/s]	0	0.5	1.5	2.5	3.5	4.5	5.5
v_{max} [m/s]	0.5	1.5	2.5	3.5	4.5	5.5	6.5
v_i [m/s]	0.25	1.00	2.00	3.00	4.00	5.00	6.00
v_r [m/s]	0.1675*	0.67	1.82	2.88	3.90	4.92	5.94
v_r/v_i	0.67*	0.67	0.91	0.96	0.97	0.98	0.99

Figure 4.10 shows a comparison of the mean annual concentrations when using the intermediate velocity and when using the representative velocity, based on the "detailed" 18-velocity-range wind distribution. According to the results, using the intermediate velocity leads to considerable underestimations of the mean annual concentrations compared to the use of the representative velocity. The underestimation is about 20%. When using the discrete methodology presented in Section 4.3.2.1. it is suggested to use the representative velocity instead of the intermediate velocity to better take into account the hyperbolic evolution of the pollutant concentrations with the wind velocity to avoid underestimating the concentrations.
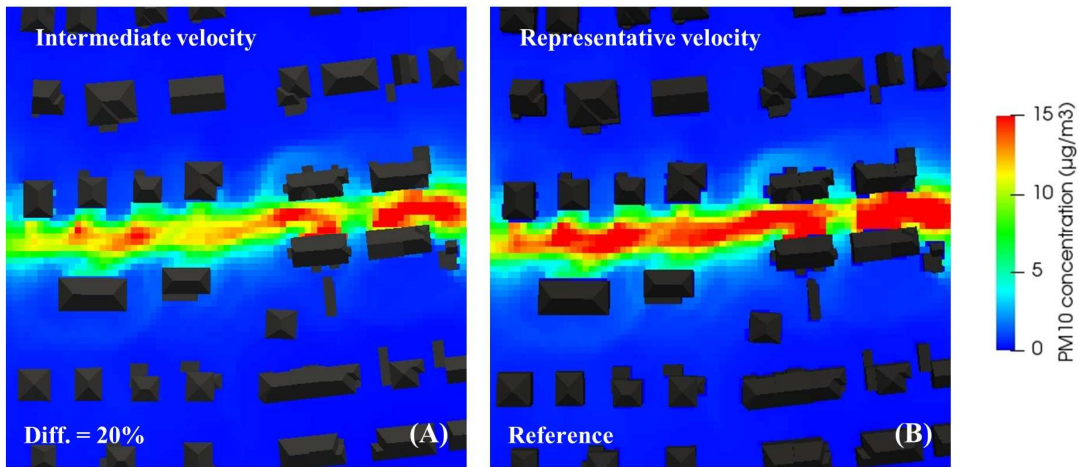
Figure 4.10 – Comparison of the mean annual concentrations based on the "detailed" 18-velocity-range wind distribution using (A) the intermediate velocity and (B) the representative velocity.

Lastly, it should be noted that the representative velocities given previously were calculated with the assumption of equation (Eq. 4.4) applied to equation (Eq. 4.10). If the function describing the evolution of the concentration with the wind speed would change, e.g. for other types of numerical models or atmospheric conditions, equation (Eq. 4.10) would need to be solved again with the new function to have a representative velocity adapted to the conditions and the numerical model considered.

4.3.2.3. Continuous methodology using the sigmoid function

For the last approach, mean annual concentrations based on CFD results can be calculated using a continuous methodology. This methodology is a combination of equation (Eq. 4.4), describing the evolution of pollutant concentration with wind velocity, and equation (Eq. 4.2), describing the evolution of wind velocity frequency with wind velocity. The equation to compute the mean annual concentrations continuously for a given direction is given in (Eq. 4.12). The annual concentration can then be calculated using (Eq. 4.9).

$$\bar{C}_d = \frac{\int_0^{+\infty} c(v).f(v).dv}{\int_0^{+\infty} f(v).dv} + C_{bg} \qquad \text{(Eq. 4.12)}$$

where $\bar{C}_d$ is the mean annual concentration for a given wind direction, $c(v)$ is the function describing the evolution of the concentration with the wind velocity, $f(v)$ is the function describing the evolution of the wind velocity frequency with the wind velocity, and C_{bg} is the background concentration.

Taking equation (4) for $c(v)$ and equation (2) for $f(v)$ leads to a mathematical problem. Indeed, $c(v)$ is not defined for $v = 0$ and the limit of $c(v).f(v)$ tends toward infinity when v tends toward 0. To avoid this problem, equation (Eq. 4.13) is suggested instead of equation (Eq. 4.12). With this equation, it is considered that a minimal velocity (v_{min}) exists for which the pollutant concentration will no longer increase when the wind velocity decreases. This hypothesis can be justified by the additional effects, such as traffic-induced turbulence (Vachon et al., 2002) and atmospheric stability (Qu et al., 2012) that may participate in pollutant dispersion for low wind velocities or become preponderant. We suggest applying a constant pollutant concentration for wind velocities ranging from 0 to v_{min} and suggest using $C_{max} = c(v_{min})$. The choice of v_{min} is particularly important when using the optimized sigmoid function.

$$\bar{C}_d = C_{max}.\frac{\int_0^{v_{min}} f(v).dv}{\int_0^{+\infty} f(v).dv} + \frac{\int_{v_{min}}^{+\infty} c(v).f(v).dv}{\int_0^{+\infty} f(v).dv} + C_{bg} \qquad \text{(Eq. 4.13)}$$

where $\bar{C}_d$ is the mean annual concentration for a given wind direction, C_{max} is the maximal concentration accepted for the calculation, v_{min} is the velocity under which $c(v)$ is considered equal to C_{max}, $f(v)$ is equation (Eq. 4.2), $c(v)$ is equation (Eq. 4.4) and C_{bg} is the background concentration.

Figure 4.11 shows a comparison between the discrete methodology with the representative velocities and the continuous methodology using the optimized sigmoid function. It can be seen that the results of the discrete methodology given in Fig. 10. (A) can be reached by the continuous methodology. Nonetheless, the difference of 5% reached using $v_{min} = 0.01$ m/s can increase when changing the value of v_{min}: lower values will lead to higher concentrations whereas higher values will lead to lower concentrations. The value of v_{min} must therefore be chosen carefully.
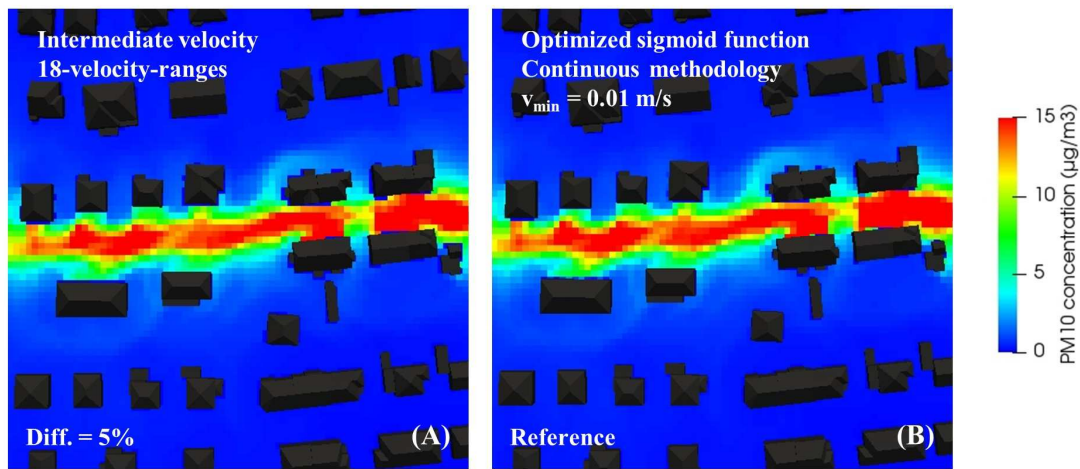
Figure 4.11 – Comparison of the mean annual concentrations (A) based on the "detailed" 18-velocity-range wind distribution and using the intermediate velocity, and (B) based on the optimized sigmoid function and $v_{min} = 0.01$ m/s.

4.4. Discussion

This study provides tools to assess wind velocity distributions based on "basic" data and mean annual air pollutant concentrations based on CFD results. Additional work should be done to improve the methodologies and the major issues are discussed hereafter.

The capability of the Weibull and the sigmoid functions to describe wind velocity distribution was assessed based on wind data from four meteorological stations in France. All of these stations were located in peri-urban environments close to large French cities. It is necessary to take into account that the results, and especially the interpolation-related errors, might be different for other types of stations such as urban and rural stations, and for other countries with different wind characteristics. In particular, the optimization suggested for the sigmoid function may not be suitable for different countries or type of station. Further works are therefore required in this direction.

The mean annual atmospheric pollutant concentrations can be calculated using a discrete methodology as done by Solazzo et al. (2011) or Rivas et al. (2019). However, this methodology has two major problems. The first concerns the choice of wind velocity for which the pollutant concentrations will be calculated: choosing an intermediate velocity is a simple

approach which can lead to considerable underestimations of pollutant concentrations, and it is better to use a representative velocity instead, as suggested in this paper. Using the representative velocity requires, however, making a choice for the first velocity range. The second problem concerns the velocity step used to build the wind velocity ranges: the result depends on the velocity step used, especially for the lower wind velocities for which a decrease in the velocity-step leads to higher mean annual concentrations. To avoid these two problems, a continuous methodology has been developed. This methodology does not have an intrinsic limitation, but dependent on the function describing the evolution of the concentration as a function of wind velocity. If we consider a hyperbolic evolution of the concentration with wind velocity, it is necessary to choose a minimal value of velocity for which it is considered that lower velocities will not increase the concentrations due to compensatory phenomena (traffic-induced turbulence, atmospheric stability, etc.). The value of the minimal velocity is open to discussion and assessing this value is outside the scope of this paper. Further works are required, for example with infield measurement campaigns and comparisons between mean annual concentrations monitored and calculated with the continuous methodology. Lastly, two methodologies therefore exist, a discrete and a continuous with the discrete one being easier to implement in a code. However, we suggest using the continuous methodology if the user can describe the evolution of the concentration with the wind speed using a given piecewise continuous function. The discrete methodology can also be employed but, when an intermediate velocity is used, the user should be aware that the assumption of a constant pollutant concentration within velocity the range is made. To avoid this assumption, the user could consider a representative velocity instead, with as an example a linear evolution of the concentration between the limits of the velocity ranges.

Finally, it should be noted that the methodologies to assess mean annual concentrations were addressed using CFD results implying a neutral case but can be used for any numerical results as long as a function describing the evolution of the concentration with the wind velocity is available.

4.5. Conclusion

The objectives of this study were to provide methodologies; (1) to assess wind velocity distribution based on "basic" data, and (2) to assess mean annual air pollutant concentrations based on numerical results. Three methodologies for each objective were described and compared throughout this paper and the main conclusions are as follows:

(1.a) The Weibull distribution and the sigmoid function can both accurately reproduce "detailed" 18-velocity-range wind distribution based on "basic" 4-velocity-range wind data with an average error of 12%. These functions can nonetheless underestimate the frequencies of low velocities.

(1.b) The optimized sigmoid function improves the wind distribution results over the standard sigmoid function, especially for low wind velocities.

(2.a) Using "basic" 4-velocity-range wind data and the discrete methodology can provide an estimation of the mean annual concentrations but is not sufficient to achieve high precision, leading to a difference of around 19% compared to the use of "detailed" 18-velocity-range wind data. Using the sigmoid function instead, based on the "basic" wind data improves the mean annual concentration results with a global error of less than 4%.

(2.b) When using the discrete methodology to assess mean annual concentrations, it is suggested to use a representative velocity of the function describing the evolution of pollutant concentrations with the wind velocities instead of an intermediate velocity. The intermediate velocity leads to underestimations of mean annual concentrations, especially when using CFD results with a neutral case hypothesis where the concentration evolves hyperbolically with the wind velocity.

(2.c) Mean annual concentrations can be assessed using a continuous methodology that does not have any of the limitations of discrete methodologies. It is, however, limited by the function describing the evolution of the concentrations with the wind velocities, which leads to the need to choose a minimal velocity when using the sigmoid function.

Finally, the methodologies presented in this paper can be used for outdoor air quality study purposes, which is a relevant starting point for improving both outdoor and indoor air quality and, therefore, a key-point to achieve smart sustainable cities. These results give insights to researchers and engineers on how to assess wind velocity distribution and mean annual concentrations for comparison with annual regulatory values given by the EU, the WHO or any other organization, and further works could be done to compare the results of the methodologies with monitored data.

Chapter 5:

Assessment of mean annual NO$_2$ concentration based on a partial dataset

This chapter has been published as an original research paper in the *Atmospheric Environment* journal:

When monitoring air pollutant concentrations, it can be difficult to compare the results of the measurement campaign with annual regulatory standards. Indeed, for nitrogen dioxides (NO$_2$), only partial data can be available (such as some month of data) or only information on nitrogen oxides (NO$_x$) concentrations. This chapter presents methodologies to assess mean annual NO$_2$ concentrations based on partial datasets including (1) methodologies to assess NO$_2$ concentrations from NO$_x$ concentrations and (2) a methodology to assess mean annual NO$_2$ concentrations based on one-month measurement periods. These methodologies were built to be used on sensor measurements in applied purposes but, they can also be applied on numerical results such as CFD results for engineering and research purposes.

The points covered in this chapter are highlighted in Figure 5.1.

---

[1] These authors contributed equally to the paper.

	Input conditions	Pre-processing	Processing	Post-processing	Output
Numerical modelling	Wind speed Wind direction Turbulence Temperature Emissions	Meshing Canopy Interface Model (CIM)	2D / 3D Turbulence model Turbulent Schmidt number Passive transport Buoyancy effects Vegetation	Interpolation over one wind direction Interpolation over the wind rose	Concentrations Mean annual concentrations
Field measurement	NO$_X$ / NO$_2$ PM$_{10}$ / PM$_{2.5}$ Monthly campaign			Analysis Extrapolation	Monthly concentrations Annual concentrations

Figure 5.1 – Main points covered in Chapter 5.

Particularly, the following question is addressed in this chapter:

(?) Is it possible to facilitate engineering studies by using existing or new methods to assess air pollutant concentrations?

(?) As the PSS is not sufficient to calculate NO$_2$ concentrations from NO$_x$ concentrations in France, are there alternatives to avoid increasing calculation costs?

5.1. Introduction

While many measures are implemented to improve air quality, atmospheric pollution still exceeds the thresholds of health standards. Next to particulate matter or ozone, nitrogen dioxide (NO$_2$) has been selected as an air pollutant with the highest priority whose monitoring must be routinely carried out (WHO, 2005). Nitrogen oxides are known to be a source of respiratory symptoms and diseases (Kagawa, 1985), and they are also harmful to the environment as they play the role of precursor in nitric acid production, leading to acid rains (Likens et al., 1979). These air pollutants are mainly due to anthropogenic sources. Indeed Thunis (2018) showed that in several cities in Europe, NO$_x$ is mainly emitted by transport and industrial sources, with varying contributions depending on the city. For example, in dense urban areas such as Paris,

56% of NO_x comes from traffic-related emissions and 18% from the tertiary and residential sectors (AIRPARIF, 2016).

Nitrogen dioxide (NO_2) is, with nitric oxide (NO), one of the two components forming nitrogen oxides. In the European Union (EU) and more generally around the world, NO_2 is the most measured component. Indeed, NO_2 can have significant harmful effects on health, inducing numerous diseases like bronchitis, pneumonias, etc. (Purvis and Ehrlich, 1963), but it can also increase the risks of viral and bacterial infections (Chauhan et al., 1998).

To obtain standard values for the purposes of comparison, the European Union (EU) and the World Health Organization (WHO) have issued critical values that should not be exceeded to protect the public from the health effect of gaseous NO_2. For this purpose, two standard values have been enforced : a hourly mean of 200 $\mu g/m^3$ and an annual mean of 40 $\mu g/m^3$ not to exceed given by both the WHO (WHO, 2017) and the EU (Directive 2008/50/EC). Studies have shown that the annual standard is generally more stringent than the hourly one (Chaloulakou et al., 2008; Jenkin, 2004). However, year-round measurements are needed to gather concentrations values that can be compared directly to this standard. This requirement is not a constraint when monitoring stations are located permanently in one area. Nonetheless, it becomes constraining when the objective is to evaluate urban planning projects over a limited period: the heterogeneity of urban areas requires controls related to the standard at several key locations where no permanent stations have been installed and where only temporary measurements are economically viable. Moreover, these temporary measurements may only provide information on NO_x concentrations but no direct information on NO_2. Thus, one question arises in such situation: how can annual mean NO_2 concentrations be determined using only a short measurement period of NO_2 or NO_x concentrations?

The Leighton relationship provides information on the ratio between NO and NO_2 concentrations as a function of O_3, a chemical constant rate and a photolysis rate considering the photochemical steady state (Leighton, 1961). Unfortunately, it was demonstrated that using this method with more than 10 ppb of O_3 leads to an increasing error by not taking into account VOC chemistry (Sanchez et al., 2016). Different methods were proposed to evaluate the photolysis rate (Wiegand and Bo, 2000), but computing an annual representative photolysis rate can still lead to a wrong evaluation of the seasonal dependencies between NO_x and NO_2.

Numerical computation based on complex chemical mechanisms involving more than 300 reactions with more than 100 species gives more accurate evaluations of NO$_2$ (Bright et al., 2013; Kim et al., 2012). Nevertheless, when NO$_2$ concentration measures are missing there is little chance that this information is known on other species such as VOCs. However, such information is needed in the numerical computations.

Furthermore, seasonal variability of NO$_2$ and NO$_x$ concentrations differs considerably between summer and winter because NO$_2$ concentrations depend on photolysis conditions, and NO$_x$ molecules play a role in several chemical mechanisms in the troposphere, involving ozone (O$_3$) and volatile organic compounds (VOC) (Seinfeld and Pandis, 2016). Robert-Semple et al. showed that there is a relative standard deviation of more than 50% when calculating the mean annual concentrations of both NO$_2$ and NO$_x$ (Roberts–Semple et al., 2012). Moreover, Kendrick et al. showed that there is a seasonal variability in NO$_2$ concentration even with constant hourly seasonal traffic (Kendrick et al., 2015). Thus, these results show that a few months of NO$_2$ monitoring are generally not representative of a mean annual concentration despite existing only slight seasonal variations of the main source, namely traffic-related emissions.

The aim of this study is first to evaluate whether one-parameter methods without any explicit chemical mechanism found in the literature are sufficiently accurate to determine NO$_2$ concentrations based on monitored NO$_x$ data in France. The second aim is to present a method capable of providing the mean annual NO$_2$ concentration from one-month period of monitoring.

5.2. Material and methods

5.2.1. Study location

This work uses NO$_2$ and NO$_x$ concentrations monitored in a large number of regions in France, including from North to South: Hauts-de-France, Grand-Est (Strasbourg region), Ile-de-France (Paris region), Pays de la Loire, Auvergne-Rhône-Alpes and Provence-Alpes-Côte d'Azur. These areas were chosen for the availability of data and to better cover the minimum and maximum latitudes and longitudes of France. The location of these regions is presented in Figure 5.2.
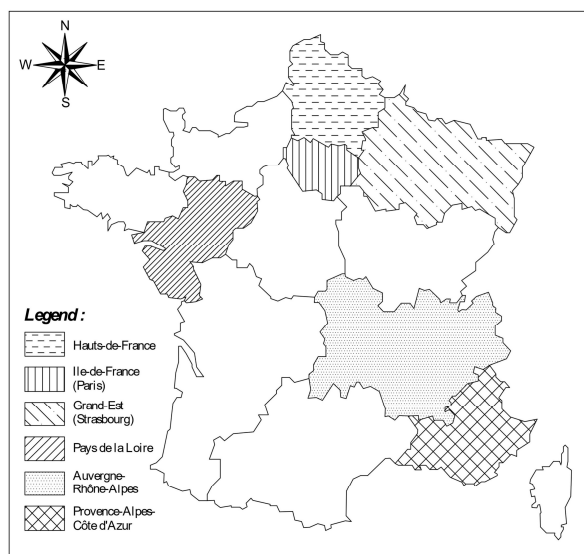
Figure 5.2 – Location of the different study areas used.

5.2.2. Data availability

The data used in this work were obtained via the open access database provided by the different air quality monitoring authorities known as AASQA, the French acronym for "Approved Air Quality Monitoring Associations". In particular, the data were provided by the organizations Atmo Hauts-de-France (Hauts-de-France), Atmo Grand-Est (Strasbourg region), AIRPARIF (Paris region), Air Pays de la Loire (Pays de la Loire), Atmo Auvergne-Rhône-Alpes (Auvergne-Rhône-Alpes), Atmo PACA (Provence-Alpes-Côte d'Azur) and Atmo Nouvelle-Aquitaine (Aquitaine Limousin Poitou-Charentes). The data are mainly mean annual NO_2 and NO_x concentrations over a five-year period from 2013 to 2017, but other data such as hourly measured concentrations for the Strasbourg region in 2018 were also obtained. Additional contacts were also made with AIRPARIF to obtain more specific data for the Paris Region like hourly measured concentrations from 2013 to 2017 with their corresponding uncertainties. A summary of the available data, corresponding to about 270 different sensors, is presented in Table 5.1.

Table 5.1 – Summary of the available data.

Region	Data availability (years)	NO$_x$			NO$_2$			Number of stations
		A	M	H	A	M	H	
Ile-de-France (Paris)	2013 - 2017			•			•	≈ 40
Grand-Est (Strasbourg)	2018			•			•	≈ 50
Hauts-de-France	2013 - 2017	•			•			≈ 15
Pays de la Loire	2013 - 2017	•			•			≈ 50
Auvergne Rhône-Alpes	2013 - 2017	•			•	•		≈ 60
Provence-Alpes-Côte d'Azur	2013 - 2017	•			•	•		≈ 25
Aquitaine Limousin Poitou-Charentes	2013 - 2017	•			•	•		≈ 30

5.2.3. Data range

The annual and monthly concentrations range from 10 to 340 µg/m^3 for NO$_x$ and from 5 to 95 µg/m^3 for NO$_2$, considering the complete dataset (all years, types and locations of stations included). According to these wide ranges, different types of stations were considered in this work including rural, suburban, urban and traffic stations. The dataset for the Paris region comprises 2% rural, 13% suburban, 54% urban and 31% traffic stations. The type of station was not always directly provided in the global France dataset. Thus, the percentage of each type of station was estimated based on the range of concentrations for each type of station in Paris. The corresponding results were 29%, 22%, 31% and 18% for rural, suburban, urban and traffic stations, respectively.

5.2.4. Monitoring method

The EU imposes a maximal uncertainty of 15% on AASQA for individual measurements averaged over the period considered regarding the limit values monitored by sensors. Thus, to satisfy the requirements, all AASQA use the same monitoring method in accordance with this constraint.

The reference method used for the measurement of nitrogen dioxide and oxides of nitrogen is known as chemiluminescence. Two chemiluminescence methods exist: on the one hand, chemiluminescence based on luminol reaction, and, on the other hand, chemiluminescence based on NO/O$_3$ reaction. The second method is the one used in France. In particular

AIRPARIF uses the AC32M EN model from ENVE and the 42i model from THERMO SCIENTIFIC.

The principle of the method was well-described by Navas et al. (1997) and is based on a reaction between NO and O_3 (Eq. 5.1). This reaction produces an excited nitrogen dioxide (NO_2^*) that emits infrared radiations when returning to a stable state (Eq. 5.2). The luminous radiation emitted and then measured is directly proportional to the NO concentration.

$$NO + O_3 \rightarrow NO_2^* + O_2 \hspace{4cm} \text{(Eq. 5.1)}$$

$$NO_2^* \rightarrow NO_2 + h\nu \hspace{4cm} \text{(Eq. 5.2)}$$

To obtain information on the NO_x concentration, it is first necessary to convert all the NO_2 into NO before the measurement. After that, the resulting NO corresponding to the initial NO and the NO derived from NO_2 are measured and the NO_x concentration is obtained. Combining both the measured NO and NO_x concentrations provides the NO_2 concentration. Thus, the uncertainties on NO_2 measurement are higher than those on NO or NO_x because the results are obtained from both NO and NO_x measurements.

Based on the work of Navas et al., this kind of technique has very low detection limits, making it a good tool for evaluating the concentration of nitrogen compounds for atmospheric purposes (Navas et al., 1997). According to a personal communication with AIRPARIF, the maximal uncertainty on the mean annual NO_2 concentration from 2015 to 2017 was lower than 10% with a mean uncertainty of 6%.

5.2.5. Empirical methods to convert concentration from NO_x to NO_2

Several one-parametric empirical methods can be found in the literature to give an estimation of NO_2 concentration based on NO_x concentration. Three methods were compared with the entire France dataset:

- Derwent and Middleton function, a polynomial-logarithmic function linking hourly averaged NO_x and NO_2 concentrations for NO_x concentrations in the range of 9.0 to 1145.1 ppb (Derwent and Middleton, 1996).

- Romberg et al. function, a rational function linking annual averaged NO$_x$ and NO$_2$ (Romberg et al., 1996).
- Bächlin et al., another rational function linking annual averaged NO$_x$ and NO$_x$ (Bächlin et al., 2008).

According to the above authors, the corresponding equations are (Eq. 5.3), (Eq. 5.4) and (Eq. 5.5) respectively, with the hourly averaged NO$_x$ and NO$_2$ concentrations noted $[NO_x]_h$ and $[NO_2]_h$ and annual averaged NO$_x$ and NO$_2$ for the two other functions noted $[NO_x]_a$ and $[NO_2]_a$. All concentrations presented below are in µg/m^3 and $A = log_{10}([NO_x]_h/1.91)$.

$$[NO_2]_h = \left(2.166 - \frac{[NO_x]_h}{1.91}(1.236 - 3.348A + 1.933A^2 - 0.326A^3) \right) \times 1.91 \qquad \text{(Eq. 5.3)}$$

$$[NO_2] = \frac{103.[NO_x]_a}{[NO_x]_a + 130} + 0.005 \times [NO_x]_a \qquad \text{(Eq. 5.4)}$$

$$[NO_2] = \frac{29.[NO_x]_a}{[NO_x]_a + 35} + 0.217 \times [NO_x]_a \qquad \text{(Eq. 5.5)}$$

For the purpose of this work, mean annual concentrations were used instead of hourly averaged concentrations for the Derwent and Middleton function.

5.3. Results

5.3.1. Evaluation of annual NO$_2$ concentration based on NO$_x$ data

5.3.1.1. Best fitting function in France

Figure 5.3 shows the evolution of mean annual NO$_2$ concentration as a function of the mean annual NO$_x$ concentration considering the total dataset (measurements from 2013 to 2017 for the six regions considered and all types of station included). The three empirical methods cited previously are also plotted.
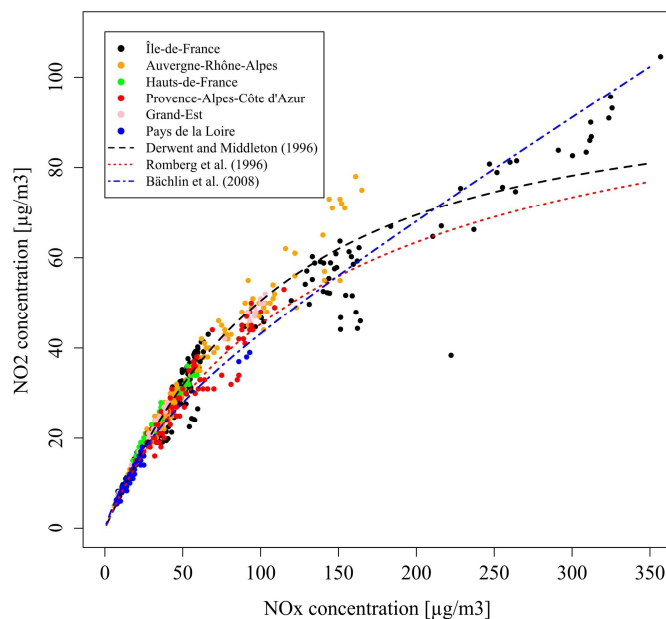
Figure 5.3 – Evolution of NO_2 concentration as a function of NO_x concentration and comparison with empirical functions.

To obtain a better comparison between the three functions, predicted NO_2 concentrations calculated with measured NO_x concentrations were plotted against measured NO_2 concentrations. The corresponding results are presented in Figure 5.4 with the first bisector corresponding to ideal results. As shown in Figure 5.4 (C), the function from Bächlin et al. is the most appropriate for high NO_2, thus high NO_x concentrations. However, based on Figure 5.4 (A) and Figure 5.4 (B) the results for lower NO_2 concentrations (less than 50 µg/m^3) are better when using the function proposed by Derwent and Middleton, and Romberg et al. Considering the difference between the predicted and measured concentrations, the function of Derwent and Middleton is the most appropriate with a deviation of less than 8%, whereas that of Romberg et al. leads to a deviation of 9.5%. Moreover, in this work, the function of Romberg et al. tends to slightly underpredict NO_2 concentrations. When choosing between two functions giving about the same deviation, the precautionary approach is to choose the function that overestimates NO_2 rather than the one which underestimates it. Hence, in France, Derwent and Middleton's function has been chosen and is advised by the authors to assess the NO_2 concentrations based on NO_x data. This is especially the case for the monitoring both in urban and rural sites. It should also be noted that these comparisons included several years of measurements and locations (various latitudes and longitudes), thus in principle giving

independence to these parameters. However, for high NO_2 concentrations (higher than 70 $\mu g/m^3$) the method fits less and less well.
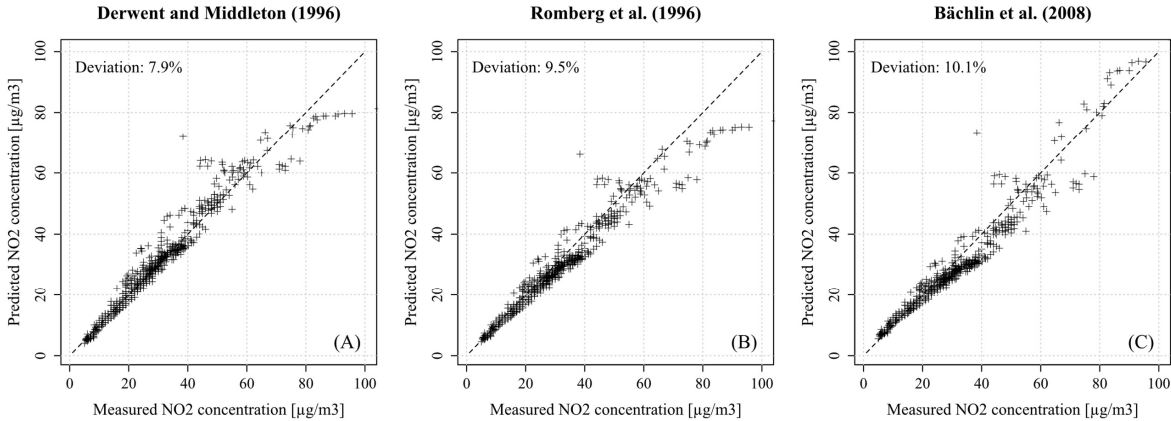
Figure 5.4 – Comparison between predicted and measured NO_2 concentrations for (A) the Derwent and Middleton function, (B) the Romberg et al. function, and (C) the Bächlin et al. function.

5.3.1.2. Application to Paris region

The information obtained in the Paris region was more detailed and included uncertainties as well as the type of station. Figure 5.5 presents the mean annual NO_2 concentration for the Paris region dataset as a function of NO_x concentration with a distinction between the different types of station. Derwent and Middleton's function is also plotted.
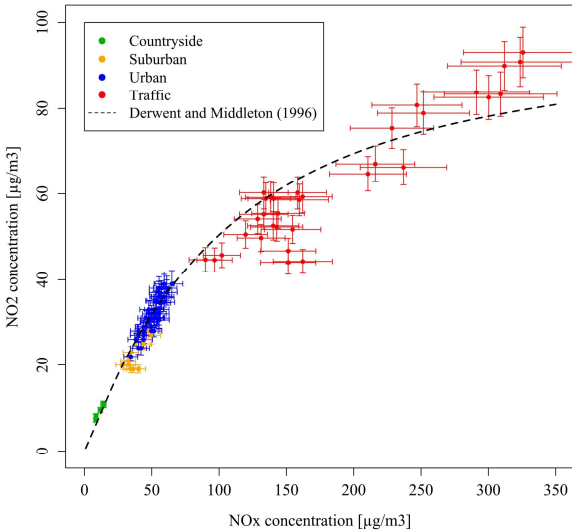
Figure 5.5 – Evolution of NO_2 concentration as a function of NO_x concentration for the Paris region dataset and comparison with Derwent and Middleton's function.

These results show that in accordance with previous observations, the best range of application for Derwent and Middleton's function is for NO_x concentrations lower than 80 µg/m^3. As can be seen in Figure 5.5. this limit corresponds to the difference between urban and traffic stations for Parisian region. Thus, Derwent and Middleton's method applies best for rural, suburban and urban stations whereas the results are less accurate for traffic. Indeed, there are 92% of the data that are within the uncertainties range both in the countryside and in urban areas, while for traffic data it falls to 71%. The mean error on predicted NO_2 concentrations is 9% with a 95th percentile of 27%.

5.3.2. Seasonal variability of NO_2 concentration

The seasonal variability of NO_2 was studied using the Paris region dataset. Hourly NO_2 concentrations were averaged for each station and each year of data, giving five mean concentrations per station and per year (one annual concentration and four seasonal concentrations). Figure 5.6 (A) shows the differences between seasonal mean NO_x concentrations for each couple of year and station. Figure 5.6 (B) shows the evolution of seasonal NO_2 concentrations as a function of the annual NO_2 concentration for the same year of measurement.
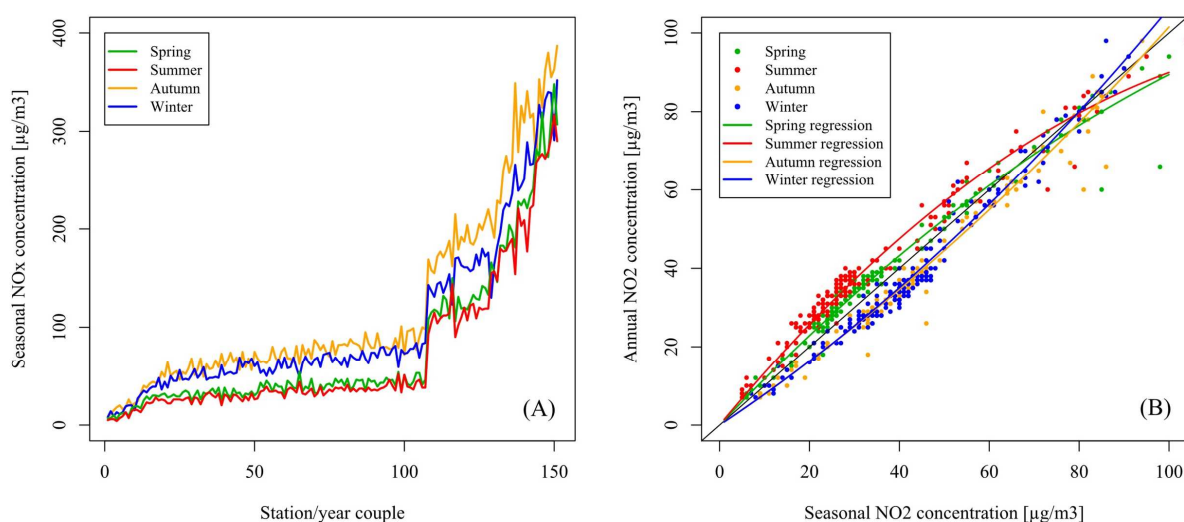
Figure 5.6 – Comparison between seasonal NO_x concentrations for a given station and year of measurement in the Paris region (A) and the evolution of the annual NO2 concentration as a function of seasonal NO2 concentrations (B).

According to Figure 5.6 (A), NO$_x$ concentrations are strongly dependent on the season. Indeed, although summer and spring NO$_x$ concentrations are similar, the concentrations are higher in winter and autumn by up to a factor of 2. These differences can be explained by several disparities between these seasons: lower boundary layer height, lower temperatures and new sources of emission due to residential heating, increased emissions by cold-started vehicles, etc.

Since the results show that NO$_x$ concentrations are higher in winter and autumn, for a given NO$_x$ concentration the seasonal NO$_2$ concentrations should also be higher in autumn and winter than in summer and spring. However, the results for the Paris region show a different trend. The result in Figure 5.6 (B) indicates a change of behavior when the annual NO$_2$ concentration increases, with the summer and spring NO$_2$ concentrations becoming higher than in autumn and winter. These results can be associated with those of other authors. Indeed, Kendrick et al. showed that NO$_2$ concentrations are higher in winter and autumn than in spring and summer, with a mean annual NO$_2$ concentration lower than 80 µg/m^3 and for three different types of station (Kendrick et al., 2015). On the contrary, Mavroidis and Ilia showed that for a traffic station (i.e. giving high NO$_2$ concentrations), NO$_2$ concentrations are generally higher during the summer and spring months than in autumn and winter, with in their case a mean annual NO$_2$ concentration higher than 80 µg/m^3 (Mavroidis and Ilia, 2012). Thus, the evolution of seasonal NO$_2$ concentrations as a function of annual NO$_2$ concentration is not well represented by a linear method unable to catch these varying trends and is much better fitted by a quadratic one. With this interpolation, the spring and summer results are described by a concave quadratic function whereas the autumn and winter ones are described by a convex quadratic function. In this case, these concavities and convexities result in a NO$_2$ concentration of about 80 µg/m^3, where the seasonal NO$_2$ concentrations are equal to the annual NO$_2$ concentration. This concentration of 80 µg/m^3 corresponds to the value for which, in the case of a measurement station giving an annual average NO$_2$ concentration lower than this value, the concentrations for winter and autumn are higher than the spring and summer concentrations. Therefore, to obtain maximized measurements in order to assess an upper limit on annual NO$_2$ concentration over a short period of time, the measurements should be carried out in winter, in case where an annual concentration of less than 80 µg/m3 is expected, otherwise measurements should be carried out in summer.

These observations are consistent with those of other research papers, despite being counter intuitive on the first point of view. Indeed, a previous observation was that NO_x concentrations are higher during autumn and winter, in theory giving higher NO_2 concentrations. Moreover, in summer and spring, the zenithal angles are generally lower, leading to increased photochemistry with higher photolysis, including NO_2 photolysis, and the production of radicals. As shown in Figure 5.7 (A), O_3 concentrations are globally much lower in autumn than in winter, and in winter than in spring and summer. These concentrations are about the same between spring and summer. Figure 5.7 (B) gives supplementary information on how much ozone is available to react with NO_2, by giving the evolution of the ratio of the seasonal O_3 concentration over the seasonal NO_2 concentration as a function of the seasonal NO_2 concentration.

The first observation is that more O_3 molecules are available in spring and summer than in winter and autumn for any NO_2 concentration. This statement is always true even when the seasonal NO_2 concentration increases, leading to a systemic reduction of available O_3. For example, for a seasonal NO_2 concentration of 15 µg/m3, the ratio of seasonal O_3 concentration over seasonal NO_2 concentration is around 3 for autumn, 4 for winter and almost 5 for spring and summer. Increasing the seasonal NO_2 concentration to 30 µg/m^3 gives ratios of 1 and 1.5 for autumn and winter respectively and almost 2 for both spring and summer. The explanation of why the seasonal NO_2 concentration is higher in spring and summer than in winter and autumn for high NO_2 concentrations can be obtained from these two observations. For low NO_2 concentrations, O_3 is readily available and the reaction is not limited by the O_3 concentration but by several other factors that lead to the commonly accepted result: NO_2 concentrations are higher in winter and autumn than in spring and summer. However, when the NO_2 concentration increases, O_3 becomes less and less available until reaching a state in which it becomes the limiting reagent of the production reaction of NO_2 from NO_x. This state is reached earlier in winter and autumn than in spring and summer, leading to a higher NO_2 concentration in summer and spring than in autumn and winter.
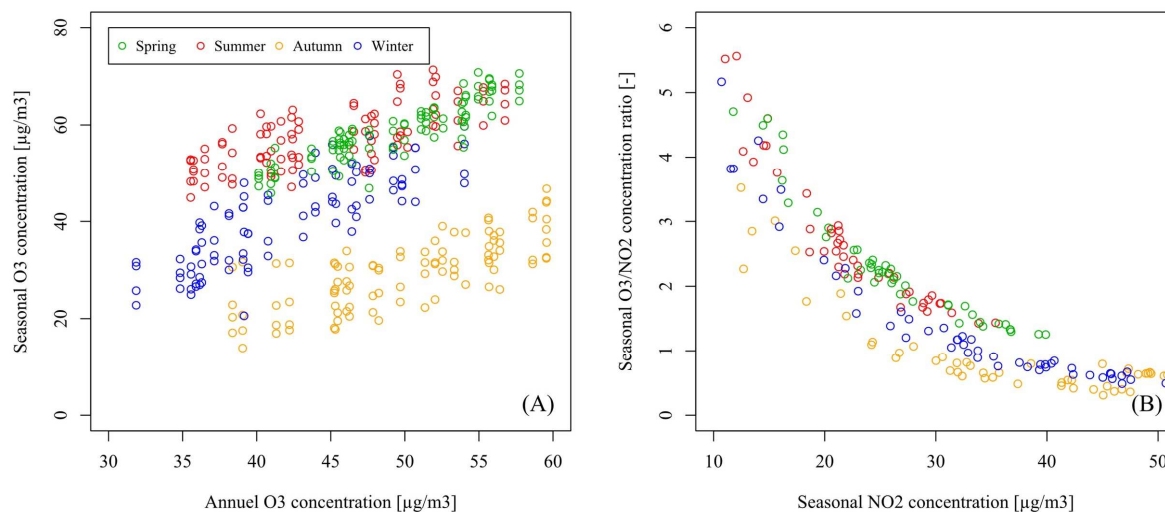
Figure 5.7 – Evolution of the seasonal O$_3$ concentration as a function of the annual O$_3$ concentration (A) in the Paris region and the evolution of the ratio between seasonal O$_3$ and NO$_2$ concentrations as a function seasonal NO$_2$ concentrations (B).

5.3.3. Assessment of annual NO$_2$ concentration

5.3.3.1. Assessment of annual NO$_2$ concentration from monthly NO$_2$ concentration

As mentioned above with regards to seasonal variability, seasonal concentrations cannot be used directly as an annual concentration. However, they seem to fit a trend and it may be possible to assess the annual mean concentration from a short period of measurement.

The NO$_2$ concentrations over the Paris region were first averaged for each month and then compared with annual NO$_2$ concentrations. The results, presented with black circles in Figure 5.8, show that, like seasonal NO$_2$ concentrations, monthly averaged NO$_2$ concentrations as a function of annual NO$_2$ concentrations seem to be better fitted by a quadric function than by a linear function. These fittings are also presented with black lines in Figure 5.8. as well as the polynomial interpolation coefficients, and the mean error between measured data and interpolation, also in black. The polynomial equation corresponds to (Eq. 5.6) with $[NO_2]_a$ and $[NO_2]_m$ being the annual mean NO$_2$ concentration and the monthly averaged NO$_2$ concentration respectively in µg/m^3, and a and b the different polynomial coefficients for each month.

$$[NO_2]_a = a.[NO_2]_m{}^2 + b.[NO_2]_m \qquad \text{(Eq. 5.6)}$$

The polynomial methods obtained have different concavities and convexities, consistent with those obtained for seasonal variability. The maximum convexity is obtained around December and January, corresponding to the transition from autumn to winter. The maximum concavity is obtained around June and July, corresponding to the transition from spring to summer. Lastly, minimal concavity and convexity is obtained around March and September, corresponding to the transition from winter to spring and from summer to autumn, respectively. For these months, monthly averaged NO_2 concentrations are almost equal to annual NO_2 concentrations. According to these polynomial methods, the maximal mean error is around 15% and corresponds to December, and the minimal mean error is around 7% and corresponds to March. The mean error averaged over all months is below 10%.

These polynomial methods can be used to assess the annual NO_2 concentration based on only one month of measurements. However, the problem is that measurements from the first day to the last day of a month are required. If one month of data is acquired that overlaps two distinct months, say from 15th January to 15th February, the interpolation is no longer appropriate. An additional study was carried out to change from discrete to continuous interpolation. To achieve this, the resulting polynomial coefficients a and b were plotted as a function of the month with 1 corresponding to January and 12 to December. Figure 5.9 shows the corresponding results.

As shown in Figure 5.9, both coefficients a and b seem to follow a cyclic trend. However, the evolution of the coefficients is inversed with a minimal value of a around June, corresponding to a maximal value of b. On the contrary, the maximal value of a is reached around January, corresponding to a minimal value of b. Considering the trends of a and b observed, a Gaussian function was used to obtain continuous values bringing two new coefficients, α and β, respectively, corresponding to the coefficients obtained from the continuous method. The corresponding equations for α and β are (Eq. 5.7) and (Eq. 5.8), respectively, with m being the month corresponding to the available data (e.g. $m = 1$ for the data from the first to the last day of January, $m = 3.5$ for the data from the middle of March to the middle of April, etc.).

$$\alpha = 0.0033 - 0.0102 . \exp\left[\frac{-(m - 6.5749)^2}{8.6962}\right] \qquad \text{(Eq. 5.7)}$$

$$\beta = 0.6945 + 0.8708. \exp\left[\frac{-(m - 6.7076)^2}{7.4328}\right] \qquad \text{(Eq. 5.8)}$$

The new curves obtained for each month with (Eq. 5.6), and the calculated α and β corresponding to a and b respectively, are presented in red dashed lines in Figure 5.8, in addition to the corresponding values of α and β, R2 and the mean error (ME) compared to the Paris data. When comparing these new curves with the previous ones obtained with a and b, they are globally the same except for May and November, for which the curves start to deviate from each other for high monthly NO$_2$ concentrations. Nonetheless, the mean error for these two months is still acceptable, with in both cases a mean error of less than 10%. The mean errors for each month are approximatively equal between both cases and give an overall error of 10% and a maximal error of 16% in December.
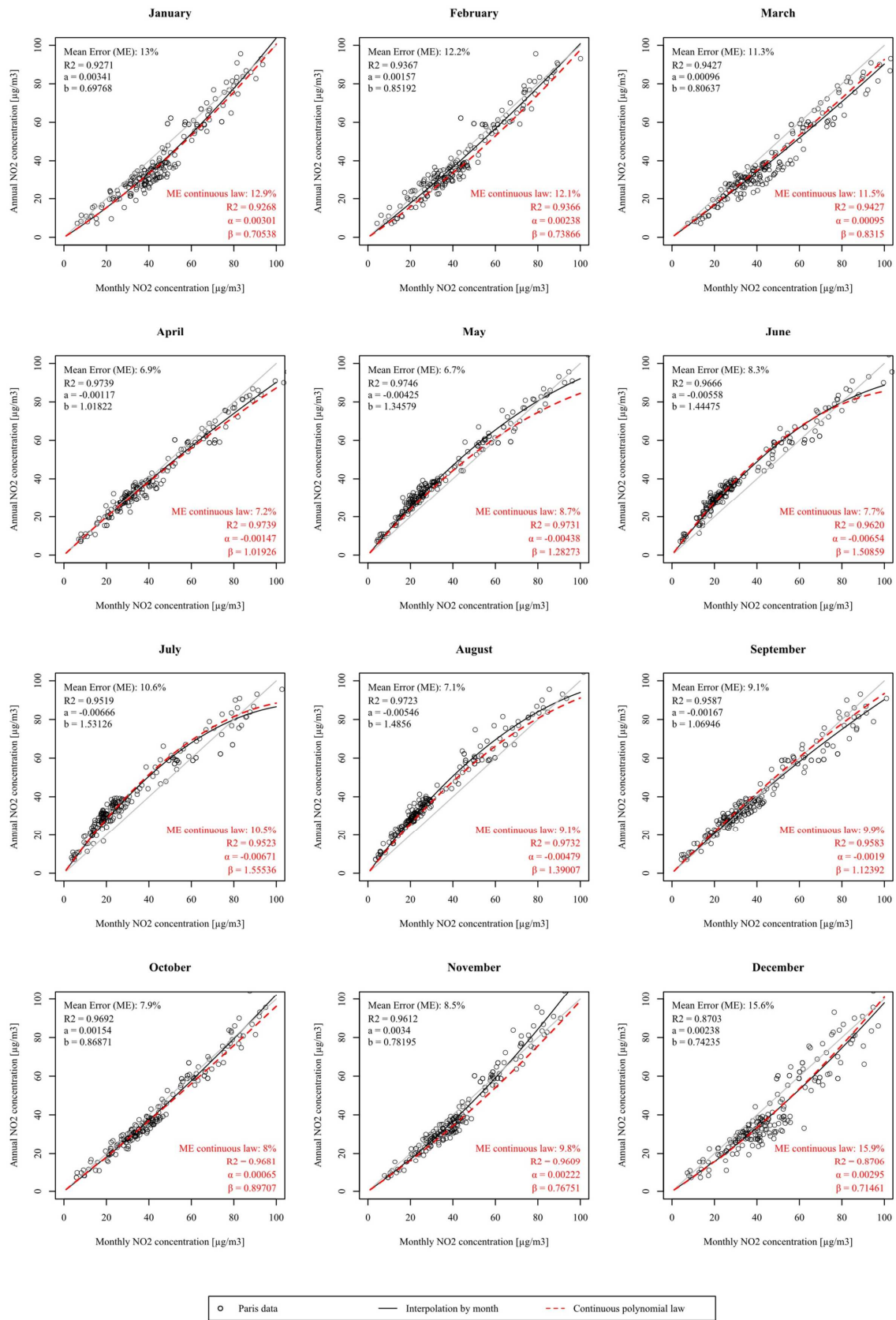
Figure 5.8 – Interpolation of annual NO$_2$ concentration as a function of monthly NO2 concentration.
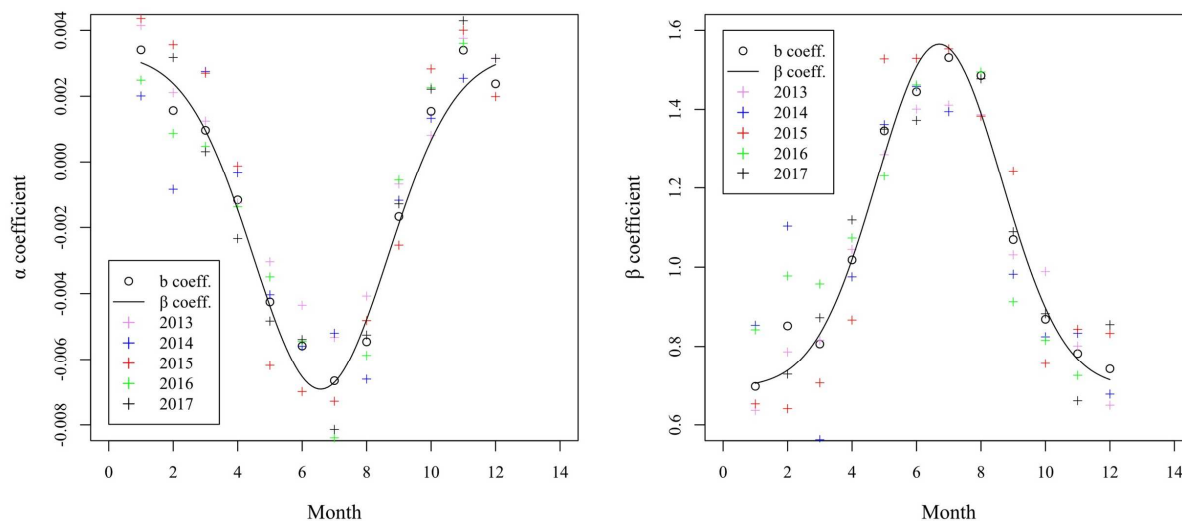
Figure 5.9 – Interpolation of *a* and *b* coefficients (for each year considered and the subsequent mean) and resulting continuous *α* and *β* coefficients.

Table 5.2 – Global results of the polynomial discrete method over regions in southern France and improvements compared to the direct utilization of monthly concentrations as annual concentrations.

Region	Year	Number of stations with a full year of data	Annual mean direct error (%)	Annual mean discrete method error (%)	Improvement between direct and discrete method error (%)	Mean annual direct error (%)	Mean annual discrete method error (%)	Mean improvement (%)
Aquitaine Limousin Poitou-Charentes	2013	31	29	17	41			
	2014	29	27	15	46			
	2015	29	32	17	46	30	17	43
	2016	35	28	16	44			
	2017	29	32	19	42			
Auvergne-Rhône-Alpes	2013	50	29	18	39			
	2014	65	29	17	41			
	2015	58	30	18	39	30	18	40
	2016	68	30	20	35			
	2017	57	30	19	38			
Provence-Alpes-Côte d'Azur	2013	21	19	14	27			
	2014	22	19	12	38			
	2015	29	19	13	29	19	13	31
	2016	27	20	14	26			
	2017	27	18	12	31			

In view to assessing the reliability of the equations, the polynomial methods were applied to several regions of France, including Aquitaine Limousin Poitou-Charentes, Auvergne-Rhône-Alpes and Provence-Alpes-Côte d'Azur from 2013 to 2017. For each month of these years, the mean annual NO_2 concentrations were calculated based on each month of data. The discrete polynomial methods were used here because the information was available for each month. The calculated annual concentrations were then compared to the measured concentrations and a mean error was obtained. The mean errors are summarized in Table 5.2. This table also gives information on the error obtained when the monthly NO_2 concentration is taken directly as an annual NO_2 concentration (called direct approach), and on the improvements between this direct approach and the approach using the suggested methods. For the three regions considered, the mean error using the discrete method is higher than for the Paris region, ranging from 12% to 20%. The errors obtained when using the direct approach range from 18% to 32%. The improvement between the two approaches depends on the regions considered and ranges from 26% to 46% with an overall improvement of 38%. According to these results, the method presented in this paper is reliable and can be used outside the Paris region in France. Overall, this simple applicable polynomial method improves the results in comparison to a direct approach by up to a factor two.

5.3.3.2. Assessment of annual NO_2 concentration from monthly NO_x concentrations

The final study was performed to give an estimation of the total error when calculating annual NO_2 concentration using monthly measured NO_x data. To manage this, data for the Paris region for the year 2017 were used. Firstly, the monthly NO_2 concentrations were calculated based on monthly NO_x concentrations measurements using the Derwent and Middleton function (Eq. 5.3). Then, annual NO_2 concentrations were calculated using (Eq. 5.6), (Eq. 5.7) and (Eq. 5.8).

Ile-de-France 2013-2017 (input data : NO2)   **Ile-de-France 2017 (input data : NOx)**
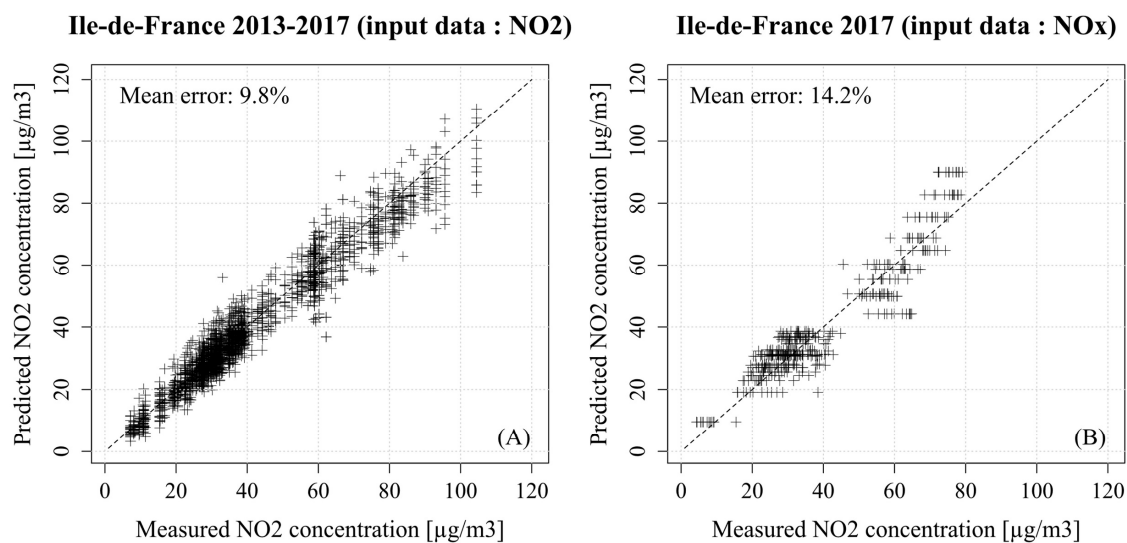
Figure 5.10 – Comparison between calculated and measured annual NO$_2$ concentrations for the Paris region from 2013 to 2017 (A) and for the Paris region based on monthly 2017 NO$_x$ concentrations (B).

The resulting annual NO$_2$ concentrations were plotted against measured annual NO$_2$ concentrations and are presented in Figure 5.10 (B). The previous results for Paris from 2013 to 2017 and for which the calculated annual NO$_2$ concentrations are based on monitored monthly NO$_2$ concentrations are also provided in Figure 5.10 (A). According to Figure 5.10 (A), a global error of 10% for Paris region is obtained and it can also be seen that the maximal errors occur for the highest NO$_2$ concentrations. The same observation can be made when comparing this result with those for Paris assessed with the monthly NO$_x$ concentrations for 2017. The global error in this case increases but does not exceed 15%.

5.4. Discussion

The seasonal variability of NO$_2$ concentrations was shown and leads to higher or lower seasonal NO$_2$ concentrations compared to annual NO$_2$ concentrations. An explanation for these observations was proposed and seems to be linked to the seasonal variability of ozone concentrations as well as the seasonal variability of available ozone to react with NO$_2$. However, this link must be quantified to better explain the phenomenon and evaluate if these observations can be fully generalized. The first hypothesis is that this phenomenon may only be generalizable to countries whose seasonal variability in ozone concentrations are like those

observed in France. Thus, in countries having other types of seasons like Indonesia, with only a dry and a monsoon season or India, with winter, summer, monsoon and post-monsoon seasons, the results would be very different, and the equations presented in this paper may not be relevant. However, it may be possible to apply the methodology and adapt the coefficients of the equations to obtain good results in these countries. Nevertheless, this would require long periods of measurements.

It should also be noted that for some specific periods, monthly NO_2 concentrations are representative of annual NO_2 concentrations. Indeed, averaging monthly concentrations measured in March, April, September or October could give good estimations of the mean annual concentrations directly. For these months, it might not be necessary to use the previous methodology to assess the annual NO_2 concentration.

Lastly, the different equations obtained that could be used to assess annual NO_2 concentrations, were built for and applied to regions having around the same latitudes, from 43° to 50°. For a very different latitude, the coefficients of the equations might not be optimized, and greater errors could occur.

5.5. Conclusion

The assessment of annual NO_2 concentrations with partial data was studied from two main approaches. The first one was to determine the annual mean NO_2 concentration with only annual mean NO_x concentration information. The second was to determine the annual mean NO_2 concentration with only a one-month period measurement. The main conclusions are as follows:

(a) Three functions giving annual NO_2 concentrations based on NO_x data were compared. These functions correspond to the methods of Derwent and Middleton, Romberg et al., and Bächlin et al. The results show that the method proposed by Derwent and Middleton is the better suited to assess the annual NO_2 concentration based on NO_x concentrations for several regions of France and for several years both for rural and urban areas in particular. However, this method has some limitations for high NO_x concentrations and gives less accurate results for traffic stations with annual NO_x

concentrations higher than 70 µg/m^3. The global error of this method for the regions of France considered is around 8%.

(b) NO$_2$ concentrations are seasonally variable and depend on the concentrations of NO$_x$ and their ratio with VOC concentrations, and on the photochemistry conditions. Hence, making it impossible to give an annual concentration directly from a seasonal concentration: for annual NO$_2$ concentrations lower than 80 µg/m^3, summer and spring NO$_2$ concentrations are lower than autumn and winter concentrations; for higher annual NO$_2$ concentrations, it is the summer and the spring NO$_2$ concentrations that become higher than the autumn and winter concentrations. Thus, to evaluate an upper limit on annual NO$_2$ concentration over a short period of time, measurements should be done in winter if an annual concentration of less than 80 µg/m3 is expected, otherwise they should be carried out in summer

(c) Monthly NO$_2$ concentrations follow the same variability trends as the seasonal concentrations which were quantified for each month. A discrete function was proposed to assess annual NO$_2$ concentrations based on monthly NO$_2$ concentrations, yielding a global error of 10% for the Paris region. The corresponding function was made continuous using two Gaussian methods to facilitate its use, leading also to a global error of 10% for the Paris region. The discrete methods applied to the southern regions of France yielded an overall error of 15% and provided an improvement ranging from 26% to 46% compared to the utilization of the direct approach.

(d) Using both the Derwent and Middleton method and the quadratic equations method both presented in this work it is possible to assess annual NO$_2$ concentrations from monthly NO$_x$ concentrations measurements. Those methods led to an overall error of 15% for the Paris region for the year 2017.

All the results and observations discussed in this paper concern NO$_x$ and NO$_2$ concentrations and it was shown that interesting results can be obtained to reduce measurement periods and estimate NO$_2$ concentrations from NO$_x$ data without introducing any chemical considerations. This methodology could be extended to other pollutants like particulate matter, which even if not highly chemically active, are subject to specific phenomena like deposition, resuspensions, etc.

SECOND PART:

APPLICATIONS FOR URBAN PLANNING: DESIGN, UNDERSTANDING, DIAGNOSIS AND OPTIMIZATION

Chapter 6:

Design – CFD evaluation of mean pollutant concentration variations in step-down street canyons

Abstract

This chapter has been published as an original research paper in the *Journal of Wind Engineering and Industrial Aerodynamics*:

Reiminger, N., Vazquez, J., Blond, N., Dufresne, M., Wertel, J., 2020. CFD evaluation of mean pollutant concentration variations in step-down street canyons. *Journal of Wind Engineering and Industrial Aerodynamics* 196, 104032. DOI: 10.1016/j.jweia.2019.104032

Numerical models can be used for practical purposes to study the evolution of air pollutant concentrations for various scenarios such as traffic evolution, built environment evolution, etc. This chapter shows how a computational fluid dynamics software can be used for building design purposes to limit pollutant concentrations in urban areas. In particular, the evolution of pollutant concentrations in step-down street canyons as a function of the building characteristic lengths (building height and the distance between the buildings) is studied, and constructive recommendations are given.

The points covered in this chapter are highlighted in Figure 6.1.
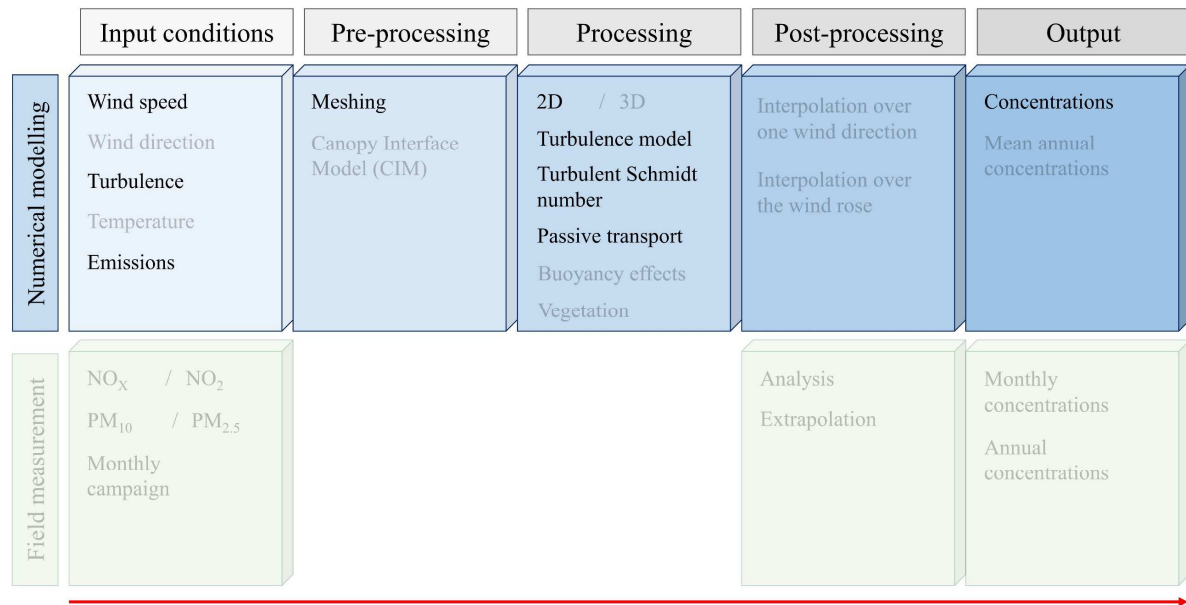
Figure 6.1 – Main points covered in Chapter 6.

Particularly, the following question is addressed:

⌾ How can a CFD-RANS model be used for engineering purposes?

6.1. Introduction

Air quality has become a major concern, especially in urban areas where air pollutant sources are numerous and population density is high. Air quality is influenced by traffic-related emissions and the local atmospheric environment which is highly dependent on street geometry. Indeed, narrow streets surrounded by high buildings are more often subject to high pollutant concentrations than wide streets with lower building heights, due to poorer ventilation. An estimation of pollutant concentrations in streets depending on building configurations could help urban planners to understand the impacts of street geometry on air quality and provide keys to making suitable choices to lessening air pollution levels, as one of the key point discussed by Bibri and Krogstie (2017) in order to achieve smart sustainable cities of the future.

The effects of street geometry on pollutant dispersion have already been studied extensively with both experimental (Gerdes and Olivari, 1999; Hotchkiss and Harlow, 1973; Pavageau and Schatzmann, 1999; Vardoulakis et al., 2003) and numerical methods (Aristodemou et al., 2018; Bijad et al., 2016; Santiago and Martin, 2005; Tominaga and Stathopoulos, 2017; Vardoulakis et al., 2003) and also at full-scale with in situ measurements (Qin and Kot, 1993; Vardoulakis et al., 2002). Some authors have even studied the effects of roof shape on pollutant dispersion (Takano and Moonen, 2013; Wen and Malki-Epshtein, 2018). However, most of these works were conducted in symmetrical street canyons using buildings with the same height. Indeed, streets surrounded by buildings of the same height do exist although streets with different building heights, so-called asymmetrical street canyons, are found more often. Addepalli and Pardyjak (2015) studied cases of step-down street canyons with a taller building on the leeward side and showed that there are significant modifications of flow patterns depending on building height and street width ratios. Xiaomin et al. (2006) performed a similar work with different kinds of streets, including deep and wide symmetrical streets and step-up and step-down asymmetrical streets, and showed that there are three major types of regimes in street canyons depending on height and width ratios, especially in the case of step-down street canyons. In spite of the several studies already done, and although there is a need for urban planners and decision makers, quantitative information on how concentrations evolve with the modification of street geometry is still lacking. Thus, further work is required in this direction.

The aim of this work is to provide information on how mean pollutant concentrations quantitatively evolve in a step-down street canyons. More specifically, it is to assess the evolution of concentration in the street according to two specific ratios: the ratio of the leeward building height to the windward building height ($H1/H2$), and the ratio of the street width to the windward building height ($W/H2$). This assessment is carried out using computational fluid dynamics (CFD) simulations.

6.2. Numerical model

6.2.1. Computational domain and boundary conditions

Figure 6.2 shows the computational domain of the street canyon, the dimensions of interest, the localization of the different boundary conditions and the emission source as well as the domain size.
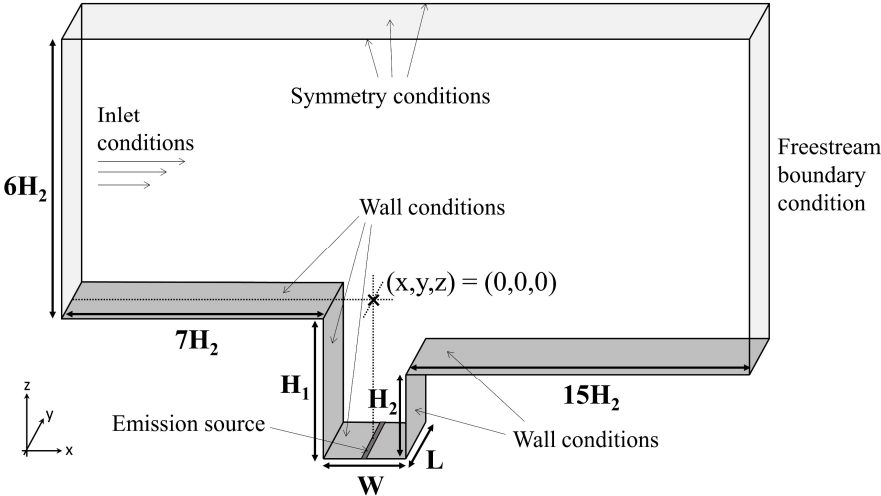
Figure 6.2 – Sketch of the computational domain

In this study, $H1$ corresponds to the height of the leeward building, $H2$ corresponds to the height of the windward building, W corresponds to the width between the two buildings and L corresponds to the length of the street. Here, we study the case of long canyons ($L/W > 7$) (Vardoulakis et al., 2003) with the assumption that the interactions in the y-direction are negligible. To ensure this assumption a 3D simulation was computed for this study, and the results were compared to 2D results. Using a street canyon with $L/W = 10$, it was found that the differences between 2D and 3D simulation are fewer than 8% for $|y| \leq 3H$ with $y = 0H$ the center plane of the street. For $3H < L/W < 5H$, differences are still acceptable but can reach 20% (more details can be found in Appendix F). According to this results, all simulations were done in 2D in order to reduce calculation costs.

We followed the recommendations given by Franke et al. (2007) concerning the boundary conditions and the domain size: the inlet boundary is placed $7 \times H2$ away from the canyon; a

symmetry condition is applied at the top and the lateral boundaries, with the top placed $6 \times H2$ away from the roofs of the buildings; the outlet boundary is placed $15 \times H2$ away from the street to allow for flow development using a freestream outlet, and no-slip conditions were applied to all the other boundaries (roofs/walls of the buildings and the ground).

Lastly, traffic exhaust is modelled by a line source along the middle of the street ($x = 0$) where a source term of emission is added in the pollutant transport equation. The source term corresponds to a mass flow rate chosen to 1.10^{-4} µg/s.

6.2.2. Governing equations

CFD simulations were carried out in OpenFOAM 5.0. Since in real contexts, full steady state is not always reached, all the simulations were performed using the unsteady *pimpleFoam* solver which is able to capture time instabilities. Reynolds-averaged Navier-Stokes (RANS) methodology was used to solve the continuity and the momentum equations throughout the computational domain by considering air as an incompressible fluid. This assumption can be made because of the low wind velocities (< 5 m/s) giving Mach numbers under 0.3 (Anderson, 2009). The corresponding continuity (Eq. 6.1) and momentum (Eq. 6.2) equations are given below:

$$\frac{\partial \bar{u}_i}{\partial x_i} = 0 \tag{Eq. 6.1}$$

$$\frac{\partial \bar{u}_i}{\partial t} + \frac{\partial (\bar{u}_i \bar{u}_j)}{\partial x_j} = -\frac{1}{\rho}\left(\frac{\partial \bar{P}}{\partial x_i}\right) + \nu\left(\frac{\partial^2 \bar{u}_i}{\partial x_j \partial x_j}\right) - \frac{\partial \overline{u_i' u_j'}}{\partial x_j} \tag{Eq. 6.2}$$

where $\bar{u}_i$ and u_i' are the ith mean and the fluctuating velocities, respectively, x_i is the ith Cartesian coordinate, $\bar{P}$ is the mean pressure and ν is the kinematic viscosity.

Using RANS to solve turbulent flows requires choosing a turbulence model to solve the Reynolds stress tensor $\overline{u_i' u_j'}$ (Eq. 6.3). The RNG k-ε turbulence model proposed by Yakhot et al. (1992) was chosen for turbulent closure because the numerical results fitted well with the experimental data (see Section 6.3.2. for further details) The corresponding equations for

turbulent kinetic energy (Eq. 6.4) and turbulent dissipation rate (Eq. 6.5) of the RNG model are given below. Taking $R = 0$ and using the correct constants, these equations also correspond to the standard k-ε turbulence model.

$$\overline{u_i' u_j'} = \frac{2}{3} k \delta_{ij} - \nu_t \left(\frac{\partial \bar{u}_i}{\partial x_j} + \frac{\partial \bar{u}_j}{\partial x_i} \right) \tag{Eq. 6.3}$$

$$\frac{\partial k}{\partial t} + \bar{u}_j \frac{\partial k}{\partial x_j} = \frac{\partial}{\partial x_j} \left(\frac{\nu_t}{\sigma_k} \frac{\partial k}{\partial x_j} \right) + \nu_t \left(\frac{\partial \bar{u}_i}{\partial x_j} + \frac{\partial \bar{u}_j}{\partial x_i} \right) \frac{\partial \bar{u}_i}{\partial x_j} - \varepsilon \tag{Eq. 6.4}$$

$$\frac{\partial \varepsilon}{\partial t} + \bar{u}_j \frac{\partial \varepsilon}{\partial x_j} = \frac{\partial}{\partial x_j} \left(\frac{\nu_t}{\sigma_\varepsilon} \frac{\partial \varepsilon}{\partial x_j} \right) + \frac{\varepsilon}{k} \left(C_{\varepsilon 1} \nu_t \left(\frac{\partial \bar{u}_i}{\partial x_j} + \frac{\partial \bar{u}_j}{\partial x_i} \right) \frac{\partial \bar{u}_i}{\partial x_j} - C_{\varepsilon 2} \varepsilon \right) - R \tag{Eq. 6.5}$$

$$R = \frac{C_\mu \eta^3 (1 - \eta/\eta_0)}{1 + \beta \eta^3} \frac{\varepsilon^2}{k} \tag{Eq. 6.6}$$

$$\nu_t = C_\mu \frac{k^2}{\varepsilon} \tag{Eq. 6.7}$$

where $\eta = Sk/\varepsilon$ and $S^2 = 2 S_{ij} S_{ij}$ the mean strain tensor, $\bar{u}_i$ is the ith mean velocity, x_i is the ith Cartesian coordinate, ν is the kinematic viscosity, k is the turbulent kinetic energy, ε is the turbulent dissipation rate, δ_{ij} is the Kronecker delta and ν_t is the turbulent viscosity. All the other parameters are model constants given in Table 6.1 for both k-ε turbulence models (standard and RNG).

Table 6.1 – Turbulence model constant values

Model	C_μ	$C_{\varepsilon 1}$	$C_{\varepsilon 2}$	σ_k	σ_ε	η_0	β
Standard k-ε	0.09	1.45	1.9	1.0	1.3	-	-
RNG k-ε	0.085	1.42	1.68	0.72	0.72	4.38	0.015

Pollutants are considered as passive scalars since no chemical effects are solved in this study. The equation governing advection-diffusion for the passive pollutant dispersion given in

OpenFOAM was modified to take into account turbulent diffusivity. The corresponding equation is given below:

$$\frac{\partial C}{\partial t} + \frac{\partial (u_i C)}{\partial x_i} - \frac{\partial}{\partial x_i}\left[\left(D_m + \frac{v_t}{Sc_t}\right)\frac{\partial C}{\partial x_i}\right] = E \qquad \text{(Eq. 6.8)}$$

where C is the pollutant concentration, D_m is the molecular diffusion coefficient, Sc_t is the turbulent Schmidt number and E is the source term of the pollutants (emissions).

The ratio v_t/Sc_t corresponds to the turbulent diffusion coefficient. The value of Sc_t is constant throughout the computational domain and fixed at 0.2. This value was chosen for the validation step (see Section 6.3.2. for further details).

6.2.3. Numerical settings

Second order schemes were adopted for all the gradient, divergent and Laplacian terms. In particular, for the Laplacian terms we used the 'Gauss linear corrected'-scheme which is an unbounded second order conservative scheme, the second order 'Gauss linear'-scheme for the gradient terms and the 'Gauss linearUpwind'-scheme for the divergent terms, the latter scheme being an unbounded upwind second order scheme.

All the simulations were run until the convergence was reached. To ensure the convergence of the simulations, the values of the streamwise velocity U and the pollutant concentration C were monitored for several points all over the canyon. Since all the simulations reached steady-state, they were stopped when the values monitored were constant over time. Moreover, at the end of the simulations all the residuals were under 10^{-5}.

6.3. Model validation

The model was validated versus the experimental wind tunnel data proposed by Soulhac et al. (2001). This experiment setup consists of a regular street canyon with *H1/H2 = 1* and *W/H2 = 1* with a gas released continuously at the center of the street. A summary of the boundary conditions used for this validation is given in Table 6.2. A comparison between experimental and numerical streamwise velocity was made to evaluate mesh sensitivity; another comparison

between experimental and numerical pollutant concentrations was made to find the turbulent Schmidt number which gave the best results compared to the experiment.

Table 6.2 – Summary of the boundary conditions

Inlet	Experimental velocity profile which corresponds to a power law profile with $U = U_{ref} \left(\frac{z}{z_{ref}} \right)^{\alpha}$, where $U_{ref} = 5.54$ m/s is the velocity at z_{ref}, $z_{ref} = 0.63$ m is the reference height, $\alpha = 0.127$ is the power law exponent and z the height from the ground. $k = 1.5(UI)^2$, with $I \approx 0.16. Re^{-1/8}$ the turbulent intensity, with $R_e = U.H/v$ the Reynolds number where $U = 4.43$ m/s is the mean inlet velocity, $H = 0.6$ m is the injection height and $v = 1.56.10^{-5}$ m²/s is the kinematic viscosity. $\varepsilon = C_\mu^{0.75} \frac{k^{1.5}}{l}$ with $C_\mu = 0.085$ the CFD constant, and l the turbulence length taken as equal to the injection height (0.6m). The inlet profiles start from the upwind roof height (z=0) and end at the domain top height ($z = 6H2$).
Outlet	Freestream outlet
Top	Symmetry plane
Lateral surfaces	Symmetry plane
Ground and building surfaces	No slip condition ($U = 0$ m/s)
Emission	Line source with emission rate $E = 1.10^{-4} \mu$g/s localized at the middle of the street

6.3.1. Mesh sensitivity

Mesh sensitivity tests were carried out and compared to the experimental streamwise velocity results to find the best compromise between the precision of the numerical results and calculation costs.

Figure 6.3 shows this comparison for three localized velocity profiles: on the leeward side of the street ($x/H = -0.2$), in the middle of the street ($x/H = 0.0$) and on the windward side of the street ($x/H = 0.2$). Three mesh-dependent results are proposed and the grid expansion ratio between the coarse and the medium grid and between the medium and the fine grid is 2. Velocities and heights are proposed in dimensionless form, corresponding to U/U_{max} with $U_{max} = 5$ m/s and z/H with $H = 0.1$ m, respectively.

The results show good agreement between the experimental and numerical data whatever the mesh refinement considered. There is a noticeable difference in the numerical results between

the coarse and the medium mesh in the street canyon ($z/H < 1$). The difference between the medium and the fine meshes is almost imperceptible apart from the low heights for which the fine mesh results are closer to the experimental results. Thus, in the light of these results, the fine mesh grid was adopted, and an illustration of the selected meshing is provided in Figure 6.4.
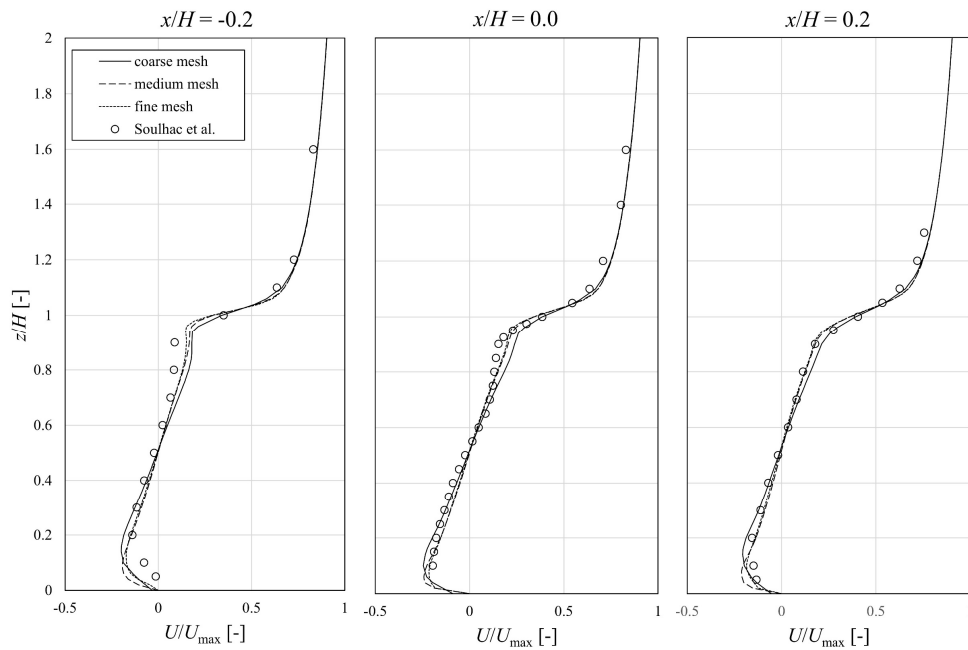
Figure 6.3 – Vertical distribution of numerical streamwise velocities for different mesh refinements compared to Soulhac et al. (2001) experimental data.
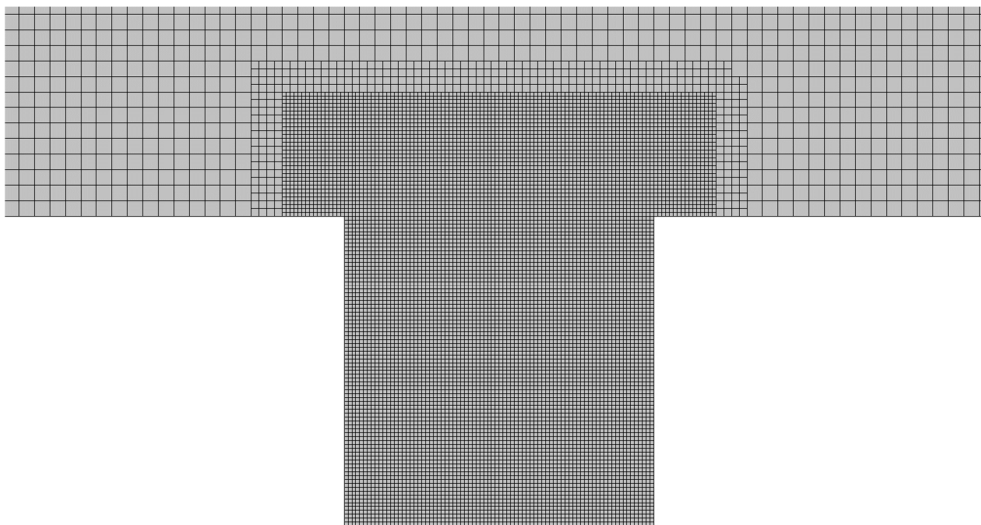
Figure 6.4 – Illustration of the selected meshes.

An additional mesh sensitivity study was performed on the variable of interest C, the pollutant concentration, using the Grid Convergence Index (GCI) methodology proposed by Roache (1994). This methodology is used to assess the mesh-related errors of a given mesh grid in view of the fine and coarse grid results and depending on the grid expansion ratio and the order of the numerical scheme used. The GCI for fine mesh grid error evaluation is given below:

$$GCI_{fine\ grid} = 3\frac{|f_2 - f_1|}{f_1}(r^p - 1)^{-1}$$

(Eq. 6.9)

where f_1 and f_2 are the results using the fine and coarse grid, respectively (here $f_1 = C_{fine}$ and $f_2 = C_{coarse}$), r is the grid expansion ratio between the fine and the coarse grid and p is the order of the numerical scheme.

The grid convergence index for the fine grid was calculated for 370 points uniformly distributed in the street canyon with $p = 2$ (second order schemes) and $r = 4$ (the fine mesh is four times smaller than the coarse mesh). The corresponding mean $GCI_{fine\ grid}$ is 2% and the maximum 4%, thus corresponding to a sufficient grid resolution. The typical dimension of the chosen cells is $0.0125 \times H2$.

6.3.2. Turbulent Schmidt number

According to Tominaga and Stathopoulos (2007), the optimal values of the turbulent Schmidt number Sc_t are widely spread between 0.2 and 1.3 and have a considerable influence on pollutant mass transfer. Thus, Sc_t must be chosen with care. To make this choice, several simulations were performed for $0.1 < Sc_t < 0.7$ with steps of 0.1 and the results were compared with the experimental data.

Figure 6.5 shows the results for three localized concentration profiles: close to the leeward building ($x/H = -0.4$), in the middle of the street ($x/H = 0.0$) and close to the windward building ($x/H = 0.4$). The three closest numerical results compared to the experiment are shown and differ only by the turbulent Schmidt number used: 0.1, 0.2 and 0.3. Concentrations and heights are proposed in dimensionless form. The same dimensionless form as before was used for the heights (z/H) and the dimensionless concentration was obtained using (Eq. 6.10).

$$C^* = C.U_H.H_2.L/q_m \tag{Eq. 6.10}$$

where C^* is the dimensionless concentration, C is the concentration, U_H is the velocity just over the windward building ($0.05 \times H2$ over the roof) and far from the canyon in the experimental setup of Soulhac et al. (2001) with $U_H = 2.75$ m/s, H_2 is the windward building height, L is the pollutant injection length and q_m is the pollutant emission rate.

The results show good agreement between the numerical and experimental data for $Sc_t = 0.2$. Regarding this turbulent Schmidt number, for the leeward side there is generally an overestimation of the concentrations in the upper part of the street and an underestimation in the lower part of street while there is a general underestimation for the windward side. The numerical results are less accurate with $Sc_t = 0.1$ and $Sc_t = 0.3$, so the value of 0.2 was kept for the rest of the study. Using this turbulent Schmidt number, the mean normalized absolute error over the experimental profiles was 10%. The corresponding 95th percentile was less than 30% and the maximal differences between the experimental and numerical results occurred near the ground.
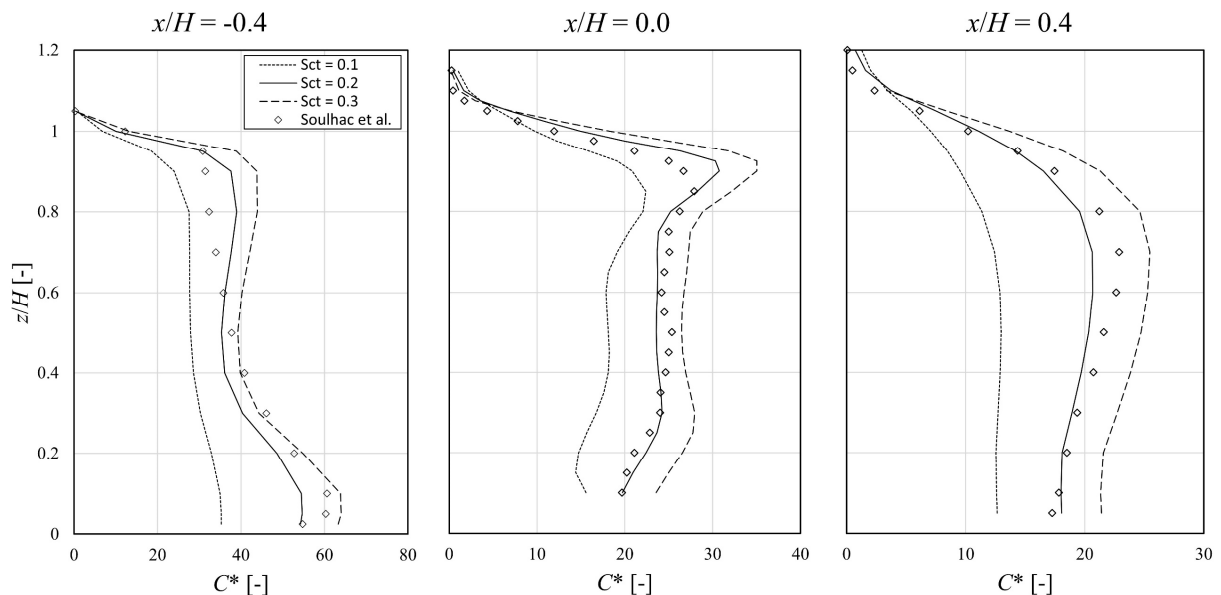
Figure 6.5 – Vertical distribution of numerical dimensionless concentrations for different Sct compared to Soulhac et al. (2001) experimental data.

The models used in the present paper (RANS and RNG k-ε) give a global underestimation of the turbulent momentum diffusion leading to low turbulent Sc_t. The turbulent Schmidt number taken as 0.2 is in coherence with other authors results who took a low Sc_t as 0.3 for the same models (Tominaga and Stathopoulos, 2007). It should be noted that the value of 0.2 could not be the best for all the geometric ratios considered in this work. However, it was decided to always use the same Sc_t in the whole study, which is a common practice done by the scientific community (Takano and Moonen, 2013 ; Wen and Malki-Epshtein, 2018 ; Cui et al., 2016), in order to only compare the influence of the geometric properties of the buildings on the mean concentrations and to avoid multi parameter comparisons.

6.4. Effects of street dimensions on mean concentrations

Exactly the same conditions as defined previously were used for the present study, except for the geometric properties of the street and in particular $H1$ and W. To study the mean concentrations in the street canyon, several couples of height ratios $H1/H2$ and width ratios $W/H2$ were considered. The present work is limited to a step-down street canyon configuration where $H1/H2 > 1.0$. The following height ratios were used: 1.0, 1.2, 1.4, 1.6, 1.8 and 2.0. For each of these height ratios, 5 width ratios were considered: 0.6, 0.8, 1.0, 1.2 and 1.4, giving a total number of 30 simulations and an overall idea of how could evolve mean concentrations in step-down street canyons. This number does not include certain particular cases that were also simulated when the results were strongly different between two cases (e.g. when for a given width ratio, two successive height ratios results in two different regimes). A case table of all the ratios considered in this work is proposed in Table 6.3.

Table 6.3 – Case table of all geometric ratios considered (● : couples of ratios initially considered, ○ : specific cases considered aftermath).

$H1/H2$ \ $W/H2$	0.6	0.8	1.0	1.2	1.4
2.0	●	●	●	●	●
1.9					
1.8	●	●	●	●	●
1.7					
1.6	●	●	●	●	●
1.5		○			
1.4	●	●	●	●	●
1.3			○	○	○
1.2	●	●	●	●	●
1.1	○	○			
1.0	●	●	●	●	●

Figure 6.6 shows the localization of the mean concentrations studied in this paper. Here, we study:

-   The concentration averaged all over the street (in the $W \times H2$ area),
-   The mean concentration on a vertical profile placed $0.1 \times H2$ from the windward building facade (concentration averaged for the $H2$ height) and another vertical profile placed $0.1 \times H2$ from the leeward building facade (concentration averaged for the $H2$ height). These mean concentrations are relevant for people living in the buildings near the street.
-   The mean concentration for a horizontal profile placed $0.1 \times H2$ from the ground (concentration averaged for the W length). This mean concentration is relevant for pedestrians in the street.
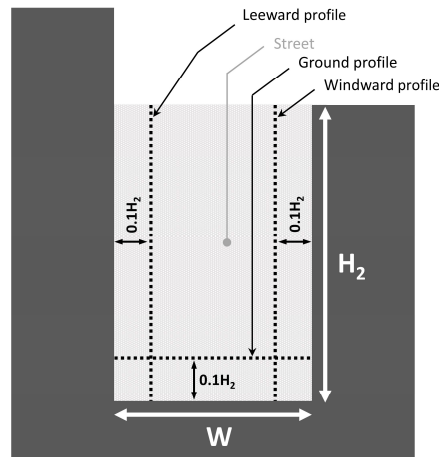
Figure 6.6 – Localization of the mean concentrations studied.

All the concentrations will be given in dimensionless form. The dimensioned concentrations could also be retrieved using (Eq. 6.10) with $U_H = 2.75$ m/s, $H_2 = 0.1$m, $L = 0.0025$ m and $q_m = 1.10^{-4}$ µg/s.

6.4.1. Vorticity and recirculation regimes in the street canyon

Flow velocities and recirculation patterns have a significant impact on pollutant dispersion and thus on pollutant concentrations inside and outside the street canyon. The modifications of flow velocities and recirculation patterns are caused solely by the geometric properties of the street ($H1/H2$ and $W/H2$) as all the simulations were run using the same velocity inlet profile.

Out of the total number of simulations performed, three types of recirculation regimes were found. Figure 6.7 shows an example of each regime with the velocity vectors and the corresponding y-vorticity ω_y given by equation (Eq. 6.11). These three regimes stand out due to their number of recirculation zones inside and outside the canyon.

$$\omega_y = \frac{\partial U_x}{\partial z} - \frac{\partial U_z}{\partial x} \qquad \text{(Eq. 6.11)}$$

Regime A corresponds to a big single vortex localized in the canyon. For this regime, vorticity is globally positive in the canyon, which means that the vortex rotates clockwise. Regime B corresponds to two vortices, one large vortex in the canyon and a second localized mostly over

the canyon and the windward building. The large vortex in the canyon is very similar to that of regime A, but here the vorticity is mostly negative, and the vortex rotates counterclockwise. The second vortex localized outside the canyon rotates clockwise. Regime C corresponds to three vortices, two contra-rotative vortices localized in the canyon and the third vortex mostly localized over the windward building. This regime appears to be a combination of regimes A and B, with the clockwise-vortex of regime A in the low part of the street and the counterclockwise-vortex of regime B situated just over it. The same clockwise-outside-vortex of regime B is also observed.
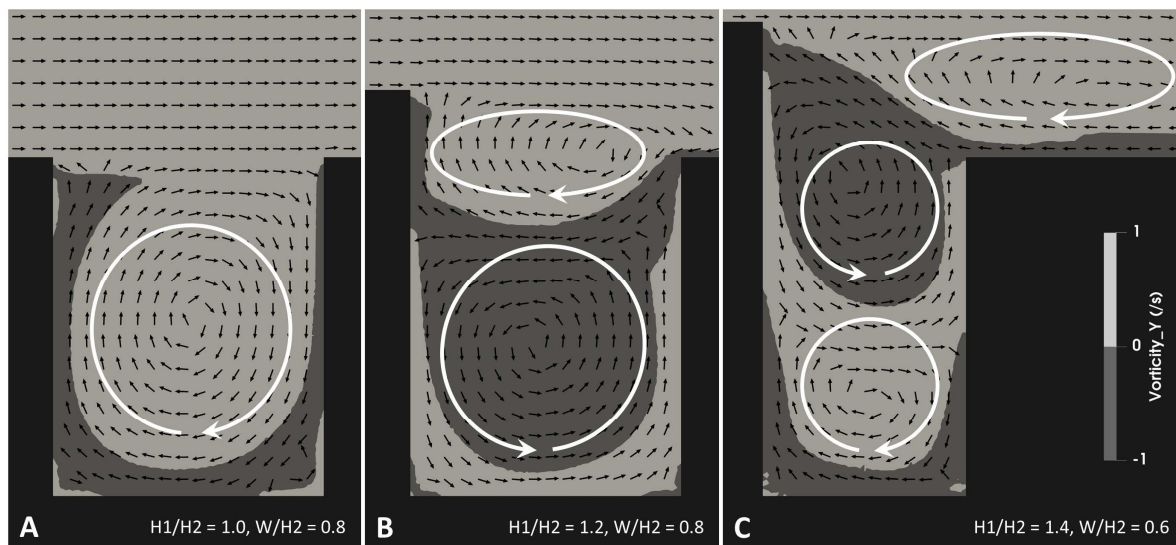
Figure 6.7 – Recirculation patterns, velocity vectors and y-vorticity for different geometric ratios *H1/H2* and *W/H2*.

Xiaomin et al. (2006) gave the critical value of $H1/H2$ for several $W/H2$ corresponding to the limit between regime A and regime B/C without distinction between B and C. Their results are compared with those of the present study for $W/H2$ from 0.6 to 1.4 and are shown in Figure 6.8 with the gray area corresponding to the switching area between regime A and regime B/C. The boundary conditions were the same between both studies.

The results obtained after the simulations showed a trend similar to that of the results of Xiaomin et al. (2006). The critical value of $H1/H2$ increases when the distance between the buildings increases and the zone of change between regime A and regime B/C is quite similar for both studies. However, critical values seem to be reached sooner according to our results

(i.e. for smaller $H1/H2$) with a maximal difference of 0.1 compared to the results of Xiaomin et al. (2006).
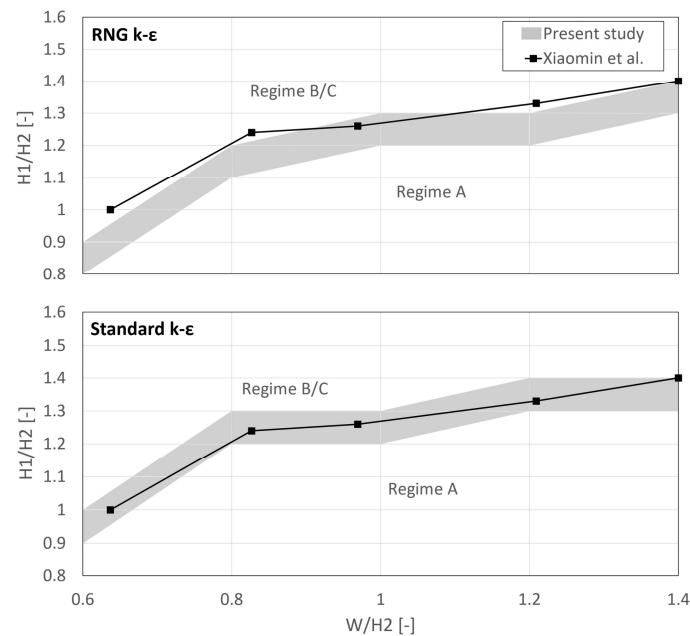
Figure 6.8 – Comparison of regime changing zones between the present study and the results of Xiaomin et al. (2006) using RNG and standard k-ε turbulent closure.

Some simulations were rerun using the turbulent conditions of Xiaomin et al. (2006), that is, using the standard k-ε turbulent closure. The results, also presented in Figure 6.8, show this time perfect concordance between both studies. Thus, turbulent closure schemes have an influence on the critical values of $H1/H2$. This difference between critical values when using standard k-ε or RNG k-ε are, however, quite small with a maximum difference of 0.1 for the ratio $H1/H2$.

6.4.2. Impact of the regimes on pollutant dispersion

Three examples of pollutant dispersion in the street canyon for each regime are shown in Figure 6.9. The overall concentrations in the street canyons being very different between the three regimes, the color scale is different for each of them. The velocity vectors are provided in order to better understand the differences in the concentration fields for the three regimes.
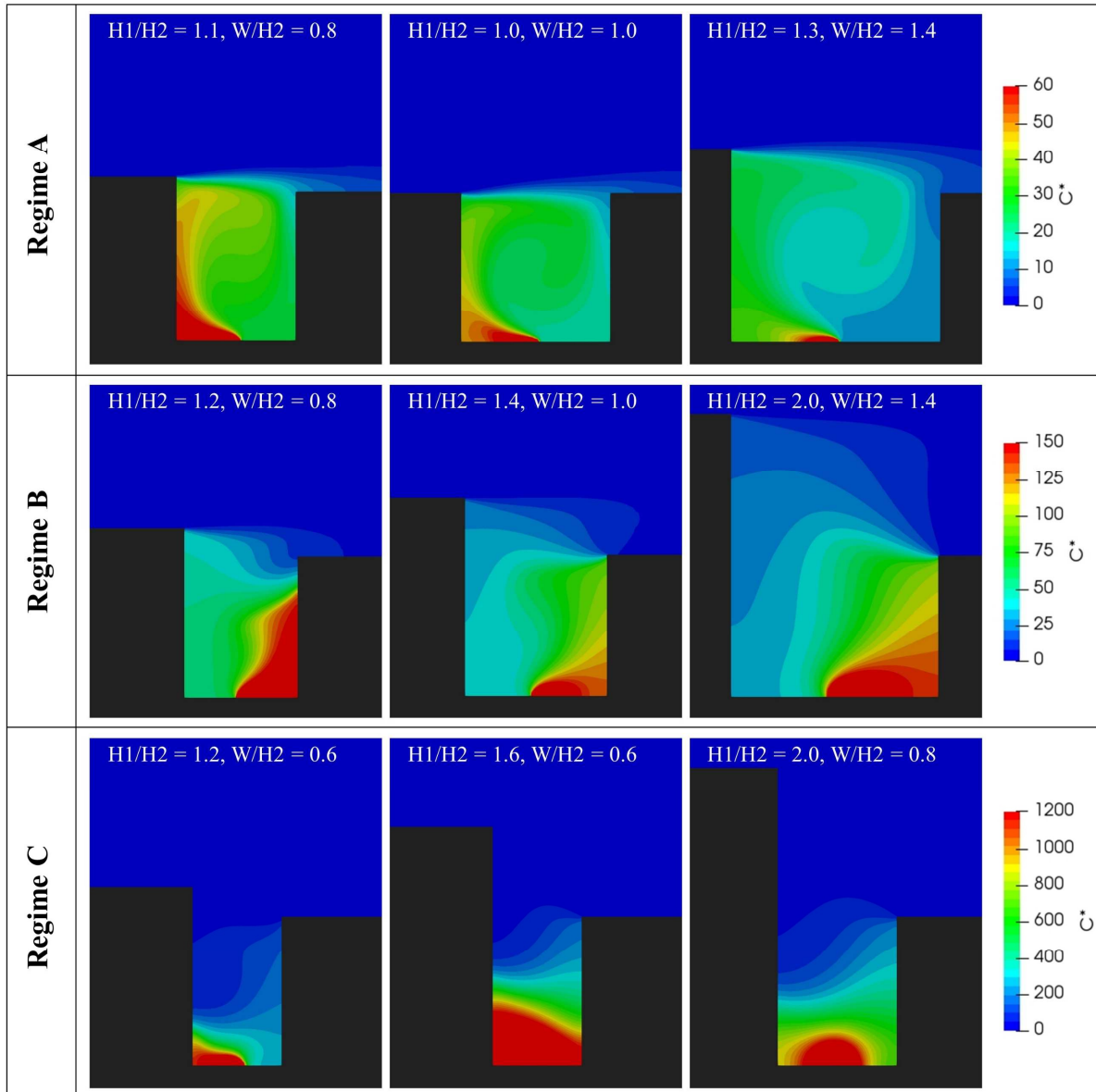
Figure 6.9 – Three examples of dimensionless concentrations in a street canyon for each type of regime.

The evolution of the concentration field, the overall magnitude of concentration, and the most impacted building are directly linked with the type of regime being established. In regime A, the pollutants released at ground level are mostly dispersed towards the leeward building due to the single clockwise vortex established in the street. In regime B, the apparition of a second vortex due to the increase of the leeward building height and the decrease of the distance between building leads to a change in the dispersion of pollutants. The vortex in the street being in this case counterclockwise, the most impacted building became the windward building. Moreover, concentrations are overall higher in this case and it seems to be the consequence of

the clockwise vortex localized just above which is driving a part of the pollutants which left the street to the street again. For the last regime, regime C, both buildings are highly impacted.

The difference with the regime B is not only the apparition of a third vortex, but the fact that two vortices are localized in the street between the buildings. Due to this two vortices, the pollutants released at ground level are dispersed to the leeward building but, because of the second vortex in the canyon, they are more homogenized in the low part of the street and seem to be more stagnant. It should also be noted that global velocities in the street tend to decrease with the increase of the leeward building height and the decrease of the distance between building which also conduct to higher pollutant concentrations.

6.4.3. Mean concentration in the street canyon

Initially, the results were studied by considering the mean concentrations of the whole street. Figure 6.10 shows the dimensionless street averaged concentrations (i.e. the mean concentration of the $W \times H2$ surface) proposed for several $H1/H2$ and $W/H2$ ratios and the different types of regime are also specified.
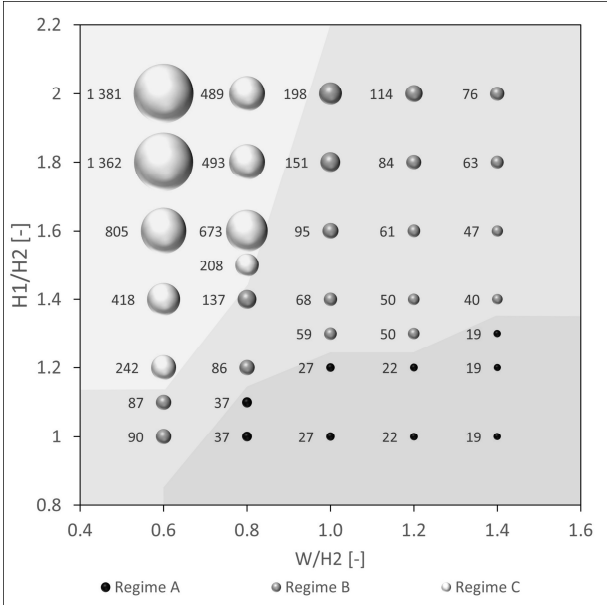
Figure 6.10 – Dimensionless street averaged concentrations according to the ratio *H1/H2* and *W/H2*.

The results show that the evolution of mean concentrations is highly dependent on the type of regime in place. The mean concentrations are indeed highest when regime C is in place and lowest when regime A is in place.

In regime A, for a given distance between buildings (i.e. a given $W/H2$), the mean concentrations are the same whatever the height of the leeward building. Thus, only the distance between buildings has an impact on the mean concentrations in the street. For a fixed leeward building height, the mean concentrations in the street increase when the distance between buildings decrease. This increase is not constant and becomes higher when ratio $W/H2$ decreases. For example, the mean concentration increases by 23% between $W/H2 = 1.2$ and $W/H2 = 1.0$ and then by 37% between $W/H2 = 1.0$ and $W/H2 = 0.8$. Lastly, for the $H1/H2$ and $W/H2$ ratios studied in this work, the factor between the lowest and the highest mean concentration for regime A is equal to 2.

In regime B, the evolution of the mean street concentrations is dependent on both ratios $H1/H2$ and $W/H2$: for a given leeward building height, the mean street concentrations increase when the distance between the buildings decreases; for a given distance between buildings, the mean concentration increases when the leeward building height increases. In addition, the increases between mean concentrations are not constant and become higher when $H1/H2$ increases and $W/H2$ decreases. The factor between the highest and lowest mean concentrations in the case of regime B is around 5.

In regime C, the evolution of the street mean concentrations is also dependent on both ratios $H1/H2$ and $W/H2$ but is no longer monotonous. Indeed, for a given distance between the buildings, the mean street concentrations first increase and then become constant. If the leeward building height is high enough, this mean concentration can then decrease. In this third case, a maximal mean concentration is reached. Mean street concentrations are highest for this regime with, in the worst-case concentrations, 50 times that of the regular case $H1/H2 = W/H2 = 1.0$.

Lastly, considering the whole series of simulations run in this study, for a given $H1/H2$ ratio, the mean concentrations increase as the distance between buildings decreases, whatever the three regimes observed. The evolution of the mean concentrations for a given $W/H2$ is nevertheless dependent on the regime.

6.4.4. Mean concentration on the building sides

The results were then studied considering only the windward and the leeward building sides. Figure 6.11 shows the dimensionless windward side averaged concentrations (i.e. the mean concentrations averaged over the windward profile) proposed for several $H1/H2$, and $W/H2$ ratios and the different types of regime are also specified. Figure 6.12 gives the same information, but considering the dimensionless, averaged leeward side concentrations (i.e. the mean concentrations averaged over the leeward profile).
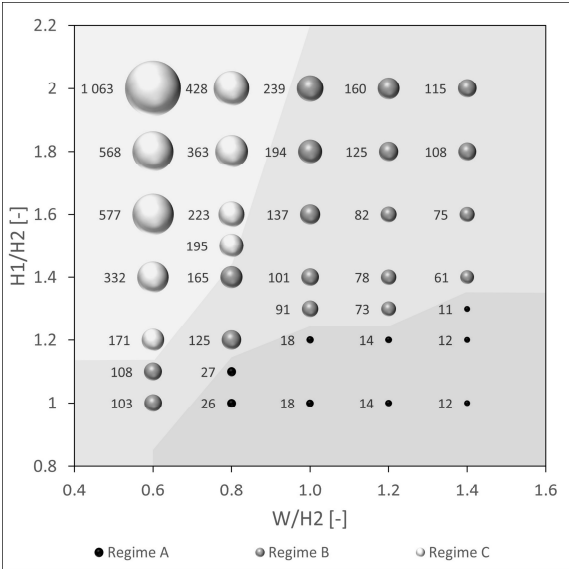
Figure 6.11 – Dimensionless windward profile averaged concentrations according to the ratios *H1/H2* and *W/H2*.
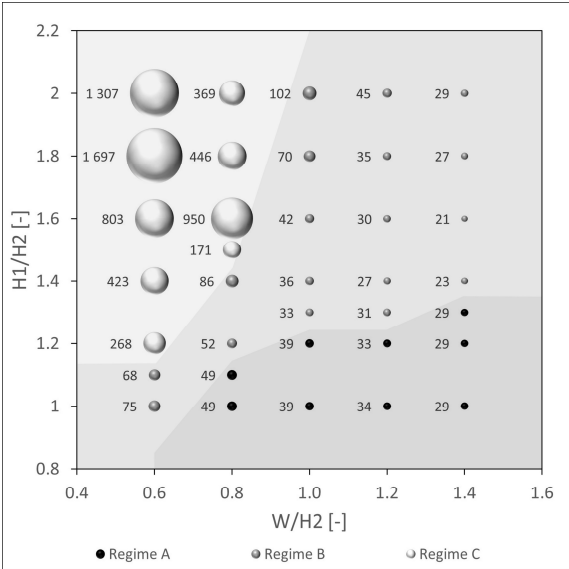
Figure 6.12 – Dimensionless leeward profile averaged concentrations according to the ratios *H1/H2* and *W/H2*.

As can be seen in Figure 6.11 and Figure 6.12, the evolution of the mean concentrations on the two building sides are similar. However, the mean concentrations could be higher or lower on the windward side, depending on the recirculation regimes.

In Regime A, for a given distance between buildings (i.e. a given $W/H2$ ratio), the mean leeward and windward concentrations are constant whatever the $H1/H2$ ratio. However, the mean concentration values are different, with concentrations globally twice as high on the leeward side. This observation is linked to the characteristics of regime A. Indeed, for all the cases in which regime A occurs, a large clockwise rotating vortex appears which spreads the pollutants released at ground level to the leeward side.

204

In regime B, the mean concentrations are no longer constant for a given distance between buildings but depend on both ratios $H1/H2$ and $W/H2$. This time the mean concentrations are higher on the windward side according to the counterclockwise vortex occurring in regime B, which spreads the pollutants released at ground level to the windward side. The mean concentrations on the windward side are globally three times higher than those of the leeward side.

In regime C, the mean concentrations still depend on both ratios $H1/H2$ and $W/H2$ and the concentrations are much higher than in regime B. The mean concentrations are globally higher on the leeward side, but this is not always true. Indeed, for $H1/H2 = 2.0$ and $W/H2 = 0.8$, the mean windward concentration is higher. It is much more difficult to interpret this difference than those of the two previous regimes because two vortices are localized in the canyon in this case. However, in this case the vortex is clockwise and localized near the emission source. The pollutants released near the ground are thus initially spread to the leeward side and it is only afterwards that the second vortex spreads them to the windward side. This explains why the mean concentrations are mostly higher on the leeward side than on the windward side.

Finally, if we focus on how the mean concentrations evolve when the regimes change (e.g. when switching from regime A to regime B), there is a notable difference between the windward and leeward sides. Indeed, for a switch from regime A to regime B, whereas the mean concentrations increase by a factor 6 on the windward side, the concentrations on the leeward side are almost equal. Moreover, on the leeward side, the mean concentration observed in the case of regime B did not increase much when $H1/H2$ increased or $W/H2$ decreased compared to the windward side.

6.4.5. Mean concentration at ground level

Finally, the results were studied at ground level and Figure 6.13 shows the dimensionless ground averaged concentrations (i.e. the mean concentrations averaged over the ground profile) proposed for several $H1/H2$ and $W/H2$ ratios; the different types of regime are also specified.
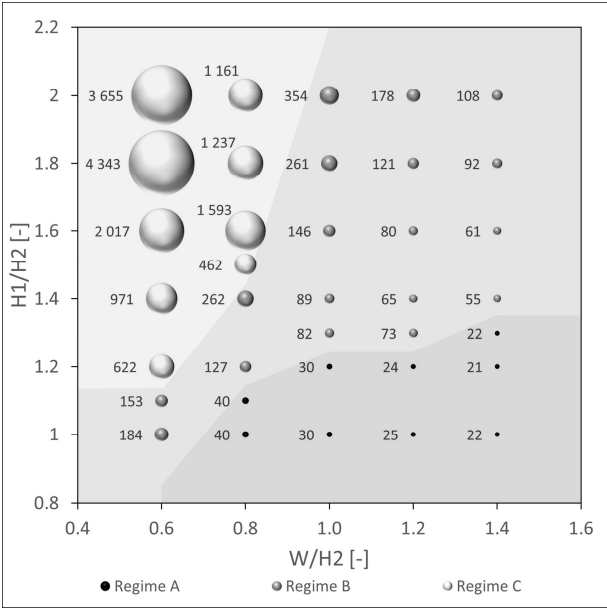
Figure 6.13 – Dimensionless ground profile averaged concentrations according to ratio *H1/H2* and *W/H2*.

At ground level, the evolution of mean concentrations is similar for the leeward profile and the whole street: regime A leads to constant mean concentrations for a given distance between buildings; regime B leads to mean concentrations depending on both the distance between buildings and difference in height between the two buildings; regime C leads to the same observation as regime B, the difference being that for a given distance between buildings, a maximal mean concentration is reached, after which this concentration decreases with the increase in the difference in height between the two buildings.

6.5. Discussion

Choices were made regarding the turbulence model used as well as the isothermal assumption taken to fulfil this work. These choices could affect the presented results and are worth discussing about.

Based on comparison with experimental data, the RNG turbulence model was selected. This model is an isotropic linear k-ε based model that is known to have some limitations for highly transient cases, especially in a wake of a body, including flows behind the leeward walls of street canyons. To avoid such problems, non-linear turbulence models or anisotropic models such as the Reynolds Stress Model (RSM) should be used. However, these models are time

consuming and are more difficult to converge. In addition, they seem to give not as much improvements as expected in the case of isolated buildings or street canyons. Indeed, Papageorgakis and Assanis (1999) showed that the linear RNG k-ε turbulence model gives significant improvements compared to the standard turbulence model for recirculatory flow such for backward facing step cases. Moreover, according to the same authors, the non-linear RNG turbulence model is not very attractive, yielding not to great improvements. Finally, Koutsouarakis et al. (2012) showed for six street canyons with different aspect ratios that the RNG turbulence model gives the best performances for each case compared to the standard turbulence model as well as compared to RSM.

The whole study was conducted considering neutral (isothermal) conditions since ambient and wall temperatures were considered equal. Thus, only the forced convection due to the wind was considered. More complex cases could appear when the building walls are heated by solar radiations conducting to unstable conditions where natural convection appears. For this cases, results in terms of recirculation regimes or pollutant concentrations can be different. Wang et al. (2011) studied the cases of leeward, ground, and windward heated walls in a regular street canyon and compared the results with the neutral case (without wall heating). They found that, except for the case of the windward heated wall, the recirculation pattern in the street is always the same. Concentrations are different depending on the case, but they are always lower than for the neutral case. These results are confirmed by Allegrini et al. (2013) who did the same work with several wind speed and also simulated a case where all walls are heated. This case also leads to the same recirculation pattern as for the neutral case. According to these results, it could be said that the results given in this study are not only good for one considering neutral cases but are also a good first approximation of thermally unstable cases. Pollutant concentrations being greater for the neutral case than for the unstable case leading thus to a safer approach.

6.6. Conclusion

The effects of step-down street canyon geometric properties on recirculation patterns and mean pollutant concentrations in a street were studied with a CFD model. This study considered 6 height ratios $H1/H2$ (from 1.0 to 2.0 with a 0.2 step) and 5 width ratios $W/H2$ (from 0.6 to 1.4 with a 0.2 step). The main conclusions are as follows:

(a) Three types of regimes can occur as a function of both the height and width ratios of the street. Flow velocities and direction in the street, and thus pollutant concentrations, depend heavily on the type of regime being established. The three types of regime were characterized by the number of vortices established and their direction: regime A corresponded to a single clockwise vortex in the canyon; regime B corresponded to a counter-clockwise vortex in the canyon and a clockwise vortex over the windward building; regime C corresponded to two contra-rotating vortices in the canyon and a clockwise vortex over the windward building.

(b) The critical values of $H1/H2$ corresponding to a change in the type of regime for a given width ratio were determined. The critical values obtained were differed as a function of the turbulence closure scheme used. These differences were never greater than 0.1 when using standard or RNG k-epsilon turbulence schemes.

(c) Whatever the mean concentration considered (in the whole canyon, at pedestrian level or near the building faces), the mean concentrations were lowest in the case of regime A and highest in the case of regime C. Regime B therefore corresponded to an intermediary state.

(d) The mean concentrations increased globally as differences in building height increased ($H1/H2$ ratio), and with the decrease of street width ($W/H2$), except for the case of regime A where the evolutions of mean concentrations depended only on street width.

(e) The quantitative evolution of the mean pollutant concentration in the whole street at pedestrian level and near the building faces was proposed.

As a summary, in order to have a good ventilation in step-down street canyons and in the perspective of reducing mean pollutant concentration of the whole street at pedestrian level and near building faces, we recommend choosing carefully the height ratio $H1/H2$ as well as the width ratio $W/H2$ in order to be in the case of a regime A.

These conclusions and results were obtained for a given type of street canyon and they should be extended to consider other types such as step-up street canyons and wider and deeper canyons. Moreover, these results were obtained considering flat roofs. However, this type of roof is not the only kind of roof used for buildings and further works should be carried out to obtain information on other types of roof.

Chapter 7:

Understanding – Effects of wind speed and atmospheric stability on the air pollution reduction rate induced by noise barriers

---

This chapter has been published as an original research paper in the *Journal of Wind Engineering and Industrial Aerodynamics*:

Reiminger, N., Jurado, X., Vazquez, J., Wemmert, C., Blond, N., Dufresne, M., Wertel, J., 2020. Effects of wind speed and atmospheric stability on the air pollution reduction rate induced by noise barriers. *Journal of Wind Engineering and Industrial Aerodynamics* 200, 104160. https://doi.org/10.1016/j.jweia.2020.104160

Numerical models are valuable tools which can be used to understand the effects of various phenomenon (thermal effects, effects of vegetation, etc.) on air pollutants dispersion. This chapter shows how a computational fluid dynamics software can be used for understanding purposes to limit pollutant concentrations in urban areas. In particular, the impact of noise barriers on the reduction of air pollution after the barriers is studied for multiple meteorological scenarios including various wind speeds, wind directions and atmospheric stabilities.

The points covered in this chapter are highlighted in Figure 7.1.

Input conditions	Pre-processing	Processing	Post-processing	Output
Wind speed Wind direction Turbulence Temperature Emissions	Meshing Canopy Interface Model (CIM)	2D / 3D Turbulence model Turbulent Schmidt number Passive transport Buoyancy effects Vegetation	Interpolation over one wind direction Interpolation over the wind rose	Concentrations Mean annual concentrations
NO_X / NO_2 PM_{10} / $PM_{2.5}$ Monthly campaign			Analysis Extrapolation	Monthly concentrations Annual concentrations

Numerical modelling (left label for first row)
Field measurement (left label for second row)

Figure 7.1 – Main points covered in Chapter 7.

Particularly, the following questions are addressed in this chapter:

(?) How can a CFD-RANS model be used for engineering purposes?

(?) How much can thermal effects change the pollutant dispersion in urban areas ? Is the stable or unstable atmosphere leading to higher pollutant concentrations

7.1. Introduction

Nowadays, more than one in two people live in urban areas with 82% in the United States and 74% in Europe, and this percentage will continue growing to reach 68% worldwide in 2050 (United Nations, 2019). Traffic-related emissions can reach high levels in such areas, particularly near heavy-traffic roads. Concentrations of air pollutants such as nitrogen dioxide (NO_2) and particulate matter (PM) can reach high values in the vicinity of this kind of road and lead to several diseases (Anderson et al., 2012; Kagawa, 1985; Kim et al., 2015). In addition, it has been shown that people living near these roads are more likely to be at risk (H. Chen et al., 2017; Finkelstein et al., 2004; Petters et al., 2004). In Europe, emissions and therefore concentrations of air pollutants are expected to decrease in the future as air quality regulations increase and actions are taken (European Commission, 2013). Nevertheless, it will take time

to achieve a significant decrease and, in the meantime, many people will still live in areas where air quality is poor. It is now necessary to find ways to limit exposure to air pollution for people living near busy roads and to better understand solutions that have already been found, like noise barriers.

Noise barriers are civil engineering elements located along roadways and designed to protect inhabitants from noise pollution. These elements, often placed between heavy-traffic roads and residences, also have a beneficial impact on air quality. Indeed, several authors have investigated the efficiency of noise barriers in reducing atmospheric pollutant concentrations behind the barriers using in-field (Baldauf et al., 2008, 2016; Finn et al., 2010; Hagler et al., 2012; Lee et al., 2018; Ning et al., 2010), wind tunnel (Heist et al., 2009) measurements and numerical models (Bowker et al., 2007; Hagler et al., 2011; Schulte et al., 2014). Some authors have studied the effects of barrier heights and distances on pollution reduction (Amini et al., 2018; Gong and Wang, 2018). Other authors have studied the effects of barrier shapes and locations on improving the reduction of atmospheric pollutants (Brechler and Fuka, 2014; Enayati Ahangar et al., 2017; Wang and Wang, 2019). However, although some of these works have been performed by considering different atmospheric stabilities, knowledge is lacking on how the combination of wind conditions and thermal effects can affect pollutant reductions behind barriers. Further work is thus required in this direction.

The aim of this work is to study the combined effects of wind and thermal effects on the reduction of pollutant concentrations behind the noise barrier. The scope of the study is limited to the study of the effects of the noise barriers and doesn't include the possible effects of buildings before and after the barriers. More specifically, computational fluid dynamics (CFD) simulations are used to assess the evolution of the concentration reduction rate behind noise barriers for several wind speeds and atmospheric stabilities, ranging from very unstable to stable conditions, including all the intermediate conditions (unstable, slightly unstable, neutral and slightly stable).

7.2. Description of the study

This paper examines the impact of wind speed and atmospheric stability on the reduction of downwind air pollution induced by the presence of noise barriers. It is therefore necessary to define two recurring parameters: the Richardson number and the concentration reduction rate.

The thermal effects can be quantified using the Richardson number noted Ri. The corresponding equation taken from (Woodward, 1998) is given in (Eq. 7.1).

$$Ri = \frac{gH}{U_H^2} \frac{(T_H - T_w)}{T_{air}} \qquad \text{(Eq. 7.1)}$$

where g is the gravitational acceleration [m.s^{-2}], H is the noise barrier height [m], U_H is the reference velocity (which is the velocity at $z = H$ in this study) [m.s^{-1}], T_{air} is the ambient temperature [K], T_H is mean air temperature at $z = H$ [K], and T_w is the surface temperature of the heated ground [K]. The difference $T_H - T_w$ will be noted ΔT in the following.

The Richardson number is also an indicator of atmospheric stability: $Ri = 0$ corresponds to isothermal (neutral) cases, $Ri < 0$ corresponds to unstable cases, and $Ri > 0$ to stable cases. A better discretization of atmospheric stability, related to Pasquill's stability classes, also exists (Woodward, 1998) and is summarized in Table 7.1.

Table 7.1 – Atmospheric stability correlated with the Richardson number (Woodward, 1998).

Atmospheric stability	Richardson number
Very unstable	$Ri < -0.86$
Unstable	$-0.86 \leq Ri < -0.37$
Slightly unstable	$-0.37 \leq Ri < -0.10$
Neutral	$-0.10 \leq Ri < 0.053$
Slightly stable	$0.053 \leq Ri < 0.134$
Stable	$0.134 \leq Ri$

The reduction of the pollution behind the noise barriers compared to an area without these barriers is quantified using an indicator called concentration reduction rate (CRR) given in (Eq. 7.2).

$$CRR\ (\%) = \left(1 - \frac{C_{nb}}{C_{ref}}\right) \times 100 \qquad \text{(Eq. 7.2)}$$

where C_{nb} is the concentration with a noise barrier [kg.m^{-3}] and C_{ref} is the reference concentration corresponding to the same case but without noise barriers [kg.m^{-3}].

The CRR provides information on both the positive and negative impact of noise barriers ($CRR > 0$ means that noise barriers reduce downwind pollution; $CRR < 0$ means that noise barriers increase downwind pollution) and their effectiveness ($CRR = 40\%$ means that the concentration behind noise barriers is reduced by 40% compared to the same case without them).

7.3. Numerical model

7.3.1. Governing equations

Simulations were performed using the *buoyantPimpleFoam* solver from OpenFOAM 6.0. This transient solver is able to resolve Navier-Stokes equations for buoyant and turbulent flows of compressible fluids including the effects of forced convection (induced by the wind) and natural convection (induced by heat transfers).

A Reynolds-averaged Navier-Stokes (RANS) methodology was used to resolve the equations. When using this methodology, a new term called Reynolds stress tensor appear and it is necessary to choose a turbulence model to resolve it. The RNG k-ε turbulence model proposed by Yakhot et al. (1992) has been selected because it gives significant improvements compared to the standard turbulence model for recirculatory flows (Papageorgakis and Assanis, 1999), whereas anisotropic models such as the Reynolds Stress Model (RSM) may not improve the results (Koutsourakis et al., 2012) for a higher calculation cost and more calculation instabilities.

The corresponding continuity (Eq. 7.3), momentum (Eq. 7.4) and energy (Eq. 7.5) equations are given below:

$$\frac{\partial \rho}{\partial t} + \nabla.(\rho u) = 0 \qquad \text{(Eq. 7.3)}$$

$$\rho\left(\frac{\partial u}{\partial t} + u.\nabla u\right) = -\nabla p + \nabla.\left(2\mu_{eff}D(u)\right) - \nabla\left(\frac{2}{3}\mu_{eff}(\nabla.u)\right) + \rho g \tag{Eq. 7.4}$$

$$\frac{\partial\rho e}{\partial t} + \nabla.(\rho u e) + \frac{\partial\rho K}{\partial t} + \nabla.(\rho u K) + \nabla.(u p) = \nabla.\left(\alpha_{eff}\nabla e\right) + \rho g.u \tag{Eq. 7.5}$$

$$D(u) = \frac{1}{2}[\nabla u + (\nabla u)^T] \tag{Eq. 7.6}$$

$$K \equiv |u|^2/2 \tag{Eq. 7.7}$$

where u is the velocity [m.s^{-1}], p the pressure [kg.m^{-1}.s^{-2}], ρ the density [kg.m^{-3}], e the thermal energy [m^2.s^{-2}], $D(u)$ the rate of strain tensor given in (Eq. 7.6), K the kinetic energy given in (Eq. 7.7) [m^2.s^{-2}], g the gravitational acceleration [m.s^{-2}], μ_{eff} the effective viscosity defined as the sum of molecular and turbulent viscosity [kg.m^{-1}.s^{-1}] and α_{eff} the effective thermal diffusivity defined as the sum of laminar and turbulent thermal diffusivities [kg.m^{-1}.s^{-1}].

No chemical reactions are considered in this study. Thus, the equation governing passive scalar transport (Eq. 7.8) has been added to the solver. This advection-diffusion equation is given hereafter:

$$\frac{\partial C}{\partial t} + \nabla.(uC) - \nabla.\left[\left(D_m + \frac{\nu_t}{Sc_t}\right)\nabla C\right] = E \tag{Eq. 7.8}$$

where C is the pollutant concentration [kg.m^{-3}], Sc_t is the turbulent Schmidt number [-], D_m is the molecular diffusion coefficient [m^2.s^{-1}], ν_t is the turbulent diffusivity [m^2.s^{-1}] and E the volumetric source term of the pollutants (emissions) [kg.m^{-3}.s^{-1}].

Each simulation was performed using second order schemes for all the gradient, divergent and Laplacian terms. The streamwise velocity U and the pollutant concentration C were monitored for several locations behind the downwind noise barrier and the results were checked to ensure that each simulation has converged. At the end of the simulations, all the residuals were under 10^{-5}.

7.3.2. Computational domain and boundary conditions

This study focuses on the concentration reduction rates induced by the presence of noise barriers. Thus, to quantify this reduction, two distinct cases have to be considered in terms of computational domain: a case with noise barriers and a case without them. Figure 7.2 shows a sketch of the computational domain and the boundary conditions used for the case with noise barriers. The second case is strictly the same but without the noise barriers.

The recommendations given by Franke et al. (2007) were followed concerning the boundary conditions and domain size. The inlet boundary is localized $10H$ before the upwind noise barrier where velocity, turbulence and temperature profiles are specified using a perpendicular wind direction, unless otherwise stated. The outlet boundary is placed $40H$ behind the downwind noise barrier with a freestream condition to allow the flow to fully develop. Symmetry conditions are applied for the upper and lateral limits, with the top of the calculation domain placed $20H$ from the ground and the lateral limits located $20H$ from each other. No-slip conditions are applied to any other boundaries including the ground and the two noise barriers, where the temperature can be specified to simulate stable and unstable cases. Finally, traffic exhausts are modeled by two volumetric sources along the y-direction, with a width of $1.4H$ each, and over one mesh height (0.25 m) where an emission source term is added in the pollutant transport equation. A mass flow rate of 100 g/s is used for all the simulations performed. Further information can be found in Table 7.2.
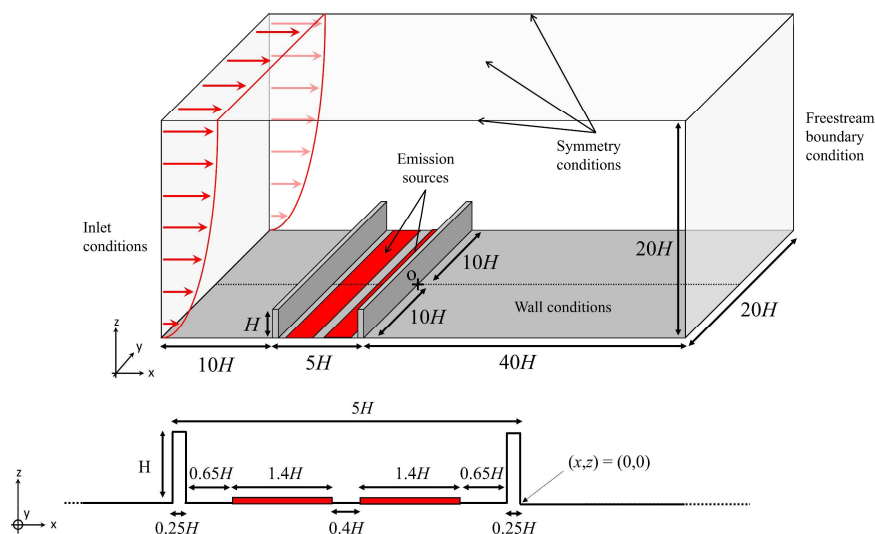
Figure 7.2 – Sketch of the computational domain with $H = 5$ m.

Table 7.2 – Summary of the boundary conditions.

Inlet	Velocity and turbulence profiles are calculated according to Richards and Hoxey (1993) and Richards and Norris (2011): $$U = \frac{u_*}{\kappa} ln\left(\frac{z}{z_0}\right) \text{ (Eq. 7.9)} \qquad k = \frac{u_*^2}{\sqrt{C_\mu}} \text{ (Eq. 7.10)} \qquad \varepsilon = \frac{u_*^3}{\kappa.z} \text{ (Eq. 7.11)}$$ with U the wind velocity, k the turbulent kinetic energy (TKE), ε the dissipation of TKE, u_* the friction velocity, κ the von Kármán constant taken to 0.41, z the altitude, z_0 the roughness height taken as 0.5 m, and C_μ a CFD constant taken as 0.085. Fixed temperature: T_{air} = 293 K.
Outlet	Freestream outlet.
Top	Symmetry plane.
Lateral surfaces	Symmetry plane.
Ground and noise barriers surfaces	No-slip condition (U = 0 m/s). Fixed temperature (T_w) depending on the case studied.
Emission	Surface source with emission rate q_m = 100 g/s.

The most part of the simulations have been carried out considering à perpendicular incident wind angle (90°) with respect to the noise barrier, but some simulations were also performed with a 60° incident angle. The boundary conditions were the same in both configurations and Figure 7.3 presents how the incidence angle is defined.
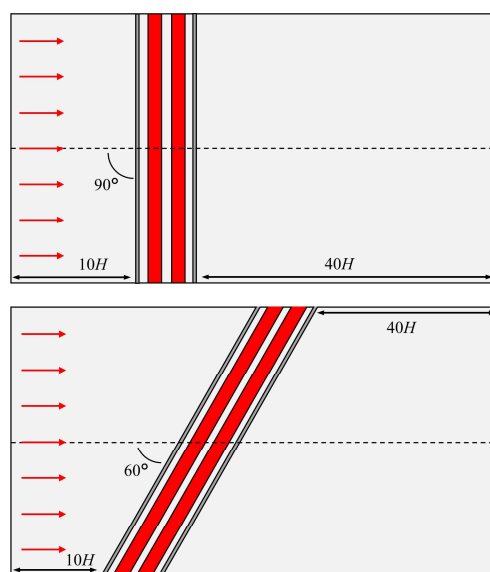
Figure 7.3 – Definition of the wind incidence angle.

Mesh sensitivity tests were carried out to ensure that the results are fully independent of mesh size. Successive simulations were performed with different mesh sizes and the Grid Convergence Index (*GCI*) methodology (Roache, 1994) was used to assess the mesh-related errors on both the flow field and the concentration field. Mean *GCIs* of 2% and 1% were obtained for flow and concentration fields, respectively, when comparing the results from mesh sizes of 0.5 m and 0.25 m. Thus, a mesh size of 0.5 m was considered sufficient to avoid excessive calculation costs and was used for the study. This mesh size corresponds to the meshes localized between an altitude of $z = 0$ and $z = 2H$. However, greater refinement was applied near the noise barrier walls and the road because of the strong gradients that can occur in these areas. This mesh size resulted in a total of 2.6 million meshes and an illustration of the meshes selected is provided in Figure 7.4. The meshing was done using the unstructured grid generator *snappyHexMesh* available with OpenFOAM.
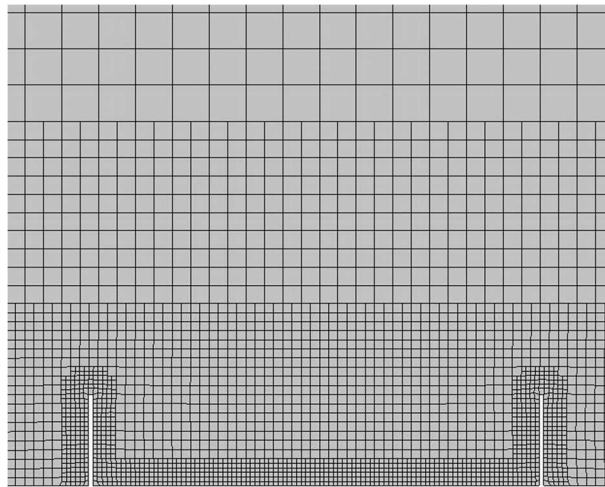
Figure 7.4 – Grid selected for computation.

Several simulations were performed to study the combined effects of wind speed and thermal effects on the concentration reduction rate behind the barriers. All the simulations performed with their specific conditions (U_H and ΔT) and their corresponding Richardson numbers are given in Table 7.3. Each of these conditions was simulated twice to obtain results with and without noise barriers to calculate the concentration reduction rates. A total of 64 simulations were carried out including:

- 24 simulations for the neutral case (6 simulations for each of the three turbulent Schmidt numbers considered to assess their impact on the concentration reduction rates and 6 supplementary simulations for a non-perpendicular case);
- 20 simulations for the stable cases;
- 20 simulations for the unstable cases.

All the results were extracted at the center of the computational domain along $y/H = 0$ with $x/H = 0$ corresponding to the end of the downwind noise barrier wall.

Finally, the turbulent Schmidt number (Sc_t) is a dimensionless number found in air pollution CFD to consider the effect of turbulent diffusivity. However, this number is widely spread between 0.2 and 1.3, depending on the situation studied, and can significantly change the results in terms of concentration (Tominaga and Stathopoulos, 2007). To assess the effect of this parameter on noise barrier studies, three Sc_t were considered: 0.3, 0.7 and 1.1.

Table 7.3 – Summary of the simulations performed with wind velocity and thermal conditions ($\Delta T = T_H - T_w$) and their corresponding Richardson numbers.

Ri [-] \ U_H [m/s]	1.18	1.96	3.15	5.51	7.87
0	$\Delta T = 0$ K		$\Delta T = 0$ K	$\Delta T = 0$ K	
0.06				$\Delta T = 10$ K	
0.17			$\Delta T = 10$ K	$\Delta T = 30$ K	$\Delta T = 62$ K
0.33		$\Delta T = 7.5$ K	$\Delta T = 19.5$ K		
0.50		$\Delta T = 11.5$ K	$\Delta T = 29.5$ K		
1.20	$\Delta T = 10$ K	$\Delta T = 27.5$ K			
-0.06				$\Delta T = -10$ K	
-0.17			$\Delta T = -10$ K	$\Delta T = -30$ K	$\Delta T = -62$ K
-0.50		$\Delta T = -11.5$ K	$\Delta T = -29.5$ K		
-0.75		$\Delta T = -17.5$ K	$\Delta T = -44.5$ K		
-1.20	$\Delta T = -10$ K		$\Delta T = -71$ K		

7.3.3. Model validation

The numerical model was compared against the experimental data proposed by Cui et al. (2016) because they provided results on both velocity and the concentration field for a complex 3D situation. Indeed, the experiment setup consists of two buildings with the downwind

building being higher than the upwind building. A gas is released at the top of the upwind building and the ground between the two buildings is heated to simulate several atmospheric stabilities and heat exchanges. The downwind building is opened and closed by two windows to simulate indoor/outdoor pollutant exchanges.

Figure 7.5 shows the comparison between the experimental data and the numerical model used in this study for an unstable case where Ri = -1.22 ($U_{free\ stream}$ = 0.7 m/s and ΔT = -135 °C) and for a vertical profile localized between the two buildings. These results are presented in a dimensionless form that can be found in the paper of Cui et al. (2016). The results show good agreement between the numerical model and the experimental data on both velocity and concentration profiles, with a mean difference of 6% between the experimental and numerical concentration profiles. The numerical model is therefore capable of accurately reproducing velocity and concentration profiles in a 3D case with a high thermal gradient. According to these results, the numerical model was considered validated for the purpose of this study.
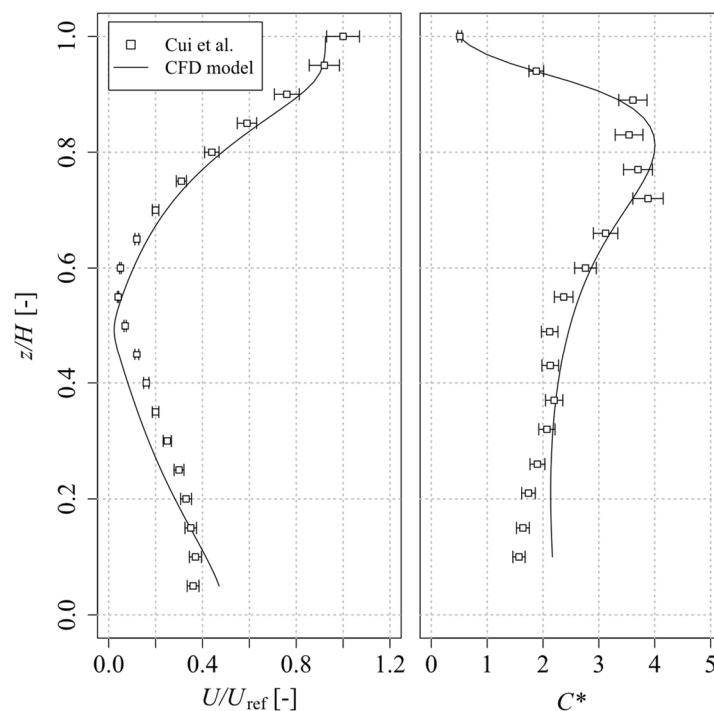
Figure 7.5 – Vertical distribution of dimensionless velocity and concentration for Ri = -1.22 given by Cui *et al.* for the wind tunnel measurements (Cui et al., 2016), and comparison with the CFD model used for this study with Sc_t = 0.25.

7.4. Results

7.4.1. Study without thermal effects

7.4.1.1. Turbulent Schmidt number sensitivity

The evolution of the CRR behind the barriers for the three Sc_t considered and for four altitudes ($z = 0.25H$, $0.50H$, $0.75H$ and $1.00H$) are presented in Figure 7.6 as a function of the dimensionless distance from the downwind noise barrier x/H, with $z = 0.25H$ the pedestrian level corresponding particularly to the size of a child (1.25 m). The results show considerable variability for the concentration reduction rate as a function of the turbulent Schmidt number and no general trend can be observed. Indeed, while for $Sc_t = 1.1$ and $z = 0.25H$ the CRR is globally higher than for other turbulent Schmidt numbers, for the three other altitudes the CRR is not globally higher. Additionally, while the CRR is globally lower with $Sc_t = 0.3$ and $z = 0.25H$, this observation is no longer true for the other altitudes. Moreover, the turbulent Schmidt number has also an impact on the distance after the barriers were there is a positive impact of the noise barriers ($CRR > 0$), this distance being higher for higher Sc_t.
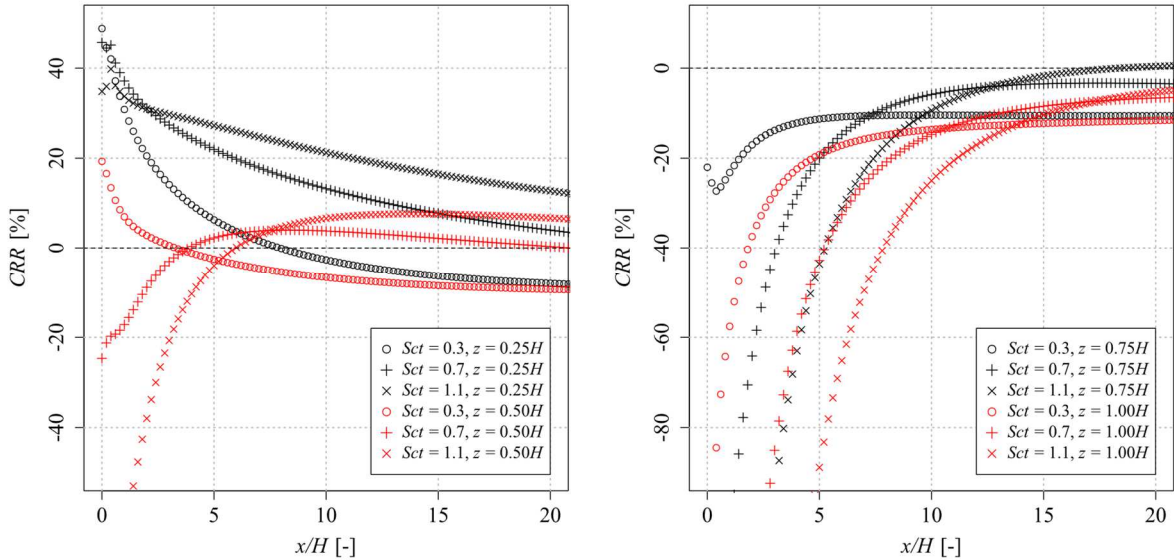
Figure 7.6 – Evolution of the concentration reduction rate behind the downwind wall as a function of Sc_t and for several altitudes with the same wind profile (U_H = 1.18 m/s).

According to these results, it is important to state that the turbulent Schmidt number is also a very sensitive parameter when studying the impacts of noise barriers and its choice should be considered carefully, especially when performing quantitative studies. For the rest of this paper, and since no information or studies to determine the best turbulent Schmidt number for noise barrier studies are available an intermediate turbulent Schmidt number of 0.7 is used, as in Tominaga and Stathopoulos (2017), and the results are presented qualitatively rather than quantitatively.

7.4.1.2. Impact of wind speed and wind direction on the CRR in neutral atmosphere

The impact of wind speed and wind direction on the concentration reduction rate was first studied in neutral atmosphere, thus, considering only forced convection (i.e. convection due to the wind).

Figure 7.7 shows the evolution of the pollutant concentrations behind the barriers for the cases with and without barriers (A) and the corresponding concentration reduction rates (B) as a function of the wind speed at $z = 0.25H$. According to Figure 7.7 (A), regardless of the wind speed and for $z = 0.25H$, pollutant concentrations were generally higher without the noise barrier than with it. Additionally, concentrations changed inversely with wind speed, leading to lower concentrations for higher wind speeds. The concentrations were thus different as a function of this parameter. However, as depicted in Figure 7.7 (B), the CRR is the same whatever the wind speed considered and this is also true for the other altitudes considered ($z = 0.5H$, $0.75H$ and $1.00H$). This result is linked to the fact that, for a given wind direction and without thermal stratification, the concentration was inversely proportional to the wind velocity (Schatzmann and Leitl, 2011). Thus, since the concentration evolved in the same way with wind speed both with and without noise barriers, the CRR remained unchanged for a given wind direction under neutral conditions.
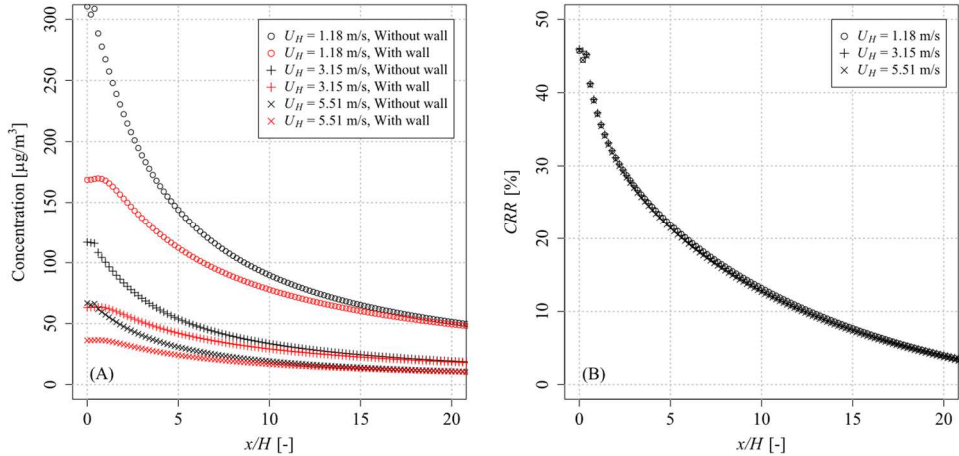
Figure 7.7 – Evolution of the concentrations with and without noise barriers (A) and the concentration reduction rates (B) as a function of wind speed for a perpendicular wind direction at $z = 0.25H$.

The effects of the wind direction under neutral conditions were also investigated and the results are presented in Figure 7.8 for a perpendicular wind (90°) and a wind oriented at 60°. Figure 7.8 (A) shows that for the 60° case, the concentrations are lower with the noise barriers and higher without the noise barriers compared to the perpendicular case. This inevitably leads to a lower CRR for the perpendicular case, as shown in Figure 7.8 (B) for $z = 0.25H$ and $z = 0.75H$. The same result was obtained for $z = 0.50H$ and $z = 1.00H$. Therefore, the CRR are higher for oblique wind directions.
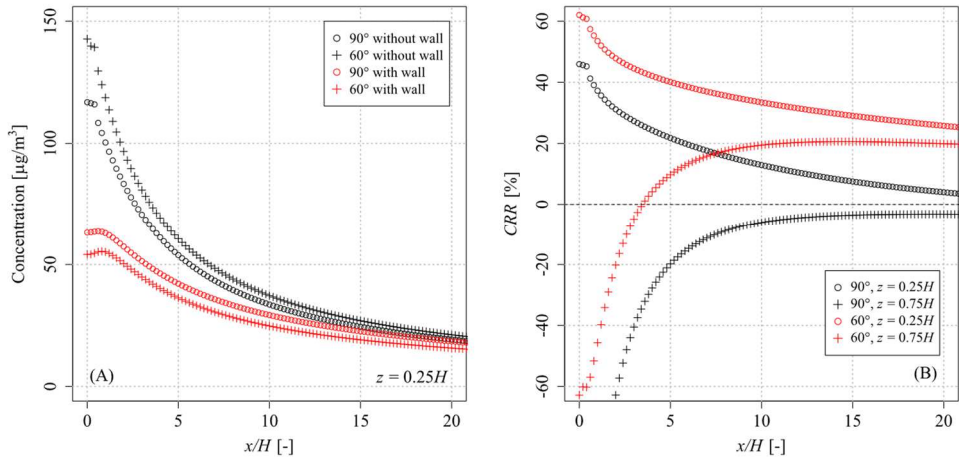
Figure 7.8 – Evolution of the concentrations with and without noise barriers (A) and the concentration reduction rates (B) as a function of the wind direction and for a given wind speed ($U_H = 3.15$ m/s).

According to the previous results, when studying the CRR behind noise barriers for neutral cases, it is necessary to study only one wind speed for each wind direction. Moreover, if the minimal CRR is assessed, the study can be reduced to only one direction. Indeed, the perpendicular direction leads to the lowest CRR while the non-perpendicular directions lead to higher CRR.

7.4.2. Study with thermal effects

7.4.2.1. Evolution of the CRR as a function of the atmospheric stability

The concentration reduction rate was then studied considering mixed convection: forced convection induced by wind speed and natural convection induced by thermal stratifications. The CRR was therefore studied as a function of the Richardson number which includes wind speed (U_H) and thermal variations (ΔT).

The first results are presented in Figure 7.9 for three different Richardson numbers: (A) $Ri = 0.17$ corresponding to a stable atmosphere; (B) $Ri = 0$ corresponding to a neutral atmosphere; and (C) $Ri = -0.17$ corresponding to a slightly unstable atmosphere, for the same wind conditions (perpendicular wind with $U_H = 3.15$ m/s). Thus, ΔT is the only variable here. For the three cases considered, the concentration is highest directly behind the barriers ($x = 0$ m), just above them ($h = 5$ m) and generally decreases as the distance from the barrier increases or the height decreases. However, the concentrations are different depending on the case. Indeed, the concentrations are lowest for the stable case (A) and highest for the slightly unstable case (C). The neutral case (B) leads to intermediate results but closer to the unstable one. For a given wind speed and direction, thermal effects therefore have a high impact on the concentration behind the barriers and seem to have a greater impact for $\Delta T > 0$ than for $\Delta T < 0$.
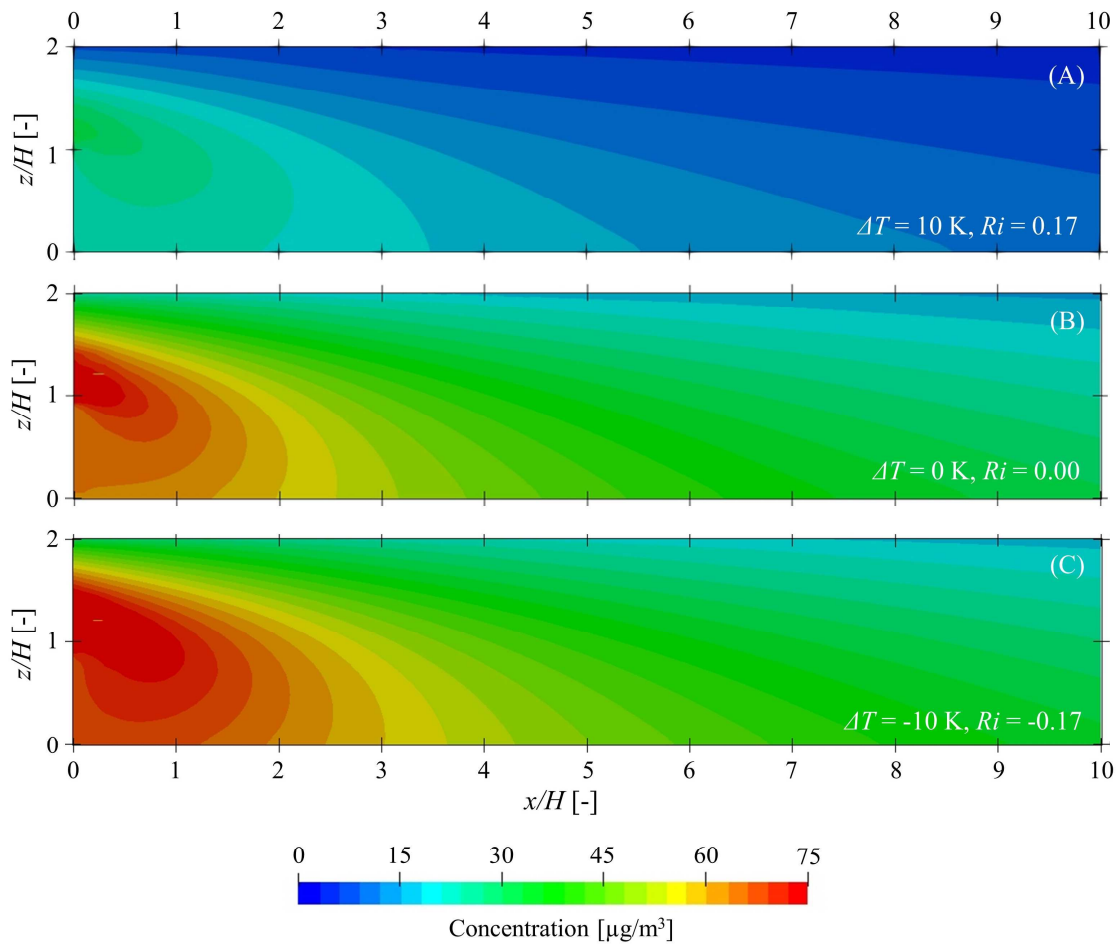
Figure 7.9 – Evolution of the concentration behind the downwind barrier as a function of the temperature variation in the same wind conditions (perpendicular wind, $U_H = 3.15$ m/s).

The evolution of the CRR as a function of the distance from the downwind barrier was studied for several atmospheric stabilities by changing both the wind speed (U_H) and the thermal variation (ΔT). The results for Ri = -1.20, -0.17, -0.06, 0.00, 0.06, 0.17 and 1.20 are given in Figure 7.10 for $z = 0.25H$ (A), $0.50H$ (B), $0.75H$ (C) and $1.00H$ (D). Further results are presented in Figure 7.10 (E) and correspond to the CRR averaged over z for z ranging from 0 to 5 m giving global information along the height of the noise barriers.

As can be seen in Figure 7.10, the evolution of the CRR follow the same trends. Indeed, for all the altitudes considered and also for the CRR averaged over $z = H$, the results for the neutral case are bounded by the results for the stable cases and the unstable cases: the unstable cases lead to lower $CRRs$ compared to the neutral case, with the lowest CRR being obtained for the highest unstability level (Ri = -1.20). On the contrary, the stable cases lead to higher $CRRs$ with

the highest CRR being obtained for the highest stability level ($Ri = 1.20$). However, the evolution of the CRR according to the level of stability or unstability is not equivalent between the two cases. Indeed, whereas the results are different for the three unstable cases presented in Figure 7.10, the CRR for the two highest stable cases ($Ri = 0.17$ and $Ri = 1.20$) are very similar. Furthermore, the CRR changes more quickly as a function of the Richardson number for the stable cases than for the unstable cases, which is consistent with the previous results discussed in relation with Figure 7.9. Thus, atmospheric stability has an impact on the CRR, leading to higher *CRRs* for stable cases ($Ri > 0$), quickly reaching maximum values, while lower *CRRs* are obtained for unstable cases ($Ri < 0$) and no maximum values were reached for the Richardson numbers considered in this study.

Figure 7.10 also shows that the CRR not only depends on the distance from the barriers but also on their height. For a given atmospheric stability, the CRR decreases with height and can reach negative values corresponding to an increase in pollutant concentration due to the barriers. These observations are related to the heights at which the plumes spread in both configurations, with and without the barriers. Indeed, without the noise barriers the plume spreads along the ground, leading to lower concentrations at $z = H$, while with the noise barriers the plume spreads from the top of the barriers and the concentrations are generally lower at ground level compared to the case without barriers.
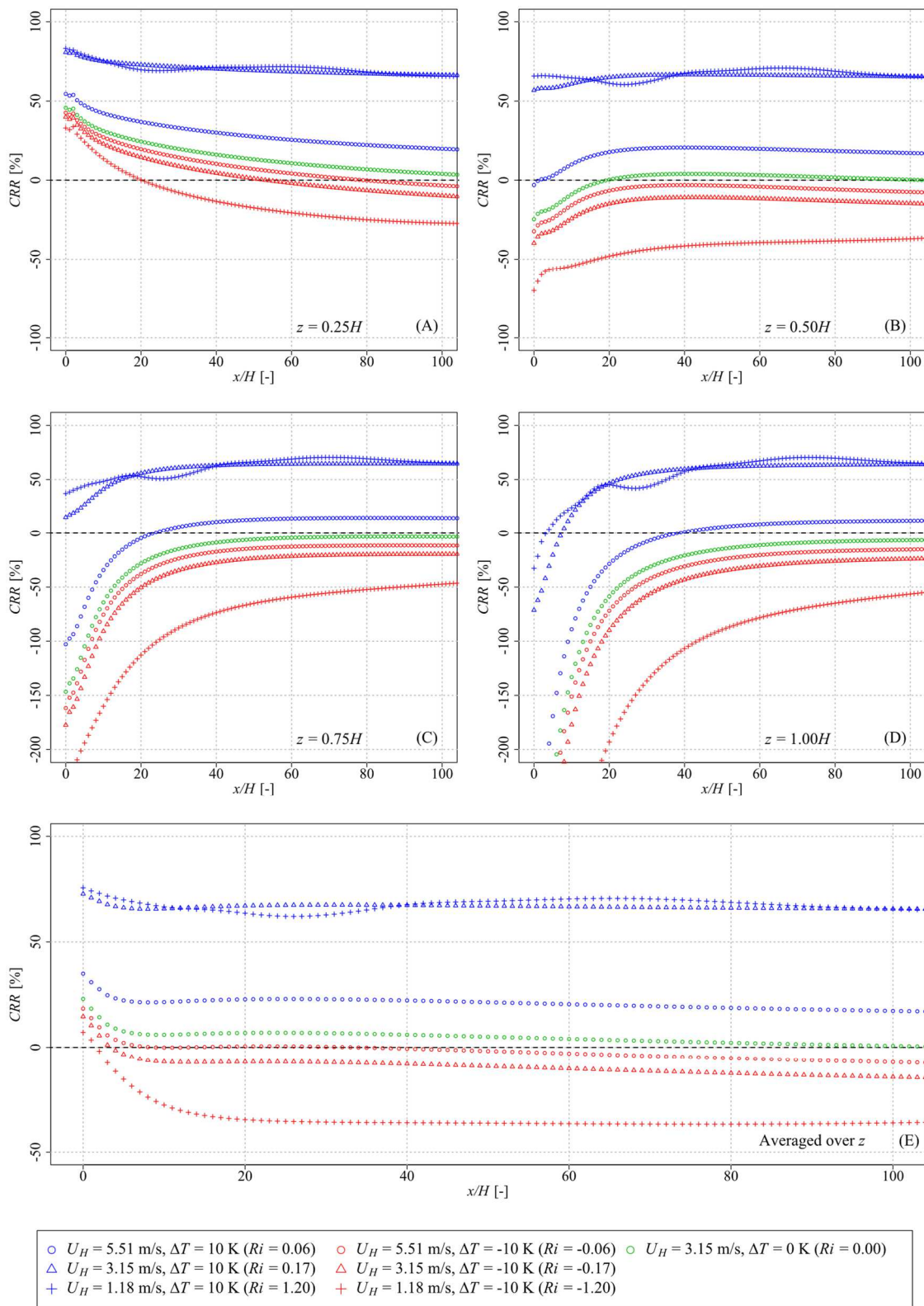
Figure 7.10 – Evolution of the concentration reduction rates for 4 given altitudes (A—D) and averaged over the noise barrier height (E) as a function of the distance from the downwind barrier and for several Richardson numbers.

7.4.2.2. Conservation of the CRR with the Richardson number

It has been shown previously that the concentration reduction rate for a given wind direction is constant when considering only forced convection (neutral atmosphere) due to an inversely proportional link between the pollutant concentrations and the wind speed. However, this link is no longer valid when considering both forced and natural convection. The question was then to assess if the CRR is still constant for stable and unstable cases. To answer this question, several simulations were performed for numerous Richardson numbers but with distinct couples of wind speed and thermal variations. The Richardson numbers considered were Ri = -1.20, -0.75, -0.50, -0.17, -0.06, 0.00, 0.06, 0.17, 0.33, 0.50 and 1.50.

Figure 7.11 (A) shows the evolution of the CRR for three couples of U_H and ΔT leading to Ri = -0.17 (slightly unstable atmosphere) while Figure 7.11 (B) shows the evolution of the CRR for two couples giving Ri = 0.50 (stable atmosphere). According to Fig. Figure 7.11 (A), the CRR can be constant for a given Ri. Indeed, with Ri = -0.17, while the pollutant concentrations are not the same for the three couples of U_H and ΔT considered, the CRR is quasi-constant ($\pm$ 3%). However, this observation is not true for all the Richardson numbers according to Figure 7.11 (B), which shows that for Ri = 0.50 the $CRRs$ are significatively different for the two couples of U_H and ΔT considered. Thus, the CRR can be constant for a given Ri but this is not generalizable.
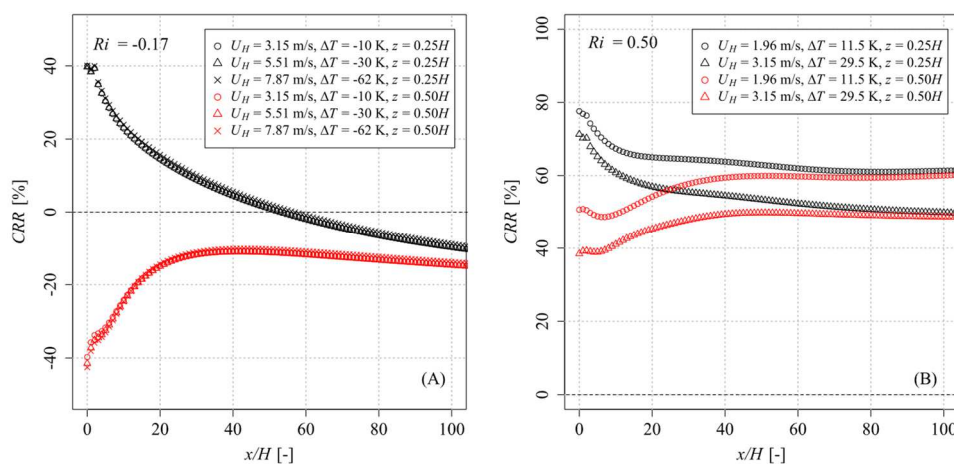
Figure 7.11 – Evolution of the concentration reduction rate for Ri = -0.17 (A) and Ri = 0.50 (B) as a function of wind speed (U_H) and thermal variation (ΔT) at z = 0.25H and z = 0.50H.

The Richardson numbers for which the CRR can be considered constant were assessed and the results are presented in Figure 7.12. The results show that, for a Ri ranging from -0.50 to 0.17, the variation over the CRR is less than 3% and the CRR can be considered as constant for a given Ri. For Richardson numbers outside this range, the variation over the CRR for a given Ri can reach 15% for a Ri ranging from -0.75 to -0.5 and 30% for a Ri ranging from -0.75 to -1.20 and from 0.17 to 1.20. According to these results, for a given Ri ranging from -0.50 to 0.17, a unique couple of U_H and ΔT must be considered when assessing the concentration reduction rates behind noise barriers in non-neutral cases.
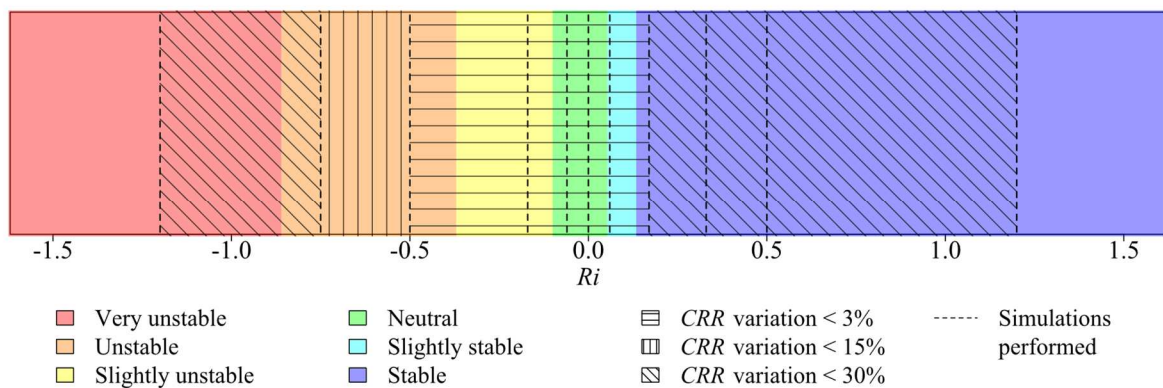
Figure 7.12 – Conservation of the concentration reduction rate with the Richardson number.

7.5. Discussion

This study provides better understanding of how noise barriers can reduce air pollution and how this reduction can vary with wind conditions and atmospheric stability. Additional work can be done to further improve this understanding and is discussed below, as is the relevance of these results.

This study considered only one noise barrier configuration, with two walls of the same height placed on either side of a heavy-traffic road. Further studies could be performed to verify if the results obtained for this configuration are generalizable, for example for noise barriers with only one upwind or downwind wall and also with a combination of solid and vegetative barriers, but also in presence of buildings before and after the barriers. Additionally, the height of $z = 0.25H$ (1.25 m) was considered to study the evolution of the CRR at the pedestrian level, which corresponds to the size of a child. The results were not provided for the size of adult

people ($z = 0.35H = 1.75$ m). However, results at this height can be approximated using both results at $z = 0.25H$ and $z = 0.50H$, for example by the means of a linear interpolation such as given in equation (Eq. 7.12).

$$CRR_{0.35H} = 0.6 \times CRR_{0.25H} + 0.4 \times CRR_{0.50H} \qquad \text{(Eq. 7.12)}$$

where $CRR_{0.35H}$ is the CRR at $z = 0.35H$, $CRR_{0.25H}$ is the CRR at $z = 0.25H$ and $CRR_{0.50H}$ is the CRR at $z = 0.50H$.

As shown in this paper, the turbulent Schmidt number has a different impact on the CRR depending on the location. There is no specific trend in the vicinity of the noise barrier. Indeed, there is an increase in the CRR when Sc_t increases at the height of the noise barrier while at ground level little variations are found. However, farther from the noise barrier, trends can be identified: the CRR systematically increases with increasing Sc_t, whatever the height considered.

It was shown that for a given Ri ranging from -0.50 to 0.17, variations over the CRR are negligible. Moreover, the evolution of the CRR as a function of distance from the downwind barrier seemed to follow the same trends, as the curves appear the same. Thus, it may be possible to find relationships between the CRR and the Richardson number in the range -0.50 to 0.17. If such relationships can be found, it will allow estimating all the $CRRs$ in this Ri range by performing only one simulation, or with only one in-field measurement.

Finally, according to the results of this study, further studies can be simplified. Indeed, for future studies in neutral atmosphere (without thermal variations), they could be reduced to only wind direction and noise barrier configuration studies when assessing the evolution of the CRR. For studies including mixed convection (with thermal variations), for a Ri ranging from -0.50 to 0.17, only one couple of wind speed and thermal variation is needed to assess the evolution of the CRR.

7.6. Conclusion

The effects of wind speed and atmospheric stability on the concentration reduction rate (CRR) of air pollutants induced by noise barriers were studied with a validated CFD model. This study considered both numerous wind conditions (wind speed and direction) and thermal variations, leading to different atmospheric stabilities ranging from very unstable cases to stable cases. Several CFD simulations were carried out and the main conclusions are as follows:

(a) When no thermal variations are considered, i.e. for a neutral atmosphere, the evolution of the CRR depends only on the wind direction: wind speed changes the pollutant concentrations behind the barriers but this parameter does not change the CRR.

(b) A non-perpendicular wind direction leads to higher pollutant concentrations without noise barriers and lower concentrations with the barriers compared to perpendicular cases. The $CRRs$ are therefore minimal for a perpendicular wind.

(c) The CRR decreases with height due to the different locations of the plume for the two cases with and without noise barriers. The global CRR decreases with distance from the downwind barrier.

(d) The CRR obtained with forced convection (neutral atmosphere) is bounded by the CRR obtained with mixed convection (stable and unstable atmospheres): higher $CRRs$ are obtained in stable conditions ($Ri > 0$) while lower $CRRs$ are obtained in unstable conditions ($Ri < 0$).

(e) For a given Richardson number ranging from -0.50 to 0.17, the CRR is constant with a variation of less than 3%. For numbers outside this range the variation increases to 15% for a Ri ranging from -0.75 to -0.5 and 30% for a Ri ranging from -1.20 to -0.75 and from 0.17 to 1.20.

Finally, these results give insights to researchers and civil engineers to better understand variations of air pollutant concentrations behind noise barriers, for example for carrying out further assessment studies on the impact of noise barriers on the reduction of air pollution, and for in-field monitoring campaigns.

Chapter 8:

Diagnosis and optimization –

In-situ application

8.1. Introduction

The application of CFD such as for design and understanding purposes has been demonstrated through the previous chapters. However, no case study of air quality assessment was yet proposed. This chapter is devoted to illustrating the operationality of CFD for studying air quality in urban areas as well as the applicability of the methodologies developed in this thesis and how they all fit together. The points covered in this chapter are highlighter in Figure 8.1.
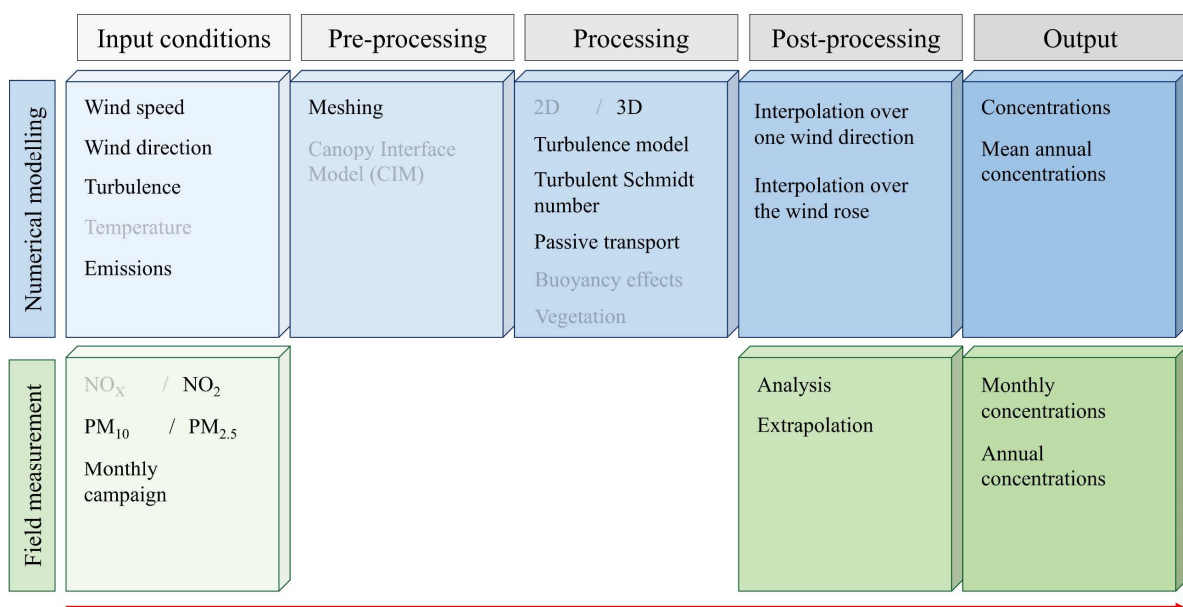
Figure 8.1 – Main points covered in Chapter 8.

This chapter provides answers to the following questions:

(?) How can the pervious methodology to assess mean annual NO_2 concentrations from monthly NO_2 concentrations be used in applied context?

(?) How can a CFD-RANS model be used for engineering purposes?

(?) How can the pervious methodology to assess mean annual concentrations based on CFD results be used in applied context?

(?) To what extent does this type of study provide recommendations for construction to limit exposure to air pollution?

8.2. Context of the study

8.2.1. Study location

The study selected for illustration purposes corresponds to an air quality study done in 2019 in Ostwald, France. The city of Ostwald is located in East France in the Grand-Est region (formerly known as Alsace region) in the Bas-Rhin department. This city, located south of Strasbourg and including around 13,000 inhabitants for a surface area of 7.11 km² according to the city website, is crossed by a major traffic artery, the A35 highway. With a daily vehicle flow rate of more than 100,000 veh/day, this highway corresponds to a major source of traffic-related emissions in Ostwald which can lead to poor air quality, especially for inhabitants living in its vicinity. In order to accommodate an ever-increasing number of inhabitants, new dwellings are constantly being built, which limits the number of areas suitable for construction. Areas initially not intended for residential use, or located close to high-traffic roads, become the only areas that can be built on with their resulting share of interrogations, especially about air quality.

The case study presented hereafter corresponds to a residential area located just next to the A35 highway. A satellite image of the area studied is given in Figure 8.2. For reasons of anonymity, the precise location of the study and the people involved will not be disclosed.

Figure 8.2 – Satellite image of Ostwald with the area studied (in red) and the highway (yellow arrow).

8.2.2. Comparison with urban scale air quality results

Outdoor air quality is the subject of numerous metrological and numerical investigations in the world. In France, the study of air quality is devoted to the AASQAs (Associations Agréées de Surveillance de la Qualité de l'Air), particularly in large cities. Most of air quality studies are based on mesoscale or urban scale models to produce annual maps of the average annual concentration of pollutants throughout the territories. Only few studies are developed using CFD models because of their time consumption, but also because their applications need specific expertise in fluid dynamics.

ATMO Grand Est is the AASQA located in the Grand Est region (eastern France) and produces studies over the "Eurométropole de Strasbourg". Concerning numerical modelling, different types of models are used, and each kind of simulation is dedicated to a specific application regarding its spatial resolution.

They provide several types of results including:
- Air quality simulations at regional scale, with mesoscale models driving to regional air quality plans and population forecasting.
- Air quality urban scale simulations to guide urban planning.
- CFD simulations to guide architectural designs for specific requests.

Figure 8.3 corresponds to Gaussian-based urban modelling results provided by ATMO Grand Est[1] in 2017. These maps allow the outdoor air quality to be gauged at urban scale, i.e. at the city level, and particularly in the area of interest highlighted by a black arrow. According to these figures, with around 32, 22 and 17 $\mu g/m^3$ for NO_2, PM_{10} and $PM_{2.5}$ respectively, annual standards given by the European Union (respectively 40, 30 and 20 $\mu g/m^3$) were not exceeded during 2017. The WHO guidelines for particulate matters (20 and 10 $\mu g/m^3$ for PM_{10} and $PM_{2.5}$ respectively) were nonetheless exceeded. The number of days on which the daily averaged PM_{10} concentration of 50 $\mu g/m^3$ PM_{10} was exceeded also complied with the standard value set by the European Union (< 35 days/year).
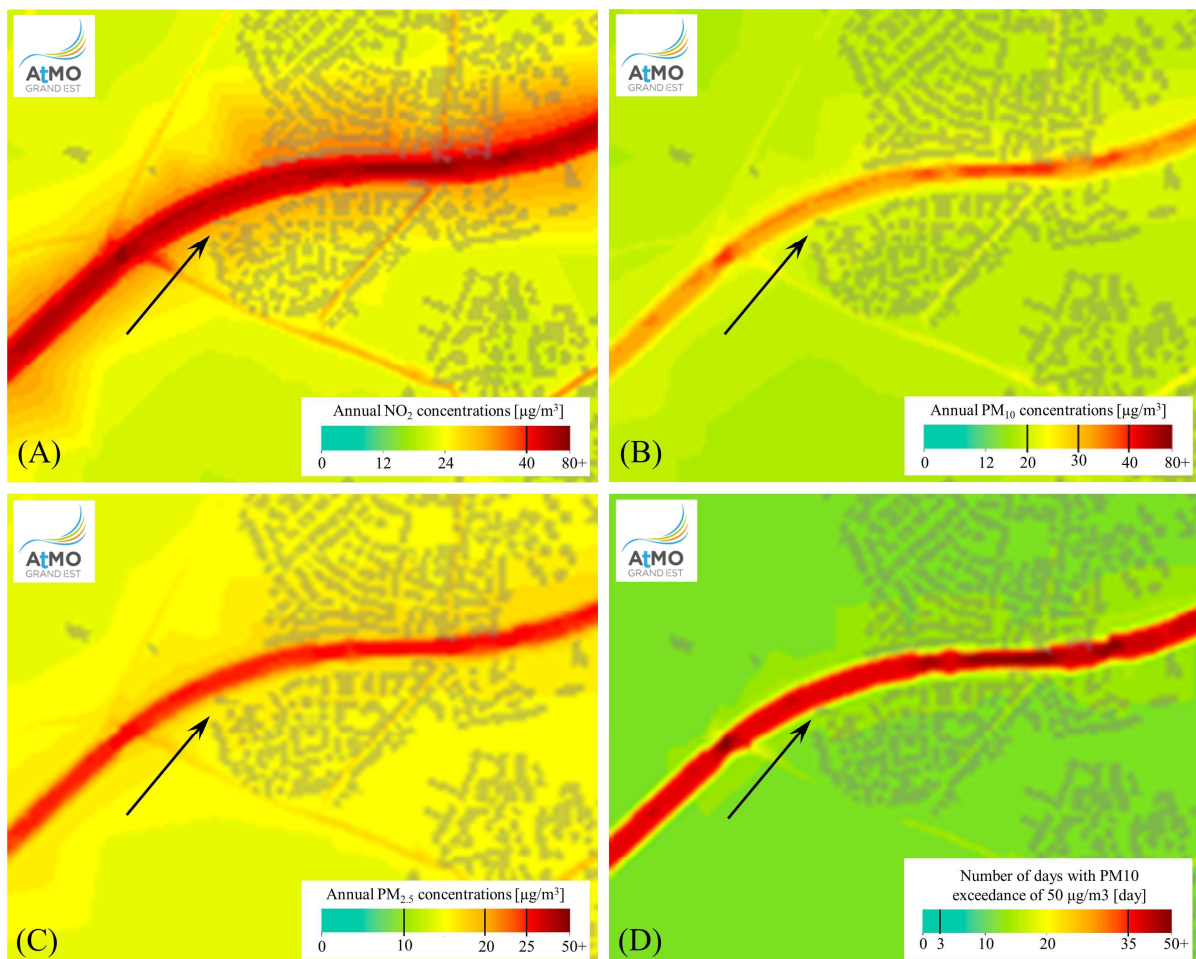
Figure 8.3 – Regional modelling results according to ATMO Grand Est with 2017 annual concentrations in (A) NO_2, (B) PM_{10} and (C) $PM_{2.5}$ and (D) the number of days with PM_{10} exceedance of 50 $\mu g/m^3$.

[1] Data provided under the reference WK-ADM-COS-18-0481

8.2.3. Aim of the study

The Gaussian model results presented in the previous section show that area of interest is subject to poor air quality due to the presence of the highway nearby: while the EU annual air quality standard and target values were not exceeded in 2017, the WHO guidelines were exceeded for particulate matter. For non-flat terrain (Kumar et al., 2015), as well as for low-level sources such as traffic-related emissions and for high densely built-up areas (Bady, 2017), Gaussian models are poor in predicting pollutant concentrations. These results alone may therefore not be sufficient to conclude on the air quality in the studied area, as they do not account for local air pollution dispersion phenomena induced by the presence of buildings of different sizes, orientations and heights Reiminger et al. (2020c) or noise barriers along the highway that can drastically modify pollution dispersion (Baldauf et al., 2008; Finn et al., 2010; Hagler et al., 2012; Reiminger et al., 2020a).

The aim of the study was the evaluation of the added value of CFD modelling and the methodologies developed to air quality assessment. The work was divided in two parts:

☞ On the one hand, the evaluation of the current on-site air quality by the means of a monthly air quality monitoring campaign on NO_2, PM_{10} and $PM_{2.5}$.

☞ On the other hand, the evaluation of annual NO_2, PM_{10} and $PM_{2,5}$ concentrations based on microscale modelling using computational fluid dynamics in order to consider the effects of buildings and, particularly, the noise barriers on the dispersion of the highway traffic-related emissions.

8.3. Winter air quality monitoring campaign

Monitoring campaigns has the disadvantage of requiring time, and does not allow the study of mobility, emissions and building evolution scenarios. However, they have the great advantage of reporting what is actually happening, and it is why it has been used to assess the current on-site air quality.

An air pollution measurement sensor supplied by Hager Services was installed in the study area for one month during winter, from 11/20/2019 to 12/19/2019. It was placed on a wire mesh (see Figure 8.4 below) at human height (approximately 1.5 m above ground level) and approximately 60 m from the noise barrier of the A35 highway. The sensor measures nitrogen dioxide (NO_2) and particulate matters (PM_{10} and $PM_{2.5}$).

Figure 8.4 – Location of the sensor in the studied area with a photography of the sensor (left) and a satellite view from Geoportail (right).

8.3.1. Results of the monitoring campaign

The evolution of NO_2, PM_{10} and $PM_{2.5}$ concentration monitored from 11/20/2019 to 12/19/2019 are presented in Figure 8.5 (the uncertainties of the sensors are around $\pm 20\%$ for $NO_2 > 40\,\mu g/m^3$ and $\pm 15\%$ for $PM > 15\,\mu g/m^3$). A summary of some statistical indicators including the three quartiles, the 95th percentile and the averaged concentration is also provided in Table 8.1.

Table 8.1 – Global results from the winter air quality monitoring campaign

Pollutant	Concentration [$\mu g/m^3$]				Average
	1st quartile	2nd quartile	3rd quartile	95th percentile	
NO_2	24	28	32	44	30
PM_{10}	25	27	27	28	26
$PM_{2.5}$	15	16	16	18	16
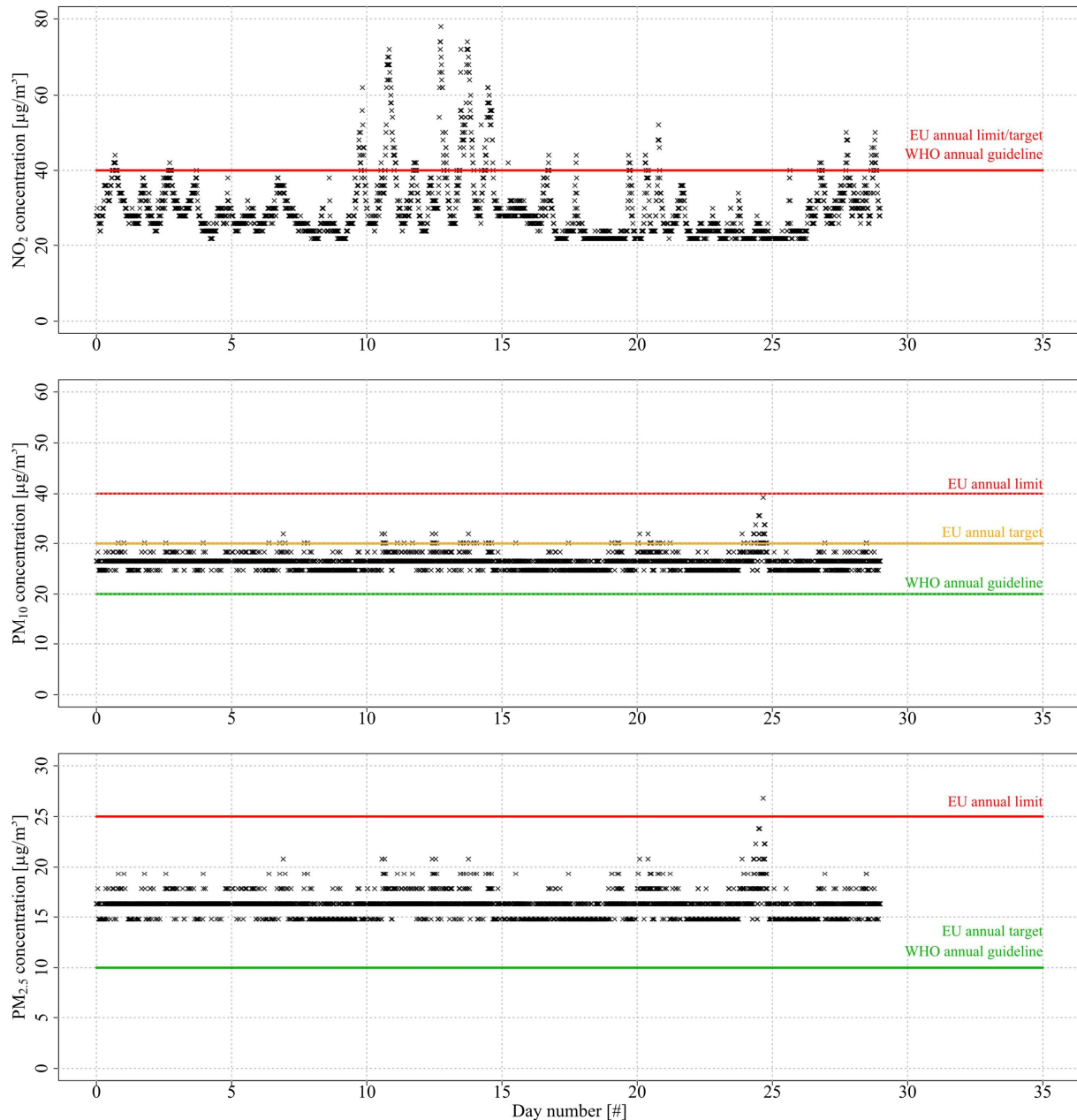
Figure 8.5 – Evolution of the NO_2, PM_{10} and $PM_{2.5}$ concentrations from 11/20/2019 to 12/19/2019.

☞ Measurements show that the NO_2 concentration at the sensor site exceeded the annual EU limit value of 40 µg/m³ several times. However, the average NO_2 concentration did not exceed 30 µg/m³, which is 25% below the annual limit value and the air quality target/guideline set by the EU and the WHO. It is also important to note that the 3rd quartile (i.e., 75th percentile) of concentrations also did not exceed the value of 40 µg/m³. Finally, no concentrations exceeded 200 µg/m³.

☞ For PM_{10}, concentrations did not exceed the annual limit value of 40 µg/m³. The average PM_{10} concentration was lower than 30 µg/m³ which is 25% below the annual EU limit value. The EU air quality objective of 30 µg/m3 was also reached, but not the WHO air quality guideline of 20 µg/m³. The 3rd quartile of concentrations also did not exceed the value of 40 µg/m³. Finally, no daily concentration exceeded 50 µg/m³.

☞ Lastly, $PM_{2.5}$ concentrations exceeded the EU annual limit value of 25 µg/m³ once. The average $PM_{2.5}$ concentration did not exceed 20 µg/m³, which is 20% below the annual EU annual limit value. However, the EU/WHO air quality target/guideline of 10 µg/m³ was not achieved during the measurement campaign. Finally, the 3rd quartile of concentrations also did not exceed the value of 25 µg/m³.

The comparisons given above can rightly be discussed. Indeed, the concentration values obtained during the measurement campaign are not annual values. The annual standards given by the EU and WHO were used for the sole purpose of having a reference for comparison, and it is not only because the monthly concentrations monitored did not exceed the annual standards that the annual concentrations will also do so. However, it should be noted that the measurement campaign was done during winter, a season usually known to have higher air pollutant concentrations due to higher emissions (cold-started vehicles, individual and district heating, etc.). Thus, it can be assumed that the annual concentrations will be lower than the concentrations measured during this campaign and, therefore, will also comply with the limit values.

8.3.2. Assessment of the corresponding mean annual NO₂ concentration

A methodology given by Jurado et al. (2020) to assess annual NO₂ concentration based on monthly concentration has been presented in Chapter 5. This methodology was applied to the results of the measurement campaign presented in the previous section firstly to assess the annual NO₂ concentration and, secondly, to illustrate practically the methodology. The methodology is based on three equations recalled below:

$$[NO_2]_a = \alpha . [NO_2]_m{}^2 + \beta . [NO_2]_m \qquad \text{(Eq. 8.1)}$$

where $[NO_2]_a$ is the annual assessed NO$_2$ concentration [µg/m³], $[NO_2]_m$ the monthly monitored NO$_2$ concentration [µg/m³] and a [m³/µg] and b [-] two parameters depending on the measurement campaign period (see the equations below).

$$\alpha = 0.0033 - 0.0102. \exp\left[\frac{-(m - 6.5749)^2}{8.6962}\right] \qquad \text{(Eq. 8.2)}$$

$$\beta = 0.6945 + 0.8708. \exp\left[\frac{-(m - 6.7076)^2}{7.4328}\right] \qquad \text{(Eq. 8.3)}$$

where m is the month corresponding to the measurement campaign and can be a float for measurement campaigns overlapping two months.

The campaign was conducted from November 20, 2020 to December 19, 2020, leading to $m = 11.67$ and, therefore, $\alpha = 2.78 \times 10^{-3}$ m³/µg and $\beta = 0.663$ according to (Eq. 8.2) and (Eq. 8.3).

With these parameters, we have $[NO_2]_a = 22.4$ µg/m³. However, the uncertainties of the methodology must be considered and especially the uncertainties over December which gave the highest deviation (15%). Finally, it leads to $[NO_2]_a = 22.4 \pm 3.4$ µg/m³.

The annual assessed NO$_2$ concentration is, as assumed previously, lower than the monthly monitored NO$_2$ concentration. This result will be compared latter with the numerical results to see if anything consistent can be obtained between this methodology and the numerical model.

8.4. CFD assessment of annual mean concentrations

The numerical modelling method chosen for this study is a Computational Fluid Dynamics method (CFD), using an Unsteady Reynolds-Averaged Navier-Stokes methodology (URANS). This method allows the complete resolution of the wind speed calculation equations without the simplifying assumptions required for other simpler models (i.e. considering a uniform velocity profile, steady state, etc.). As a result, the wind speed at each point of the model is computed in three dimensions, taking into account the presence and the particular layout of the building (dimensions, orientation, heights, etc.). The complexity of the flow and also the

turbulence linked to the presence of obstacles (buildings) is finally taken into account in the evolution of the pollution plume.

8.4.1. Numerical domain

8.4.1.1. Creation of the 3D geometry

The first step in the modelling process is the creation of the numerical domain with all existing buildings. The area of interest has then been reproduced in 3D using the Salome software and 3D data given in open access by the "Eurometropole de Strasbourg". This study also requires the consideration of buildings external to the development project, i.e. located upstream (noise barriers), downstream and on the edges of the study area, as these can significantly impact the numerical results. Finally, it should be noted that the recommendations given by the COST Action 732 guidelines were followed (see Section 3.2.1. for further details). The resulting geometry is illustrated in Figure 8.6.

Then, the resulting domain has been decomposed into grids in all the three dimensions using 1 m meshes in the area of interest and a finer refinement of 0.5 m near the ground and the obstacles (buildings, noise barriers, etc.) to allow the resolution of flow and transport equations (see Section 3.2.2. for further details on meshing). An illustration of the resulting grid is given in Figure 8.7 which lead to a total number of around 3 million cells, a grid sensitivity of less than 5% according to the grid convergence index and $y^+ = 350$ included in the usual range (from 30 to 500, see Section 3.2.2.1. for further information).
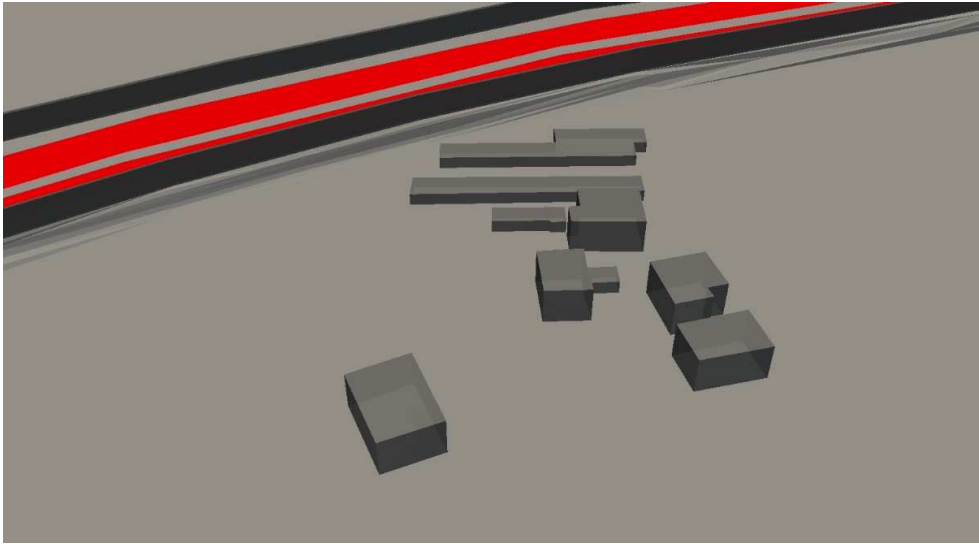
Figure 8.6 – Illustration of the 3D geometry obtained.
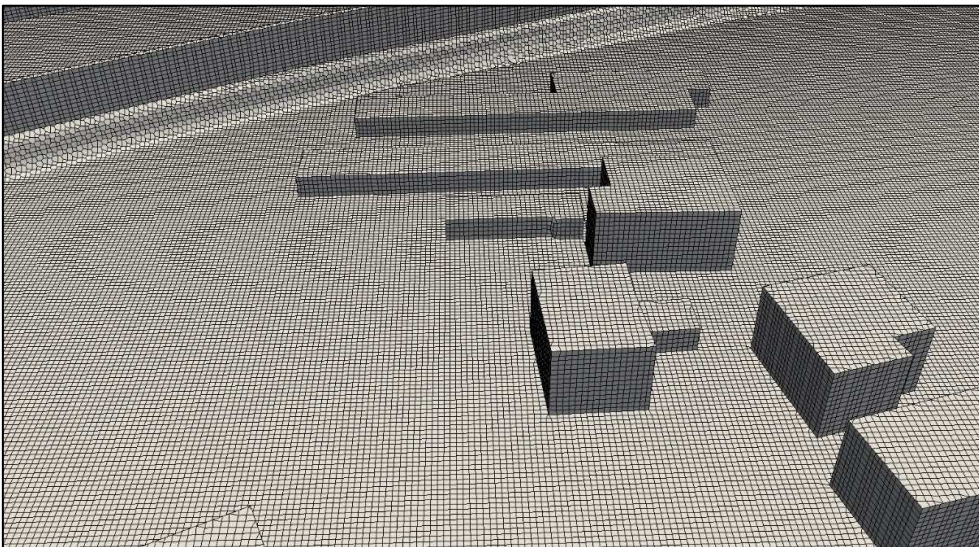
Figure 8.7 – Illustration of the grid obtained.

8.4.1.2. Solver and boundary conditions

For this study, only the Forced Convection Solver described in Section 2.2. was considered since no methodology to compute annual concentration based on non-neutral CFD results are yet available.

The recommendations of the COST Action 732 guidelines were also followed concerning the boundary conditions. In particular, the following boundary conditions were used:

- **Inlet boundary:** the log law velocity profile and it corresponding turbulent kinetic energy and dissipation profiles given by Richards and Norris (2011) with U_h = 1.5 m/s for the reference height of h = 10 m.

- **Outlet boundary:** an open boundary with a constant static pressure set to the atmospheric pressure.

- **Top and lateral boundaries:** symmetry conditions to enforce a parallel flow.

- **Wall boundaries:** no slip conditions.

A full description of the boundary conditions above-mentioned can be found in Section 3.3.
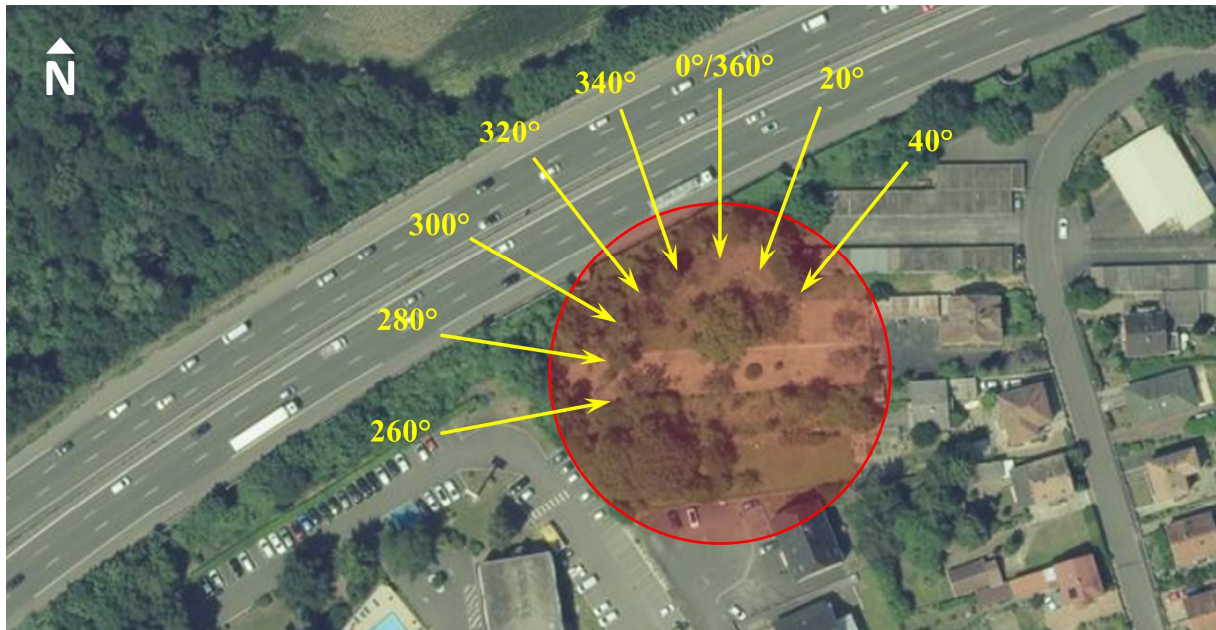
Figure 8.8 – Illustration of the wind directions carrying pollutants from the highway to the area of interest and considered for the simulations.

Finally, since the A35 highway is the only significant source of traffic-related emissions near the area, the simulations can be restrained to the sole wind directions carrying pollutants from the highway to the area of interest. Considering a 20° step, it corresponds to 8 wind directions from 260° North to 40° North which are illustrated in Figure 8.8.

8.4.1.3. Emissions assessment

Emissions were calculated on the basis of methods proposed by the European Environment Agency (EEA) in their guidebook entitled "EMEP/EEA Air pollutant emission inventory guidebook 2016" (see Section 3.3.3. for further details). In particular, the following methods were used:

- Tier 3 method for engine-related emissions of NO_x, PM_{10} and $PM_{2.5}$ considering both hot and cold emissions.
- Tier 2 method for PM_{10} and $PM_{2.5}$ emissions related to brake, tyre and road wear.

In order to calculate traffic-related emissions with the EEA methodology, the following assumptions were made:

- The French metropolitan fleet in 2017 given by the CITEPA in terms of the share of different vehicles and technologies (see Table 3.8 and Table 3.9) considering 10% of heavy-duty trucks according to the DIREST (Interdepartmental Directorate of Eastern Roads).
- A road of 400 m long was considered which corresponds to the length of the road in the computational domain with a 0% slope.
- A load of heavy-duty trucks of 50% considering one half of unloaded trucks and one half fully loaded.
- A cold start share of 30% because of the proximity of the highway access roads and nearby dwellings.

The last data needed corresponds to the speed and the number of vehicles. The A35 highway is known to have high variations in these two parameters due to its proximity with the Strasbourg City where traffic jams are common during weekday rush hours. Thus, considering daily averaged speed and number of vehicles could lead to high underestimations of the emissions. To prevent that, hourly averaged speed and number of vehicles were considered instead distinguishing between weekdays (WD), Saturdays/holiday eve (SAT) and Sundays/holidays (SUN). These data, near the area of interest and for the year 2018, were obtained from the DIREST and are presented in Figure 8.9. This figure shows that variations over the vehicle's

speed is mostly observed during weekdays around 8:00 A.M. and 5:00 P.M. where pikes of vehicle numbers are also recorded.
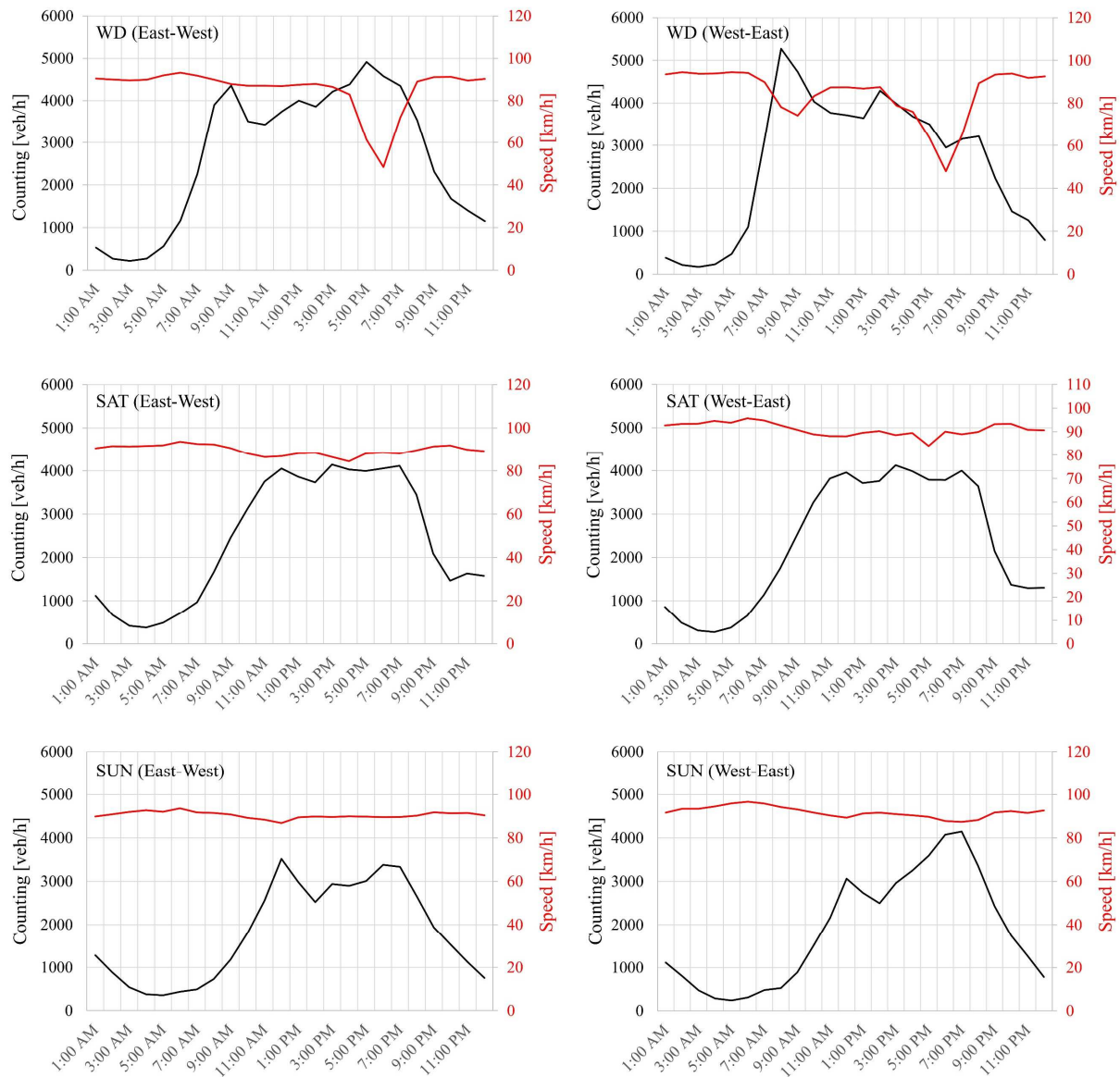
Figure 8.9 – Counting and speed of vehicles on the A35 highway next to the area of interest according to the type of day and the travelled direction.

Emissions in NO_x, PM_{10} and $PM_{2.5}$ were calculated based on the previously cited methods and assumptions for each hour of each type of day and travelled directions. The resulting emissions in both travelled directions were then summed for each hour of each type of day to consider simultaneously both directions of traffic. Finally, the weighted hourly averaged emissions were

calculated taking into account the number of occurrences on the different types of days per year and a representative averaged daily emission related to traffic was obtained.

The corresponding emissions are 348 mg/s, 28 mg/s and 21.5 mg/s, respectively for NO_x, PM_{10} and $PM_{2.5}$ pollutants, and where specified in the computational domain in the first layer of cells adjacent to the highway.

8.4.1.4. Background concentration

Simulation results are composed of background pollution from unmodelled external sources and concentrations from the sources included in the simulation. The background concentrations selected for this study correspond to the annual averaged concentrations in 2018 available for specific background stations near Ostwald managed by ATMO Grand Est.

Particularly, we have:

- The stations "STG Est" and "STG Ouest" for the nitrogen dioxides NO_2, with respectively 25 µg/m^3 and 19 µg/m^3 in 2018, leading to an average value of 22 µg/m^3.
- The station "STG Nord" for PM_{10} with 21 µg/m^3 in 2018.
- The station "STG Est" for $PM_{2.5}$ with 14 µg/m^3 in 2018.

Note: A methodology suggested by Gómez-Losada et al. (2016a) based on the Hidden Markov Model was previously described in Section 3.3.4. with the aim of assessing background concentrations from non-background stations. It was shown that the results of this methodology are fluctuating around the 1st quartile of concentrations with more or less 10% of difference. It should be noted that the first quartiles of concentrations obtained during the monitoring campaign were 24 µg/m^3, 25 µg/m^3 and 15 µg/m^3 respectively for NO_2, PM_{10} and $PM_{2.5}$ which are, considering a variation of 10%, really close to the actual background concentrations. Additionally, the other suggested methodology considering monitored data during the night (from 2:00 A.M. to 5:00 P.M.) lead to closer results to those from the background stations with 21 µg/m^3, 21 µg/m^3 and 12 µg/m^3 respectively for NO_2, PM_{10} and $PM_{2.5}$.

8.4.2. Results of the numerical study

8.4.2.1. Impact of the noise barriers and the buildings on the fluid flow

An illustration of the evolution of the wind speed and the wind directions (velocity vectors) is proposed in Figure 8.10. This figure shows how obstacles such as the noise barriers or the buildings can highly impact the fluid flow. As an example, it can be observed that the velocities can become twice lower downstream the highway than upstream for the same altitude, and several tens of meters are needed to recover the initial wind speed. Moreover, while the wind direction is globally directed to the highway (south direction), the global direction of the wind direction after the highway tends to be southwesterly and numerous recirculation areas can be observed.
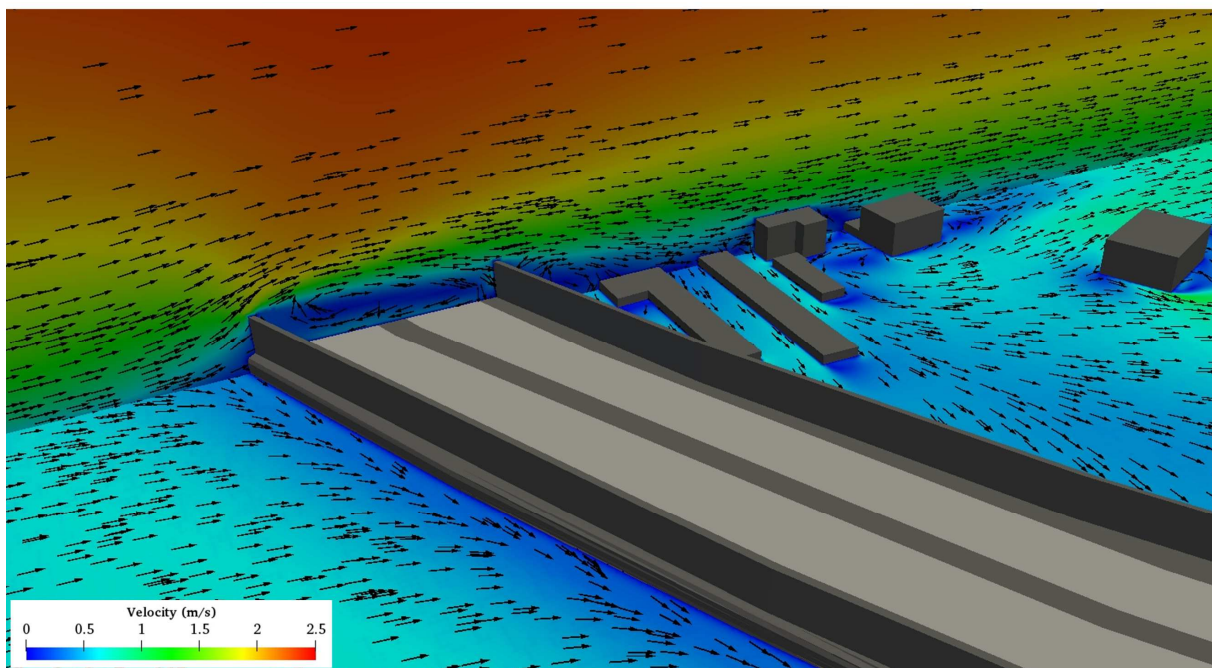
Figure 8.10 – 3D view of the evolution of the wind speeds and directions for an inlet wind direction of 0° north and an initial wind speed of 1.5 m/s at 10 meters high.

8.4.2.2. Assessment of the mean annual concentrations

The results on pollutant concentrations cannot be directly compared to the regulatory values and the guidelines given by the European Union and the World Health Organization. Indeed, these results are wind speed and wind direction dependent while the regulatory values and the

guidelines are not. It is therefore necessary to combine all numerical results in order to obtain concentration values comparable with these standards. It is particularly necessary to have an idea of the annual concentrations.

The annual concentrations based on the CFD results were assessed according to the methodology of Reiminger et al. (2020b) described in Chapter 4. Firstly, the wind distribution of each wind direction considered was assessed based on the wind rose data given by Météo-France at the nearest meteorological station from the area of interest (see Section 4.3.1. for further details), the wind rose being proposed in Figure 8.11. Secondly, based on the wind distributions previously obtained, the NO_2, PM_{10} and $PM_{2.5}$ mean annual concentrations were assessed using the continuous methodology (see Section 4.3.2. fort further details). It should also be noted that a part of the CFD results was obtained in terms of NO_x concentrations and not NO_2. The NO_2 concentrations were calculated using the methodology described in Section 5.3.1. and based on the modelled NO_x results. The annual concentrations finally obtained are presented in Figure 8.12.
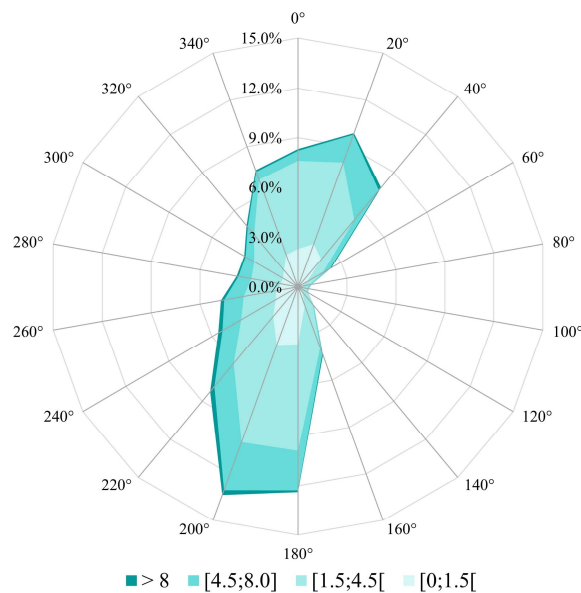
Figure 8.11 – Wind rose, Entzheim meteorological station, 1991-2010, data from Météo-France [m/s]
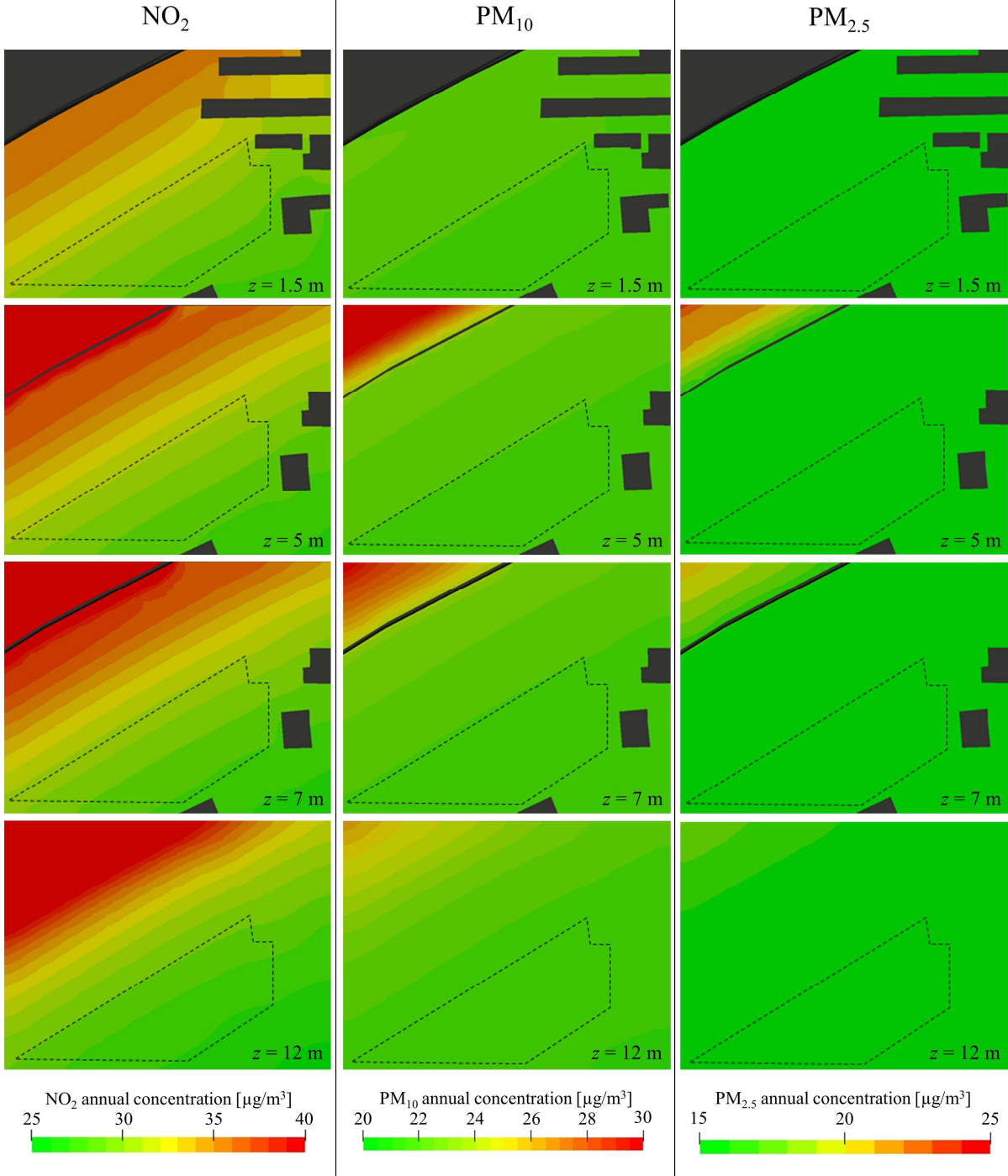
Figure 8.12 – Annual NO$_2$, PM$_{10}$ and PM$_{2.5}$ concentrations modelled for different altitudes with the area planned to be built delimited with dashed lines.

The results presented in the previous figures show that, in the studied area, NO_2 mean annual concentrations are more variable than PM_{10} and $PM_{2.5}$ annual concentration. The main results are as follows:

- **Regarding NO₂:** A mean annual concentration of around 40 µg/m^3 is obtained for 7 m and 12 m high in the vicinity of the downwind noise barriers which correspond to the non-constructible area. In the area planned to be built, which is highlighted in the previous figures, NO_2 annual concentrations are ranging from 25 µg/m^3 to 32 µg/m^3 depending on the distance from the highway. Also, in this area, annual concentrations decrease with the altitude and lead to maximal annual NO_2 concentrations of around 27 µg/m^3 for 12 m high nearest to the highway.

- **Regarding PM₁₀:** A maximal mean annual concentration of 23 µg/m^3 is observed in the area planned to be built.

- **Regarding PM₂.₅:** A maximal mean annual concentration of 16 µg/m^3 is observed in the area planned to be built.

It is important to note that in the non-constructible area near the highway, concentrations tend to increase with altitude due to the plume coming from the top of the downwind noise barrier. The observation is different in the area planned to be built, where higher elevations result in lower concentrations. Finally, whatever the pollutant under consideration, concentrations are lowering the further away from the highway.

Lastly, a comparison can be made between the annual NO_2 concentration previously assessed based on the winter monitoring campaign and the annual NO_2 concentrations modelled. The value of 22.4 ± 3.4 µg/m^3 previously obtained as a result of the methodology presented in Chapter 5 applied to the winter monitoring campaign is really close to the annual NO_2 concentration modelled where a value of around 25 µg/m^3 is obtained. This result is very promising, since it shows a strong concordance between a methodology applied to experimental field data and methodologies applied to a CFD-type numerical model.

8.5. Conclusions

8.5.1. Conclusion of the study and recommendations

The aim of the study was:

1. On the one hand, the evaluation of the current on-site air quality by the means of a monthly air quality monitoring campaign on NO_2, PM_{10} and $PM_{2.5}$.

2. On the other hand, the evaluation of annual NO_2, PM_{10} and $PM_{2.5}$ concentrations based on microscale modelling using computational fluid dynamics in order to consider the effects of buildings and, particularly, the noise barriers on the dispersion of the highway traffic-related emissions.

The conclusions of the study are as follows:

1. (a) Mean concentrations measured between the 20[th of] November 2019 and the 19[th of] December 2019 during the winter campaign (30, 26 and 16 $\mu g/m^3$ for NO_2, PM_{10} and $PM_{2.5}$ respectively) did not exceed the annual EU regulatory values. In addition, the values corresponding to the 3rd quartile of concentrations also did not exceed them.

   (b) The air quality guidelines and targets set by the EU and the WHO are met for NO_2 during the measurement campaign as well as the EU target for PM_{10}.

   (c) The air quality guidelines set by the WHO for PM_{10} and $PM_{2.5}$ were exceeded during the monitoring campaign.

2. (a) In terms of annual concentrations and according to the results proposed by ATMO Grand Est in 2017, the study area was subject to pollutant concentrations lower than the regulatory values given by the European Union with mean annual concentrations of around 32 $\mu g/m^3$ for NO_2, 22 $\mu g/m^3$ for PM_{10} and 17 $\mu g/m3$ for $PM_{2.5}$.

   (b) According to the CFD results, the maximum mean annual concentrations of NO_2, PM_{10} and $PM_{2.5}$ in the area planned to be built are 32, 23 and 16 $\mu g/m^3$ respectively, which is below the annual regulatory values set by the European Union of around 20 to

40% depending on the pollutant considered. This finding, which is consistent with the results proposed by ATMO Grand Est, is valid up to an altitude of 12 m.

(c) The air quality guidelines and target set by the European Union and the World Health Organization are respected for NO_2. The air quality target set by the European Union for PM_{10} is also met.

(d) The air quality guidelines set by the WHO for PM_{10} and $PM_{2.5}$ are exceeded.

On the basis of the *in-situ* measurement campaign as well as the numerous 3D simulations carried out, the area planned to be built complies with European regulations from the point of view of air quality. However, air pollution is responsible for effects on health and it is important to limit the exposure to pollution of future people living in this area. Recommendations can then be made in this regard.

According to both urban scale ATMO Grand Est and microscale CFD results, air pollution is the higher near the highway and decreases with increasing distance. Based on this observation, it is recommended to place air intakes for ventilation on the face(s) of the building(s) facing south-southeast. A double flow type ventilation system with an efficient filtration system is recommended to limit the contribution of pollutants to the indoor air in the dwellings. In the same vein, balconies will have to be placed on the south-southeast side of the buildings. Such arrangements could also be made on the north side if loggia-type airtightness devices are provided.

The CFD results have shown an additional information which was not possible to know with the urban scale model: air pollution is globally increasing with the altitude due to the noise barrier. Thus, it can be recommended that the dwellings must have no more than two levels (ground floor and first floor). Attics may be developed as long as the regulations in force in the local urban plan are respected regarding maximum heights under gutters (7 m) and overall (12 m).

Finally, recommendations can also be made concerning terraces and gardens. To protect people, the mask effect of the dwellings can be used. To do so, gardens and terraces should be placed in the south-south-eastern part of the plots as close as possible to the buildings. To go further, they might be bordered by impermeable (wooden or glass palisades, etc.) or almost

impermeable surfaces (hedges or dense permanent vegetation, i.e. also present in winter) in order to limit the input of pollutants to the gardens. When using plants, it is preferable to choose non-allergenic plants.

8.5.2. Conclusion of the chapter

The aims of this chapter were to illustrate the operationality of CFD for studying air quality in urban areas as well as the applicability of the methodologies developed in this thesis and how they all fit together. To do so, full-scale study has been conducted in Ostwald, France, with the aim of assessing air quality in an area planned to be built located near a major highway.

The whole chapters presented in the first part of this thesis have contributed to the completion of this study. Indeed, the Forced Convection Solver described and validated in Chapter 2 has been used with many concepts discussed in Chapter 3 including computational domain extension, boundary conditions, emissions, and background concentration. Then, the methodologies developed in Chapter 5 were used, firstly to convert modelled NO_x concentrations into NO_2 concentrations and, secondly, to assess the annual NO_2 concentration based on a one-month monitoring campaign done in winter. The methodologies described in Chapter 4 were lastly used to assess the wind distribution based on basic wind rose data and to put together all CFD results in order to have annual concentrations to compare with regulatory values. With these results, several recommendations were issued to limit the exposure of future inhabitants.

Finally, this chapter has shown the interest of CFD modelling to assess air quality in urban areas but also the interest of the different methodologies developed in this thesis.

Chapter 9:

General conclusion and beyond

9.1. General conclusion

The aim of this thesis was the development and the validation of Computational Fluid Dynamics (CFD) solvers and new methodologies to assess air quality in urban areas, intended for an operational audience dealing with engineering issues.

In the first part of this thesis, new CFD solvers as well as tools and methodologies were developed considering the scientific state-of-the-art and the engineering needs.

Regarding the development of CFD solvers for air pollution modelling

The choice was made to RANS-CFD (Reynolds-Averaged Navier-Stokes) and, especially, Unsteady RANS (URANS) in order to guarantee calculation times and, therefore, calculations costs consistent with engineering requirements. Two OpenFOAM based URANS-CFD solvers were developed including a solver for incompressible flows intended for neutral atmospheres modelling, called the *Forced Convection Solver*, and a solver for compressible flows intended for stable and unstable atmospheres modelling, called the *Mixed Convection Solver*. Additional phenomena were included is both codes with the effects of vegetation on the air flow and also on the pollutant (deposition) as well as the photostationary steady-state equilibrium. Both solvers were proven based on seven wind tunnel and *in-situ* test cases which included 2D and 3D configurations as well as thermal and vegetation effects, and the results showed that the model performed well. Modelled concentrations with less than 10% of error can be obtained

with accurate and reliable representation of the velocity field and also, accurate indoor/outdoor exchanges modelling using isotropic turbulence models such as the standard k-ε turbulence model.

Regarding the use of CFD solvers to assess air quality in urban areas

Research and improvements have been undertaken on the computational domain and the solver parametrization since the state-of-the-art showed that several issues can be attributed to these points. The COST Action 732 guidelines gave adequate recommendations in terms of minimal distances to include in the computational domain, nonetheless, it has been shown that a vertical distance of at least 96 m must be considered even in absence of buildings. It was shown that meshing satisfying a y^+ criterion ranging from 30 to 500 cannot be obtained without drastically increasing calculations times. However, 1 m hexametric cells in the area of interest and a finer refinement 0.5 m near the walls and at the emission source is a good compromise between calculation speed and mesh size, leading to grid independent results. Concerning boundary conditions, they can be highly improved especially for the inlet boundary by considering a coupling with 1D models such as the Canopy Interface Model which will compute reliable wind velocity and turbulence profiles consistent with such profiles found in urban areas. Lastly, emissions must be calculated with care using as an example the European Environment Agency guidebooks, and background concentrations carefully chosen to avoid final errors in the numerical results.

Regarding existing and new methodologies to assess air quality at urban scale

In order to make CFD modelling fully operational for engineering purposes, existing methodologies were proven, and several tools and new methodologies were developed

The Derwent and Middleton law, a one-parameter function to assess annual nitrogen dioxide (NO_2) concentrations based on annual nitrogen oxides (NO_x) concentrations, has been proven based on five years of monitored data in several regions in France. This function can be used instead of the Photostationary Steady-State equilibrium (PSS) in the CFD solver since it needs only one parameter, the NO_x concentration, and lead to less than 10% of error.

A new methodology using a quadratic and two gaussian-based functions was developed with the aim of assessing annual NO_2 concentrations with only one month of data. This methodology, leading to a maximal error of 15% and an overall one of around 10%, is highly relevant for numerical modelling, since it can for example be used to assess annual background concentrations quickly based on only one month of concentrations monitored with background stations.

A 5-parameters sigmoid function was developed to assess continuous wind distributions based on simplified and discrete data such as available with wind roses. This new function gives overall improvements over the Weibull distribution usually used and leads to an averaged error of 12% on wind distributions for four given wind roses in France. An optimization of this function was also developed in order to better assess some particular wind distributions, leading to lower errors.

The limits of discrete methodologies to assess annual concentrations based on punctual numerical results as well as their implicit assumptions were lastly discussed, and alternative methodologies were presented. It includes a variation over the discrete methodology considering representative velocities instead of intermediate velocities to avoid underestimations of pollutant concentrations, and a new continuous methodology to assess mean annual concentrations illustrated with CFD results.

Regarding the use of the CFD solvers and methodologies for design, understanding and diagnosis purposes

In the second part of this thesis, the CFD solvers as well as the methodologies developed were used to illustrate the interest and the powerfulness of such tools for urban planning design, understanding and diagnosis purposes.

The Forced Convection Solver has illustrated the potential of CFD solvers for design purposes through street canyons modelling. In particular, the effects of geometric properties of a step-down street canyon, which included buildings height and street width, were studied. The results showed that the recirculation patterns in the streets can change when the upwind building height increase and/or when the street width decrease, leading to a significant increase in the mean concentrations in the street.

The Mixed Convection Solver, for his part, has illustrated the usefulness of CFD solvers for understanding purposes through modelling the impact of noise barriers on pollutant dispersion. The evolution of the pollutant concentrations after the downwind noise barrier was studied as a function of the wind speed and the temperatures, thus, the atmospheric stability. The results showed that noise barriers can decrease pollutant concentrations, but differently depending on the atmospheric stability, the stable case leading to higher concentrations decreases. This study also showed that, for atmospheres neither too stable nor too unstable, results are only depended on the Richardson number.

Lastly, a real *in-situ* study involving many of the tools and the methodologies presented in this thesis demonstrated that the CFD model is able to evaluate air quality at the neighbourhood scale. Beyond the scope to explain how the concepts, the tools and the methodologies may be interconnected, and work together, few recommendations were proposed to reduce exposure to air pollution. It appears that the use of 3D CFD modelling to assess air pollution at urban scale is primordial to help architectural design. Surface air quality mapping may not be sufficient to define sustainable urban planning. A summary diagram of these interconnections is finally presented in Figure 9.1.

9.2. Beyond this thesis

The numerical solvers, the concepts and the methodologies developed and discussed in this thesis have been thought for operational applications in an applied context, particularly for engineering purposes, to be able to assess accurately air pollution in urban areas at microscale to guide planners and decision makers' choices. Their field of application is, however, broader, and can be extended to all aspects of applied and theoretical research. From a general perspective, several possible follow-up can be considered beyond this thesis, both scientific (numerical and experimental) and industrial:

From a numerical point of view:

- Including the effects of Vehicles Induced Turbulence (VIT) in the numerical solvers to consider the traffic effects on the airflow and the pollutants dispersion. In doing so, it will be necessary to verify the applicability of the methodology presented in this thesis

to assess the annual concentrations and, especially, to verify if the function describing the evolution of the concentration with the wind speed remains valid.

- Deepen the use of anisotropic turbulence models such as the Reynolds Stress Model (RSM) to consider the anisotropic nature of turbulence. It will be necessary to include the new turbulence parameters in the pollutant transport equation and, in particular, in the turbulent diffusion term.

- Generalizing the use of 1D models, such as the Canopy Interface Model (CIM), to improve the inlet boundary conditions when modelling densely built urban areas. In is particularly to verify if the results obtained in this thesis can be generalized for any wind condition (speed and direction) and any urban area. Later, this coupling should also be verified by including a variation in atmospheric stability.

- Applying the methodologies presented in this thesis, and especially the methodology to assess mean annual concentrations, to other computational fluid dynamics models such as the Large-Eddy Simulation (LES) to ensure that their applicability is not restrained to Reynolds-Averaged Navier-Stokes (RANS) modelling.

- Coupling the Mixed Convection Solver (MCS) with a radiation model. The MCS is able to consider thermal variations, and therefore different atmospheric stability, that can modify the airflow and the pollutants dispersion, but air and surface temperatures need to be specified. A radiation model is therefore necessary to compute these temperatures from meteorological and solar data.

From an experimental point of view:

- Monitoring annual air pollutant concentrations and meteorological data such as wind speed, wind direction, air temperature, solar radiation, etc. in an urban area to perform a final *in-situ* validation of the Forced and Mixed Convection Solvers (FCS/MCS) also implying the various methodologies proposed in this thesis.

- Monitoring air pollutant concentrations and meteorological data including thermal data (air temperature, solar radiation, etc.) in vegetated areas to validate the combined effects of vegetation and thermal stratification in the CFD solvers.
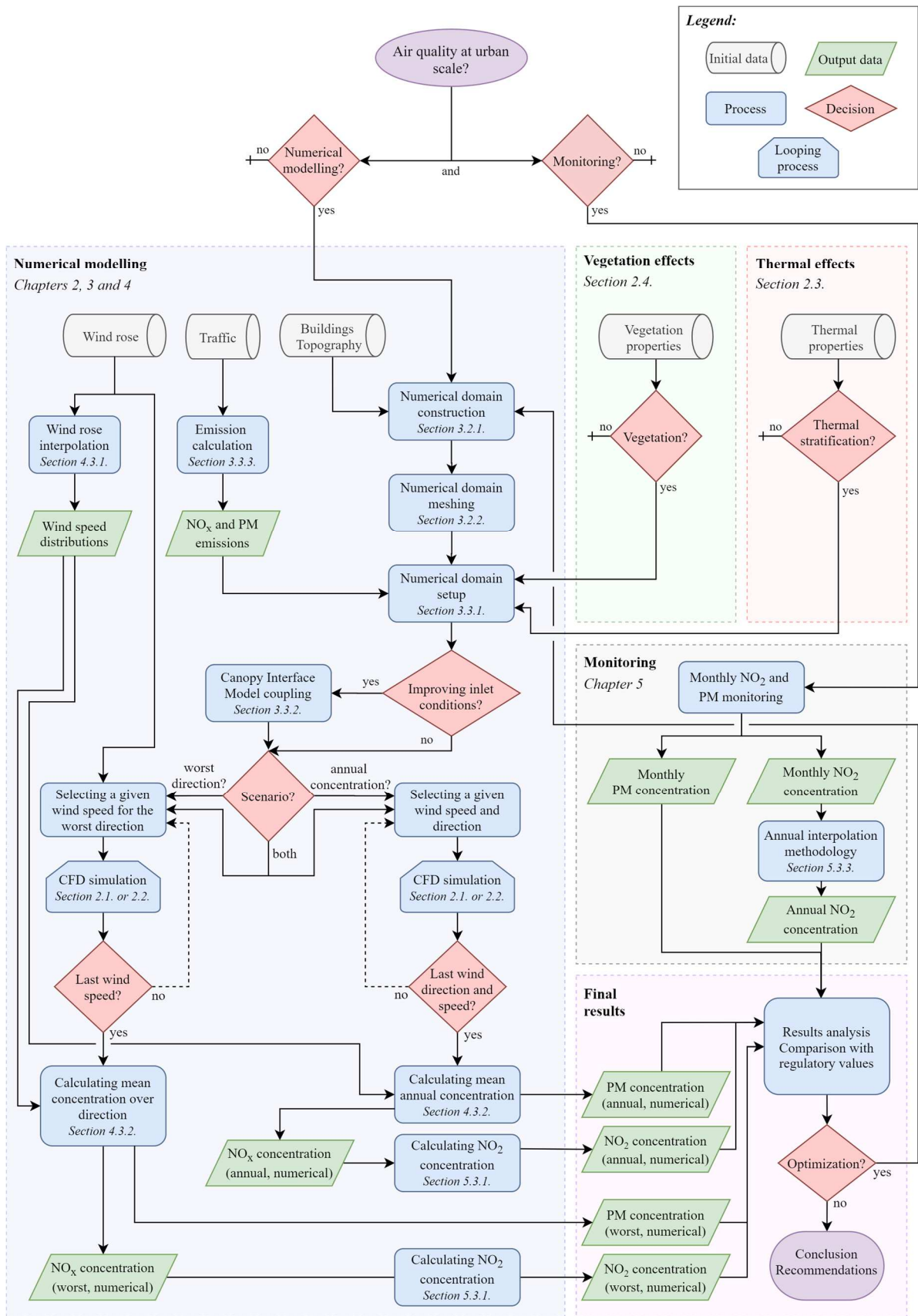
Figure 9.1 – Summary diagram of the concepts, tools and methodologies interconnections.

From an industrial point of view:

- Applying the concepts, solvers and methodologies presented in this thesis to assess air quality in other areas planned to be built for architecture purposes by making recommendations on building heights and morphologies to limit future inhabitants' exposure.

- Using the solvers and the methodologies to model other pollutants not considered in this thesis such as black carbon or sulfur dioxide (SO_2) but also heavier air pollutants such as allergenic particles (pollen) considering an adjustment of the transport equations in the solvers.

- Modelling larger urban areas to find out the limits of CFD models and, in particular, to what extent it is relevant to use them in terms of calculation costs and speed.

- Applying the Forced and Mixed Convection Solvers (FCS/MCS) to other fields of applications including urban pedestrian comfort, indoor/outdoor exchanges as well as indoor air quality assessments.

RESUME ETENDU EN FRANÇAIS

Modélisation 3D de la pollution de l'air à l'échelle urbaine

1. Introduction

La qualité de l'air est devenue au fil des années un enjeu de taille en France et dans le monde. En 2016, ce n'est pas moins de 8 millions de personnes qui sont décédées des suites à une trop forte exposition à la pollution de l'air (WHO, 2016a, 2016b), ce qui correspond à 7.6% des décès totaux dans le monde cette année-là. Toujours en 2016, en France, c'est approximativement 48 000 personnes qui sont décédées prématurément suite à une exposition aux particules fines de type PM$_{2.5}$ (Santé Publique France, 2016). Au-delà du seul aspect léthal engendré par la pollution de l'air, cette pollution cause également de nombreuses maladies (Anderson et al., 2012; Chauhan et al., 1998; Kagawa, 1985; Kim et al., 2015) et affecte aussi l'environnement (Likens et al., 1979).

Pour pallier ce problème, l'Union Européenne (UE), mais aussi plus globalement l'Organisation Mondiale de la Santé (OMS), ont mis en place des valeurs réglementaires ainsi que des valeurs cibles de concentrations en polluants à ne pas dépasser (EU, 2008; WHO, 2017). Parmi les différents polluants ciblés, le dioxyde d'azote (NO$_2$) et les particules fines (PM) ont été reconnus comme étant de la plus haute importance (WHO, 2005). En France, des Plans de Protection de l'Atmosphère (PPA) ont vu le jour et de nombreuses actions ont été entreprises afin de respecter ces valeurs réglementaires et protéger les populations.

Parmi les méthodes utilisées pour évaluer les concentrations en polluants auxquels sont exposées les populations, la modélisation numérique a connu un réel essor durant les dernières années en permettant de pallier à certains inconvénients de la seule mesure sur site (données ponctuelles, temps d'acquisition nécessaire, représentation spatiale limitée, etc.). De nombreux modèles existent pour modéliser la pollution de l'air (Korsakissok, 2009; Michelot et al., 2015). Parmi ceux-ci, la mécanique des fluides numériques (CFD, Computational Fluid Dynamics) a montré un réel intérêt pour la modélisation à micro échelle (à l'échelle du quartier) sur des distances allant de 100 m à 1 km (Korsakissok, 2009), offrant des résultats plus probants en présence de bâtiments que de simples modèles gaussiens à cette échelle (Bady, 2017). De plus, de nombreux phénomènes physiques et chimiques tels que les effets de la végétation, ou encore les effets de la stabilité atmosphérique sur le transport des polluants de l'air peuvent y être modélisés.

Cette thèse fait partie d'un cadre multidisciplinaire incluant des notions de qualité de l'air, de chimie, mais aussi de physique atmosphérique ainsi que mécanique des fluides et de modélisation numérique, et est restreinte au développement de modèles CFD pour la modélisation de la dispersion des oxydes d'azote et des particules fines en milieu urbain. Elle a deux principaux objectifs qui se complètent : (1) un objectif purement scientifique en développant un modèle 3D pour la modélisation de la pollution de l'air à l'échelle urbaine et en y incluant tous les phénomènes pouvant impacter la dispersion des polluants dans les villes ; (2) un objectif technique en améliorant l'applicabilité de ce type de modèle à des fins d'ingénieur dans des contextes techniques de conception, compréhension et diagnostic.

2. Modélisation CFD de la qualité de l'air à l'échelle du quartier

2.1. Développement de nouveaux codes de calcul CFD

La modélisation CFD de la dispersion des polluants de l'air en zone urbaine nécessite la prise en compte de nombreux phénomènes tels que la stabilité atmosphérique liée aux échanges thermiques, l'impact de la végétation sur l'écoulement, mais également sur le transport des polluants, la chimie atmosphérique, etc. Ces différents phénomènes sont illustrés en Fig. 1. Dans le cadre de cette thèse, deux nouveaux modèles CFD basés sur la bibliothèque OpenFOAM ont été développés pour pouvoir modéliser les différentes stabilités

atmosphériques et plusieurs modules ont également été développés pour inclure les phénomènes additionnels liés à la végétation et de chimie atmosphérique. Ces modèles, leurs équations directrices et leurs hypothèses sous-jacentes sont résumés ci-après.
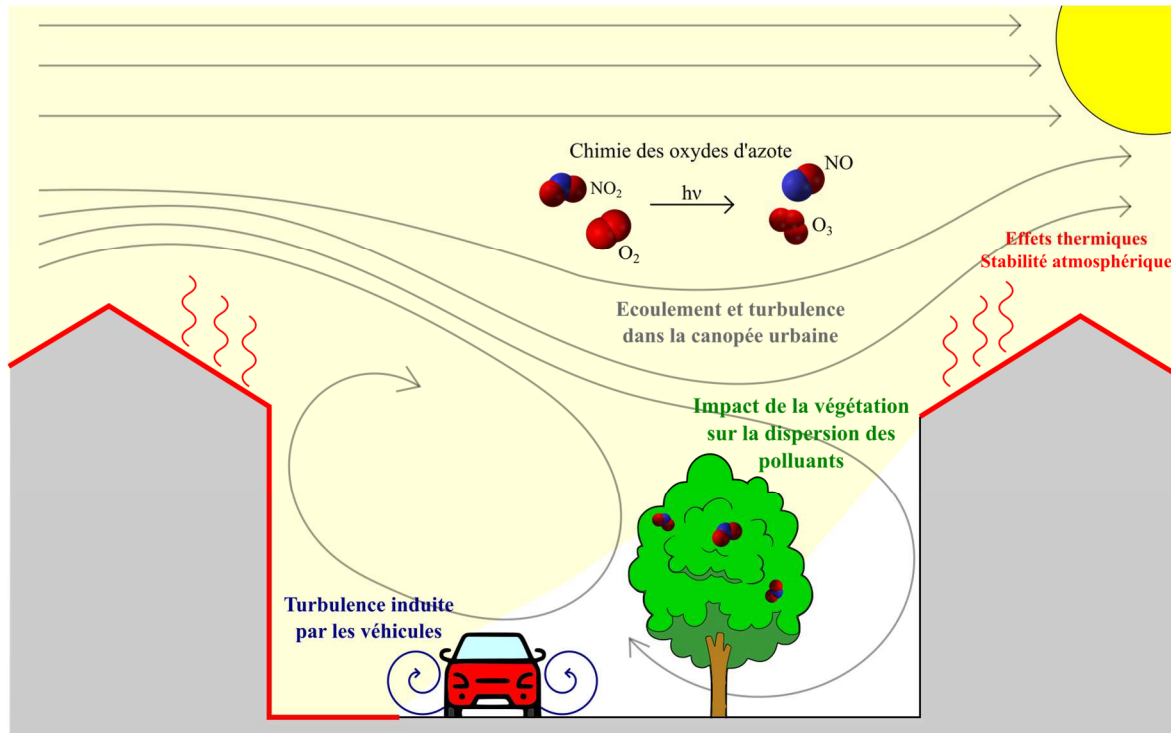
Fig. 1 – Illustration des processus physiques et chimiques gouvernant l'évolution des polluants atmosphériques dans la canopée urbaine.

2.1.1. Le cas isotherme des atmosphères neutres

Le premier modèle qui a été développé, et nommé Solveur à Convection Forcée (Forced Convection Solver, FCS), s'est basé sur le solveur *pimpleFoam* de la bibliothèque OpenFOAM. Ce dernier, destiné à la modélisation des écoulements de fluides incompressibles et turbulent est tout à fait désigné pour la modélisation des écoulements d'air en atmosphère neutre. En effet, d'une part l'air peut être considéré comme un fluide incompressible pour des vitesses inférieures à 100 m/s, car conduisant un nombre de Mach inférieur à 0.3 (Amiroudine and Battaglia, 2014; Anderson, 2009) et, d'autre part, l'écoulement de l'air dans l'atmosphère est fortement turbulent (Sportisse, 2008). Les équations directrices résolues par ce solveur correspondent aux équations de Navier-Stokes pour un fluide incompressible et sont données

ci-dessous avec l'équation de conservation de la masse (1) et de conservation de la quantité de mouvement (2).

$$\nabla . u = 0 \tag{1}$$

$$\frac{\partial u}{\partial t} + u.(\nabla u) = -\frac{1}{\rho}\nabla p + \nu \Delta u \tag{2}$$

avec u la vitesse, t le temps, ρ la masse volumique, p la pression et ν la viscosité cinématique.

Plusieurs méthodologies existent en mécanique des fluides numérique afin de résoudre ces équations et inclus les méthodes DNS (Direct Numerical Simulation), LES (Large-Eddy Simulation) et RANS (Reynolds-Averaged Navier-Stokes). Dans le cadre de ce travail, la méthodologie RANS a été retenue, car étant la plus appropriée à la modélisation dans un contexte d'ingénierie et pour des échelles allant de la centaine de mètres au kilomètre (Korsakissok, 2009; Michelot et al., 2015). L'idée derrière cette méthodologie et de transformer les quantités instantanées (vitesse, pression, etc.) en une composante moyenne et une composante fluctuante. Les équations précédentes, respectivement (1) et (2), sont alors remplacées par les équations ci-après, respectivement (3) et (4).

$$\nabla . U = 0 \tag{3}$$

$$\frac{\partial U}{\partial t} + U.(\nabla U) = -\frac{1}{\rho}\nabla P + \nu \Delta U - \nabla . \overline{u'u'} \tag{4}$$

avec U la composante moyennée de la vitesse, t le temps, ρ la masse volumique, P la composante moyennée de la pression, ν la viscosité cinématique, u' la composante fluctuante de la vitesse et $\overline{u'u'}$ le tenseur des contraintes de Reynolds.

L'utilisation d'une méthodologie de type RANS entraine l'apparition d'un nouveau terme, le tenseur des contraintes de Reynolds, qui nécessite alors l'utilisation d'un schéma de fermeture des flux turbulents. Ces schémas, ou modèles de turbulence sont de plusieurs types et les plus communément utilisés en modélisation atmosphérique sont les modèles isotropiques à deux équations de type k-ε avec en particulier les modèles standard et RNG (Franke et al., 2004).

Enfin, ce solveur en l'état ne permet que le calcul de l'écoulement d'air. Une nouvelle équation a donc dû être implémentée afin de résoudre le transport de polluants et correspond à l'équation d'advection-diffusion turbulente (5) donnée ci-dessous et fréquemment retrouvée dans la littérature scientifique (Di Sabatino et al., 2007; Takano and Moonen, 2013; Wen and Malki-Epshtein, 2018).

$$\frac{\partial C}{\partial t} + \nabla.(CU) - \nabla.\left[\left(D_m + \frac{\nu_t}{Sc_t}\right)\nabla C\right] = E \tag{5}$$

avec C la concentration en polluants, t le temps, U la vitesse, D_m le coefficient de diffusion moléculaire, ν_t la viscosité turbulente, Sc_t le nombre de Schmidt turbulent et E le terme source d'émissions.

Il est finalement nécessaire de noter que le nombre de Schmidt turbulent, Sc_t, est un paramètre important afin de tenir compte de la diffusion turbulente, mais n'est pas calculable. De plus, la valeur de ce paramètre varie généralement entre 0.3 et 1.2 et impacte significativement le résultat final Tominaga and Stathopoulos (2007). Sa valeur doit donc être choisie avec soin et, le plus souvent, après comparaison avec des résultats de référence.

2.1.2. Le cas des atmosphères stables et instables

Le second modèle qui a été développé, et nommé Solveur à Convection Mixte (Mixed Convection Solver, MCS), s'est basé sur le solveur *buoyantPimpleFoam* de la bibliothèque OpenFOAM.

Ce solveur est très similaire à celui utilisé précédemment pour le modèle à convection forcée à la différence qu'il s'affranchit de l'hypothèse d'incompressibilité du fluide et qu'il permet la modélisation des échanges thermiques au sein de l'atmosphère rendant alors possible la modélisation d'atmosphères stables et instables.

Les équations de Navier-Stokes incompressibles données précédemment sont alors remplacées par leurs homologues compressibles présentées ci-après avec l'équation de conservation de la masse (6), de la quantité de mouvement (7) et de l'énergie (8).

$$\frac{\partial \rho}{\partial t} + \nabla.(\rho u) = 0 \tag{6}$$

$$\rho\left(\frac{\partial u}{\partial t} + u.\nabla u\right) = -\nabla p + \nabla.\left(2\mu_{eff}D(u)\right) - \nabla\left(\frac{2}{3}\mu_{eff}(\nabla.u)\right) + \rho g \tag{7}$$

$$\frac{\partial \rho e}{\partial t} + \nabla.(\rho u e) + \frac{\partial \rho K}{\partial t} + \nabla.(\rho u K) + \nabla.(up) = \nabla.\left(\alpha_{eff}\nabla e\right) + \rho g.u \tag{8}$$

Avec u la vitesse, t le temps, p la pression, ρ la masse volumique, e l'énergie thermique, $D(u)$ le tenseur des déformations précisé en (9), K l'énergie cinétique précisée en (10), g l'accélération de pesanteur, μ_{eff} la viscosité effective définit comme étant la somme entre la viscosité moléculaire et turbulente et α_{eff} la diffusion thermique effective définit comme étant la somme des diffusions thermiques laminaire et turbulente.

$$D(u) = \frac{1}{2}[\nabla u + (\nabla u)^T] \tag{9}$$

$$K \equiv |u|^2/2 \tag{10}$$

Comme pour le cas du solveur à convection forcée, la méthodologie RANS est utilisée afin de résoudre les équations du solveur à convection mixte et l'équation d'advection-diffusion turbulente a été implémentée dans le code de calcul afin de pouvoir résoudre le transport des polluants atmosphériques.

2.1.3. Autres phénomènes considérés

Au-delà des considérations de stabilité atmosphérique, d'autres phénomènes peuvent avoir un impact sur le transport des polluants dans l'atmosphère. En l'occurrence, la végétation (Buccolieri et al., 2018), la chimie des oxydes d'azote (Seinfeld and Pandis, 2016) et la turbulence induite par les véhicules (Vachon et al., 2002) sont communément cités comme étant des phénomènes ayant des impacts significatifs sur les concentrations en polluants atmosphériques et devant donc être considérés.

Des modules ont été ajoutés aux deux solveurs cités précédemment afin de prendre en compte les effets de la végétation ainsi qu'une chimie simplifiée des oxydes d'azote et un descriptif des équations directrices pour ces différents phénomènes est donné ci-après. La turbulence induite par les véhicules n'a cependant pas pu être traitée dans les délais impartis.

Prise en compte des effets de la végétation sur le transport des polluants

La végétation peut agir de plusieurs façons sur le transport des polluants dans l'air. Parmi les différents phénomènes existants, certains ont déjà été bien investigués dans le cadre de la modélisation CFD comme par exemple l'impact de la végétation sur l'écoulement de l'air et la génération de turbulence (Buccolieri et al., 2018; Dalpé and Masson, 2009; Katul et al., 2004; Santiago et al., 2017b). D'après ces auteurs, ces effets peuvent être modélisés par l'ajout de termes source et puit dans l'équation du moment, de l'énergie cinétique turbulente et du taux de dissipation de l'énergie turbulente. Les termes source/puit correspondants sont respectivement donnés ci-après en (11), (12) et (13).

$$S_u = -\rho C_D \alpha |u| u_i \tag{11}$$

$$S_k = \rho C_D \alpha \left[\beta_p |u|^3 - \beta_d k |u| \right] \tag{12}$$

$$S_\varepsilon = \rho C_D \alpha \frac{\varepsilon}{k} \left[C_{4\varepsilon} \beta_p |u|^3 - C_{5\varepsilon} \beta_d k |u| \right] \tag{13}$$

avec ρ la masse volumique, C_D le coefficient de trainée, α la densité du feuillage (également noté LAD), u la vitesse, k l'énergie cinétique turbulente, ε le taux de dissipation de la turbulence, β_p la fraction d'énergie cinétique convertie en énergie cinétique turbulente par les effets de trainée (Buccolieri et al., 2018), β_d un coefficient sans dimensions pour tenir compte des courts-circuits dans les cascades de turbulence (Buccolieri et al., 2018) et $C_{4\varepsilon}$ et $C_{5\varepsilon}$ deux nouvelles constantes de turbulence.

Au-delà de l'impact sur l'écoulement de l'air, la végétation a également un impact direct sur la concentration en polluants par dépôt sur les surfaces végétalisées. Ce phénomène peut également être modélisé comme un terme puit de concentration (Buccolieri et al., 2018; Santiago et al., 2017b) selon l'équation (14).

$$S_d = -\alpha V_d C \qquad\qquad (14)$$

avec α la densité du feuillage, V_d la vitesse de dépôt et C la concentration en polluants.

Enfin, une partie des polluants déposés sur les surfaces végétalisées peuvent également être remis en suspension et ce phénomène peut être modélisé à l'aide d'un terme source de concentration (Hong et al., 2018) donné ci-dessous en (15).

$$S_r = -\alpha V_r C_{déposé} \qquad\qquad (15)$$

avec α la densité du feuillage, V_r la vitesse de remise en suspension et $C_{déposé}$ la concentration en polluant déposé sur la surface végétalisée.

Ce phénomène de remise en suspension n'étant actuellement que très peu étudié, seuls les effets de la végétation sur l'écoulement, la turbulence et le dépôt ont été implémentés dans le cadre de cette thèse. Ainsi, les termes S_u et S_d ont été inclus aux deux solveurs de calcul (FCS et MCS), et un nouveau modèle de turbulence incluant les termes S_k et S_ε a été développé sur la base du modèle standard k-ε.

Prise en compte d'une chimie simplifiée des oxydes d'azote

Dans l'atmosphère, les oxydes d'azote (NO$_x$) sont impliqués dans de nombreux mécanismes chimiques avec d'autres composés tels que l'ozone (O$_3$), des radicaux libres, les composés organiques volatils (COV), le formaldéhyde, etc. (Bliefert and Perraud, 2008). Le dioxyde d'azote (NO$_2$), faisant l'objet de contraintes réglementaires européennes et OMS, ne peut donc être directement modélisé, car les concentrations résultantes pourraient être biaisées par la non-prise en compte de ces mécanismes.

Des mécanismes complexes de chimie troposphérique ont déjà été inclus par le passé dans des modèles de CFD (Bright et al., 2013; Kim et al., 2012; Sanchez et al., 2016). Cependant, inclure ces mécanismes dans les modèles de mécanique des fluides numérique augmente considérablement les temps de calcul jusqu'à un facteur deux (Sanchez et al., 2016), les rendant incompatibles avec le domaine de l'ingénierie où la nécessité d'obtenir des résultats rapidement et à moindre coût est primordiale.

Il existe toutefois une alternative, moins coûteuse en termes de temps de calcul, et qui permet la prise en compte d'une chimie simplifiée des oxydes d'azote : l'équilibre photochimique. L'équation régissant cet équilibre, appelée équation de Leighton (Leighton, 1961), est donnée ci-dessous en (16).

$$[O_3]_{PSS} = \frac{J_1\,[NO_2]_{PSS}}{k_3\,[NO]_{PSS}} \tag{16}$$

avec $[O_3]_{PSS}$, $[NO_2]_{PSS}$ et $[NO]_{PSS}$ les concentrations en ozone, dioxyde d'azote et monoxyde d'azote à l'équilibre photochimique respectivement, J_1 le taux de photolyse du dioxyde d'azote, k_3 la constante cinétique de la réaction impliquant le monoxyde d'azote et l'ozone.

Les constantes J_1 et k_3 sont quant à elle calculable à l'aide des équations (17) et (18).

$$k_3 = \frac{15.33}{T}\,.\,e^{\frac{-1450}{T}} \tag{17}$$

avec k_3 la constante cinétique en ppb^{-1}/s et la T température en K.

$$J_1 = A.\,e^{(-B.sec\,\theta)} \tag{18}$$

avec J_1 le taux de photolyse du dioxyde d'azote, θ l'angle zénithal solaire et A et B deux constantes pouvant varier selon les auteurs ($A = 0.0167$ et $B = 0.575$ d'après Dickerson et al. (1982), $A = 0.0130$ et $B = 0.360$ d'après Parrish et al. (1983) ou encore d'après Lattuati (1997) $A = 0.0155$ et $B = 0.526$).

L'équation de Leighton permet de calculer de façon analytique les concentrations en NO$_2$ sur la base des concentrations en NO$_x$ et O$_3$, ce qui n'augmente que marginalement le temps de calcul nécessaire. Les équations (16), (17) et (18) ont donc été implémentées dans les deux solveurs de calcul. Il reste toutefois important de noter que l'équilibre photochimique ne permet pas un calcul des concentrations en NO$_2$ aussi fin que la prise en compte des mécanismes complexes cités précédemment, et pour cause, une erreur supérieure à 15% entre ces deux modèles chimiques peut être observée pour des températures estivales, des concentrations en ozone supérieures à 10 ppb et un rapport VOC/NO$_x$ de 0.5 (Sanchez et al., 2016). Une alternative est donc nécessaire pour calculer de façon plus fiable les concentrations en dioxyde d'azote (Cf. Section 3.3).

Prise en compte de la turbulence induite par les véhicules

La turbulence induite par les véhicules (VIT, Vehicle-Induced Turbulence) dépend de nombreux paramètres tels que le nombre de voies de circulation, de véhicules, etc. (Kastner-Klein et al., 2001) et sa prépondérance varie en fonction de la vitesse du vent (Di Sabatino et al., 2007). Ce phénomène peut être modélisé comme un terme source supplémentaire dans l'équation de l'énergie cinétique turbulente (Klein et al. 2000). Ce terme source, noté P_T, est donné ci-dessous en (19).

$$P_T = \frac{\rho C_d A_T \eta_T v_v^{\,3}}{BH} \tag{19}$$

avec P_T le terme source de turbulence induite par les véhicules, ρ la masse volumique du fluide, C_d le coefficient de trainée du véhicule, A_T la surface frontale du véhicule, η_T le nombre de véhicules par unité de longueur de route, v_v la vitesse des véhicules, B la largeur de la route et H une hauteur caractéristique.

2.2. Notions de domaine de calcul et de conditions aux limites pour la modélisation CFD à l'échelle urbaine

En mécanique des fluides numérique, et plus généralement en modélisation numérique, le choix du modèle est d'une importante capitale. Cependant, sa paramétrisation, mais aussi les hypothèses de calcul nécessaires peuvent engendrer une variation importante dans les résultats du modèle et doit donc également être renseignée et choisie avec soin. Dans le cadre de cette thèse, un travail important a été consacré aux notions de domaine de calcul (dimensions du domaine, maillage, etc.), conditions aux limites, émissions ainsi qu'à la concentration de fond en polluants.

2.2.1. Domaine de calcul

Le domaine de calcul correspond au volume dans lequel les différentes équations vont être résolues. Le choix du domaine de calcul est crucial, car, si ce dernier est trop grand, les temps de calcul nécessaires peuvent devenir très importants et, à l'inverse, si il est trop petit, des effets de bords altérant la qualité des résultats peuvent être observés.

Afin de limiter le temps de calcul nécessaire tout en conservant la qualité des résultats du modèle, des recommandations nommées « COST Action 732 guidelines » ont été formulées (Franke et al., 2007). En considérant que H est la hauteur du bâtiment le plus haut dans le domaine, une distance minimale de $5H$ doit être appliquées entre les bâtiments et les parois latérales du domaine, la paroi supérieure et la paroi en amont des bâtiments. Une distance supérieure de $15H$ doit être appliquée entre les bâtiments et la sortie du domaine de calcul, mais cette distance peut être réduite si l'intérêt n'est pas porté sur l'évolution du fluide en aval de la zone. Ces recommandations, communément admises par la communauté scientifique (Blocken, 2015, 2014) sont souvent retrouvées dans les divers travaux portant sur la modélisation CFD de la pollution de l'air (Allegrini et al., 2013; Santiago et al., 2019, 2017b).

Une étude réalisée dans le cadre de cette thèse a toutefois montré que, en l'absence de bâtiments, les résultats dans le domaine de calcul variaient avec le choix de la hauteur du domaine jusqu'à atteindre une hauteur de 96 m. Ces résultats suggèrent qu'en plus de la recommandation d'une distance minimale de $5H$ entre les bâtiments et la hauteur du domaine, une distance minimale de 96 m doit également être vérifiée.

Au-delà de la dimension du domaine de calcul, le choix du maillage est également très important. En effet, des mailles trop grandes peuvent entrainer des erreurs numériques tandis que des mailles trop petites garantiront une certaine qualité dans les résultats obtenus, mais entraineront également un temps de calcul plus élevé.

De façon générale en mécanique des fluides numérique, la taille des mailles est choisie en utilisant un indicateur sans dimensions noté y^+. Cet indicateur qui dépend de la vitesse de l'écoulement, du type de fluide, mais également de la taille des mailles doit être compris entre 30 et 500 pour la modelisation RANS (Versteeg and Malalasekera, 2007). Cependant, pour la modélisation grandeur nature de zones urbaines, respecter ces valeurs entraine une taille de maille allant de quelques millimètres à quelques centimètres pouvant entrainer des temps de calcul très importants. De ce fait, des mailles entrainant un y^+ supérieur à 500 sont généralement utilisées (Allegrini et al., 2015) avec en règle générale des mailles de 1 m dans la zone d'intérêt et de 0.5 m à proximité des murs des bâtiments, du sol et des sources d'émissions (Di Sabatino et al., 2007; Flores et al., 2013; Sanchez et al., 2017; Vranckx et al., 2015).

Des études réalisées dans le cadre de cette thèse ont montré qu'une telle résolution (0.1 m et 0.5 m à proximité des parois et des sources d'émission) est suffisante à l'obtention de résultats insensibles à la taille des mailles tout en entrainant un nombre de mailles et donc un temps de calcul raisonnable pour des applications au domaine de l'ingénierie.

2.2.2. Conditions aux limites

Conditions usuelles

Les conditions aux limites sont des valeurs ou des fonctions spécifiées au niveau des limites du domaine de calcul. Elles sont entre autres spécifiées afin de prendre en compte les phénomènes extérieurs au domaine de calcul, mais agissant à l'intérieur de celui.

En mécanique des fluides numérique appliquée à la qualité de l'air, les conditions aux limites au niveau des parois latérales du domaine ainsi que du toit sont presque toujours les mêmes et correspondent à une condition de symétrie. Cette condition est choisie afin de créer un tunnel artificiel afin de guider l'écoulement de la face d'entrée d'air vers la face de sortie, il est donc nécessaire d'avoir une distance suffisante entre ces parois et la zone d'intérêt afin d'éviter de contraindre l'écoulement et donc, de biaiser les résultats (Franke et al., 2007). La condition au niveau des murs des bâtiments (et autres obstacles) ainsi que du sol est une condition de non-glissement entrainant une vitesse nulle. La condition au niveau de la face de sortie est quant à elle une condition de pression constante entrainant un gradient de vitesse nul (Franke et al., 2007).

La condition au niveau de la face d'entrée est enfin sujette à variation selon les auteurs et on trouvera d'une part ceux qui utilisent une condition dite « en loi puissance » et ceux qui utilisent une condition dite « logarithmique ».

La condition en loi puissance est décrite par Tominaga et al. (2008). Les équations de la vitesse, de l'énergie cinétique turbulente ainsi que de la dissipation d'énergie cinétique turbulente sont données en (20), (21) et (22).

$$U(z) = U_{ref} \left(\frac{z}{z_{ref}} \right)^\alpha \tag{20}$$

$$k(z) = [U(z)I(z)]^2 \tag{21}$$

$$\varepsilon(z) = \alpha k(z) C_\mu^{\frac{1}{2}} \frac{U_{ref}}{z_{ref}} \left(\frac{z}{z_{ref}} \right)^{\alpha-1} \tag{22}$$

$$I(z) = 0.1 \left(\frac{z}{z_G} \right)^{(-\alpha-0.05)} \tag{23}$$

avec $U(z)$ la vitesse, z l'altitude, U_{ref} la vitesse de référence à l'altitude de référence z_{ref}, α le coefficient de la loi puissance, $k(z)$ est l'énergie cinétique turbulente, $I(z)$ est l'intensité turbulente calculée avec (23), $\varepsilon(z)$ le taux de dissipation de l'énergie cinétique turbulente, C_μ une constante CFD (généralement égale à 0.09) et z_G la hauteur de la couche limite qui peut être déterminée suivant le terrain d'après Tominaga et al. (2008).

La condition logarithmique est décrite par Richards and Norris (2011). Les équations de la vitesse, de l'énergie cinétique turbulente ainsi que de la dissipation d'énergie cinétique turbulente sont données en (24), (25) et (26).

$$U(z) = \frac{u_*}{\kappa_{k-\varepsilon}} ln \left(\frac{z}{z_0} \right) \tag{24}$$

$$k(z) = \frac{u_*^2}{\sqrt{C_\mu}} \tag{25}$$

$$\varepsilon(z) = \frac{u_*^3}{\kappa_{k-\varepsilon} z} \tag{26}$$

avec $U(z)$ la vitesse, u_* la vitesse de friction, $\kappa_{k-\varepsilon}$ la constante de von Kármán impliquée par le modèle k-ε, z l'altitude, z_0 la longueur de rugosité, $k(z)$ l'énergie cinétique turbulente, $\varepsilon(z)$ le taux de dissipation de l'énergie cinétique turbulente et C_μ une constante CFD (généralement égale à 0.09).

La vitesse de friction peut être calculée sur la base d'une vitesse U_h à une hauteur h donnée en utilisant l'équation (27) dérivée de l'équation (24) et $\kappa_{k-\varepsilon}$ peut être calculé en utilisant l'équation (28) sur la base des constantes $C_{\varepsilon 1}$, $C_{\varepsilon 2}$ et σ_ε du modèle de turbulence.

$$u_* = \frac{\kappa_{k-\varepsilon} U_h}{\ln\left(h/z_0\right)} \tag{27}$$

$$\kappa_{k-\varepsilon} = \sqrt{(C_{\varepsilon 2} - C_{\varepsilon 1})\sigma_\varepsilon \sqrt{C_\mu}} \tag{28}$$

Les deux types de conditions aux limites de vitesse et turbulence en entrée du domaine de calcul sont disponibles dans OpenFOAM. Sauf mention contraire, la condition logarithmique donnée par Richards and Norris (2011) est préférée dans le cadre de cette thèse.

Amélioration de la condition aux limites en entrée du domaine de calcul

Les conditions d'entrée citées précédemment sont régulièrement utilisées dans la littérature comme condition d'entrée de vent en zones urbanisées ou non. Ces conditions, bien qu'adéquates pour des terrains plats sans grands obstacles, ne sont cependant pas adaptées dans la canopée urbaine. En effet, en zones urbaines, les profils de vitesse en présence de bâtiments sont fortement modifiés et diffèrent des profils logarithmiques ou de type puissance qui ne sont atteints que pour des altitudes bien supérieures à celle du bâti (Coceal et al., 2007). Les mêmes observations ont été faites plus récemment par Mauree et al. (2017b), sur la base de résultats de campagnes de mesures réalisées sur un campus universitaire en Suisse.

Afin de spécifier des profils de vitesse et de turbulence plus cohérents en entrée du domaine de calcul, deux options sont possibles : (1) déterminer le nombre minimal de bâtiments à mettre en amont de la zone d'intérêt afin de passer d'un profil logarithmique à un profil impacté par le bâti ou, (2), spécifier en condition d'entrée des profils de vitesse et turbulence pré-impacté par le bâti. Dans le cadre de cette thèse, la seconde option a été étudiée et, pour cela, un couplage avec un modèle 1D nommé CIM (Canopy Interface Model) a été étudié.

Le modèle CIM, conçu dans le cadre de la thèse à Mauree (2014), est un code de calcul développé en langage Fortran et capable de reproduire des profils 1D de vitesse, de turbulence

et de température en zone urbaine sur la base de conditions de vent (vitesse, direction, température) impactées par la présence de bâtiments.

Avant de coupler le modèle CIM au modèle CFD, des profils de vitesse obtenus par ces deux modèles ont été comparés pour une zone urbaine donnée afin de vérifier la capacité de CIM à reproduire un profil de vitesse calculé en CFD. Les résultats de cette comparaison sont proposés en Fig. 2 et ce pour deux cas de figure : cas 1, où CIM est paramétré avec une évolution constante des dimensions des bâtiments selon l'altitude et, cas 2, où CIM est paramétré avec une évolution variable des dimensions des bâtiments selon l'altitude.
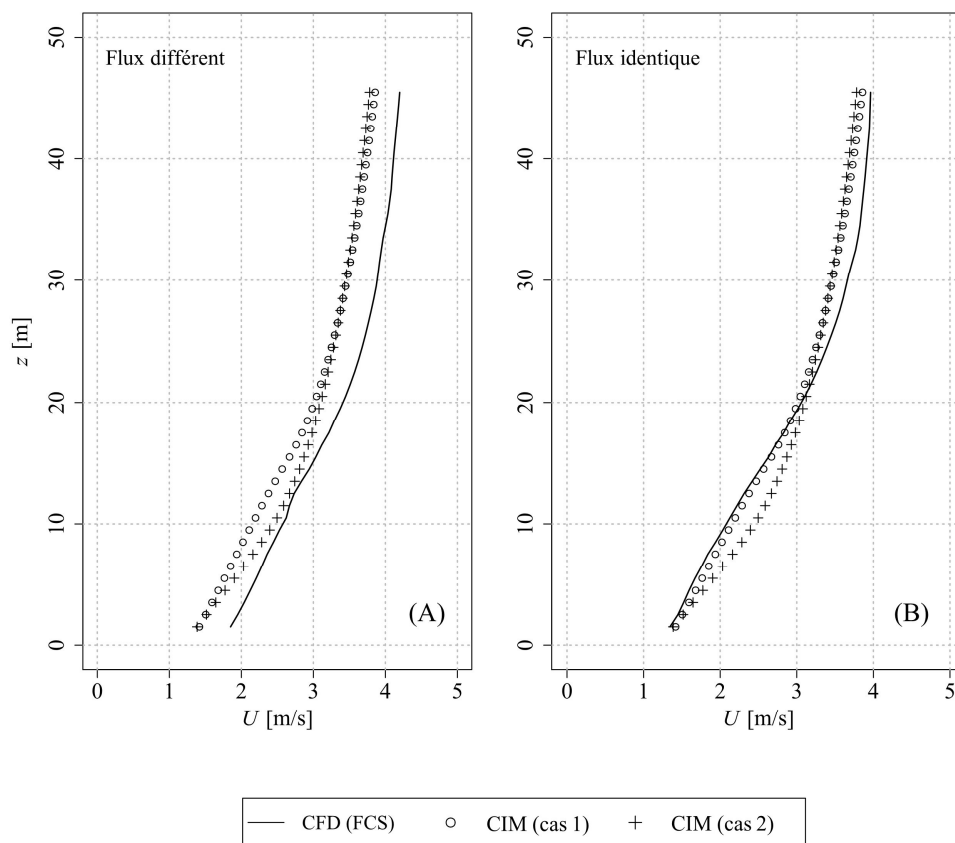
Fig. 2 – Comparaison entre les profils de vitesse obtenus avec la CFD et avec le modèle CIM (à gauche avant égalisation des flux, à droite après égalisation des flux).

Les premiers résultats de comparaison, présentés en Fig. 2 (A), montrent que le profil de vitesse obtenu avec le modèle CIM a une allure très proche de celui obtenu en CFD notamment dans le cas 1. Les vitesses sont cependant plus fortes avec le modèle CFD qu'avec le modèle CIM. Ce constat est normal, car le modèle CIM est en réalité non conservatif sur le flux pour permettre une perte de quantité de mouvement dans le domaine. Ainsi, pour une condition de vitesse donnée, une modification des dimensions des bâtiments entrainera des profils de vitesse avec des flux différents. Afin de pouvoir comparer les résultats des deux modèles à flux identique, la simulation CFD a été relancée avec une vitesse plus faible correspondant au même flux que celui obtenu avec CIM. Les résultats correspondants sont proposés en Fig. 2 (B). Les résultats obtenus avec CIM dans le cas 1 ne diffèrent que de l'ordre de 5% par rapport au modèle CFD pour les plus basses altitudes ($z < 20$ m) et de 10% au-delà. Le modèle CIM est ainsi capable de reproduire des profils de vitesse similaires à ceux que l'on peut obtenir avec le modèle CFD à convection forcée. Ces résultats sont d'autant plus intéressants que le temps de calcul pour leur obtention était de l'ordre de quelques dizaines de seconds pour CIM contre près d'un jour sur 48 cœurs CPU en CFD.

Compte tenu des résultats précédents, le modèle CIM a été couplé avec le modèle CFD à convection forcée et une nouvelle comparaison a été réalisée afin de comparer les résultats obtenus sur la dispersion des polluants. Trois cas ont été considérés et sont illustrés en Fig. 3 :

- Cas 1 : un domaine numérique complet est considéré avec un profil logarithmique de vent en entrée du domaine (cas de référence).

- Cas 2 : le domaine numérique précédent est considéré avec les mêmes conditions d'entrée, mais la première ligne de bâtiment a été supprimée (cas de contrôle).

- Cas 3 : le domaine numérique a été réduit entre l'entrée du domaine et les bâtiments et débute après la première ligne de bâtiments supprimée dans le cas 2. Les résultats du modèle CIM appliqués à la première ligne de bâtiments (non pris en compte dans le domaine numérique) et suivant un pas de 24 m dans la direction transverse à l'écoulement ont été pris comme condition d'entrée du modèle CFD (cas de couplage CIM/CFD).
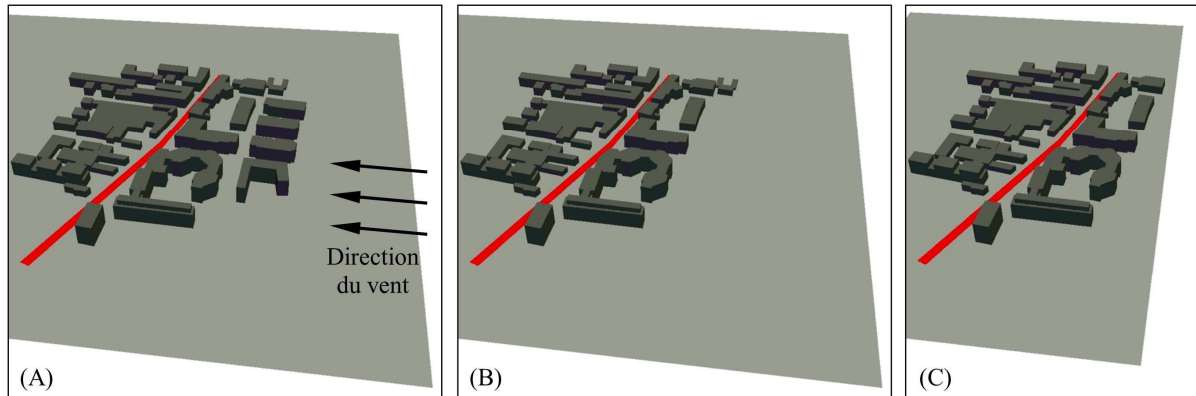
Fig. 3 – Illustration des trois cas considérés avec (A) le cas 1 avec tous les bâtiments, (B) le cas 2 avec la première ligne de bâtiments supprimée et les mêmes conditions d'entrée et (C) le cas 3 où le domaine numérique a été réduit et les conditions obtenues avec CIM ont été utilisées en entrée.
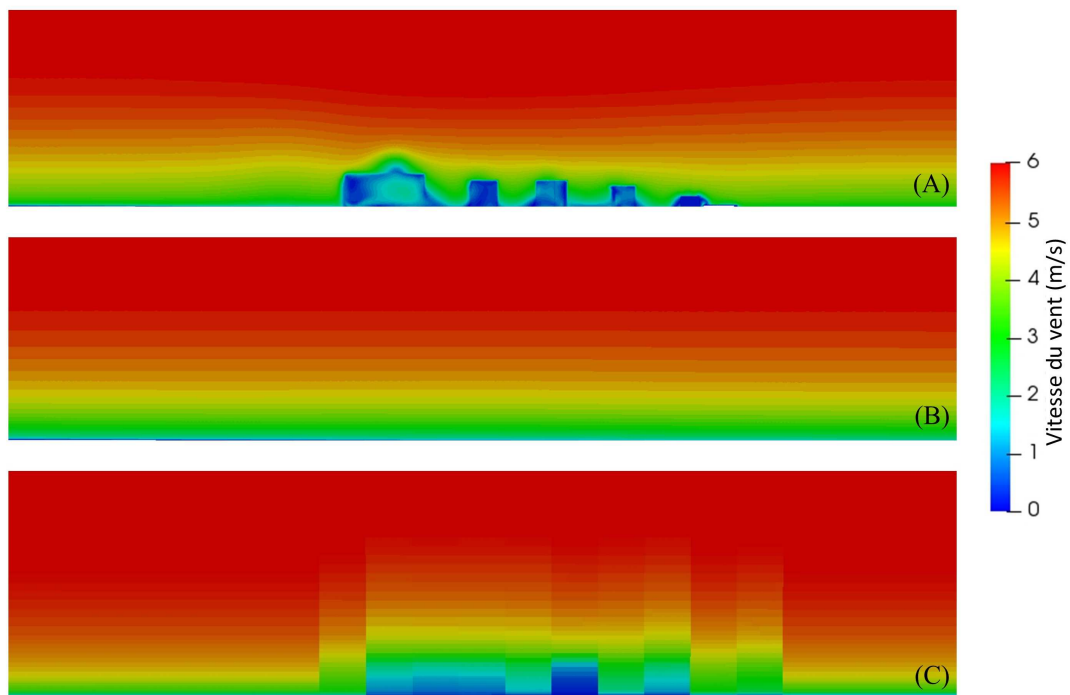
Fig. 4 – Comparaison des champs de vitesse dans la zone où les bâtiments ont été supprimés pour (A) le cas 1, (B) le cas 2 et (C) le cas 3.

Avant de comparer les résultats sur les concentrations, une première comparaison peut être réalisée sur le champ de vitesse au niveau d'un plan vertical et transverse à l'écoulement pris au niveau de la ligne de bâtiments supprimée (Cf. Fig. 4). Ces résultats montrent que le champ de vitesse obtenu avec le couplage CIM/CFD (cas 3) est proche de celui obtenu pour le cas de

référence (cas 1). Le cas 2 entrainant en toute logique des résultats très différents, constants sur toute la largeur du domaine (absence de bâtiments et condition logarithmique en entrée du domaine).
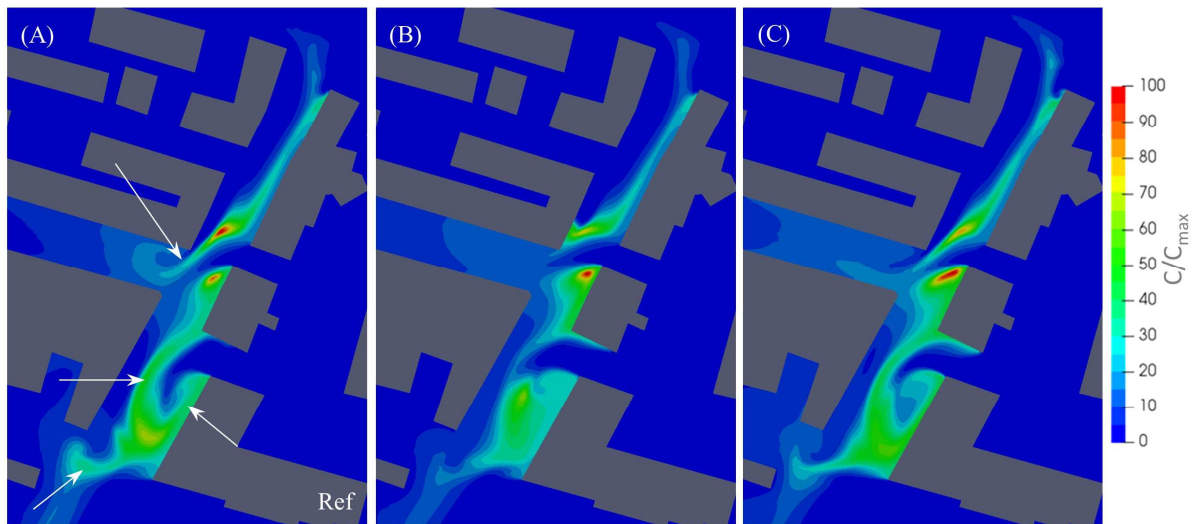
Fig. 5 – Comparaison des résultats sur les concentrations en polluants pour les trois cas considérés avec (A) le cas 1, (B) le cas 2 et (C) le cas 3.

Les résultats sur les concentrations en polluants sont enfin présentés en Fig. 5. D'après les Fig. 5 (A) et Fig. 5 (B) des différences peuvent être observées sur les concentrations en polluants modélisées lorsque l'on supprime la première ligne de bâtiments dans la direction de l'écoulement (les principales différences sont précisées par les flèches blanches). Les résultats obtenus après couplage CIM/CFD et présentés en Fig. 5 (C) sont pour leur part plus proches de la référence, montrant que la suppression de la première ligne de bâtiments a été compensée par l'utilisation de CIM. Enfin, il faut noter que le maillage utilisé dans le cas 1 et 2 est composé de 7,25 millions de mailles contre 5.5 millions pour le cas 3. Le couplage CIM/CFD a ainsi permis de diminuer le nombre de mailles ce qui a diminué de 20% le temps de calcul nécessaire.

2.3. Validation des modèles CFD

Les différents modèles CFD développés dans le cadre de cette thèse ont été validés sur un total de 7 cas tests. Un résumé des cas tests est proposé dans le Tableau 1. Dans le cadre de ce résumé étendu, seul un cas test est présenté et correspond au cas test de Cui et al. (2016). Ce dernier a été retenu, car il correspond au cas test le plus complexe parmi tous ceux étudiés. En effet, ce cas test comprend des bâtiments asymétriques, et effets de bords au niveau des bâtiments et des structures d'écoulement 3D. De plus, les résultats expérimentaux sont donnés à la fois pour les vitesses et les concentrations à l'intérieur et à l'extérieur des bâtiments et le tout, en considérant une atmosphère très instable.

Tableau 1 – Résumé des cas tests utilisés pour la validation des modèles CFD développés.

Auteurs	Types de données		Type de zone étudiée		Type de mesures		Phénomènes additionnels		Paramètres disponibles		
	2D	3D	Bâtiments	Rue canyon	Soufflerie	In-situ	Effets thermiques	Végétation	Vitesse	Concentration	Température
Soulhac et al. (2001)	✔			✔	✔				✔	✔	
Gamel (2015)	✔		✔		✔				✔	✔	
CODASC database		✔		✔	✔					✔	
Uehara et al. (2000)	✔			✔	✔		✔		✔		✔
Cui et al. (2016)		✔	✔		✔		✔		✔	✔	✔
Irvine et al. (1997)	✔					✔		✔	✔		
Vermeulen et al. (2009)		✔				✔		✔	✔	✔	

Cui et al. (2016) ont étudié en soufflerie l'évolution de la vitesse du vent et des concentrations en polluants pour un profil vertical entre deux bâtiments ($x = L/2$), et, pour un profil horizontal à l'intérieur d'une pièce située dans le bâtiment aval ($z = 5L/8$). Le sol entre les deux bâtiments a été chauffé avec une température T_g variable selon les cas étudiés et l'air a été injecté dans la soufflerie avec une température fixée à T_a = 288 K. Parmi les cas disponibles, un cas très instable entrainant un nombre de Richardson négatif (Ri = -1.22) a été utilisé. Leur cas expérimental était totalement en trois dimensions avec un bâtiment en aval plus grand, ouvert

vers l'extérieur dans le sens de l'écoulement. Une source d'émissions était également placée sur le toit du bâtiment amont en $x = y = 0$ et où une émission de 0.087 g/s a été appliquée.

Les simulations ont été réalisées à l'aide du solveur à convection mixte et le modèle de turbulence RNG k-ε, en spécifiant une température au niveau du sol (entre les bâtiments) de $T_g = 423$ K et en utilisant les mêmes conditions d'entrée (vitesse, turbulence et température) que celles mesurées par Cui et al. (2016). Une condition de sortie libre à pression atmosphérique a été spécifiée en sortie du domaine et des conditions de symétrie ont été appliquées au niveau des parois latérales et du toit du domaine. Une condition de non-glissement avec loi de paroi standard a été appliquée au niveau du sol et des parois des bâtiments. Enfin, les recommandations de Franke et al. (2007) ont été suivies concernant les dimensions minimales dans le domaine de calcul. Une illustration du domaine de calcul ainsi obtenu est présentée en Fig. 6.
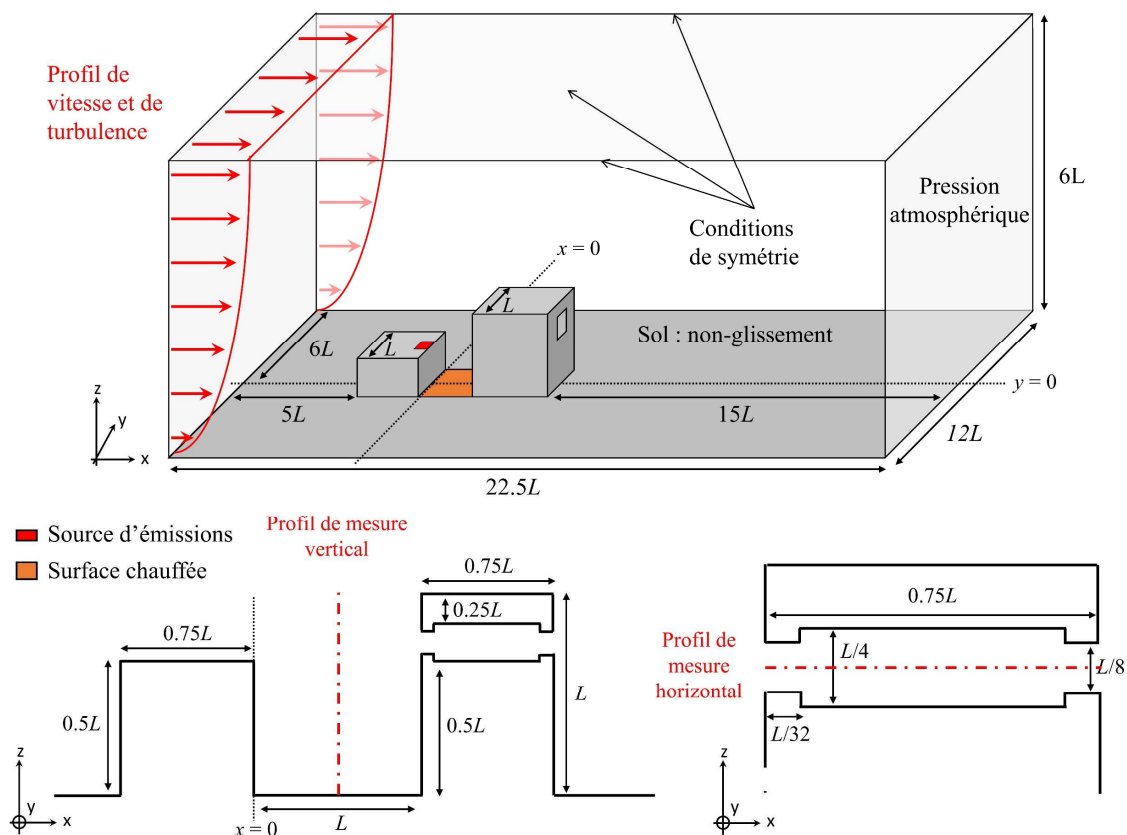
Fig. 6 – Illustration des conditions aux limites et dimensions du domaine de calcul pour le cas test de Cui et al. (2016) avec $L = 0.16$ m.

Un test de sensibilité au maillage a été réalisé en utilisant le *GCI* (Grid Convergence Index) formulé par Roache (1994). Ce paramètre a été étudié d'une part à l'extérieur des bâtiments et, d'autre part, à l'intérieur de ceux-ci. Un *GCI* inférieur à 5% a été obtenu pour des mailles de 2.5 mm à l'extérieur et de 0.625 mm à l'intérieur du bâtiment en comparaison de mailles de 5 mm et 1.25 mm respectivement. Ce maillage a ainsi été retenu pour les modélisations. Le y^+ correspondant est de l'ordre de 50 à l'extérieur et 15 dans le bâtiment. Une illustration des maillages obtenus est proposée en Fig. 7.
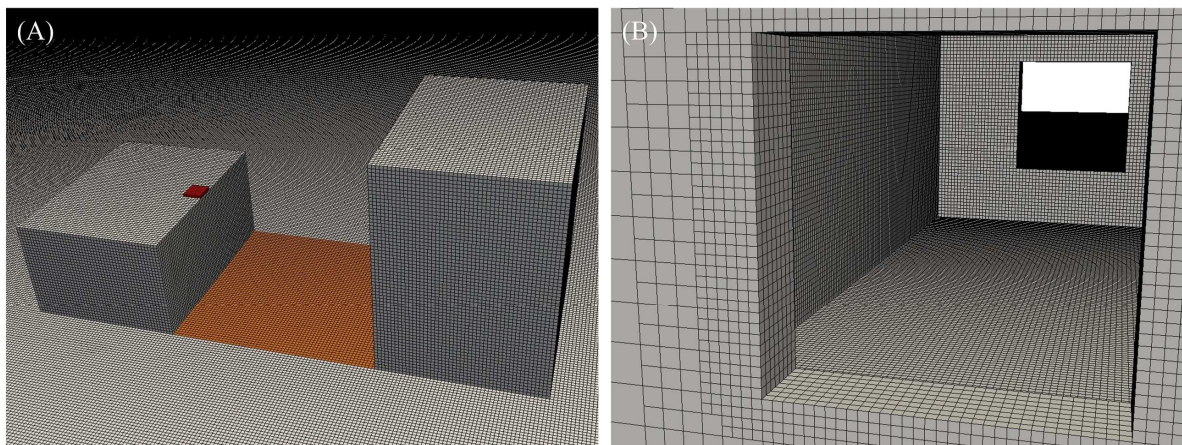
Fig. 7 – Illustration du maillage (A) au niveau des deux bâtiments avec la surface chauffée en orange et la source d'émission en rouge (taille des mailles de 2.5 mm) et (B) au niveau de la fenêtre amont et à l'intérieur de la pièce (taille des mailles de 0.625 mm).

La vitesse adimensionnelle dans le sens de l'écoulement U/U_{ref} ainsi que la concentration adimensionnelle C^* entre les bâtiments ($x = L/2$) en fonction de la hauteur adimensionnelle z/L sont proposés en Fig. 8. La concentration adimensionnelle a été calculée à l'aide de l'équation (29) avec U_{ref} = 0.7 m/s, H_{ref} = 0.08 m, L = 0.16 m et q_m = 0.087 g/s selon Cui et al. (2016).

$$C^* = \frac{C.U_H.H}{q_m/L} \tag{29}$$

D'après la Fig. 8, le profil de vitesse à l'extérieur des bâtiments est correctement reproduit par le modèle numérique. En effet, les résultats numériques sont très proches des résultats expérimentaux, en particulier pour $z/L > 0.55$. Les vitesses sont toutefois légèrement sous-estimées pour les altitudes plus basses. Pour ce qu'il s'agit des concentrations, les résultats

expérimentaux sont bien reproduits par le modèle numérique avec les nombres de Schmidt turbulent considérés (0,2, 0,25 et 0,3). Les meilleurs résultats sont obtenus avec $Sc_t = 0.2$.
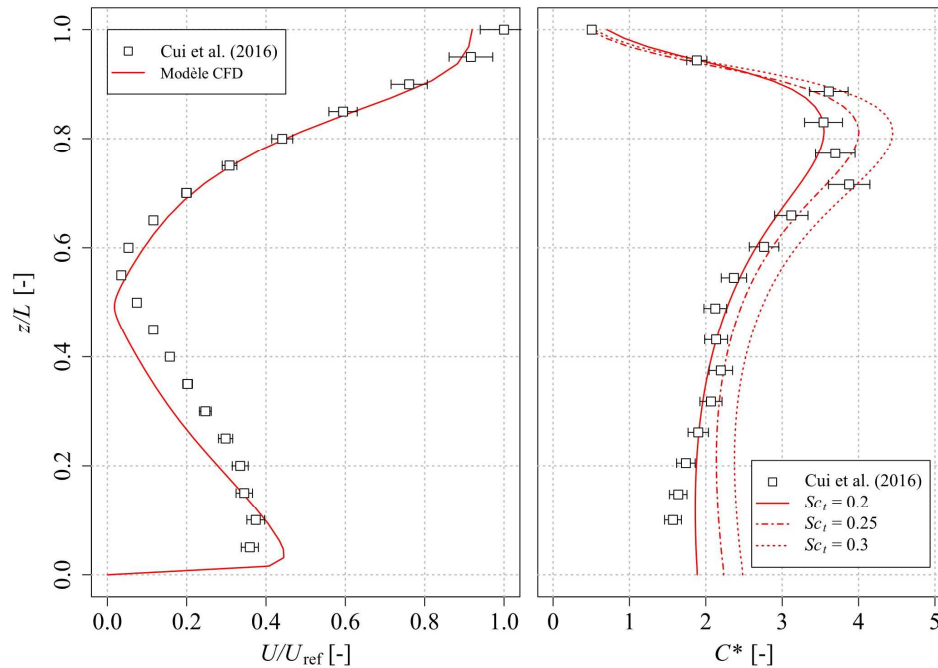
Fig. 8 – Comparaison entre la vitesse adimensionnelle dans le sens de l'écoulement et la concentration adimensionnelle entre les résultats numériques du modèle CFD et les mesures expérimentales de Cui et al. (2016) à l'extérieur.

La vitesse adimensionnelle dans le sens de l'écoulement U/U_{ref} ainsi que la concentration adimensionnelle C^* dans le bâtiment à l'aval en fonction de la distance adimensionnelle x/L sont proposés en Fig. 9.

Les résultats montrent une importante surestimation des vitesses juste après la première fenêtre ($x/L = 1.0$). Les vitesses sont toutefois très bien reproduites au-delà à partir de $x/L = 1,2$ et jusqu'à la seconde fenêtre. En termes de concentrations, les résultats expérimentaux sont également très bien reproduits et en particulier avec $Sc_t = 0.25$. Il faudra enfin noter que, quel que soit le nombre de Schmidt turbulent considéré, le modèle numérique donne globalement une concentration constante dans toute la pièce du bâtiment aval tandis que les résultats expérimentaux montrent des variations selon l'emplacement dans la pièce. Ces variations sont cependant faibles et globalement incluses dans les incertitudes des mesures.
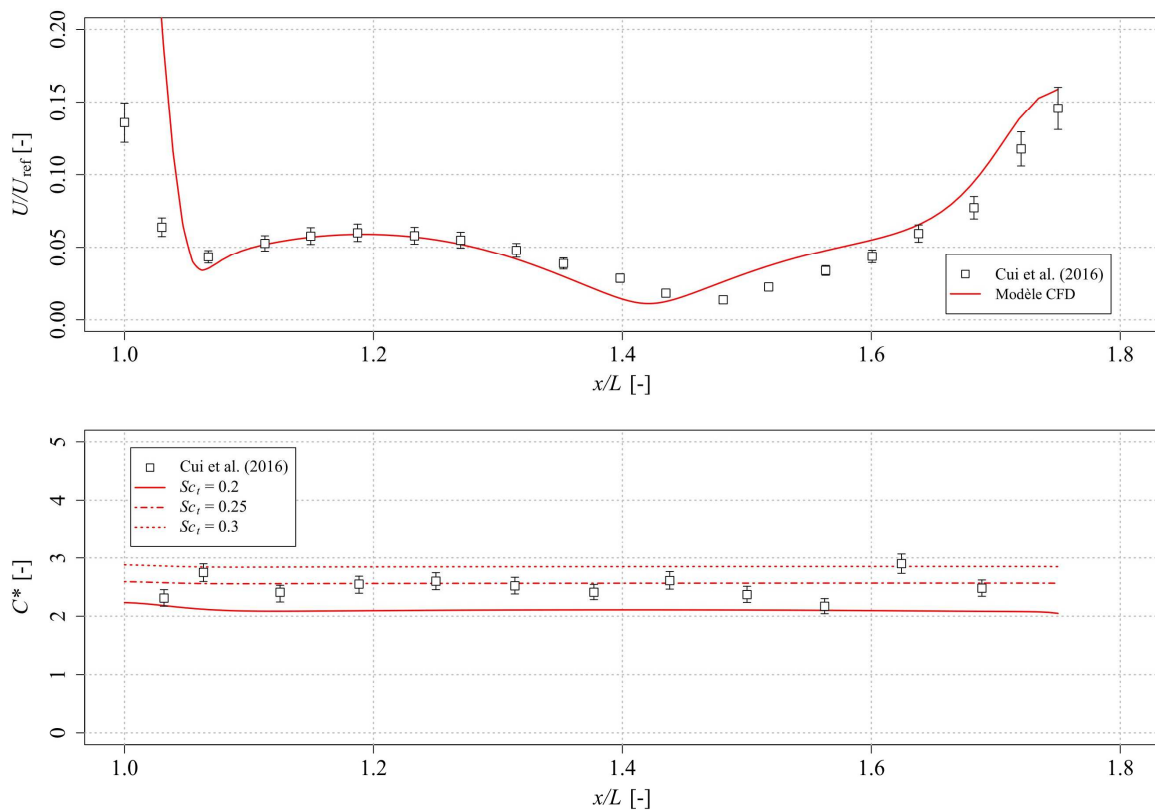
Fig. 9 – Comparaison de la concentration adimensionnelle dans le sens de l'écoulement et de la concentration adimensionnelle entre le modèle numérique et les résultats expérimentaux de Cui et al. (2016) à l'intérieur du bâtiment aval.

En dernier lieu, plusieurs critères de performances ont été calculés afin de comparer les résultats et en distinguant les résultats à l'intérieur et à l'extérieur des bâtiments. Ces critères correspondent au FB (Fractional Bias), au MG (Geometric Mean bias), au VG (Geometric Variance), au $NMSE$ (Normalized Mean Square Error), au $FAC2$ (the fraction of predictions within a factor of two observations), au NAE (Normalized Absolute Error), et à la *Target*. La définition de ces critères ainsi que les objectifs et valeurs généralement admises peuvent être retrouvés dans Chang and Hanna (2004) et Thunis et al. (2012). Les résultats sont quant à eux proposés dans le Tableau 2.

D'après les données présentées dans le Tableau 2, les meilleurs résultats à l'extérieur des bâtiments sont obtenus avec $Sc_t = 0,2$ conduisant à une erreur globale de 8%. Les résultats avec $Sc_t = 0,25$ sont également bons avec une erreur globale de 10%. Les meilleurs résultats à l'intérieur du bâtiment sont obtenus pour $Sc_t = 0,25$ entrainant une erreur globale de 6%. Le

nombre de Schmidt turbulent permettant de minimiser l'erreur dans les deux cas (intérieur est extérieur) est donc 0,25.

Tableau 2 – Evaluation des performances du solveur à convection mixte sur la base des données de Cui et al. (2016) à l'intérieur et à l'extérieur des bâtiments.

	FB	MG	VG	NMSE	FAC2	NAE	Target
RNG k-ε, extérieur							
$Sc_t = 0.2$	0.016	1.016	1.014	0.000	1.024	8%	0.27
$Sc_t = 0.25$	-0.070	0.932	1.018	0.005	1.090	10%	0.32
$Sc_t = 0.3$	-0.175	0.839	1.047	0.031	1.210	17%	0.57
RNG k-ε, intérieur							
$Sc_t = 0.2$	0.173	1.189	1.036	0.030	0.846	17%	2.27
$Sc_t = 0.25$	-0.023	0.977	1.006	0.001	1.029	6%	1.01
$Sc_t = 0.3$	-0.128	0.879	1.023	0.017	1.143	13%	2.01
Objectif							
Valeur cible	0	1	0	0	1	0%	0
Gamme admise	-0.3 < x < 0.3	0.7 < x < 1.3	< 4	< 1.5	0.5 < x < 1.5	-	< 0.5

D'après les résultats précédents, le solver à convection mixte est capable de bien reproduire des profils de vent et concentration en polluants en environnement à la fois extérieur et intérieur dans le cas d'une atmosphère très instable.

Sur la base de ce résultat, mais également d'après les résultats des autres cas tests non présentés ici, les différents modèles CFD (à convection forcée et à convection mixte, avec ou sans végétation) sont valides pour la modélisation des écoulements d'air en milieu urbain, pour diverses stabilités atmosphériques et en présence ou absence de végétation.

3. Méthodologies pour l'évaluation de la qualité de l'air à l'échelle urbaine

Dans le cadre de ce travail de thèse, outre le développement de différents modèles CFD, de nombreuses méthodologies ont été développées pour l'étude et la modélisation 3D de la qualité de l'air et valorisées sous forme d'articles de recherche publiés dans des journaux à portée internationale. Ces différentes méthodologies sont données ci-après.

3.1. Evaluation de la distribution continue des vitesses de vent sur la base de données discrètes

Il est possible dans certains cas que les données continues de vent ne soient pas disponibles et que seules des données issues de roses des vents le soient. Ces dernières rendent compte du taux d'occurrence d'uniquement quelques gammes de vitesses (4 gammes dans l'exemple de la Fig. 10) quand les premières rendent compte des fréquences de toutes les vitesses de vent. Or, en modélisation, et notamment en mécanique des fluides numériques, chaque vitesse de vent entraine un résultat en concentration en polluant différent. Il serait donc intéressant de pouvoir évaluer la distribution continue des fréquences du vent sur la base de données discrète de roses des vents lorsque seules ces dernières sont disponibles. Ce point fait l'objet de la première méthodologie présentée ici et conçue dans le cadre de cette thèse.
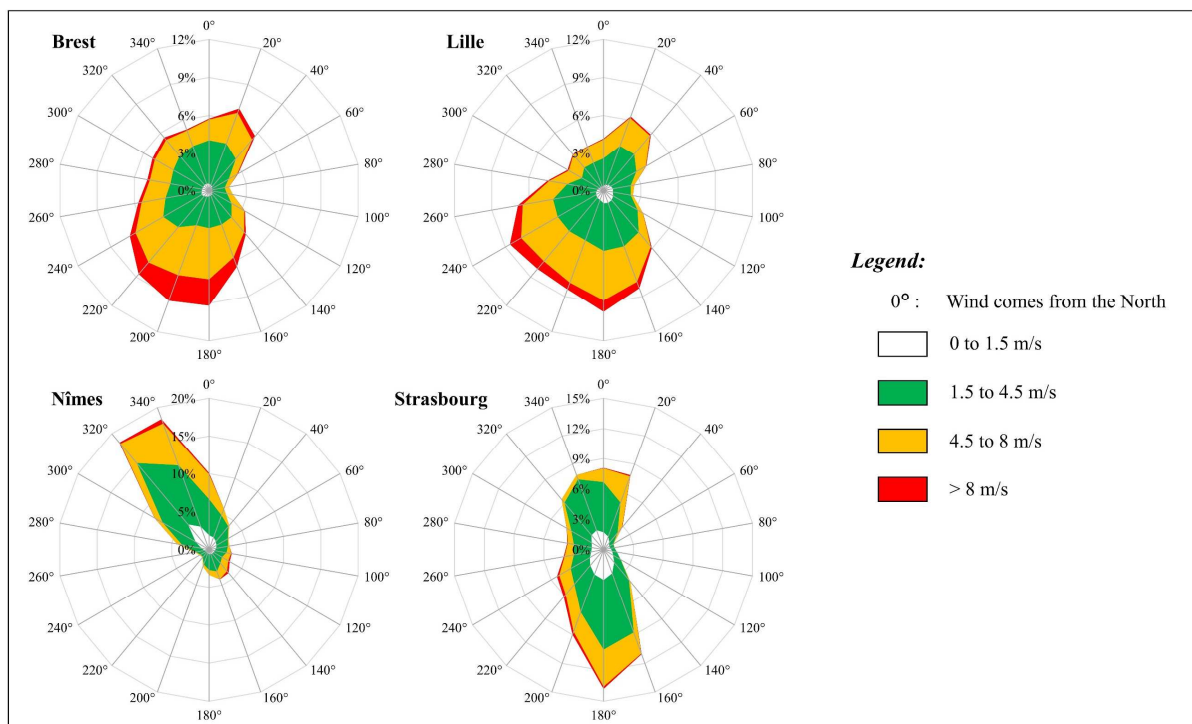
Fig. 10 – Exemple de roses des vents à Brest, Lille, Nîmes et Strasbourg (Reiminger et al., 2020b).

Cette méthodologie repose sur une fonction sigmoïde à cinq paramètres (α, β_1, β_2, γ_1 et γ_2, tous positifs) donnée ci-après en (30).

$$f(v) = \alpha.\left(-1 + \frac{1}{1 + \beta_1.e^{-\gamma_1.v}} + \frac{1}{1 + \beta_2.e^{\gamma_2.v}}\right) \tag{30}$$

Les paramètres de l'équation (30) peuvent être déterminés à l'aide d'un solveur et des données de rose des vents. Pour cela, deux équations supplémentaires sont nécessaires : l'équation (31) pour chaque gamme de vitesse disponible dans la rose des vents, et l'équation (32) pour fermer le système d'équations (dans le cas de la Fig. 10, les roses des vents donnent les fréquences de vent pour quatre gammes de vitesse et une cinquième équation est nécessaire pour déterminer les cinq paramètres inconnus).

$$\int_a^b f(v).dv = FVR_{[a;b[} \tag{31}$$

$$f(0) = 0 \tag{32}$$

avec $f(v)$ la fonction sigmoïde (30) et $FVR_{[a;b[}$ la fréquence de vent relative donnée par la rose des vents pour une gamme de vitesse allant de a inclus à b exclu.

Un exemple de résultat d'interpolation est proposé en Fig. 11 (A) avec (A1) la distribution initiale avec quatre gammes de vitesse issue de la rose des vents et (A2) la distribution réelle des données météorologiques ainsi que le résultat continu de la fonction sigmoïde en rouge. En appliquant cette méthodologie à toutes les directions de vent des roses présentées en Fig. 10, l'erreur de l'interpolation est en moyenne de 11.7%.

Cette méthodologie peut cependant sous-estimer la fréquence des faibles vitesses de vent (voir Fig. 11 (B2), courbe rouge) ce qui devient problématique pour la modélisation. En effet, plus la vitesse du vent est faible, plus la concentration en polluants modélisée est élevée. Sous-estimer la fréquence des vitesses faibles c'est donc sous-estimer les plus fortes concentrations en polluants. Pour pallier à ce problème, une fonction sigmoïde optimisée a été proposée.
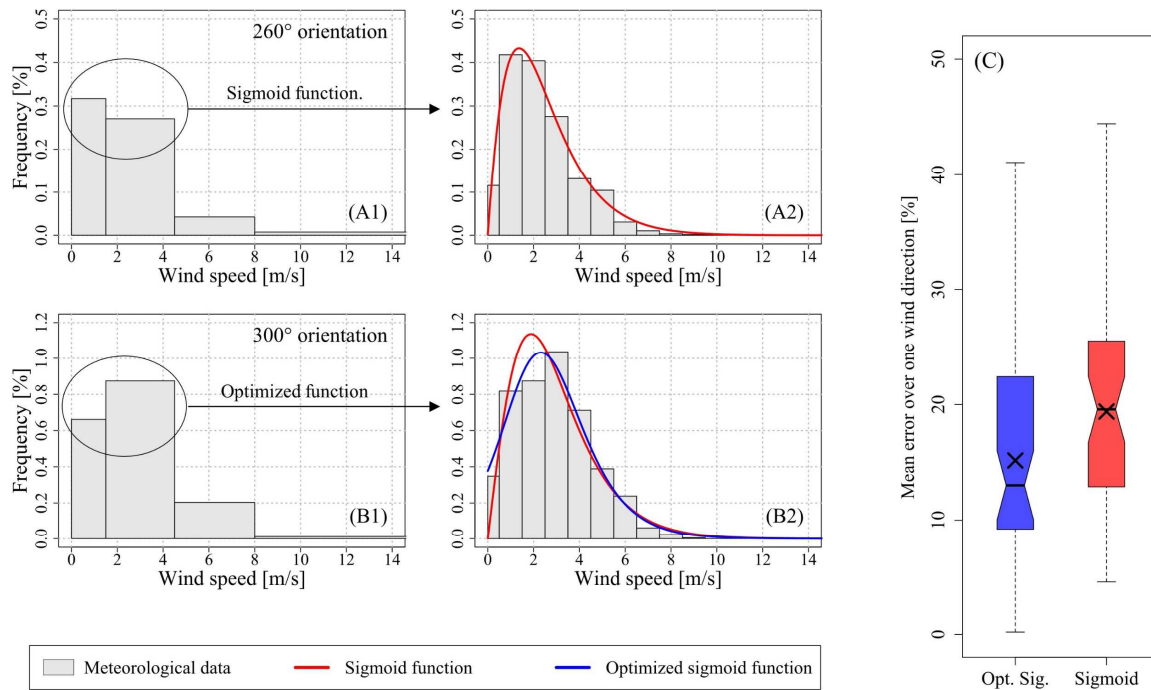
Fig. 11 – (A-B) Illustration des résultats de la fonction sigmoïde et de la fonction sigmoïde optimisée et (C) comparaison des deux méthodes (Reiminger et al., 2020b).

La fonction sigmoïde optimisée se base toujours sur les équations (30) et (31) mais cette fois-ci, l'équation (33) remplace de l'équation (32).

$$f(0) = FVR_{[0;\alpha[} \frac{FVR_{[0,\alpha[}}{FVR_{[\alpha,\beta[}}}$$
(33)

avec $FVR_{[0,\alpha[}$ la fréquence de vent relative pour la première gamme de vitesse de la rose des vents et $FVR_{[\alpha,\beta[}$ la fréquence pour la seconde gamme de vitesse (en gardant l'exemple précédent $\alpha = 1.5$ et $\beta = 4.5$).

Cette fonction est à appliquer si et seulement si la fréquence de la première gamme de vitesse dans la rose des vents est inférieure à celle de la seconde gamme, comme dans l'exemple donné en Fig. 11 (B1). Dans le cas contraire, la méthodologie non optimisée utilisant l'équation (32) reste valable et doit être appliquée. Le résultat de cette optimisation est illustré par la courbe bleue en Fig. 11 (B2).

Enfin, l'apport de cette optimisation a été quantifié sur la base des directions de vent des quatre roses des vents précédentes nécessitant d'utiliser la méthode optimisée (49 directions sur un total de 72). La Fig. 11 (C) montre le résultat de cette comparaison : la fonction optimisée engendre une erreur plus faible que la fonction basique par rapport aux données météorologiques réelles avec en moyenne 15.2% d'erreur contre 19.4% respectivement, soit une amélioration de la précision de près de 25%.

Tous les détails de cette méthodologie pourront être retrouvés dans l'article originel :

Reiminger, N.[1], Jurado, X.[1], Vazquez, J., Wemmert, C., Dufresne, M., Blond, N., Wertel, J., **2020**. Methodologies to assess mean annual air pollution concentration combining numerical results and wind roses. *Sustainable Cities and Society*, 59, 102221. DOI: 1016/j.scs.2020.102221

3.2. Calcul de la concentration moyenne annuelle en polluants sur la base de résultats numériques

L'Union Européenne (UE) ainsi que l'Organisation Mondiale de la Santé (OMS) ont fixé des concentrations seuils et des concentrations cibles en polluants atmosphériques à respecter pour limiter l'impact de la pollution de l'air sur la santé. Il existe plusieurs types de valeurs seuils et cibles tels que les valeurs moyennes annuelles, les valeurs moyennes journalières ainsi que les valeurs moyennes horaires.

Des études ont montré que les valeurs moyennes annuelles sont généralement plus difficiles à atteindre (Chaloulakou et al., 2008; Jenkin, 2004). La mesure sur site permet d'évaluer les concentrations moyennes annuelles, toutefois, ce procédé est couteux, car il nécessite un an de mesure et, de plus, il ne permet de connaitre les concentrations que ponctuellement. Il est donc nécessaire d'être en mesure de calculer les concentrations annuelles sur la base de résultats numériques tels que des résultats CFD.

En l'état, la modélisation CFD ne permet pas d'établir de concentration moyenne annuelle, car chaque résultat dépend de la direction et de la vitesse du vent utilisé. Il faudrait donc en théorie

---

[1] Ces auteurs ont contribué de manière égale.

réaliser une infinité de modélisations pour pouvoir déterminer une concentration moyenne annuelle.

Dans la pratique, il est possible de ne réaliser qu'une seule simulation par direction de vent dans le cas d'une atmosphère neutre. En effet, pour ce cas précis de stabilité atmosphérique, la concentration en polluants n'est fonction que de la direction du vent. Ainsi, sur la base d'une seule modélisation et à l'aide de l'équation (34) formulée par (Schatzmann and Leitl, 2011), il est possible de retrouver les champs de concentrations quel que soit la vitesse du vent considérée.

$$C_u = U_{ref}.\frac{C_{ref}}{u} \tag{34}$$

avec C_u la concentration en polluant pour la vitesse de vent u non modélisée et C_{ref} la concentration en polluant pour la vitesse modélisée U_{ref}.

La question de la concaténation de ces résultats et la prise en compte de la fréquence d'apparition des différentes vitesses de vent reste toutefois en suspens. Il est possible de faire le calcul de façon discrète, mais de cette façon, une importante sous-estimation des concentrations moyennes annuelles peut avoir lieu suivant les hypothèses de calcul (Reiminger et al., 2020b).

Pour pallier à ce problème, une méthodologie de concaténation continue des résultats a été développée. Cette méthodologie se base partiellement sur la méthodologie présentée dans la précédente section avec la fonction sigmoïde (30).

$$\bar{C}_d = \frac{\int_0^{+\infty} c(v).f(v).dv}{\int_0^{+\infty} f(v).dv} + C_{bg} \tag{35}$$

avec $\bar{C}_d$ la concentration moyenne annuelle pour une direction de vent donnée, $c(v)$ est la fonction décrivant l'évolution de la concentration en polluant avec la vitesse du vent (34), $f(v)$ est la fonction décrivant l'évolution de la fréquence d'apparition du vent en fonction de sa vitesse (30), et C_{bg} est la concentration de fond en polluants.

L'utilisation des équations (30) et (34) dans l'équation (35) conduit cependant à un problème mathématique lorsque v tend vers 0. Une alternative est donc proposée en équation (36).

$$\bar{C}_d = C_{max} \cdot \frac{\int_0^{v_{min}} f(v).dv}{\int_0^{+\infty} f(v).dv} + \frac{\int_{v_{min}}^{+\infty} c(v).f(v).dv}{\int_0^{+\infty} f(v).dv} + C_{bg} \qquad (36)$$

avec C_{max} la concentration maximale tolérée et v_{min} la vitesse pour laquelle $c(v)$ est considérée égal à C_{max}.

Enfin, la concentration moyenne annuelle peut être calculée à l'aide de l'équation (37).

$$\bar{C} = \frac{\sum_{d=1}^{n} \bar{C}_d \cdot f_d}{\sum_{d=1}^{n} f_d} \qquad (37)$$

avec $\bar{C}_d$ la concentration moyenne annuelle pour une direction de vent donnée d, $\bar{C}$ est la concentration moyenne annuelle et f_d est la fréquence totale de la direction de vent d.
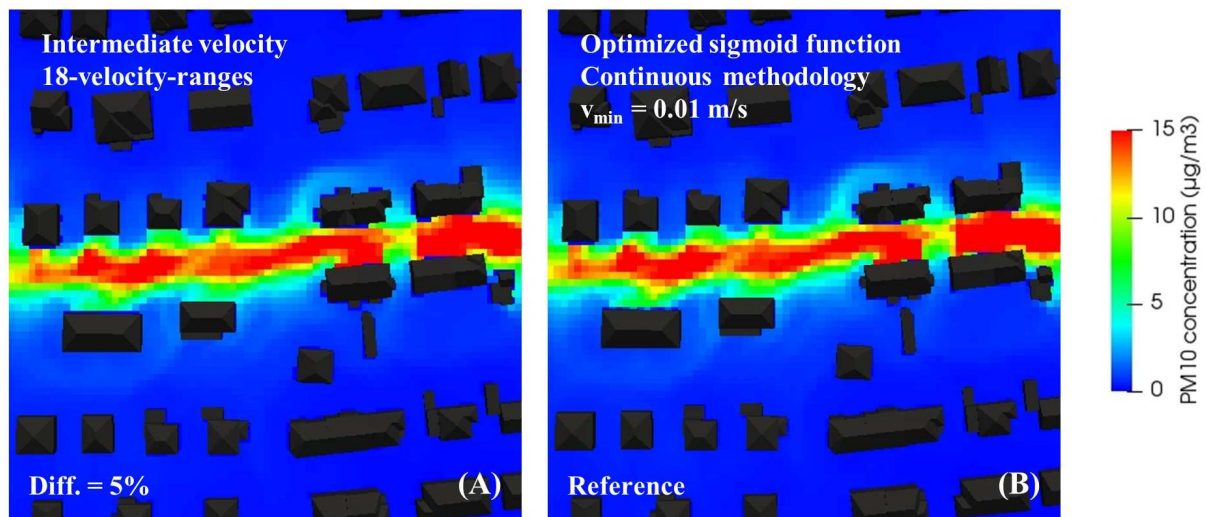
Fig. 12 – Comparaison entre la concentration moyenne annuelle (A) basé sur les données réelles de distribution de vent et (B) basé sur la fonction sigmoïde optimisée et l'équation (36) avec v_{min} = 0.01 m/s (Reiminger et al., 2020b).

Une comparaison a été réalisée sur la base de résultats CFD entre l'utilisation de cette méthode avec une rose des vents classique et l'utilisation de données réelles de distribution des vitesses. Pour cette comparaison, la vitesse minimale v_{min} = 0.01 m/s a été utilisée et $C_{max} = c(v_{min})$. Les résultats de cette comparaison sont proposés en Fig. 12. Ces résultats montrent la

performance de la méthodologie précédente associée à l'interpolation de la distribution des fréquences de vent en partant de données de roses des vents. En effet, ces méthodes de calcul n'entrainent que 5% de différence par rapport à l'utilisation de distribution des vitesses réelles et sont donc adaptées au calcul des concentrations moyennes annuelles sur la base de résultats numériques.

Tous les détails de cette méthodologie pourront être retrouvés dans l'article originel :

Reiminger, N.[1], Jurado, X.[1], Vazquez, J., Wemmert, C., Dufresne, M., Blond, N., Wertel, J., **2020**. Methodologies to assess mean annual air pollution concentration combining numerical results and wind roses. *Sustainable Cities and Society*, 59, 102221. DOI: 1016/j.scs.2020.102221

3.3. Estimation des concentrations en dioxyde d'azote sur le base de concentrations en oxydes d'azotes

La problématique entourant les oxydes d'azote (NO_x) et le dioxyde d'azote (NO_2) a été précédemment développée. Le NO_2 est l'acteur de nombreuses réactions chimiques et il est préférable de modéliser la dispersion des NO_x pour éviter de biaiser les résultats. Toutefois, la règlementation porte uniquement sur les NO_2 et il est nécessaire de pouvoir calculer les concentrations correspondantes sur la base des concentrations en NO_x. De prime abord, le plus simple serait l'utilisation de l'équilibre photochimique, mais celui peut entrainer une importante erreur dans certains cas. Une alternative est donc nécessaire pour calculer de façon plus fiable les concentrations en dioxyde d'azote.

Plusieurs alternatives correspondant à des lois empiriques peuvent être trouvées dans la littérature. En particulier, les lois suggérées par Derwent and Middleton (1996), Romberg et al. (1996) et Bächlin et al. (2008), et présentées en (38), (39) et (40) respectivement, ont été comparées. Cette comparaison a été réalisée contre plusieurs années de mesure fournies par certaines AASQA (Associations Agrées de Surveillance de la Qualité de l'Air) dans cinq régions de France. Les résultats de cette comparaison sont proposés en Fig. 13.

---

[1] Ces auteurs ont contribué de manière égale à l'article.

$$[NO_2] = \left(2.166 - \frac{[NO_x]}{1.91}(1.236 - 3.348A + 1.933A^2 - 0.326A^3)\right) \times 1.91 \qquad (38)$$

$$[NO_2] = \frac{103.[NO_x]}{[NO_x] + 130} + 0.005 \times [NO_x] \qquad (39)$$

$$[NO_2] = \frac{29.[NO_x]}{[NO_x] + 35} + 0.217 \times [NO_x] \qquad (40)$$

avec $[NO_2]$ la concentration en NO_2 en µg/m^3, $[NO_x]$ la concentration en NO_x en µg/m^3 et $A = log_{10}([NO_x]/1.91)$.
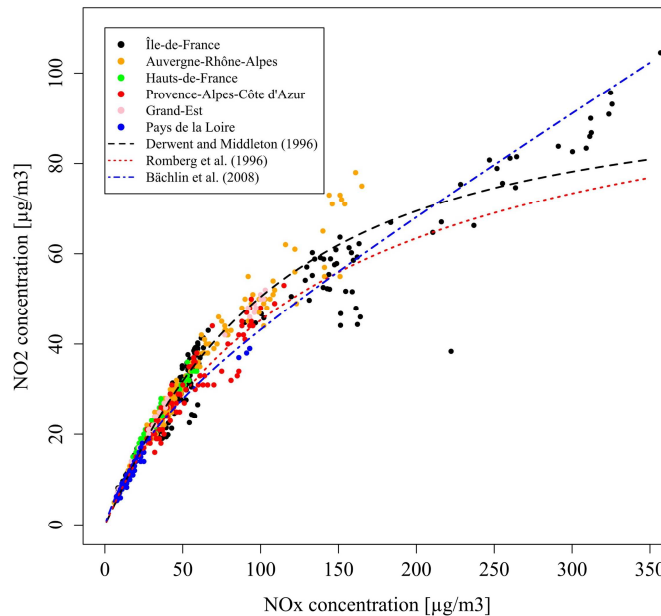
Fig. 13 – Evolution de la concentration en NO_2 en fonction de la concentration en NO_x et comparaison avec des lois empiriques (Jurado et al., 2020).

D'après la figure précédente, les trois lois reproduisent toutes plus ou moins précisément l'évolution des concentrations en NO_2 en fonction des concentrations en NO_x. Les erreurs commises par les trois lois par rapport aux données expérimentales ont été quantifiées et sont de 7,9% pour la loi de Derwent et Middleton, 9,5% pour la loi de Romberg et al. et 10,1% pour la loi de Bächlin et al. On notera toutefois que cette dernière loi, bien qu'étant celle ayant la plus grande déviation par rapport aux données expérimentales, est celle qui entraine le moins d'erreurs pour les concentrations en NO_x les plus élevées.

294

La meilleure loi pour calculer les concentrations en NO_2 sur la base des concentrations en NO_x en France est donc la loi de Derwent et Middleton entrainant une erreur globale de 8%, mais pouvant s'avérer plus faible pour les concentrations en NO_x inférieure à 70 µg/m³. Cette loi peut ainsi être utilisée à la place de l'équilibre photochimique étant plus facile d'application et entrainant une erreur moindre.

Tous les détails de cette étude ainsi que des précisions supplémentaires pourront être retrouvés dans l'article originel :

Jurado, X.[1], Reiminger, N.[1], Vazquez, J., Wemmert, C., Dufresne, M., Blond, N., Wertel, J., **2020**. Assessment of mean annual NO2 concentration based on a partial dataset. *Atmospheric Environment* 221, 117087. DOI: 10.1016/j.atmosenv.2019.117087

3.4. Détermination de la concentration moyenne annuelle en dioxyde d'azote sur la base de données mensuelles

La dernière méthodologie développée dans le cadre de cette thèse correspond à la détermination des concentrations moyennes annuelles en NO_2 sur la base de données mensuelles issues de capteurs.

Comme expliqué précédemment, la mesure de la qualité de l'air est une option coûteuse, notamment lorsqu'il est nécessaire d'avoir un an de données pour comparer avec les valeurs règlementaires. De plus, la mesure n'offre un résultat qu'en un point donné (latitude, longitude, altitude). Être en mesure d'estimer les concentrations moyennes annuelles sur la base de périodes de mesure plus courtes, comme un mois, permettrait donc de diminuer le coût nécessaire ou de multiplier le nombre de points de mesure sur une même période totale. Toujours avec l'exemple du mois, pour un point de mesure le coût pourrait être diminué d'un facteur douze où, pour un an de mesure, la qualité de l'air en douze points de mesure différents pourrait être évaluée.

---

[1] Ces auteurs ont contribué de manière égale à l'article.

Dans ce but, une nouvelle loi a été développée sur la base des données de mesures précédemment utilisées pour valider la loi de Derwent et Middleton en France. Cette loi, présentée ci-dessous, permet d'estimer les concentrations annuelles en NO₂ sur la base de 30 jours de mesure consécutifs, quels que soient le mois et le premier jour de la campagne de mesure.

$$[NO_2]_a = \alpha.[NO_2]_m^2 + \beta.[NO_2]_m \tag{41}$$

$$\alpha = 0.0033 - 0.0102.\exp\left[\frac{-(m - 6.5749)^2}{8.6962}\right] \tag{42}$$

$$\beta = 0.6945 + 0.8708.\exp\left[\frac{-(m - 6.7076)^2}{7.4328}\right] \tag{43}$$

avec $[NO_2]_a$ la concentration annuelle en NO₂ en µg/m³, $[NO_2]_m$ la concentration mensuelle en NO₂ en µg/m³, α et β deux paramètres calculés respectivement avec (42) et (43) et m un nombre réel positif correspondant au début du mois de la campagne de mesure (e.g. $m = 1$ pour une campagne de mesure du premier au dernier jour du mois de janvier, $m = 3,5$ pour une campagne de mesure du 15 mars au 15 avril, etc.).

Cette méthodologie permet de calculer les concentrations annuelles en NO₂ sur la base de concentrations mesurées pendant 30 jours avec une incertitude de l'ordre de 10% en Ile-de-France et 15% plus généralement en France. Il faudra noter toutefois que l'incertitude dépend du mois où la campagne de mesure est réalisée et peut être plus faible, notamment en avril avec seulement 7% d'erreur.

Tous les détails de cette étude ainsi que des précisions supplémentaires pourront être retrouvés dans l'article originel :

Jurado, X.[1], Reiminger, N.[1], Vazquez, J., Wemmert, C., Dufresne, M., Blond, N., Wertel, J., **2020**. Assessment of mean annual NO2 concentration based on a partial dataset. *Atmospheric Environment* 221, 117087. DOI: 10.1016/j.atmosenv.2019.117087

---

[1] Ces auteurs ont contribué de manière égale à l'article.

4. Application à des fin de conception, compréhension et diagnostic

Un des objectifs de cette thèse était également de prouver l'applicabilité des modèles CFD, ainsi que d'illustrer les méthodes développées et présentées précédemment, pour l'étude de la qualité de l'air en zone urbaine à des fins de conception, compréhension et diagnostic.

4.1. Conception : impact des dimensions des bâtiments sur la qualité de l'air extérieur

Une étude a été réalisée en deux dimensions à l'aide du modèle à convection forcée afin d'étudier l'impact des dimensions d'une rue canyon asymétrique descendante (bâtiment amont plus grand) sur les concentrations moyennes en polluants atmosphériques observées dans cette rue. En particulier, cette étude s'intéresse à l'évolution des concentrations moyennes en polluants dans la rue en fonction du rapport de hauteur des bâtiments $H1/H2$ et du rapport de largeur de la rue $W/H2$ avec $H1$ la hauteur du bâtiment amont, $H2$ la hauteur du bâtiment aval et W la longueur de la rue.

A l'issue des 36 simulations réalisées, et en fonction des ratios de hauteur et de longueur utilisés, trois types de régimes ont été mis en évidence dans la rue canyon. Ces régimes sont présentés en Fig. 14.
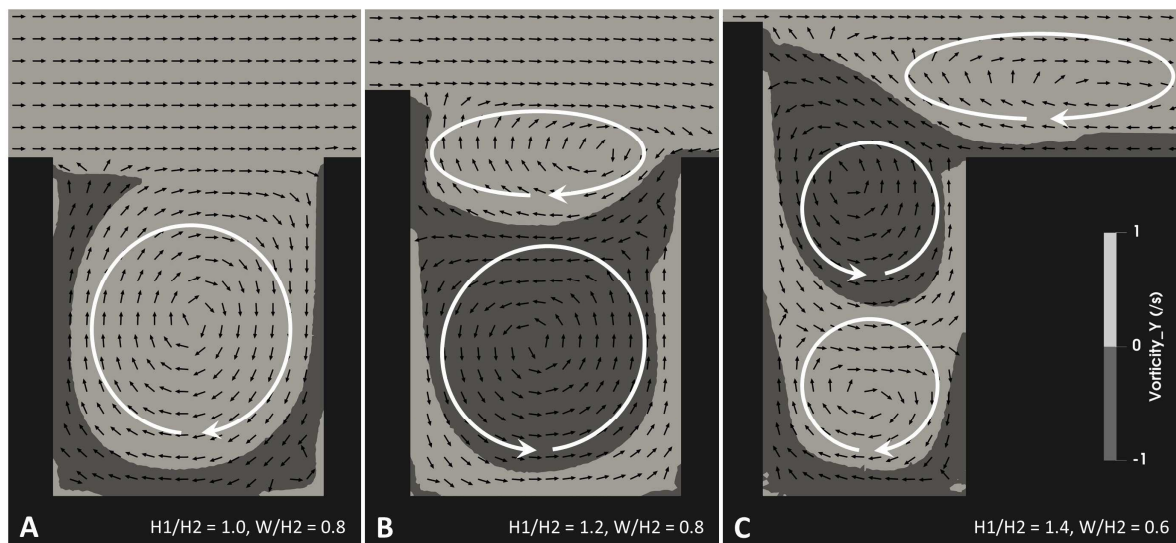
Fig. 14 – Régimes d'écoulement, vecteurs vitesse et vorticité selon *y* pour différents ratios *H1/H2* et *W/H2* (Reiminger et al., 2020c).

En particulier, on observe :

- Dans le cadre d'un régime A, un unique vortex dans la rue canyon tournant dans le sens horaire.

- Dans le cadre d'un régime B, un vortex dans la rue canyon tournant dans le sens antihoraire et un second vortex au-dessus, tournant dans le sens horaire.

- Dans le cadre d'un régime C, deux vortex dans la rue canyon avec un premier tournant dans le sens horaire, un second au-dessus tournant dans le sens antihoraire, et enfin un troisième vortex en dehors de la rue tournant dans le sens horaire.
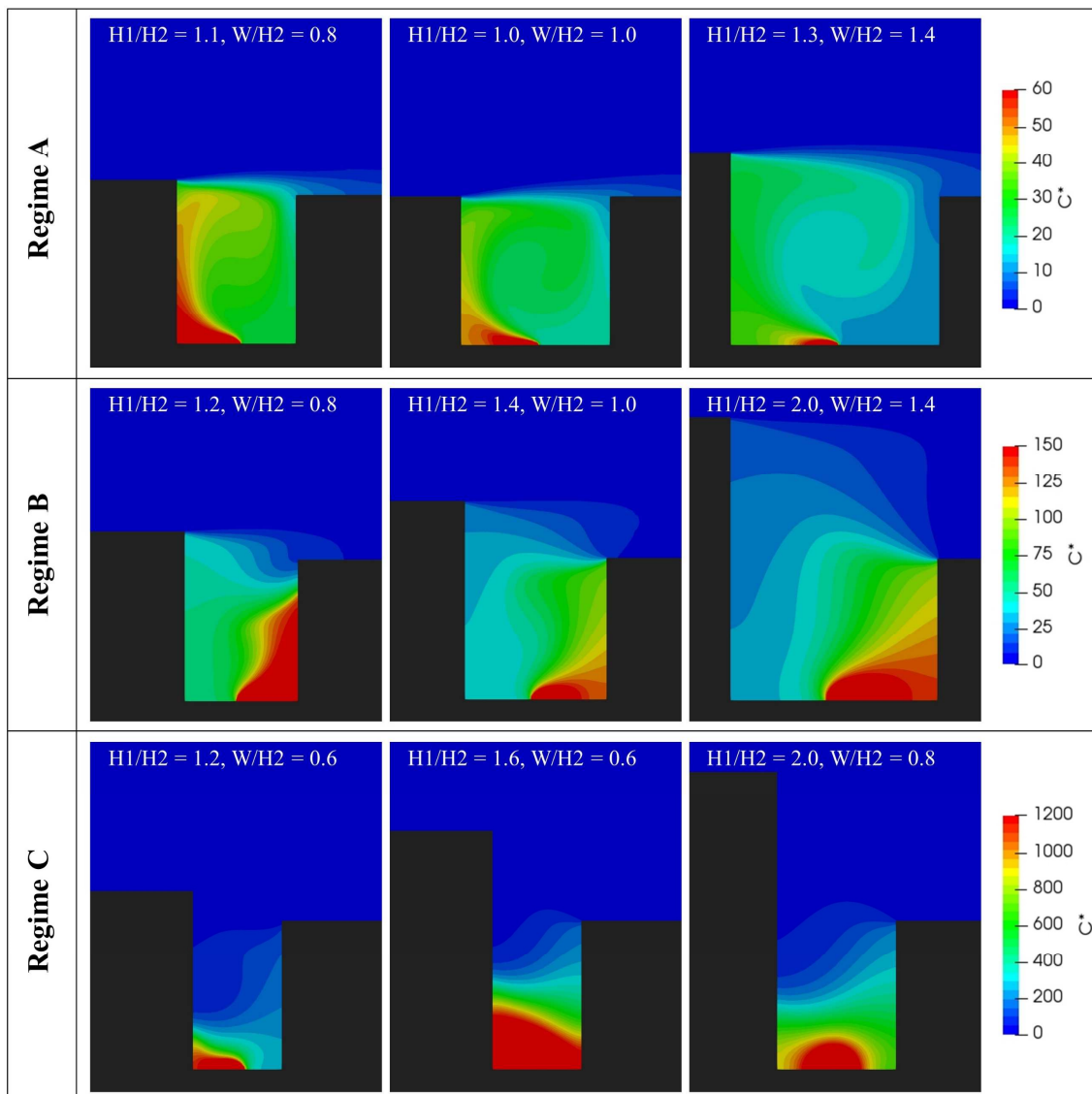
Fig. 15 – Trois exemples de concentration adimensionnelle dans la rue canyon en fonction de chaque type de régime observes (Reiminger et al., 2020c).

L'impact de ces trois régimes sur les concentrations en polluants est illustré en Fig. 15 avec trois exemples par régime. Les résultats montrent qu'en fonction du régime d'écoulement dans la rue canyon, des concentrations maximales très différentes sont observées : la concentration maximale est 2,5 fois plus élevée pour le régime B par rapport au régime A et 20 fois plus élevée pour le régime C par rapport au régime A. De plus, la localisation des concentrations maximales est également différente avec des concentrations globalement plus élevées au niveau du bâtiment amont pour le régime A, au niveau du bâtiment aval pour le régime B et dans toute la rue pour le régime C.

Enfin, l'évolution de la concentration moyenne dans la rue a été étudiée en fonction des deux ratios de hauteur et de longueur. Les résultats sont présentés en Fig. 16. Ces résultats sont un exemple concret de l'intérêt d'un modèle de mécanique des fluides numérique à des fins de conception. En effet, la figure ci-dessous peut être considérée comme un abaque afin de choisir au mieux les hauteurs des bâtiments et la longueur de la rue pour maintenir une bonne ventilation et donc limiter les concentrations en polluants. Dans le cas présent, il est ainsi conseillé de rester dans la zone correspondant au régime A.
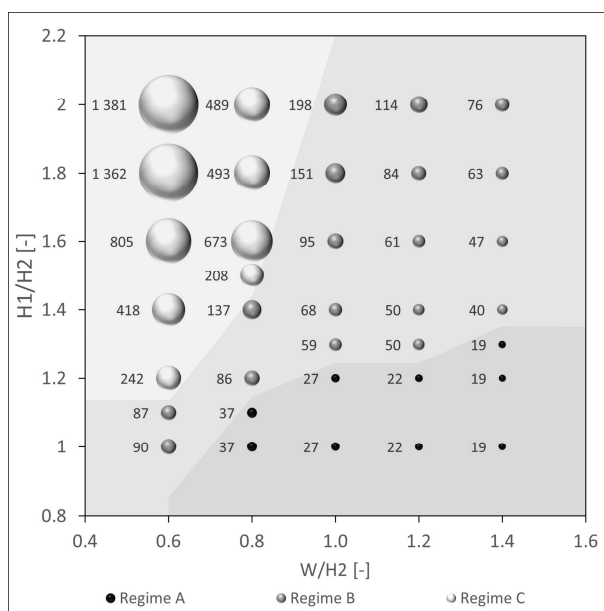
Fig. 16 – Concentration adimensionnelle moyenne dans la rue en fonction des ratios *H1/H2* et *W/H2* (Reiminger et al., 2020c).

Tous les détails de cette étude ainsi que des résultats supplémentaires pourront être retrouvés dans l'article originel :

Reiminger, N., Vazquez, J., Blond, N., Dufresne, M., Wertel, J., **2020**. CFD evaluation of mean pollutant concentration variations in step-down street canyons. *Journal of Wind Engineering and Industrial Aerodynamics* 196, 104032. DOI: 10.1016/j.jweia.2019.104032

4.2. Compréhension : effet de la stabilité atmosphérique sur la dispersion des polluants

L'intérêt d'un modèle de mécanique des fluides numérique réside également dans le fait de pouvoir étudier l'impact de phénomènes complexes agissant sur la dispersion des polluants de l'air. Dans le cadre de cette thèse, une étude a porté la dispersion de polluants issus du trafic routier au niveau d'une autoroute, en présence de murs antibruit. En particulier, cette étude s'intéressait à l'impact des murs antibruit sur la diminution ou l'augmentation des concentrations en polluants en aval des murs antibruit pour plusieurs cas météorologiques entrainant des stabilités atmosphériques différentes.

Pour cette étude, le modèle à convection mixte a été considéré et des modélisations 3D ont été réalisées en présence ainsi qu'en absence des murs antibruit afin de quantifier les variations de concentrations observées entre les deux cas.

Les résultats ont montré en premier lieu que, dans un cas isotherme, c'est-à-dire avec une stabilité dite neutre, la variation de concentration en aval entre un cas avec et un cas sans murs antibruit ne dépend que de la direction de vent et non de sa vitesse, une direction non orthogonale de vent entrainant des concentrations plus élevées sans murs et plus faibles avec murs.

En second lieu, l'étude a montré que la stabilité atmosphérique a un impact sur les effets bénéfiques des murs antibruit, c'est-à-dire sur leur capacité à réduire les concentrations en polluants à l'aval. D'après les résultats obtenus, une atmosphère stable améliore la réduction des polluants après les murs tandis qu'une atmosphère instable entraine l'effet inverse.

Ce dernier résultat, étant contraire aux résultats auxquels on pourrait s'attendre dans les rues canyon (Allegrini et al., 2015), il prouve l'intérêt des modèles de mécanique des fluides

numérique dans la modélisation et la compréhension des phénomènes complexes de ventilation et transport de polluants en zones urbaines.

Plus de détails et de résultats pourront être retrouvés dans l'article originel :

Reiminger, N., Jurado, X., Vazquez, J., Wemmert, C., Blond, N., Dufresne, M., Wertel, J., **2020**. Effects of wind speed and atmospheric stability on the air pollution reduction rate induced by noise barriers. *Journal of Wind Engineering and Industrial Aerodynamics* 200, 104160. DOI : 10.1016/j.jweia.2020.104160

4.3. Diagnostic : étude de la qualité de l'air à proximité d'une voie rapide

Enfin, un modèle de mécanique des fluides numérique peut également être utilisé à des fins d'ingénierie pour le diagnostic de la qualité de l'air dans des zones où la dispersion des polluants est régie par des phénomènes complexes. Dans le cadre de cette thèse, ce point a été traité à de nombreuses reprises et un exemple d'illustration est donné ci-après.

L'étude retenue à des fins d'illustration a été réalisée au niveau de l'Eurométropole de Strasbourg et plus particulièrement au niveau d'une zone située à proximité de l'autoroute A35. Cette autoroute représente une source majeure d'émissions en polluants atmosphériques qui peut entrainer d'importantes concentrations en polluants dans la zone d'étude. Toutefois, un mur antibruit les sépare. Une modélisation numérique avancée de type CFD est alors nécessaire pour évaluer de façon précise les concentrations en polluants dans la zone d'étude (NO$_2$, PM$_{10}$ et PM$_{2.5}$), étant donné le caractère complexe de l'écoulement et de la dispersion des polluants après un mur antibruit (Reiminger et al., 2020c).

La zone d'étude est illustrée en Fig. 17 (cercle rouge). Cette figure montre également quelles directions de vent il est nécessaire de modéliser afin de prendre en compte la dispersion des polluants depuis l'A35, vers la zone d'étude. La zone d'intérêt a été reproduite en trois dimensions et maillée afin de pouvoir lancer les modélisations. Des mailles de 1 m avec un raffinement à 0.5 m à proximité des parois ont été utilisées, entrainant un total de 3 millions de mailles. Ce maillage a été retenu, car il entraine une sensibilité au maillage inférieure à 5% et $y^+ = 350$. Une illustration de la géométrie 3D et du maillage est proposée en Fig. 18 et Fig. 19 respectivement.
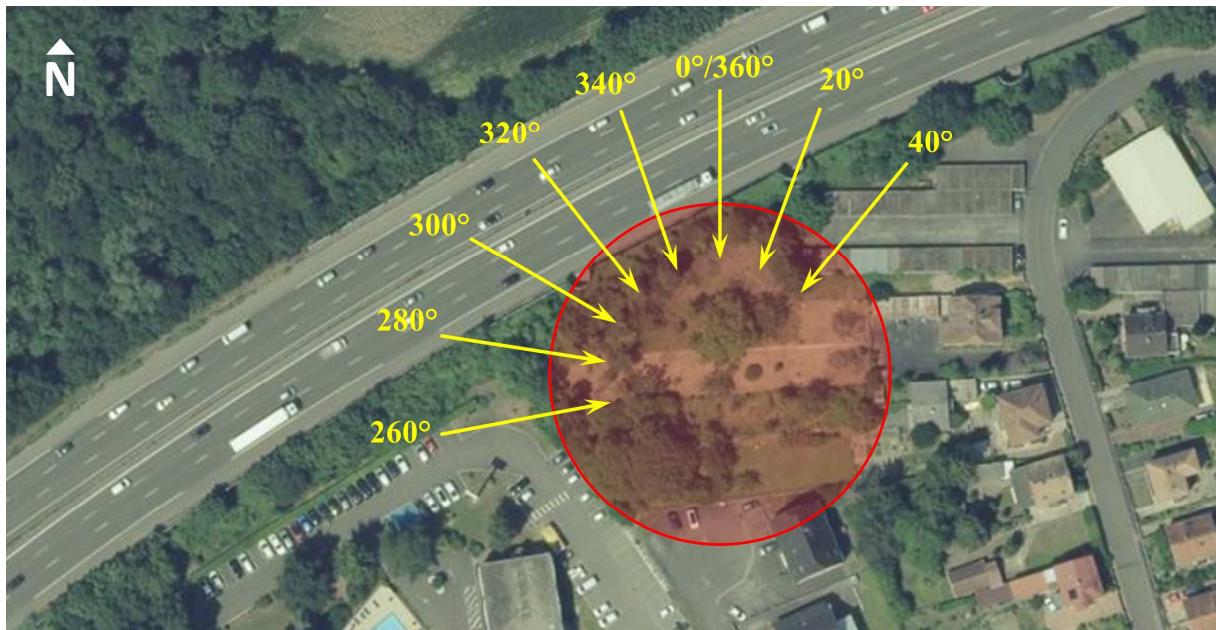
Fig. 17 – Illustration de la zone d'étude (en rouge) et des directions de vent modélisées transportant les polluants depuis l'A35 vers la zone d'étude (en jaune).
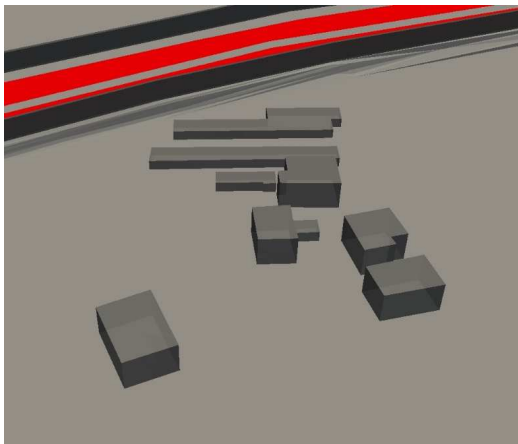
Fig. 18 - Illustration de la géométrie 3D.
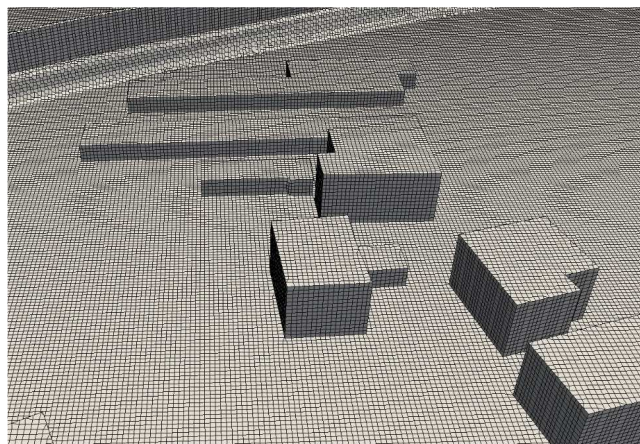
Fig. 19 - Illustration du maillage.

Les recommandations données par Franke et al., (2007) en termes de distance minimale dans le domaine et conditions aux limites ont été respectées (Cf. Section 2.2.1 et Section 2.2.2). Les émissions ont été estimées à 348 mg/s, 28 mg/s et 21,5 mg/s pour les NO_x, PM_{10} et $PM_{2,5}$ respectivement sur la base des données de comptage fournies par la DIREST (Direction Interdépartementale des Routes de l'Est). Enfin, les concentrations de fond en polluants ont été fixées à 22 µg/m³, 21 µg/m³ et 14 µg/m³ respectivement pour les NO_2, PM_{10} et $PM_{2,5}$, ce qui

correspond aux concentrations moyennes annuelles relevées en 2018 au niveau des stations de fond d'ATMO Grand-Est à Strasbourg.

Un exemple de résultat sur les champs de vitesse obtenu pour un vent provenant du nord et se dirigeant vers le sud est proposé en Fig. 20. Cette figure illustre bien toute la complexité de l'écoulement en présence de structures telles que bâtiments, talus et mur antibruit. En effet, ces structures entrainent d'importantes décélérations dans la vitesse de l'écoulement, mais également des changements de directions de vent. On remarque par exemple, juste après le mur antibruit aval, que la direction de l'écoulement devient orthogonale à sa direction initiale, en amont de l'autoroute. Ces changements entrainent par définition des modifications dans la dispersion des polluants atmosphériques.
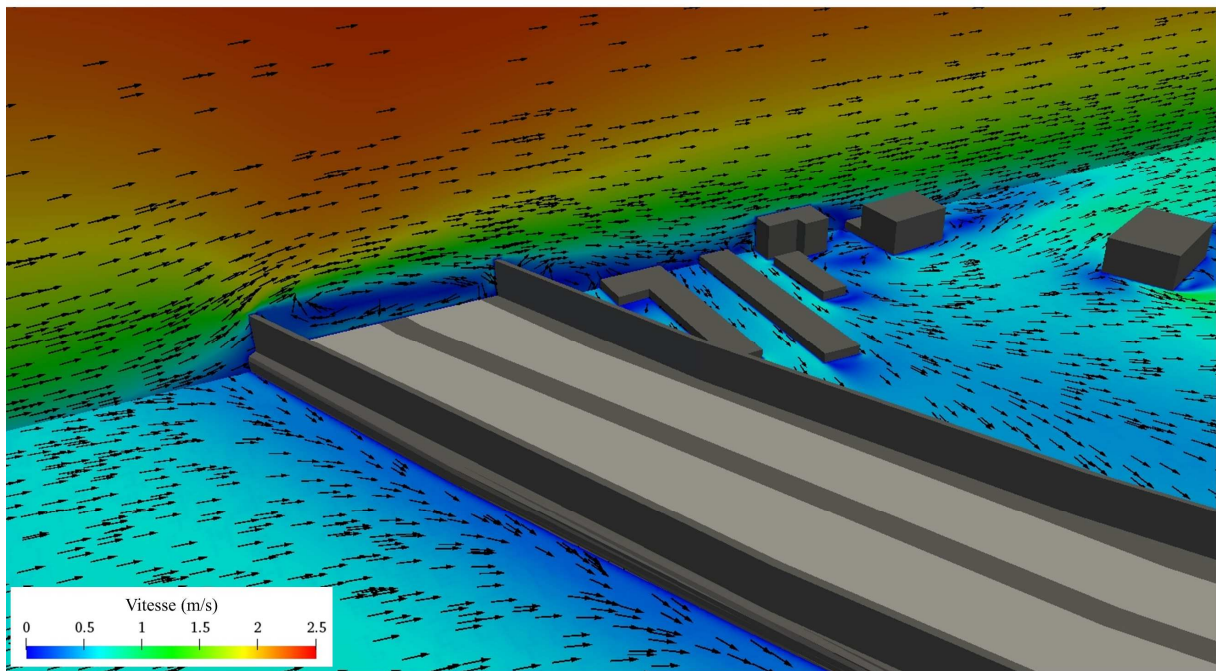
Fig. 20 – Vue 3D de l'évolution de la vitesse et de la direction du vent pour un vent provenant du nord avec une vitesse initiale de 1.5 m/s à 10m d'altitude.

Un total de huit directions de vent a été modélisé dans le cadre de cette étude. Sur la base des résultats obtenus, ainsi que des méthodologies proposées en Section 3.1 et Section 3.2 (Reiminger et al., 2020b), les concentrations moyennes annuelles en NO_2, PM_{10} et $PM_{2,5}$ ont pu être estimées. Pour les concentrations annuelles en NO_2, la méthodologie présentée en Section 3.3 (Jurado et al., 2020) fut également nécessaire. Les résultats correspondants sont présentés en Fig. 21.
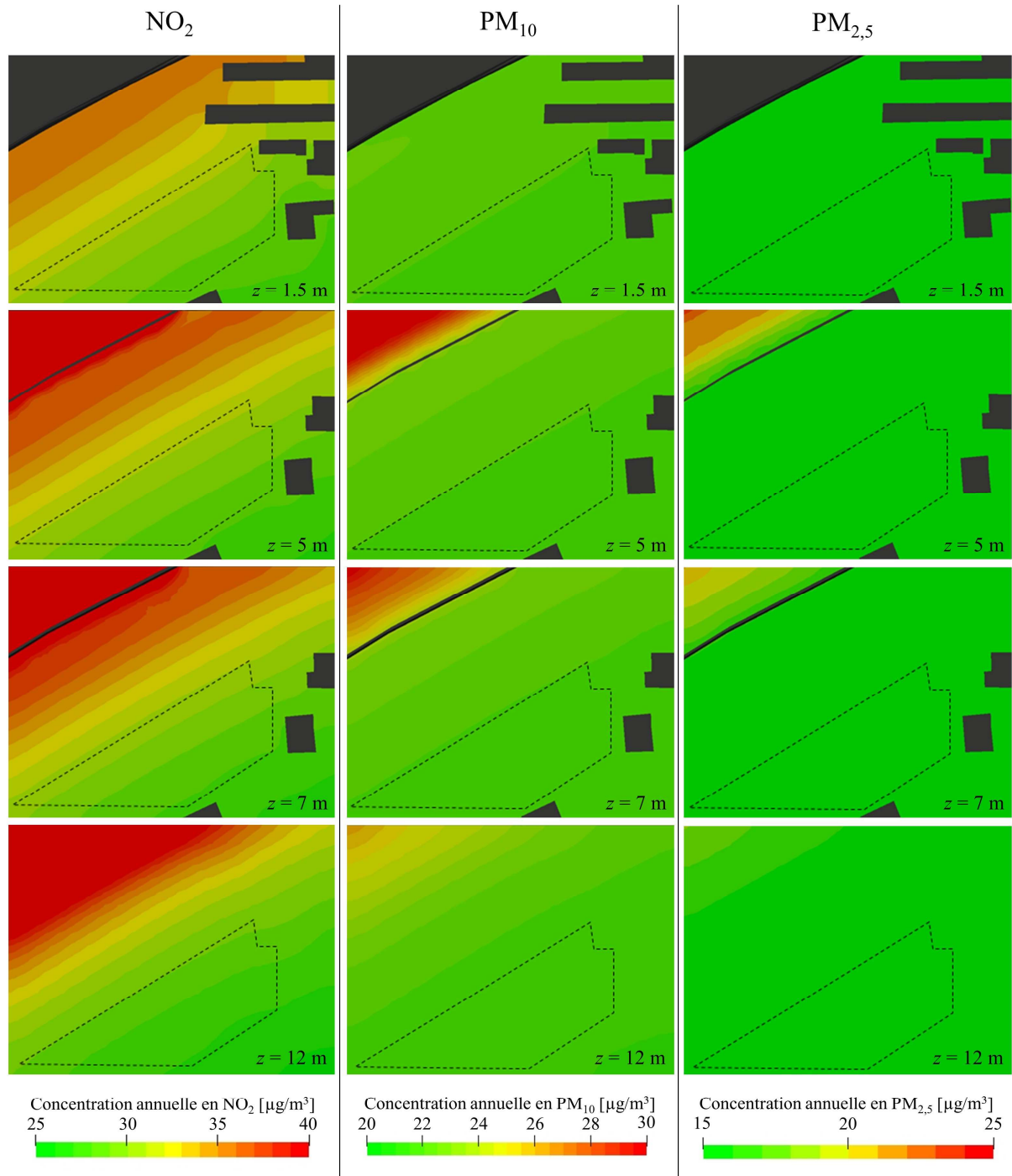
Fig. 21 – Concentration annuelle en NO₂, PM₁₀ et PM₂,₅ modélisées pour différentes altitudes avec la zone prévue pour aménagement délimitée par des traits discontinus.

Les résultats présentés dans la figure précédente montrent que, dans la zone étudiée, les concentrations annuelles moyennes en NO_2 sont plus variables que les concentrations annuelles de PM_{10} et $PM_{2,5}$. Les principaux résultats sont les suivants :

- **Concernant le NO_2 :** Une concentration annuelle moyenne d'environ 40 µg/m3 est obtenue pour 7 m et 12 m de hauteur à l'aval de l'autoroute, à proximité des murs antibruit, ce qui correspond à la zone non constructible. Dans la zone prévue pour être aménagée, les concentrations annuelles en NO_2 varient de 25 µg/m3 à 32 µg/m3 selon la distance à l'autoroute. En outre, dans cette zone, les concentrations annuelles diminuent avec l'altitude et conduisent à des concentrations annuelles maximales en NO_2 d'environ 27 µg/m3 pour une hauteur de 12 m à proximité de l'autoroute.

- **Concernant les PM_{10} :** une concentration annuelle moyenne maximale de 23 µg/m3 est observée dans la zone prévue pour être aménagée.

- **Concernant les $PM_{2,5}$:** une concentration annuelle moyenne maximale de 16 µg/m3 est observée dans la zone prévue pour être aménagée.

Il est important de noter que dans la zone non constructible proche de l'autoroute, les concentrations ont tendance à augmenter avec l'altitude en raison du panache provenant du haut du mur antibruit. L'observation est différente dans la zone prévue pour être construite, où des altitudes plus élevées se traduisent par des concentrations plus faibles. Enfin, quel que soit le polluant considéré, les concentrations diminuent au fur et à mesure que l'on s'éloigne de l'autoroute.

Cette étude a permis de mettre en exergue le rôle des murs antibruit dans la dispersion des polluants atmosphériques et, plus précisément, l'abattement de leur concentration dans des zones situées à proximité d'axes à fort trafic. Les résultats permettent également de formuler des préconisations.

Selon les résultats d'ATMO Grand Est à l'échelle urbaine et de CFD à l'échelle micro, la pollution de l'air est la plus élevée à proximité de l'autoroute et diminue avec l'augmentation de la distance à la route. Sur la base de cette observation, il est recommandé de placer des prises d'air pour la ventilation sur la ou les faces du ou des bâtiments orientées sud-sud-est. Un système

de ventilation de type double flux avec un système de filtration efficace est recommandé pour limiter la contribution des polluants à l'air intérieur des logements. Dans le même ordre d'idée, les balcons devront être placés sur la façade sud-sud-est des bâtiments. De telles dispositions pourraient également être prises du côté nord si des dispositifs d'étanchéité à l'air de type loggia sont prévus.

Les résultats CFD ont montré une information supplémentaire qu'il n'était pas possible de connaître avec le modèle à échelle urbaine : la pollution de l'air augmente globalement avec l'altitude en raison de la barrière antibruit. Ainsi, on peut recommander que les logements n'aient pas plus de deux niveaux (rez-de-chaussée et premier étage). Les greniers peuvent être aménagés à condition de respecter la réglementation en vigueur dans le plan d'urbanisme local en ce qui concerne la hauteur maximale sous les gouttières (7 m) et la hauteur totale (12 m).

Enfin, des recommandations peuvent également être faites concernant les terrasses et les jardins. Pour protéger les personnes, l'effet de masque des habitations peut être utilisé. Pour ce faire, jardins et terrasses doivent être placées dans la partie sud-sud-est des parcelles, au plus près des bâtiments. Pour aller plus loin, elles peuvent être bordées de surfaces imperméables (palissades de bois ou de verre, etc.) ou presque imperméables (haies ou végétation permanente dense, c'est-à-dire également présente en hiver) afin de limiter l'apport de polluants dans les jardins. Lors de l'utilisation des plantes, il est préférable de choisir des plantes non allergènes.

5. Conclusion générale

L'objectif de cette thèse était le développement et la validation de solveurs de mécanique des fluides numérique (CFD) et de nouvelles méthodologies pour évaluer la qualité de l'air dans les zones urbaines, destinées à un public opérationnel traitant de questions d'ingénierie.

Dans la première partie de cette thèse, de nouveaux solveurs CFD ainsi que des outils et des méthodologies ont été développés en tenant compte de l'état de l'art scientifique et des besoins en ingénierie.

Concernant le développement de codes CFD pour la modélisation de la pollution de l'air

Le choix s'est porté sur une méthodologie RANS (Reynolds-Averaged Navier-Stokes) afin de garantir des temps de calcul et, par conséquent, des coûts de calcul conformes aux exigences techniques. Deux solveurs RANS transitoires basés sur OpenFOAM ont été développés, dont un solveur pour les flux incompressibles destiné à la modélisation des atmosphères neutres, appelé solveur à convection forcée, et un solveur pour les flux compressibles destiné à la modélisation des atmosphères stables et instables, appelé solveur à convection mixte. Des phénomènes supplémentaires ont été inclus dans les deux codes avec les effets de la végétation sur le flux d'air et également sur le polluant (dépôt) ainsi que l'équilibre photochimique. Les deux solveurs ont été testés sur la base de sept cas tests réalisés en soufflerie et *in situ* qui comprenaient des configurations 2D et 3D, ainsi que des effets thermiques et de la végétation. En utilisant ces codes de calcul, des concentrations modélisées avec moins de 10% d'erreur peuvent être obtenues avec une représentation précise et fiable du champ de vitesse et aussi, une modélisation précise des échanges intérieur/extérieur en utilisant des modèles de turbulence isotropique tels que le modèle standard de turbulence k-ε.

Concernant l'utilisation de solveurs CFD pour évaluer la qualité de l'air dans les zones urbaines

Des recherches et des améliorations ont été entreprises au sujet du domaine de calcul et de la paramétrisation du solveur. Les lignes directrices de COST Action 732 ont donné des recommandations adéquates en termes de distances minimales à inclure dans le domaine de calcul, néanmoins, il a été démontré qu'une distance verticale d'au moins 96 m doit être prise en compte même en l'absence de bâtiments. Il a été également démontré qu'un maillage satisfaisant un critère y^+ allant de 30 à 500 ne peut être obtenu sans une augmentation drastique des temps de calcul. Cependant, des cellules hexamétriques de 1 m dans la zone d'intérêt et un raffinement plus fin de 0,5 m près des murs et à la source d'émission sont un bon compromis entre vitesse de calcul et dimensions du maillage, ce qui permet d'obtenir des résultats indépendants de ce dernier. En ce qui concerne les conditions aux limites, elles peuvent être grandement améliorées, en particulier pour la condition en entrée, en envisageant un couplage avec des modèles 1D tels que le modèle CIM qui permet de calculer des profils de vitesse du vent et de turbulence fiables et cohérents avec ceux que l'on trouve dans les zones urbaines.

Enfin, les émissions doivent être calculées avec soin en utilisant comme exemple les guides de l'Agence européenne pour l'environnement, et les concentrations de fond doivent être soigneusement choisies pour éviter les erreurs finales dans les résultats numériques.

Concernant les méthodologies existantes et nouvelles pour évaluer la qualité de l'air à l'échelle urbaine

Afin de rendre la modélisation CFD pleinement opérationnelle à des fins d'ingénierie, des méthodologies existantes ont été éprouvées et plusieurs outils et nouvelles méthodologies ont été développés

La loi de Derwent et Middleton, une fonction à un paramètre permettant d'évaluer les concentrations annuelles de dioxyde d'azote (NO_2) en fonction des concentrations annuelles d'oxydes d'azote (NO_x), a fait ses preuves sur la base de cinq années de données de qualité de l'air mesurée dans plusieurs régions de France. Cette fonction peut être utilisée à la place de l'équilibre photochimique dans le solveur CFD puisqu'elle ne nécessite qu'un seul paramètre, la concentration en NO_x, et entraîne moins de 10% d'erreur.

Une nouvelle méthodologie utilisant une fonction quadratique et deux fonctions gaussiennes a été développée dans le but d'évaluer les concentrations annuelles de NO_2 avec seulement un mois de données. Cette méthodologie, qui conduit à une erreur maximale de 15 % et à une erreur moyenne d'environ 10 % est très pertinente pour la modélisation numérique, car elle peut par exemple être utilisée pour évaluer rapidement les concentrations de fond annuelles sur la base d'un seul mois de mesures réalisées avec des stations de fond.

Une fonction sigmoïde à 5 paramètres a été développée pour évaluer les distributions continues du vent sur la base de données simplifiées et discrètes comme celles disponibles avec les roses des vents. Cette nouvelle fonction apporte des améliorations par rapport à la distribution de Weibull habituellement utilisée et conduit à une erreur moyenne de 12% sur les distributions de vent pour quatre roses des vents données en France. Une optimisation de cette fonction a également été développée afin de mieux évaluer certaines distributions de vent particulières, ce qui permet de réduire encore plus les erreurs.

Les limites des méthodologies discrètes pour évaluer les concentrations annuelles sur la base de résultats numériques ponctuels ainsi que leurs hypothèses implicites ont été discutées en dernier lieu, et des méthodologies alternatives ont été présentées. Elle comprend une variante de la méthodologie discrète qui tient compte des vitesses représentatives au lieu des vitesses intermédiaires pour éviter les sous-estimations des concentrations de polluants, et une nouvelle méthodologie continue pour évaluer les concentrations annuelles moyennes illustrées par les résultats de la CFD.

Concernant l'utilisation des solveurs et des méthodologies CFD à des fins de conception, de compréhension et de diagnostic

Dans la deuxième partie de cette thèse, les solveurs CFD ainsi que les méthodologies développées ont été utilisés pour illustrer l'intérêt et la puissance de tels outils à des fins de conception, de compréhension et de diagnostic.

Le solveur à convection forcée a illustré le potentiel des solveurs CFD à des fins de conception par la modélisation des rues canyon. En particulier, les effets des propriétés géométriques d'une rue canyon descendante, qui comprennent la hauteur des bâtiments et la largeur de la rue, ont été étudiés. Les résultats ont montré que les recirculations de polluants dans les rues peuvent changer lorsque la hauteur des bâtiments en amont augmente et/ou lorsque la largeur de la rue diminue, ce qui entraîne une augmentation significative des concentrations moyennes dans la rue.

Le solveur à convection mixte, pour sa part, a illustré l'utilité des solveurs CFD à des fins de compréhension en modélisant l'impact des barrières antibruit sur la dispersion des polluants. L'évolution des concentrations de polluants après le mur antibruit a été étudiée en fonction de la vitesse du vent et de la stabilité atmosphérique. Les résultats ont montré que les barrières antibruit peuvent diminuer les concentrations de polluants, mais différemment selon la stabilité atmosphérique, le cas stable conduisant à des diminutions de concentration plus importantes. Cette étude a également montré que, pour les atmosphères ni trop stables ni trop instables, les résultats ne dépendent que du nombre de Richardson.
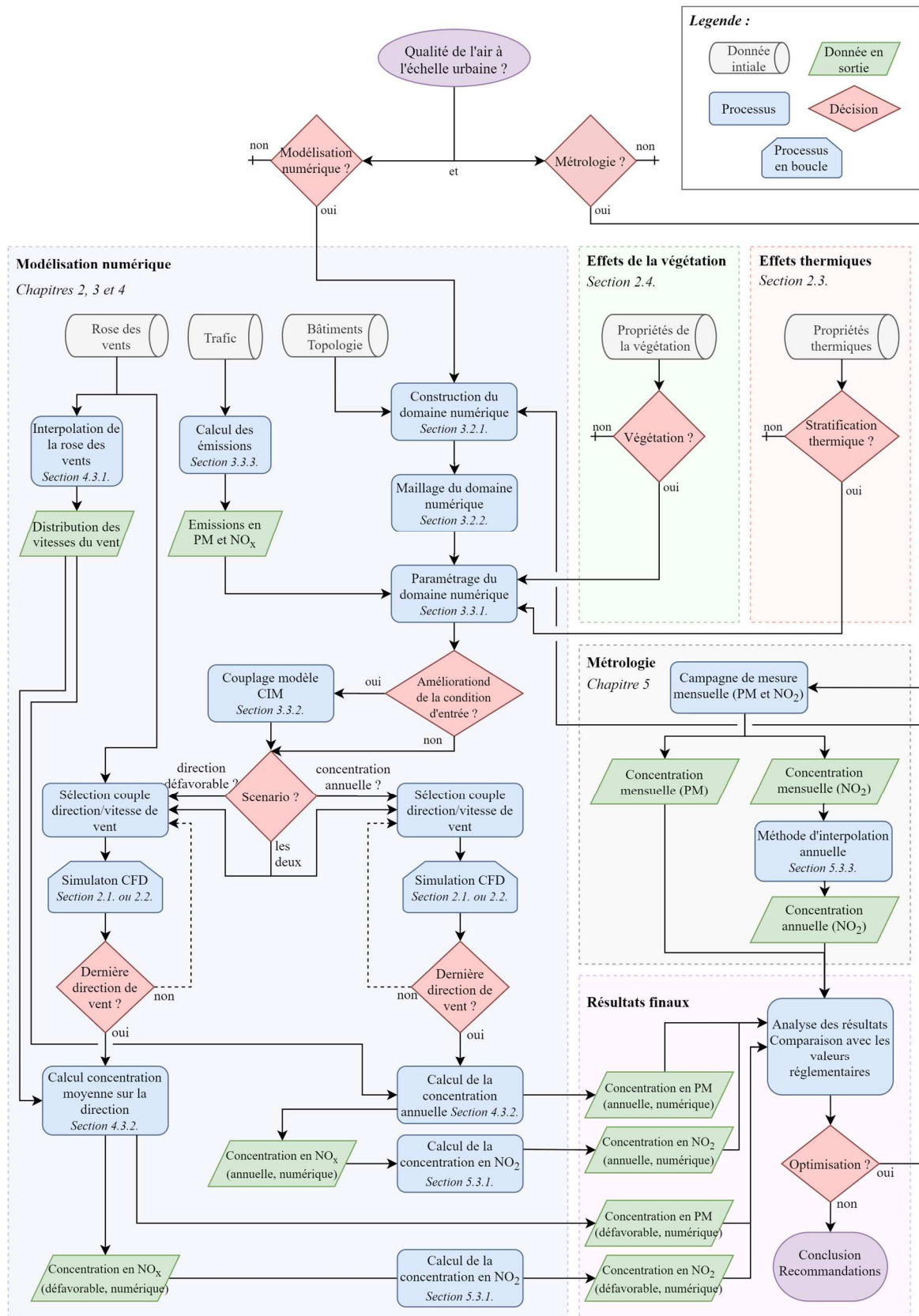
Fig. 22 – Schéma bilan de l'interconnexion des concepts, méthodes et outils développés dans cette thèse (les sections et chapitres renvoient au corps du mémoire et non au résumé étendu).

Enfin, une véritable étude in situ a été présentée, impliquant un grand nombre des outils et des méthodologies présentés dans cette thèse. Les résultats et les conclusions de cette étude sont importants, mais le point le plus important est que cette étude montre la façon dont les concepts, les outils et les méthodologies sont interconnectés et fonctionnent ensemble pour améliorer l'opérationnalité de l'utilisation de la modélisation CFD 3D pour évaluer la pollution atmosphérique à l'échelle urbaine. Un diagramme récapitulatif de ces interconnexions est finalement présenté en Fig. 22.

References

Addepalli, B., Pardyjak, E.R., 2015. A study of flow fields in step-down street canyons. Environmental Fluid Mechanics 15, 439–481. https://doi.org/10.1007/s10652-014-9366-z

AIRPARIF, 2016. Inventaire régional des émissions en Île-de-France - Année de référence 2012 - éléments synthétiques - Édition mai 2016 32.

Alfonsi, G., 2009. Reynolds-Averaged Navier–Stokes Equations for Turbulence Modeling. Applied Mechanics Reviews 62, 040802. https://doi.org/10.1115/1.3124648

Allegrini, J., Dorer, V., Carmeliet, J., 2015. Coupled CFD, radiation and building energy model for studying heat fluxes in an urban environment with generic building configurations. Sustainable Cities and Society 19, 385–394. https://doi.org/10.1016/j.scs.2015.07.009

Allegrini, J., Dorer, V., Carmeliet, J., 2013. Wind tunnel measurements of buoyant flows in street canyons. Building and Environment 59, 315–326. https://doi.org/10.1016/j.buildenv.2012.08.029

Amini, S., Ahangar, F.E., Heist, D.K., Perry, S.G., Venkatram, A., 2018. Modeling dispersion of emissions from depressed roadways. Atmospheric Environment 186, 189–197. https://doi.org/10.1016/j.atmosenv.2018.04.058

Amiroudine, S., Battaglia, J.-L., 2014. Mécanique des fluides - Cours et exercices corrigés, 2e édition. ed. Dunod.

Anderson, J.D., 2009. Fundamentals of Aerodynamics 1131.

Anderson, J.O., Thundiyil, J.G., Stolbach, A., 2012. Clearing the Air: A Review of the Effects of Particulate Matter Air Pollution on Human Health. J. Med. Toxicol. 8, 166–175. https://doi.org/10.1007/s13181-011-0203-1

Aristodemou, E., Boganegra, L.M., Mottet, L., Pavlidis, D., Constantinou, A., Pain, C., Robins, A., ApSimon, H., 2018. How tall buildings affect turbulent air flows and dispersion of pollution within a neighbourhood. Environmental Pollution 233, 782–796. https://doi.org/10.1016/j.envpol.2017.10.041

ATMO Grand-Est, 2017. Consommation et production d'énergie, emissions de GES et de polluants - Chiffres clés 2014 - Région Grand-Est. Observatoire Climat Air Energie du Grand Est.

Aumont, B., 2015. Modélisation de la chimie troposphérique. Université Paris 12.

Bächlin, W., Bösinger, R., Brandt, A., Schultz, T., 2008. Überprüfung des NO-NO2-Umwandlungsmodells für die Anwendung bei Immissionsprognosen für bodennahe Stickoxidfreisetzung. Reinhaltung der Luft 66, 154–157.

References

Bady, M., 2017. Evaluation of Gaussian Plume Model against CFD Simulations through the Estimation of CO and NO Concentrations in an Urban Area. American Journal of Environmental Sciences 13, 93–102. https://doi.org/10.3844/ajessp.2017.93.102

Bai, L., He, Z., Li, C., Chen, Z., 2020. Investigation of yearly indoor/outdoor PM2.5 levels in the perspectives of health impacts and air pollution control: Case study in Changchun, in the northeast of China. Sustainable Cities and Society 53, 101871. https://doi.org/10.1016/j.scs.2019.101871

Baik, J.-J., Kim, J.-J., Fernando, H.J.S., 2003. A CFD Model for Simulating Urban Flow and Dispersion. JOURNAL OF APPLIED METEOROLOGY 42, 13.

Baldauf, R., Thoma, E., Khlystov, A., Isakov, V., Bowker, G., Long, T., Snow, R., 2008. Impacts of noise barriers on near-road air quality. Atmospheric Environment 6. https://doi.org/10.1016/j.atmosenv.2008.05.051

Baldauf, R.W., Isakov, V., Deshmukh, P., Venkatram, A., Yang, B., Zhang, K.M., 2016. Influence of solid noise barriers on near-road and on-road air quality. Atmospheric Environment 129, 265–276. https://doi.org/10.1016/j.atmosenv.2016.01.025

Belalcazar, L.C., Clappier, A., Blond, N., Flassak, T., Eichhorn, J., 2010. An evaluation of the estimation of road traffic emission factors from tracer studies. Atmospheric Environment 44, 3814–3822. https://doi.org/10.1016/j.atmosenv.2010.06.038

Bibri, S.E., Krogstie, J., 2017. Smart sustainable cities of the future: An extensive interdisciplinary literature review. Sustainable Cities and Society 31, 183–212. https://doi.org/10.1016/j.scs.2017.02.016

Bijad, E., Delavar, M.A., Sedighi, K., 2016. CFD simulation of effects of dimension changes of buildings on pollution dispersion in the built environment. Alexandria Engineering Journal 55, 3135–3144. https://doi.org/10.1016/j.aej.2016.08.024

Bliefert, C.A., Perraud, R.A. (Trans.), 2008. Chimie de l'environnement: air, eau, sols, déchets. De Boeck, DL 2008, Bruxelles, Belgique.

Blocken, B., 2015. Computational Fluid Dynamics for urban physics: Importance, scales, possibilities, limitations and ten tips and tricks towards accurate and reliable simulations. Building and Environment 91, 219–245. https://doi.org/10.1016/j.buildenv.2015.02.015

Blocken, B., 2014. 50 years of Computational Wind Engineering: Past, present and future. Journal of Wind Engineering and Industrial Aerodynamics 129, 69–102. https://doi.org/10.1016/j.jweia.2014.03.008

Blocken, B., Stathopoulos, T., Carmeliet, J., 2007. CFD simulation of the atmospheric boundary layer: wall function problems. Atmospheric Environment 41, 238–252. https://doi.org/10.1016/j.atmosenv.2006.08.019

Borge, R., Santiago, J.L., de la Paz, D., Martín, F., Domingo, J., Valdés, C., Sánchez, B., Rivas, E., Rozas, M.T., Lázaro, S., Pérez, J., Fernández, Á., 2018. Application of a short term air quality action plan in Madrid (Spain) under a high-pollution episode - Part II: Assessment from multi-scale modelling. Science of The Total Environment 635, 1574–1584. https://doi.org/10.1016/j.scitotenv.2018.04.323

Bottillo, S., De Lieto Vollaro, A., Galli, G., Vallati, A., 2014. CFD modeling of the impact of solar radiation in a tridimensional urban canyon at different wind conditions. Solar Energy 102, 212–222. https://doi.org/10.1016/j.solener.2014.01.029

Bowker, G.E., Baldauf, R., Isakov, V., Khlystov, A., Petersen, W., 2007. The effects of roadside structures on the transport and dispersion of ultrafine particles from highways. Atmospheric Environment 41, 8128–8139. https://doi.org/10.1016/j.atmosenv.2007.06.064

Brechler, J., Fuka, V., 2014. Impact of Noise Barriers on Air-Pollution Dispersion. NS 06, 377–386. https://doi.org/10.4236/ns.2014.66038

Bright, V.B., Bloss, W.J., Cai, X., 2013. Urban street canyons: Coupling dynamics, chemistry and within-canyon chemical processing of emissions. Atmospheric Environment 68, 127–142. https://doi.org/10.1016/j.atmosenv.2012.10.056

Bruse, M., 2007. Particle filtering capacity of urban vegetation: A microscale numerical approach 6.

Buccolieri, R., Santiago, J.-L., Rivas, E., Sanchez, B., 2018. Review on urban tree modelling in CFD simulations: Aerodynamic, deposition and thermal effects. Urban Forestry & Urban Greening 31, 212–220. https://doi.org/10.1016/j.ufug.2018.03.003

Cao, J., Tamura, Y., Yoshida, A., 2012. Wind tunnel study on aerodynamic characteristics of shrubby specimens of three tree species. Urban Forestry & Urban Greening 11, 465–476. https://doi.org/10.1016/j.ufug.2012.05.003

Chaloulakou, A., Mavroidis, I., Gavriil, I., 2008. Compliance with the annual NO2 air quality standard in Athens. Required NOx levels and expected health implications. Atmospheric Environment 42, 454–465. https://doi.org/10.1016/j.atmosenv.2007.09.067

Chang, J.C., Hanna, S.R., 2004. Air quality model performance evaluation. Meteorology and Atmospheric Physics 87. https://doi.org/10.1007/s00703-003-0070-7

Chauhan, A.J., Krishna, M.T., Frew, A.J., Holgate, S.T., 1998. Exposure to nitrogen dioxide (NO2) and respiratory disease risk. Rev Environ Health 13, 73–90.

Chen, H., Kwong, J.C., Copes, R., Tu, K., Villeneuve, P.J., van Donkelaar, A., Hystad, P., Martin, R.V., Murray, B.J., Jessiman, B., Wilton, A.S., Kopp, A., Burnett, R.T., 2017. Living near major roads and the incidence of dementia, Parkinson's disease, and multiple sclerosis: a population-based cohort study. The Lancet 389, 718–726. https://doi.org/10.1016/S0140-6736(16)32399-6

Chen, L., Liu, C., Zhang, L., Zou, R., Zhang, Z., 2017. Variation in Tree Species Ability to Capture and Retain Airborne Fine Particulate Matter (PM2.5). Sci Rep 7, 3206. https://doi.org/10.1038/s41598-017-03360-1

Cheng, W.C., Liu, C.-H., Leung, D.Y.C., 2009. On the correlation of air and pollutant exchange for street canyons in combined wind-buoyancy-driven flow. Atmospheric Environment 43, 3682–3690. https://doi.org/10.1016/j.atmosenv.2009.04.054

CITEPA, 2019. Organisation et méthodes des inventaires nationaux des émissions atmosphériques en France - OMINEA -16e édition.

References

Coceal, O., Dobre, A., Thomas, T.G., Belcher, S.E., 2007. Structure of turbulent flow over regular arrays of cubical roughness. J. Fluid Mech. 589, 375–409. https://doi.org/10.1017/S002211200700794X

Cui, P.-Y., Li, Z., Tao, W.-Q., 2016. Buoyancy flows and pollutant dispersion through different scale urban areas: CFD simulations and wind-tunnel measurements. Building and Environment 104, 76–91. https://doi.org/10.1016/j.buildenv.2016.04.028

Dalpé, B., Masson, C., 2009. Numerical simulation of wind flow near a forest edge. Journal of Wind Engineering and Industrial Aerodynamics 97, 228–241. https://doi.org/10.1016/j.jweia.2009.06.008

de Lieto Vollaro, A., De Simone, G., Romagnoli, R., Vallati, A., Botillo, S., 2014. Numerical Study of Urban Canyon Microclimate Related to Geometrical Parameters. Sustainability 6, 7894–7905. https://doi.org/10.3390/su6117894

Derwent, R.G., Middleton, D.R., 1996. An empirical function for the ratio [NO2]:[NOx]. Clean Air 26, 57–60.

Di Sabatino, S., Buccolieri, R., Pulvirenti, B., Britter, R., 2007. Simulations of pollutant dispersion within idealised urban-type geometries with CFD and integral models. Atmospheric Environment 41, 8316–8329. https://doi.org/10.1016/j.atmosenv.2007.06.052

Dickerson, R.R., Stedman, D.H., Delany, A.C., 1982. Direct measurements of ozone and nitrogen dioxide photolysis rates in the troposphere. Journal of Geophysical Research 87, 4933. https://doi.org/10.1029/JC087iC07p04933

DREAL, 2014. Plan de protection de l'atmosphère de l'agglomération strasbourgeoise, Direction régionale de l'environnement, de l'aménagement et du logement. Strasbourg.

EEA, 2019a. EMEP/EEA air pollutant emission inventory guidebook 2019 - 1.A.3.b.i-iv Road transport 2019.

EEA, 2019b. EMEP/EEA air pollutant emission inventory guidebook 2019 - 1.A.3.b.i-iv Road Transport Appendix 4 Emission Factors 2019.

EEA, 2019c. EMEP/EEA air pollutant emission inventory guidebook 2019 - 1.A.3.b.vi-vii Road tyre and brake wear 2019.

Enayati Ahangar, F., Heist, D., Perry, S., Venkatram, A., 2017. Reduction of air pollution levels downwind of a road with an upwind noise barrier. Atmospheric Environment 155, 1–10. https://doi.org/10.1016/j.atmosenv.2017.02.001

EU, 2008. Directive 2008/50/EC of the european parliament and of the council of 21 May 2008 on ambient air quality and cleaner air for Europe, European Union.

European Commission, 2013. Proposal for a Directive of the European Parliament and of the Council on the reduction of national emissions of certain atmospheric pollutants and amending Directive 2003/35/EC. European Commission (EC), Brussels, Belgium.

European Environment Agency, 2019. Air quality in Europe: 2019 report.

Fiates, J., Vianna, S.S.V., 2016. Numerical modelling of gas dispersion using OpenFOAM. Process Safety and Environmental Protection 104, 277–293. https://doi.org/10.1016/j.psep.2016.09.011

Finkelstein, M.M., Jerrett, M., Sears, M.R., 2004. Traffic Air Pollution and Mortality Rate Advancement Periods. American Journal of Epidemiology 160, 173–177. https://doi.org/10.1093/aje/kwh181

Finn, D., Clawson, K.L., Carter, R.G., Rich, J.D., Eckman, R.M., Perry, S.G., Isakov, V., Heist, D.K., 2010. Tracer studies to characterize the effects of roadside noise barriers on near-road pollutant dispersion under varying atmospheric stability conditions. Atmospheric Environment 11. https://doi.org/10.1016/j.atmosenv.2009.10.012

Flores, F., Garreaud, R., Muñoz, R.C., 2013. CFD simulations of turbulent buoyant atmospheric flows over complex geometry: Solver development in OpenFOAM. Computers & Fluids 82, 1–13. https://doi.org/10.1016/j.compfluid.2013.04.029

Franke, J., Hellsten, A., Schlünzen, H., Carissimo, B., 2007. Best practice guideline for the CFD simulation of flows in the urban environment. COST Action 732.

Franke, J., Hirsch, C., Jensen, A.G., Krüs, H.W., Schatzmann, M., 2004. Recommandations on the use of cfd in wind engineering.

Fu, X., Liu, J., Ban-Weiss, G.A., Zang, J., Huang, X., Ouyang, B., Popoola, O.A.M., Tao, S., 2017. Effects of canyon geometry on the distribution of traffic-related air pollution in a large urban area: Implications of a multi-canyon air pollution dispersion model. Atmospheric Environment 165. https://doi.org/10.1016/j.atmosenv.2017.06.031

Gamel, H., 2015. Caractérisation expérimentale de l'écoulement et de la dispersion autour d'un obstacle bidimensionnel. Lyon, Ecole Centrale de Lyon.

Gerdes, F., Olivari, D., 1999. Analysis of pollutant dispersion in an urban street canyon. Journal of Wind Engineering and Industrial Aerodynamics 82, 105–124. https://doi.org/10.1016/S0167-6105(98)00216-5

Gómez-Losada, Á., Pires, J.C.M., Pino-Mejías, R., 2016a. Characterization of background air pollution exposure in urban environments using a metric based on Hidden Markov Models. Atmospheric Environment 127, 255–261. https://doi.org/10.1016/j.atmosenv.2015.12.046

Gómez-Losada, Á., Pires, J.C.M., Pino-Mejías, R., 2016b. Characterization of background air pollution exposure in urban environments using a metric based on Hidden Markov Models - Supplementary material. Atmospheric Environment 127, 255–261. https://doi.org/10.1016/j.atmosenv.2015.12.046

Gong, L., Wang, X., 2018. Numerical Study of Noise Barriers' Side Edge Effects on Pollutant Dispersion near Roadside under Various Thermal Stability Conditions. Fluids 3, 105. https://doi.org/10.3390/fluids3040105

Gromke, C., Ruck, B., 2007. Influence of trees on the dispersion of pollutants in an urban street canyon—Experimental investigation of the flow and concentration field. Atmospheric Environment 41, 3287–3302. https://doi.org/10.1016/j.atmosenv.2006.12.043

Hagler, G.S.W., Lin, M.-Y., Khlystov, A., Baldauf, R.W., Isakov, V., Faircloth, J., Jackson, L.E., 2012. Field investigation of roadside vegetative and structural barrier impact on near-road ultrafine

References

particle concentrations under a variety of wind conditions. Science of The Total Environment 419, 7–15. https://doi.org/10.1016/j.scitotenv.2011.12.002

Hagler, G.S.W., Tang, W., Freeman, M.J., Heist, D.K., Perry, S.G., Vette, A.F., 2011. Model evaluation of roadside barrier impact on near-road air pollution. Atmospheric Environment 45, 2522–2530. https://doi.org/10.1016/j.atmosenv.2011.02.030

Hanrahan, P.L., 1999. The Plume Volume Molar Ratio Method for Determining NO2/NOx Ratios in Modeling—Part I: Methodology. Journal of the Air & Waste Management Association 49, 1324–1331. https://doi.org/10.1080/10473289.1999.10463960

Hargreaves, D.M., Wright, N.G., 2007. On the use of the k– model in commercial CFD software to model the neutral atmospheric boundary layer. Journal of Wind Engineering and Industrial Aerodynamics 95, 355–369. https://doi.org/10.1016/j.jweia.2006.08.002

Heist, D.K., Perry, S.G., Brixey, L., 2009. A wind tunnel study of the effect of roadway configurations on the dispersion of traffic-related pollution. Atmospheric Environment 43(32). https://doi.org/10.1016/j.atmosenv.2009.06.034

Holzmann, T., 2016. Mathematics, Numerics, Derivations and OpenFOAM®. Holzmann CFD. https://doi.org/10.13140/rg.2.2.27193.36960

Hong, B., Qin, H., Lin, B., 2018. Prediction of Wind Environment and Indoor/Outdoor Relationships for PM2.5 in Different Building–Tree Grouping Patterns. Atmosphere 9, 39. https://doi.org/10.3390/atmos9020039

Hotchkiss, R.S., Harlow, F.H., 1973. Air Pollution Transport in Street Canyons. U.S. Environmental Protection Agency Report (EPA-R4-73-029), pp.129.

Irvine, M.R., Gardiner, B.A., Hill, M.K., 1997. The Evolution Of Turbulence Across A Forest Edge. Boundary-Layer Meteorology 84, 467–496. https://doi.org/10.1023/A:1000453031036

Jenkin, M.E., 2004. Analysis of sources and partitioning of oxidant in the UK—Part 1: the NOX-dependence of annual mean concentrations of nitrogen dioxide and ozone. Atmospheric Environment 38, 5117–5129. https://doi.org/10.1016/j.atmosenv.2004.05.056

Jurado, X., Reiminger, N., Vazquez, J., Wemmert, C., Dufresne, M., Blond, N., Wertel, J., 2020. Assessment of mean annual NO2 concentration based on a partial dataset. Atmospheric Environment 221, 117087. https://doi.org/10.1016/j.atmosenv.2019.117087

Kagawa, J., 1985. Evaluation of biological significance of nitrogen oxides exposure. Tokai J. Exp. Clin. Med. 10, 348–353.

Kastner-Klein, P., Fedorovich, E., Rotach, M.W., 2001. A wind tunnel study of organised and turbulent air motions in urban street canyons. Journal of Wind Engineering and Industrial Aerodynamics 89, 849–861. https://doi.org/10.1016/S0167-6105(01)00074-5

Katul, G.G., Mahrt, L., Poggi, D., Sanz, C., 2004. ONE- and TWO-Equation Models for Canopy Turbulence. Boundary-Layer Meteorology 113, 81–109. https://doi.org/10.1023/B:BOUN.0000037333.48760.e5

Kendrick, C.M., Koonce, P., George, L.A., 2015. Diurnal and seasonal variations of NO, NO 2 and PM 2.5 mass as a function of traffic volumes alongside an urban arterial. Atmospheric Environment 122, 133–141. https://doi.org/10.1016/j.atmosenv.2015.09.019

Kim, J.-J., Pardyjak, E., Kim, D.-Y., Han, K.-S., Kwon, B.-H., 2014. Effects of building-roof cooling on flow and air temperature in urban street canyons. Asia-Pacific J Atmos Sci 50, 365–375. https://doi.org/10.1007/s13143-014-0023-8

Kim, K.-H., Kabir, E., Kabir, S., 2015. A review on the human health impact of airborne particulate matter. Environment International 74, 136–143. https://doi.org/10.1016/j.envint.2014.10.005

Kim, M.J., Park, R.J., Kim, J.-J., 2012. Urban air quality modeling with full O3–NOx–VOC chemistry: Implications for O3 and PM air quality in a street canyon. Atmospheric Environment 47, 330–340. https://doi.org/10.1016/j.atmosenv.2011.10.059

Kim, Y., Huang, L., Gong, S., Jia, C.Q., 2016. A new approach to quantifying vehicle induced turbulence for complex traffic scenarios. Chinese Journal of Chemical Engineering 24, 71–78. https://doi.org/10.1016/j.cjche.2015.11.025

Klein, P.K., Berkowicz, R., Plate, E.J., 2000. Modelling of vehicle-induced turbulence in air pollution studies for streets. IJEP 14, 496. https://doi.org/10.1504/IJEP.2000.000573

Korsakissok, I., 2009. Changements d'échelle en modélisation de la qualité de l'air et estimation des incertitudes associées. Paris-Est, Université de Paris-Est.

Koutsourakis, N., Bartzis, J.G., Markatos, N.C., 2012. Evaluation of Reynolds stress, k-ε and RNG k-ε turbulence models in street canyon flows using various experimental datasets. Environmental Fluid Mechanics 12, 379–403. https://doi.org/10.1007/s10652-012-9240-9

Kumar, M.B.H., Balasubramaniyan, S., Padmanaban, S., Holm-Nielsen, J.B., 2019. Wind Energy Potential Assessment by Weibull Parameter Estimation Using Multiverse Optimization Method: A Case Study of Tirumala Region in India. Energies 12, 2158. https://doi.org/10.3390/en12112158

Kumar, P., Feiz, A.-A., Ngae, P., Singh, S.K., Issartel, J.-P., 2015. CFD simulation of short-range plume dispersion from a point release in an urban like environment. Atmospheric Environment 122, 645–656. https://doi.org/10.1016/j.atmosenv.2015.10.027

Lalic, B., Mihailovic, D.T., 2004. An Empirical Relation Describing Leaf-Area Density inside the Forest for Environmental Modeling. Journal of Applied Meteorology 43, 641–645. https://doi.org/10.1175/1520-0450(2004)043<0641:AERDLD>2.0.CO;2

Lattuati, M., 1997. Contribution à l'étude du bilan de l'ozone troposphérique à l'interface de l'Europe et de l'Atlantique nord : modélisation lagrangienne et mesures en altitude. Université de Paris IV.

Lee, E.S., Ranasinghe, D.R., Ahangar, F.E., Amini, S., Mara, S., Choi, W., Paulson, S., Zhu, Y., 2018. Field evaluation of vegetation and noise barriers for mitigation of near-freeway air pollution under variable wind conditions. Atmospheric Environment 175, 92–99. https://doi.org/10.1016/j.atmosenv.2017.11.060

Leighton, P.A., 1961. Photochemistry of air pollution, Physical chemistry. New-York Acad.

References

Li, X.-X., Britter, R.E., Koh, T.Y., Norford, L.K., Liu, C.-H., Entekhabi, D., Leung, D.Y.C., 2010. Large-Eddy Simulation of Flow and Pollutant Transport in Urban Street Canyons with Ground Heating. Boundary-Layer Meteorology 137, 187–204. https://doi.org/10.1007/s10546-010-9534-8

Likens, G.E., Wright, R.F., Galloway, J.N., Butler, T.J., 1979. Acid Rain. Scientific American 241, 43–51.

Liu, J., Heidarinejad, M., Guo, M., Srebric, J., 2015. Numerical Evaluation of the Local Weather Data Impacts on Cooling Energy Use of Buildings in an Urban Area. Procedia Engineering 121, 381–388. https://doi.org/10.1016/j.proeng.2015.08.1082

Mahmood, F.H., Resen, A.K., Khamees, A.B., 2019. Wind characteristic analysis based on Weibull distribution of Al-Salman site, Iraq. Energy Reports S2352484719308716. https://doi.org/10.1016/j.egyr.2019.10.021

Marchesse, Y., 2009. Modélisation de la turbulence.

Mauree, D., 2014. Development of a multi-scale meteorological system to improve urban climate modeling. Strasbourg.

Mauree, D., Blond, N., Kohler, M., Clappier, A., 2017a. On the Coherence in the Boundary Layer: Development of a Canopy Interface Model. Front. Earth Sci. 4. https://doi.org/10.3389/feart.2016.00109

Mauree, D., Sang-Hoon Lee, D., Naboni, E., Coccolo, S., Scartezzini, J.-L., 2017b. Localized meteorological variables influence at the early design stage. Energy Procedia 122, 325–330. https://doi.org/10.1016/j.egypro.2017.07.331

Mavroidis, I., Ilia, M., 2012. Trends of NOx, NO2 and O3 concentrations at three different types of air quality monitoring stations in Athens, Greece. Atmospheric Environment 63, 135–147. https://doi.org/10.1016/j.atmosenv.2012.09.030

Mazzoldi, A., Hill, T., Colls, J.J., 2008. CFD and Gaussian atmospheric dispersion models: A comparison for leak from carbon dioxide transportation and storage facilities. Atmospheric Environment 42, 8046–8054. https://doi.org/10.1016/j.atmosenv.2008.06.038

Meir, P., Grace, J., Miranda, A.C., 2000. Photographic method to measure the vertical distribution of leaf area density in forests. Agricultural and Forest Meteorology 102, 105–111. https://doi.org/10.1016/S0168-1923(00)00122-2

Michelot, N., Carrega, P., Rouïl, L., 2015. Panorama de la modélisation de la dispersion atmosphérique Atmospheric dispersion models: An overwiew. POLLUTION ATMOSPHÉRIQUE 9.

Navas, M.J., Jiménez, A.M., Galán, G., 1997. Air analysis: determination of nitrogen compounds by chemiluminescence. Atmospheric Environment 31, 3603–3608. https://doi.org/10.1016/S1352-2310(97)00153-2

Ning, Z., Hudda, N., Daher, N., Kam, W., Herner, J., Kozawa, K., Mara, S., Sioutas, C., 2010. Impact of roadside noise barriers on particle size distributions and pollutants concentrations near freeways. Atmospheric Environment 44, 3118–3127. https://doi.org/10.1016/j.atmosenv.2010.05.033

Nowak, D.J., Hirabayashi, S., Bodine, A., Hoehn, R., 2013. Modeled PM2.5 removal by trees in ten U.S. cities and associated health effects. Environmental Pollution 178, 395–402. https://doi.org/10.1016/j.envpol.2013.03.050

Papageorgakis, G.C., Assanis, D.N., 1999. COMPARISON OF LINEAR AND NONLINEAR RNG-BASED k-epsilon MODELS FOR INCOMPRESSIBLE TURBULENT FLOWS. Numerical Heat Transfer, Part B: Fundamentals 35, 1–22. https://doi.org/10.1080/104077999275983

Parrish, D.D., Murphy, P.C., Albritton, D.L., Fehsenfeld, F.C., 1983. The measurement of the photodissociation rate of NO2 in the atmosphere. Atmospheric Environment (1967) 17, 1365–1379. https://doi.org/10.1016/0004-6981(83)90411-0

Pavageau, M., Schatzmann, M., 1999. Wind tunnel measurements of concentration fluctuations in an urban street canyon. Atmospheric Environment 33, 3961–3971. https://doi.org/10.1016/S1352-2310(99)00138-7

Perini, K., Magliocco, A., 2014. Effects of vegetation, urban density, building height, and atmospheric conditions on local temperatures and thermal comfort. Urban Forestry & Urban Greening 13, 495–506. https://doi.org/10.1016/j.ufug.2014.03.003

Petters, A., von Klot, S., Heier, M., Trentinaglia, I., 2004. Exposure to Traffic and the Onset of Myocardial Infarction. The New England Journal of Medicine 351, 1721–1730. https://doi.org/10.1056/NEJMoa040203

Purvis, M.R., Ehrlich, R., 1963. Effect of Atmospheric Pollutants on Susceptibility to Respiratory Infection: II. Effect of Nitrogen Dioxide. The Journal of Infectious Diseases 113, 72–76.

Qin, Y., Kot, S.C., 1993. Dispersion of vehicular emission in street canyons, Guangzhou City, South China (P.R.C.). Atmospheric Environment. Part B. Urban Atmosphere 27, 283–291. https://doi.org/10.1016/0957-1272(93)90023-Y

Qu, Y., Milliez, M., Musson-Genon, L., Carissimo, B., 2012. Numerical study of the thermal effects of buildings on low-speed airflow taking into account 3D atmospheric radiation in urban canopy. Journal of Wind Engineering and Industrial Aerodynamics 104–106, 474–483. https://doi.org/10.1016/j.jweia.2012.03.008

Reiminger, N., Jurado, X., Vazquez, J., Wemmert, C., Blond, N., Dufresne, M., Wertel, J., 2020a. Effects of wind speed and atmospheric stability on the air pollution reduction rate induced by noise barriers. Journal of Wind Engineering and Industrial Aerodynamics 200, 104160. https://doi.org/10.1016/j.jweia.2020.104160

Reiminger, N., Jurado, X., Vazquez, J., Wemmert, C., Dufresne, M., Blond, N., Wertel, J., 2020b. Methodologies to assess mean annual air pollution concentration combining numerical results and wind roses. Sustainable Cities and Society 59, 102221. https://doi.org/10.1016/j.scs.2020.102221

Reiminger, N., Vazquez, J., Blond, N., Dufresne, M., Wertel, J., 2020c. CFD evaluation of mean pollutant concentration variations in step-down street canyons. Journal of Wind Engineering and Industrial Aerodynamics 196, 104032. https://doi.org/10.1016/j.jweia.2019.104032

References

Reynolds, O., 1895. On the dynamical theory of incompressible viscous fluids and the determination of the criterion. Philosophical Transactions of the Royal Society of London A. 186, 123–164. https://doi.org/10.1098/rsta.1895.0004

Richards, P.J., Hoxey, R.P., 1993. Appropriate boundary conditions for computational wind engineering models using the k-E turbulence model 9.

Richards, P.J., Norris, S.E., 2011. Appropriate boundary conditions for computational wind engineering models revisited. Journal of Wind Engineering and Industrial Aerodynamics 99, 257–266. https://doi.org/10.1016/j.jweia.2010.12.008

Rivas, E., Santiago, J.L., Lechón, Y., Martín, F., Ariño, A., Pons, J.J., Santamaría, J.M., 2019. CFD modelling of air quality in Pamplona City (Spain): Assessment, stations spatial representativeness and health impacts valuation. Science of the Total Environment 19.

Roache, P.J., 1994. Perspective: A Method for Uniform Reporting of Grid Refinement Studies. Journal of Fluids Engineering 116, 405. https://doi.org/10.1115/1.2910291

Roberts–Semple, D., Song, F., Gao, Y., 2012. Seasonal characteristics of ambient nitrogen oxides and ground–level ozone in metropolitan northeastern New Jersey. Atmospheric Pollution Research 3, 247–257. https://doi.org/10.5094/APR.2012.027

Romberg, E., Bösinger, R., Lohmeyer, A., Ruhnke, R., 1996. NO-NO2-Umwandlung für die Anwendung bei Immissionsprognosen für Kfz-Abgase. Reinhaltung der Luft 56, 215–218.

Ross, J., Ross, V., Koppel, A., 2000. Estimation of leaf area and its vertical distribution during growth period. Agricultural and Forest Meteorology 101, 237–246. https://doi.org/10.1016/S0168-1923(00)00089-7

Salesky, S.T., Giometto, M.G., Chamecki, M., Lehning, M., 2019. The transport and deposition of heavy particles in complex terrain: insights from an Eulerian model for large eddy simulation. Water ressources research 21.

Salmond, J.A., Tadaki, M., Vardoulakis, S., Arbuthnott, K., Coutts, A., Demuzere, M., Dirks, K.N., Heaviside, C., Lim, S., Macintyre, H., McInnes, R.N., Wheeler, B.W., 2016. Health and climate related ecosystem services provided by street trees in the urban environment. Environ Health 15, S36. https://doi.org/10.1186/s12940-016-0103-6

Sanchez, B., Santiago, J.L., Martilli, A., Martin, F., Borge, R., Quaassdorff, C., de la Paz, D., 2017. Modelling NOX concentrations through CFD-RANS in an urban hot-spot using high resolution traffic emissions and meteorology from a mesoscale model. Atmospheric Environment 163, 155–165. https://doi.org/10.1016/j.atmosenv.2017.05.022

Sanchez, B., Santiago, J.-L., Martilli, A., Palacios, M., Kirchner, F., 2016. CFD modeling of reactive pollutant dispersion in simplified urban configurations with different chemical mechanisms. Atmospheric Chemistry and Physics 16, 12143–12157. https://doi.org/10.5194/acp-16-12143-2016

Santé Publique France, 2016. Impacts sanitaires de la pollution de l'air en France : nouvelles données et perspectives, Communiqué de presse.

Santiago, J.L., Borge, R., Martin, F., de la Paz, D., Martilli, A., Lumbreras, J., Sanchez, B., 2017a. Evaluation of a CFD-based approach to estimate pollutant distribution within a real urban canopy by means of passive samplers. Science of The Total Environment 576, 46–58. https://doi.org/10.1016/j.scitotenv.2016.09.234

Santiago, J.-L., Buccolieri, R., Rivas, E., Sanchez, B., Martilli, A., Gatto, E., Martín, F., 2019. On the Impact of Trees on Ventilation in a Real Street in Pamplona, Spain. Atmosphere 10, 697. https://doi.org/10.3390/atmos10110697

Santiago, J.L., Martilli, A., Martin, F., 2017b. On Dry Deposition Modelling of Atmospheric Pollutants on Vegetation at the Microscale: Application to the Impact of Street Vegetation on Air Quality. Boundary-Layer Meteorology 162, 451–474. https://doi.org/10.1007/s10546-016-0210-5

Santiago, J.L., Martin, F., 2005. Modelling the air flow in symmetric and asymmetric street canyons. International Journal of Environment and Pollution 25, 145. https://doi.org/10.1504/IJEP.2005.007662

Schatzmann, M., Leitl, B., 2011. Issues with validation of urban flow and dispersion CFD models. Journal of Wind Engineering and Industrial Aerodynamics 99, 169–186. https://doi.org/10.1016/j.jweia.2011.01.005

Schulte, N., Snyder, M., Isakov, V., Heist, D., Venkatram, A., 2014. Effects of solid barriers on dispersion of roadway emissions. Atmospheric Environment 97, 286–295. https://doi.org/10.1016/j.atmosenv.2014.08.026

Ścibor, M., Balcerzak, B., Galbarczyk, A., Targosz, N., Jasienska, G., 2019. Are we safe inside? Indoor air quality in relation to outdoor concentration of PM10 and PM2.5 and to characteristics of homes. Sustainable Cities and Society 48, 101537. https://doi.org/10.1016/j.scs.2019.101537

Seinfeld, J.H., Pandis, S.N., 2016. Atmospheric Chemistry and Physics: From Air Pollution to Climate Change, 3rd Edition, Wiley-Blackwell. ed.

Shaw, C., Boulic, M., Longley, I., Mitchell, T., Pierse, N., Howden-Chapman, P., 2020. The association between indoor and outdoor NO2 levels: A case study in 50 residences in an urban neighbourhood in New Zealand. Sustainable Cities and Society 56, 102093. https://doi.org/10.1016/j.scs.2020.102093

Solazzo, E., Vardoulakis, S., Cai, X., 2011. A novel methodology for interpreting air quality measurements from urban streets using CFD modelling. Atmospheric Environment 45, 5230–5239. https://doi.org/10.1016/j.atmosenv.2011.05.022

Soulhac, L., Mejean, P., Perkins, R.J., 2001. Modelling the transport and dispersion of pollutants in street canyons. International Journal of Environment and Pollution 16, 404. https://doi.org/10.1504/IJEP.2001.000636

Sportisse, B., 2008. Pollution atmosphérique: des processus à la modélisation. Springer, Paris.

Stadt, K.J., Lieffers, V.J., 2000. MIXLIGHT: a flexible light transmission model for mixed-species forest stands. Agricultural and Forest Meteorology 102, 235–252. https://doi.org/10.1016/S0168-1923(00)00128-3

References

Takano, Y., Moonen, P., 2013. On the influence of roof shape on flow and dispersion in an urban street canyon. Journal of Wind Engineering and Industrial Aerodynamics 123, 107–120. https://doi.org/10.1016/j.jweia.2013.10.006

Thaker, P., Gokhale, S., 2016. The impact of traffic-flow patterns on air quality in urban street canyons. Environmental Pollution 208, 161–169. https://doi.org/10.1016/j.envpol.2015.09.004

Thunis, P., 2018. On the validity of the incremental approach to estimate the impact of cities on air quality. Atmospheric Environment 173, 210–222. https://doi.org/10.1016/j.atmosenv.2017.11.012

Thunis, P., Georgieva, E., Pederzoli, A., 2012. A tool to evaluate air quality model performances in regulatory applications. Environmental Modelling & Software 38, 220–230. https://doi.org/10.1016/j.envsoft.2012.06.005

Tominaga, Y., Mochida, A., Yoshie, R., Kataoka, H., Nozu, T., Yoshikawa, M., Shirasawa, T., 2008. AIJ guidelines for practical applications of CFD to pedestrian wind environment around buildings. Journal of Wind Engineering and Industrial Aerodynamics 96, 1749–1761. https://doi.org/10.1016/j.jweia.2008.02.058

Tominaga, Y., Stathopoulos, T., 2017. Steady and unsteady RANS simulations of pollutant dispersion around isolated cubical buildings: Effect of large-scale fluctuations on the concentration field. Journal of Wind Engineering and Industrial Aerodynamics 165, 23–33. https://doi.org/10.1016/j.jweia.2017.02.001

Tominaga, Y., Stathopoulos, T., 2007. Turbulent Schmidt numbers for CFD analysis with various types of flowfield. Atmospheric Environment 41, 8091–8099. https://doi.org/10.1016/j.atmosenv.2007.06.054

Toparlar, Y., Blocken, B., Maiheu, B., van Heijst, G.J.F., 2017. A review on the CFD analysis of urban microclimate. Renewable and Sustainable Energy Reviews 80, 1613–1640. https://doi.org/10.1016/j.rser.2017.05.248

Uehara, K., Murakami, S., Oikawa, S., Wakamatsu, S., 2000. Wind tunnel experiments on how thermal stratification affects flow in and above urban street canyons. Atmospheric Environment 10.

United Nations, Department of Economic and Social Affairs, Population Division, 2019. World Urbanization Prospects: The 2018 Revision (ST/ESA/SER.A/420). New York: United Nations.

Vachon, G., Louka, P., Rosant, J.-M., Mestayer, P.G., Sini, J.-F., 2002. Measurements of Traffic-Induced Turbulence within a Street Canyon during the Nantes'99 Experiment, in: Sokhi, R.S., Bartzis, J.G. (Eds.), Urban Air Quality — Recent Advances. Springer Netherlands, Dordrecht, pp. 127–140. https://doi.org/10.1007/978-94-010-0312-4_10

Vardoulakis, S., Fisher, B.E.A., Pericleous, K., Gonzalez-Flesca, N., 2003. Modelling air quality in street canyons: a review. Atmospheric Environment 37, 155–182. https://doi.org/10.1016/S1352-2310(02)00857-9

Vardoulakis, S., Gonzalez-Flesca, N., Fisher, B.E.A., 2002. Assessment of traffic-related air pollution in two street canyons in Paris: implications for exposure studies. Atmospheric Environment 36, 1025–1039. https://doi.org/10.1016/S1352-2310(01)00288-6

Vermeulen, A.T., Kraai, A., Duyzer, J.H., Klok, E.J., Pronk, A.A., 2009. Vegetatie langs wegen en Luchtkwaliteit; Perceel I:A50 Vaassen (Rapport final), Rapport IPL. ECN/TNO/PRI, 1755 ZG Petten, Pays-Bas.

Versteeg, H.K., Malalasekera, W., 2007. An introduction to computational fluid dynamics: the finite volume method, 2nd ed. ed. Pearson Education Ltd, Harlow, England ; New York.

Vos, P.E.J., Maiheu, B., Vankerkom, J., Janssen, S., 2013. Improving local air quality in cities: To tree or not to tree? Environmental Pollution 183, 113–122. https://doi.org/10.1016/j.envpol.2012.10.021

Vranckx, S., Vos, P., Maiheu, B., Janssen, S., 2015. Impact of trees on pollutant dispersion in street canyons: A numerical study of the annual average effects in Antwerp, Belgium. Science of The Total Environment 532, 474–483. https://doi.org/10.1016/j.scitotenv.2015.06.032

Wang, P., Zhao, D., Wang, W., Mu, H., Cai, G., Liao, C., 2011. Thermal Effect on Pollutant Dispersion in an Urban Street Canyon. International Journal of Environmental Research 5, 813–820. https://doi.org/10.22059/ijer.2011.388

Wang, S., Wang, X., 2019. Modeling and Analysis of the Effects of Noise Barrier Shape and Inflow Conditions on Highway Automobiles Emission Dispersion. Fluids 4, 151. https://doi.org/10.3390/fluids4030151

Wang, Z., Wei, W., Zheng, F., 2020. Effects of industrial air pollution on the technical efficiency of agricultural production: Evidence from China. Environmental Impact Assessment Review 83, 106407. https://doi.org/10.1016/j.eiar.2020.106407

Wen, H., Malki-Epshtein, L., 2018. A parametric study of the effect of roof height and morphology on air pollution dispersion in street canyons. Journal of Wind Engineering and Industrial Aerodynamics 175, 328–341. https://doi.org/10.1016/j.jweia.2018.02.006

White, F.M., 2003. Fluid mechanics, 5. ed., International ed. ed, McGraw-Hill series in mechanical engineering. McGraw-Hill, Boston.

WHO, 2018. Burden of disease from ambient air pollution for 2016, World Health Organization 2018.

WHO, 2017. Evolution of WHO air quality guidelines past, present and future, Copenhagen: WHO Regional Office for Europe.

WHO, 2016a. Mortality and burden of disease from ambient air pollution, Global Health Observatory data [WWW Document]. Word Health Organization. URL http://www.who.int/gho/phe/outdoor_air_pollution/burden/en/ (accessed 11.20.19).

WHO, 2016b. Mortality from household air pollution, Global Health Observatory data [WWW Document]. Word Health Organization. URL http://www.who.int/gho/phe/indoor_air_pollution/burden/en/ (accessed 11.20.19).

WHO (Ed.), 2005. WHO Air quality guidelines for particulate matter, ozone, nitrogen dioxide and sulfur dioxide. Global update 2005. World Health Organization.

References

Wiegand, A.N., Bo, N.D., 2000. Review of empirical methods for the calculation of the diurnal NO2 photolysis rate coefficient. Atmospheric Environment 10. https://doi.org/10.1016/S1352-2310(99)00294-0

Woodward, J.L., 1998. Estimating the flammable mass of a vapor cloud, A CCPS concept book. Center for Chemical Process Safety of the American Institute of Chemical Engineers, New York, N.Y.

Xiaomin, X., Huang, Z., Wang, J., 2006. The impact of urban street layout on local atmospheric environment. Building and Environment 41, 1352–1363. https://doi.org/10.1016/j.buildenv.2005.05.028

Yakhot, V., Orszag, S.A., Thangam, S., Gatski, T.B., Speziale, C.G., 1992. Development of turbulence models for shear flows by a double expansion technique. Physics of Fluids A: Fluid Dynamics 4, 1510–1520. https://doi.org/10.1063/1.858424

Yang, J., Shi, B., Shi, Y., Marvin, S., Zheng, Y., Xia, G., 2020. Air pollution dispersal in high density urban areas: Research on the triadic relation of wind, air pollution, and urban form. Sustainable Cities and Society 54, 101941. https://doi.org/10.1016/j.scs.2019.101941

Yuan, J., Chen, Z., Zhong, L., Wang, B., 2019. Indoor air quality management based on fuzzy risk assessment and its case study. Sustainable Cities and Society 50, 101654. https://doi.org/10.1016/j.scs.2019.101654

LIST OF FIGURES

List of figures

List of figures

List of figures

LIST OF TABLES

List of tables

APPENDICES

Appendix A – Incompressible Navier-Stokes equations

The incompressible Navier-Stokes momentum equation comes from the Cauchy momentum equation given in Eq. A.1.

$$\rho\left(\frac{\partial \vec{u}}{\partial t} + \vec{u}.\left(\bar{\bar{\nabla}}\vec{u}\right)\right) = \vec{\nabla}.\bar{\bar{\sigma}} + \rho\vec{g} \qquad \text{(Eq. A.1)}$$

The Cauchy stress tensor $\bar{\bar{\sigma}}$ can be decomposed in two distinct parts, a deviatoric stress tensor $\bar{\bar{\tau}}$ which corresponds to the viscosity term, and a volumetric stress term $-p\bar{\bar{I}}$ which corresponds to the pressure term (Amiroudine and Battaglia, 2014). This decomposition leads to Eq. A.2 and Eq. A.3.

$$\rho\left(\frac{\partial \vec{u}}{\partial t} + \vec{u}.\left(\bar{\bar{\nabla}}\vec{u}\right)\right) = \vec{\nabla}.\left(\bar{\bar{\tau}} - p\bar{\bar{I}}\right) + \rho\vec{g} \qquad \text{(Eq. A.2)}$$

$$\rho\left(\frac{\partial \vec{u}}{\partial t} + \vec{u}.\left(\bar{\bar{\nabla}}\vec{u}\right)\right) = -\vec{\nabla}p + \vec{\nabla}.\bar{\bar{\tau}} + \rho\vec{g} \qquad \text{(Eq. A.3)}$$

Considering a homogeneous and isotropic Newtonian fluid, the stress tensor $\bar{\bar{\tau}}$ corresponds to Eq. A.4, with $\bar{\bar{\varepsilon}}$ the rate-of-strain tensor corresponding to Eq. A.5 (Amiroudine and Battaglia, 2014).

$$\bar{\bar{\tau}} = 2\mu\bar{\bar{\varepsilon}} - \frac{2}{3}\mu(\nabla.\vec{u})\bar{\bar{I}} \qquad \text{(Eq. A.4)}$$

$$\bar{\bar{\varepsilon}} = \frac{1}{2}\left[\bar{\bar{\nabla}}\vec{u} + \left(\bar{\bar{\nabla}}\vec{u}\right)^T\right] = D(u) \qquad \text{(Eq. A.5)}$$

Thus, Eq. A.3 becomes Eq. A.6.

$$\rho\left(\frac{\partial \vec{u}}{\partial t} + \vec{u}.\left(\bar{\bar{\nabla}}\vec{u}\right)\right) = -\vec{\nabla}p + \vec{\nabla}.\left(2\mu\frac{1}{2}\left[\bar{\bar{\nabla}}\vec{u} + \left(\bar{\bar{\nabla}}\vec{u}\right)^T\right] - \frac{2}{3}\mu(\nabla.\vec{u})\bar{\bar{I}}\right) + \rho\vec{g} \qquad \text{(Eq. A.6)}$$

With the incompressibility assumption ($\nabla.\vec{u} = 0$), it comes:

$$\rho\left(\frac{\partial \vec{u}}{\partial t} + \vec{u}.\left(\bar{\bar{\nabla}}\vec{u}\right)\right) = -\vec{\nabla}p + \vec{\nabla}.\mu\bar{\bar{\nabla}}\vec{u} + \vec{\nabla}.\mu\left(\bar{\bar{\nabla}}\vec{u}\right)^{T} + \rho\vec{g} \qquad \text{(Eq. A.7)}$$

It can be demonstrated that $\vec{\nabla}.\left(\bar{\bar{\nabla}}\vec{u}\right)^{T} = \vec{\nabla}(\nabla.\vec{u})$. With also $\nu = \mu/\rho$, Eq. A.7 becomes Eq. A.8:

$$\frac{\partial \vec{u}}{\partial t} + \vec{u}.\left(\bar{\bar{\nabla}}\vec{u}\right) = -\frac{1}{\rho}\vec{\nabla}p + \nu\Delta\vec{u} + \rho\vec{g} \qquad \text{(Eq. A.8)}$$

While $\rho\vec{g}$ is not changing the momentum equation results for incompressible flow it can be neglected (Holzmann, 2016), and the incompressible Navier-Stokes momentum equation is obtained:

$$\frac{\partial \vec{u}}{\partial t} + \vec{u}.\left(\bar{\bar{\nabla}}\vec{u}\right) = -\frac{1}{\rho}\vec{\nabla}p + \nu\Delta\vec{u} \qquad \text{(Eq. A.9)}$$

Note: the density in the incompressible solvers from OpenFOAM is always taken equal to one ($\rho = 1$). The incompressible Navier-Stokes momentum equations in these solvers correspond therefore to Eq. A.10.

$$\frac{\partial \vec{u}}{\partial t} + \vec{u}.\left(\bar{\bar{\nabla}}\vec{u}\right) = -\vec{\nabla}p + \nu\Delta\vec{u} \qquad \text{(Eq. A.10)}$$

Appendix B – Reynolds-Averaged Navier-Stokes equations for incompressible flows

The incompressible Navier-Stokes continuity and momentum equations are respectively given as follows:

$$\nabla . u = 0 \tag{Eq. B.1}$$

$$\frac{\partial \vec{u}}{\partial t} + \vec{u} . (\bar{\bar{\nabla}} \vec{u}) = -\frac{1}{\rho} \vec{\nabla} p + \nu \Delta \vec{u} \tag{Eq. B.2}$$

These equations can also be written according to the Einstein summation convection and gives Eq. B.3 and Eq. B.4.

$$\frac{\partial u_i}{\partial x_i} = 0 \tag{Eq. B.3}$$

$$\frac{\partial u_i}{\partial t} + u_j \frac{\partial u_i}{\partial x_j} = -\frac{1}{\rho} \frac{\partial p}{\partial x_i} + \nu \frac{\partial^2 u_i}{\partial x_j \partial x_j} \tag{Eq. B.4}$$

To time-averaging the Navier-Stokes momentum equation according to the Reynolds' methodology, some notions must first be defined:

Reynolds' decomposition

By definition, Reynolds decomposition decomposes a variable X into a sum of its mean value $\bar{X}$ and a fluctuating value X':

$$X = \bar{X} + X' \tag{Eq. B.5}$$

Time-averaging

The average operator used to average the Navier-Stokes equations is the time average $\bar{X}$ of the variable x defined by the equation Eq. B.6.

$$\bar{X} = \lim_{T \to \infty} \frac{1}{T} \int_{t_0}^{t_0+T} x . dt \tag{Eq. B.6}$$

And, by definition, we have:

$$\overline{f + g} = \bar{f} + \bar{g} \quad and \quad \overline{af} = a\bar{f} \tag{Eq. B.7}$$

$$\overline{\frac{\partial \psi}{\partial x_i}} = \frac{\partial \bar{\psi}}{\partial x_i} \quad and \quad \overline{\frac{\partial \psi}{\partial t}} = \frac{\partial \bar{\psi}}{\partial t} \tag{Eq. B.8}$$

$$\overline{\bar{f}.g} = \bar{f}.\bar{g} \implies \bar{\bar{f}} = \bar{f} \tag{Eq. B.9}$$

$$\overline{f.g} = \overline{(\bar{f} + f').(\bar{g} + g')} = \bar{f}.\bar{g} + \overline{f'.g'} \tag{Eq. B.10}$$

Firstly, applying the Reynolds' decomposition to the continuity equation, Eq. B.3 becomes Eq. B.10:

$$\frac{\partial(\bar{u}_i + u_i')}{\partial x_i} = 0 \tag{Eq. B.11}$$

After time-averaging the previous equation, it comes:

$$\overline{\frac{\partial(\bar{u}_\iota + u_\iota')}{\partial x_i}} = 0 \tag{Eq. B.12}$$

Which leads to:

$$\frac{\partial \bar{u}_i}{\partial x_i} = 0 \tag{Eq. B.13}$$

Secondly, applying the same methodology on to the momentum equation, Eq. B.4 becomes Eq. B.14 and we have:

$$\frac{\partial(\bar{u}_i + u_i')}{\partial t} + \frac{\partial(\bar{u}_i + u_i')(\bar{u}_j + u_j')}{\partial x_j} = -\frac{1}{\rho}\frac{\partial(\bar{p} + p')}{\partial x_i} + \nu\frac{\partial^2(\bar{u}_i + u_i')}{\partial x_j \partial x_j} \tag{Eq. B.14}$$

$$\overline{\frac{\partial(\bar{u}_\iota + u_\iota')}{\partial t}} + \overline{\frac{\partial(\bar{u}_\iota + u_\iota')(\bar{u}_j + u_j')}{\partial x_j}} = -\frac{1}{\rho}\overline{\frac{\partial(\bar{p} + p')}{\partial x_i}} + \nu\overline{\frac{\partial^2(\bar{u}_\iota + u_\iota')}{\partial x_j \partial x_j}} \tag{Eq. B.15}$$

$$\frac{\partial \bar{u}_i}{\partial t} + \frac{\partial \overline{u_\iota'}}{\partial t} + \frac{\partial \bar{u}_i \bar{u}_j}{\partial x_j} + \frac{\partial \overline{u_\iota' u_j'}}{\partial x_j} = -\frac{1}{\rho}\left(\frac{\partial \bar{p}}{\partial x_i} + \frac{\partial \overline{p'}}{\partial x_i}\right) + \nu\left(\frac{\partial^2 \bar{u}_i}{\partial x_j \partial x_j} + \frac{\partial^2 \overline{u_\iota'}}{\partial x_j \partial x_j}\right) \tag{Eq. B.16}$$

$$\frac{\partial \bar{u}_i}{\partial t} + \bar{u}_j \frac{\partial(\bar{u}_i)}{\partial x_j} = -\frac{1}{\rho}\left(\frac{\partial \bar{p}}{\partial x_i}\right) + \nu\left(\frac{\partial^2 \bar{u}_i}{\partial x_j \partial x_j}\right) - \frac{\partial \overline{u'_i u'_j}}{\partial x_j} \qquad \text{(Eq. B.17)}$$

Finally, we have the Reynolds-Averaged Navier-Stokes continuity and momentum equation, respectively Eq. B.13 and Eq. B.19:

$$\frac{\partial \bar{u}_i}{\partial x_i} = 0 \qquad \text{(Eq. B.13)}$$

$$\frac{\partial \bar{u}_i}{\partial t} + \bar{u}_j \frac{\partial(\bar{u}_i)}{\partial x_j} = -\frac{1}{\rho}\left(\frac{\partial p}{\partial x_i}\right) + \nu\left(\frac{\partial^2 \bar{u}_i}{\partial x_j \partial x_j}\right) - \frac{\partial \overline{u'_i u'_j}}{\partial x_j} \qquad \text{(Eq. B.18)}$$

Or, under another notation:
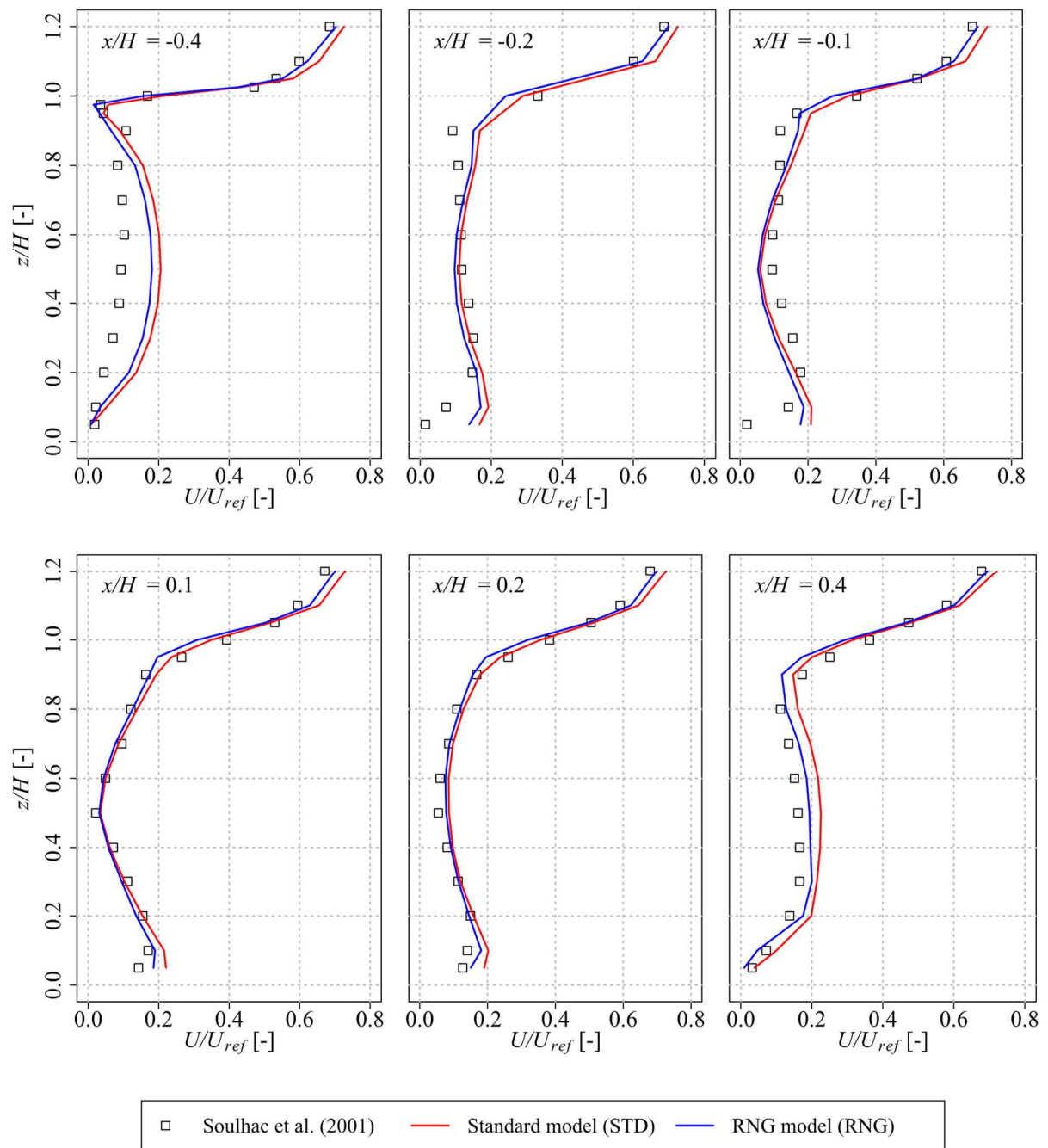
$$\nabla . U = 0 \qquad \text{(Eq. B.19)}$$
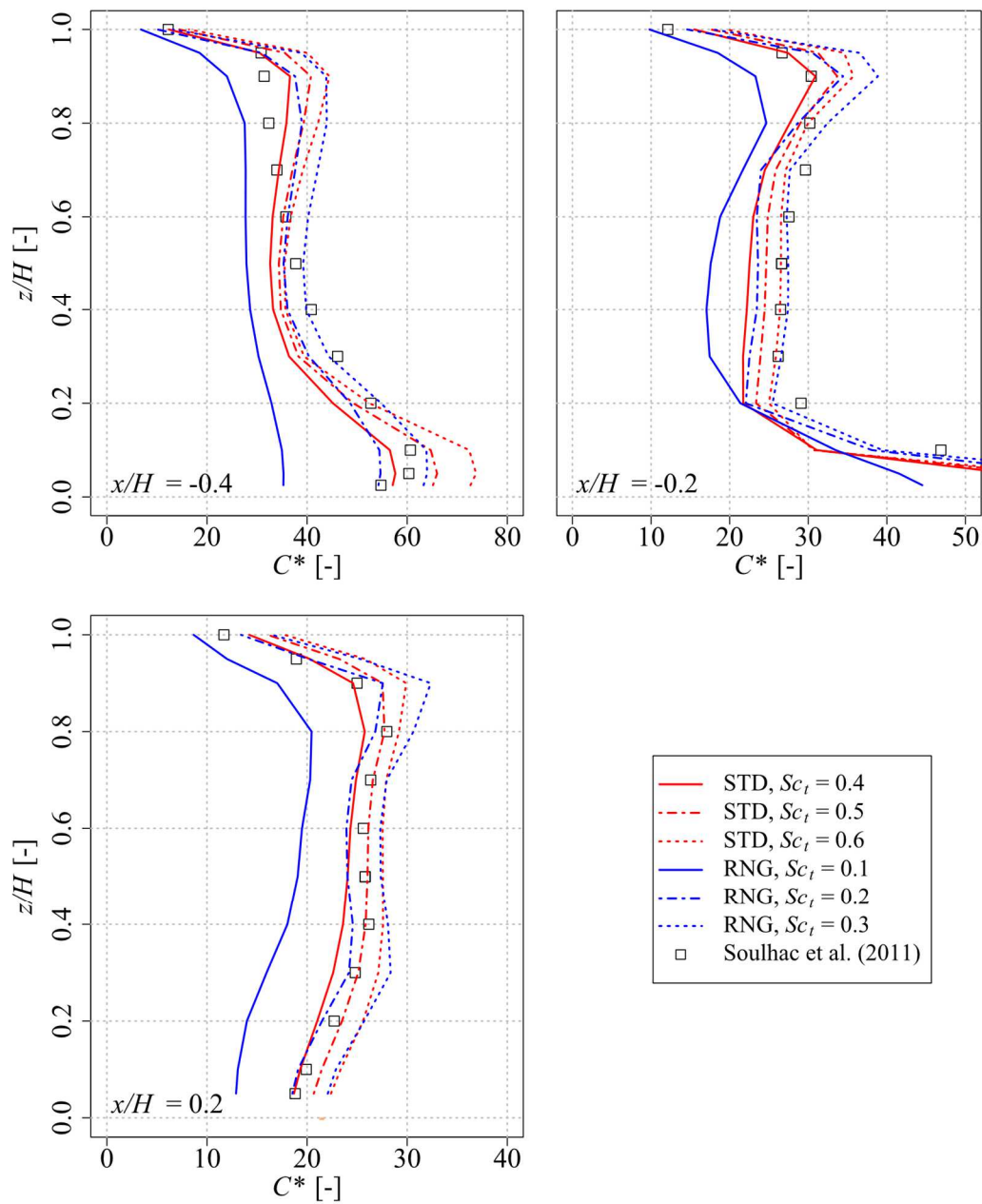
$$\frac{\partial U}{\partial t} + U.(\nabla U) = -\frac{1}{\rho}\nabla P + \nu \Delta U - \nabla . \overline{u'u'} \qquad \text{(Eq. B.20)}$$

Appendix C – Additional results for the model validation against Soulhac et al. (2001) data

▼ Additional results on the velocities comparison

▼ Additional results on the concentrations comparison

Appendix D – Air quality models performance criteria

- Fractional Bias:

$$FB = \frac{(\overline{C_O} - \overline{C_P})}{0.5(\overline{C_O} + \overline{C_P})} \qquad \text{(Eq. D.1)}$$

- Geometric Mean bias:

$$MG = exp\,(\overline{ln\,C_O} - \overline{ln\,C_P}) \qquad \text{(Eq. D.2)}$$

- Geometric Variance:

$$VG = exp\left[\overline{\left(ln\,C_O - ln\,C_p\right)^2}\right] \qquad \text{(Eq. D.3)}$$

- Normalized Mean Square Error:

$$NMSE = \frac{\overline{(C_O - C_P)^2}}{\overline{C_O} * \overline{C_P}} \qquad \text{(Eq. D.4)}$$

- Fraction of predictions within a factor of two of observations:

$$FAC2 = \frac{C_P}{C_O} \qquad \text{(Eq. D.5)}$$

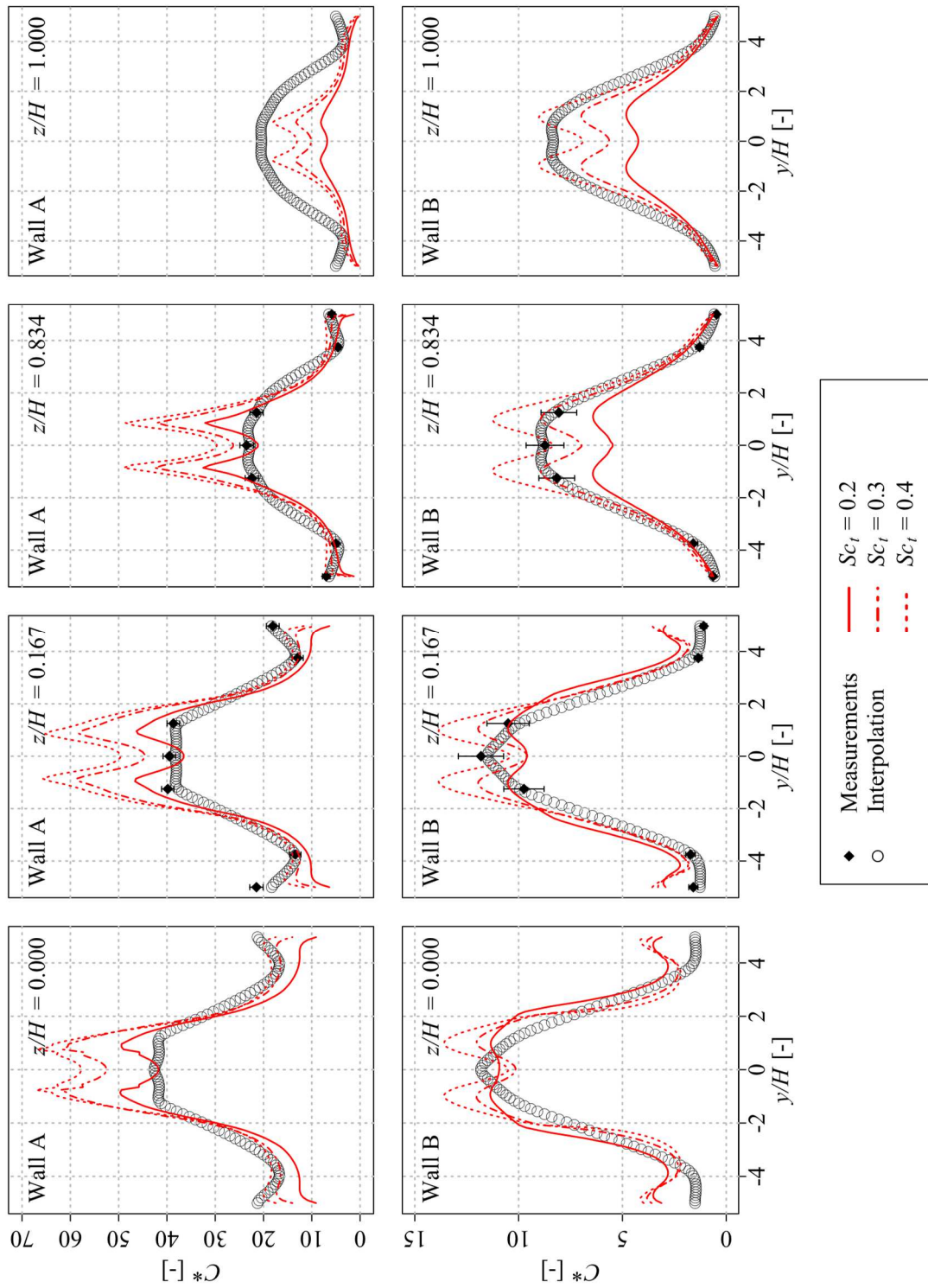- Normalized Absolute Error:

$$NAE = \frac{|\overline{C_o - C_p}|}{0.5(\overline{C_o} + \overline{C_p})} \qquad \text{(Eq. D.6)}$$

- Target

$$Target = \frac{RMSE}{\sigma_o} = \sqrt{\frac{\sum_{i=1}^{N}\left[C_{p_i} - C_{o_i}\right]^2}{\sum_{i=1}^{N}\left[C_{o_i} - \overline{C_o}\right]^2}} \qquad \text{(Eq. D.7)}$$

Appendix E – Additional results for the model validation against CODASC data

# Appendix F – Comparison between 2D and 3D results

Two simulations were compared to have an idea of the differences that could occur in terms of pollutant concentration between a 2D and a 3D street canyon and for a perpendicular wind. Both simulations correspond to a regular street canyon with $H = W$, with H the height of both windward and leeward buildings and W the width of the street. The only difference is the length of the street which is one mesh for the 2D case and is $10H$ for the 3D case. The fine mesh grid was used for both cases giving a typical dimension of the cells of $0.0125 \times H$. The number of meshes for each case was really different with around 100,000 meshes for the 2D case and 10,000,000 for the 3D case.

The dimensionless concentrations in the canyon were compared between the 2D and the 3D cases for 6 different vertical planes in the street : $y = 0H$, $1H$, $2H$, $3H$, $4H$ and $5H$, where $y = 0H$ is the middle of the street. The dimensionless concentration is calculated using (Eq. F.1) where C^* is the dimensionless concentration, C is the concentration [µg/m^3], U_H is the velocity just over the windward building and far from the canyon in the experimental setup of Soulhac et al. (2001) (2.75 m/s), H is the buildings height (0.1 m), L is the pollutant injection length and thus, the length of the street (0.0025 m for the 2D case and 1m for the 3D case) and q_m is the pollutant emission rate (1.10^{-4} µg/s).

$$C^* = C.U_H.H.L/q_m \qquad \text{(Eq. F.1)}$$

Appendix F.1 shows the results of the 2D simulation. The 3D simulation results for four given profiles : $y = 0H$, $1H$, $3H$ and $5H$, are also presented in this figure. Some differences can be seen when comparing the 2D and 3D results and also between the 3D results themselves. The concentrations seem also to be higher in the 3D case especially in the middle of the street. However, these differences seem to be quite small. To make sure of that, and also to quantify the differences, quantitative results were compared. This comparison was conducted over the parameters of interest of the study : the averaged concentrations in the street, near the windward wall, near the leeward wall and near the ground. The dimensionless concentration results are presented in Appendix F.2 for each profile considered and the difference between the 2D and 3D cases calculated with (Eq. F.2) are presented in Appendix F.3.

$$Difference = \frac{|C^*{}_{3D} - C^*{}_{2D}|}{C^*{}_{3D}} \qquad \text{(Eq. F.2)}$$
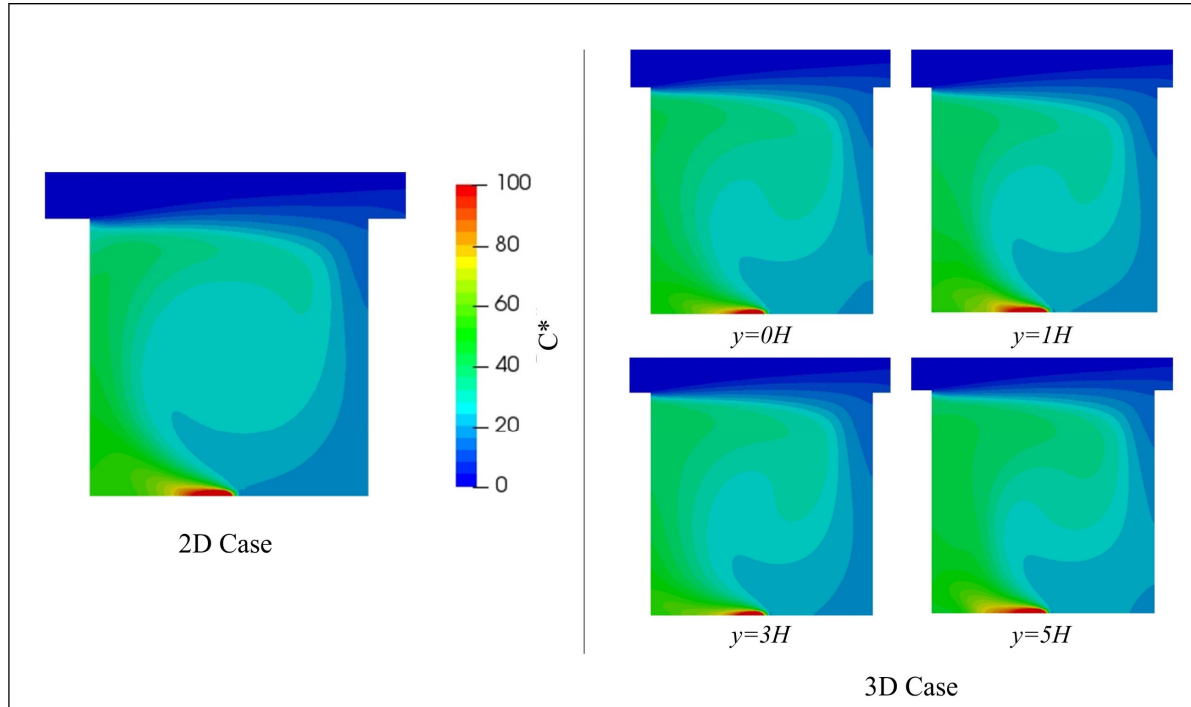
Appendix F.1 – Comparison of the dimensionless concentrations between the 2D and 3D simulation

Appendix F.2 – Averaged dimensionless concentrations over the different locations considered

Location	2D case	3D case					
		y = 0H	y = 1H	y = 2H	y = 3H	y = 4H	y = 5H
Street	27.3	29.7	29.8	29.6	29.0	31.0	34.3
Windward wall	18.4	20.0	19.2	19.6	18.9	19.2	21.3
Leeward wall	38.9	40.3	42.4	40.2	40.0	43.5	44.9
Ground	30.1	31.0	32.8	30.8	29.8	35.9	37.9

Appendix F.3 – Relative differences between 2D and 3D case for the different locations considered

Location	3D case						Mean difference	
	y = 0H	y = 1H	y = 2H	y = 3H	y = 4H	y = 5H	$0H \leq y \leq 3H$	$3H < y \leq 5H$
Street	8%	8%	8%	6%	12%	20%	8%	16%
Windward wall	8%	4%	6%	3%	4%	14%	5%	9%
Leeward wall	3%	8%	3%	3%	11%	13%	4%	12%
Ground	3%	8%	2%	1%	16%	21%	4%	18%

According to Appendix F.3, the 2D simulation give globally lower concentrations than the 3D simulation whatever the location considered. The differences are nonetheless quite small for $y \leq 3H$ with around 5% of difference for the windward and the leeward wall as well as at ground level. In the whole street, the difference increases to reach around 8%. For $3H < y \leq 5H$ the difference between 2D and 3D simulation grows to reach a maximal difference of around 20%. Thus, an acceptable difference between 2D and 3D results is obtained, which allows 2D simulations to be performed instead of 3D to reduce calculation costs.

Appendix G – Calculating the wall spacing based on the y^+ criterion

The wall spacing Δs can be calculated using Eq. G.1.

$$\Delta s = \frac{y^+ \mu}{u^* \rho}$$ (Eq. G.1)

where y^+ is the dimensionless criterion normally ranging from 30 to 500, μ is the fluid viscosity, ρ is the fluid density and u^* is the friction velocity calculated with Eq. G.2.

$$u^* = \sqrt{\frac{\tau_{wall}}{\rho}}$$ (Eq. G.2)

where τ_{wall} is the shear stress at the wall calculated with Eq. G.3.

$$\tau_{wall} = \frac{C_f \rho U_\infty{}^2}{2}$$ (Eq. G.3)

where C_f is the skin friction calculated with Eq. G.4 and U_∞ the freestream velocity.

$$C_f = \frac{0.026}{Re^{1/7}}$$ (Eq. G.4)

where Re is the Reynolds number calculated with Eq. G.5 and L the turbulent characteristic length.

$$Re = \frac{\rho U_\infty L}{\mu}$$ (Eq. G.5)

Combining all these equations together lead to Eq. G.6.

$$\Delta s = \frac{\left(\frac{2}{0.026}\right)^{\frac{1}{2}} y^+ \mu^{\frac{13}{14}}}{(\rho U)^{\frac{13}{14}} L^{-\frac{1}{14}}}$$ (Eq. G.6)

These different equations are taken from (White, 2003).

Nicolas Reiminger

3D Modelling of Air Pollution at Urban Scale

Résumé

Le but de ce travail de thèse est le développement et la validation de codes de calcul de type mécanique des fluides numérique, ou CFD (Computational Fluid Dynamics), ainsi que de nouvelles méthodologies pour évaluer la qualité de l'air en zone urbaine. Pour cela, la méthodologie RANS en écoulement transitoire (Unsteady Reynolds-Averaged Navier-Stokes) est retenue et deux nouveaux codes de calcul sont développés. Ceci inclut un modèle à convection forcée (FCS) pour modéliser les atmosphères neutres, ainsi qu'un modèle à convection mixte (MCS) pour modéliser les atmosphères stables et instables, mais aussi d'autres phénomènes tels que les effets de la végétation. Les résultats de ces deux codes de calcul sont comparés à sept cas tests expérimentaux réalisés en soufflerie, mais aussi sur le terrain et les résultats montrent que des erreurs de moins de 10% peuvent être attendues au sujet des concentrations modélisées, mais aussi que les échanges intérieurs/extérieurs peuvent être modélisés de façon performante. La question du domaine de calcul incluant les dimensions du domaine, le maillage, les conditions aux limites, les émissions ainsi que la concentration de fond dans le cadre de la modélisation de la qualité de l'air en environnement urbain est traitée dans une approche d'amélioration et, particulièrement dans le contexte de l'ingénierie. Plusieurs nouvelles méthodologies sont développées et validées incluant des méthodologies pour évaluer les concentrations en dioxyde d'azote sur la base des concentrations en oxydes d'azote, pour évaluer la distribution continue du vent sur la base de données discrètes issues des roses des vents, ou encore pour évaluer les concentrations moyennes annuelles sur la base de résultats numériques ponctuels. L'intérêt et le potentiel de ce type de modèle numérique et de méthodologies sont enfin mis en avant et des exemples d'application à des fins de conception, compréhension et diagnostic sont présentés.

Mots-clefs : CFD, RANS, qualité de l'air, pollution atmosphérique, zones urbaines, environnement.

Abstract

The aim of this thesis is the development and the validation of Computational Fluid Dynamics (CFD) solvers and new methodologies to assess air quality in urban areas. To do so, the Unsteady Reynolds-Averaged Navier-Stokes methodology (URANS) is chosen and two new solvers are built. It includes a Forced Convection Solver (FCS) for neutral atmospheres modelling and a Mixed Convection Solver (MCS) for stable and unstable atmospheres modelling where other important phenomena such as the effects of vegetation are also considered. The results of these solvers were compared to seven test cases including wind tunnel and in-situ experiments which show that an error of less than 10% can be expected on modelled concentrations, but also that indoor/outdoor exchange can be efficiently modelled. The issue of computational domain including domain extension, meshing, boundary conditions emissions and background concentrations for air quality modelling in urban areas are dealt in an improvement approach, especially in the engineering context. Numerous new methodologies are developed and validated, and their limits assessed including methodologies to assess nitrogen dioxide concentrations based on nitrogen oxides concentrations, to assess continuous wind distributions based on discrete data such as given by wind roses or to assess mean annual concentration based on punctual numerical results. The interest and potential of such numerical models and methodologies is lastly highlighted and examples of application for the purpose of design, understanding and diagnosis are presented.

Keywords: CFD, RANS, air quality, atmospheric pollution, urban areas, environment.